

Dual sourced pulsed plasmas for the deposition of high performance, low friction, hard wearing films

John Alan Freeman

Thesis submitted for the degree of PhD.

Surface Science and Coatings Characterisation Group

In collaboration with Teer Coatings Ltd

January 2012

For Susan and Poppy.

With thanks to my supervisor Peter Kelly for his support and commitment to seeing me to the end of this, to my fellow students for commiserating and celebrating with me, and to my family for their staggering patience, empathy, and support. Also with thanks to Ivanka Iordanova, Oxford University's TEM group, UCLANs surface science group, for their support and expertise.

Table of contents:

Title Page.....	Page i
Dedication & thanks.....	Page ii
Table of contents.....	Page iii
Tables.....	Page vii
Figures.....	Page viii
Abstract.....	Page xix
1. Introduction to the project.....	Page 1
1.1. Project background and aims.....	Page 1
1.2. Project outline.....	Page 2
1.3. Project plan.....	Page 4
2. Physical vapour deposition.....	Page 6
2.1. Basic PVD.....	Page 6
2.2. Sputter deposition.....	Page 7
2.3. Magnetron sputtering.....	Page 10
2.4. Reactive sputtering.....	Page 22
2.5. Film growth.....	Page 26
2.6. Effects of ion bombardment on the growing film.....	Page 28
3. Cr _x N.....	Page 32
3.1. Chromium Nitride: A transition metal nitride.....	Page 32
3.2. CrN.....	Page 35
3.3. Cr ₂ N.....	Page 36
3.4. Applications of Cr _x N.....	Page 36

4. UDP 350 deposition system.....	Page 37
4.1. System overview.....	Page 37
4.2. Vacuum system.....	Page 39
4.3. Rotary pump.....	Page 40
4.4. Diffusion pump.....	Page 41
4.5. Temperature sensors.....	Page 42
4.6. Pressure sensors.....	Page 43
4.7. Substrate holder.....	Page 44
4.8. Magnetrons.....	Page 45
4.9. Optical Emissions Monitoring (OEM) system.....	Page 45
4.10. Gas inlets and flow control.....	Page 46
4.11. Oscilloscope.....	Page 47
5. Advanced Energy Pinnacle Plus power supply.....	Page 51
6. Standard methods.....	Page 54
6.1. Standard preparations.....	Page 54
6.2. Standard deposition conditions.....	Page 55
6.3. Standard tribological tests.....	Page 55
7. System characterisation.....	Page 67
7.1. Introduction.....	Page 67
7.2. Recapping hysteresis theory.....	Page 67
7.3. Experimental.....	Page 69
7.4. Results.....	Page 73
7.5. Discussion.....	Page 82

8.	Influence of the pulsed substrate biasing on deposition and coating performance...	Page 85
8.1.	Introduction.....	Page 85
8.2.	Experimental.....	Page 86
8.3.	Results.....	Page 92
8.4.	Discussion.....	Page 117
8.5.	Conclusion.....	Page 120
9.	Pulsed substrate bias deposition as part of layered coating architectures.....	Page 122
9.1.	Introduction.....	Page 122
9.2.	Substrate preparation, deposition conditions, and analytical techniques.....	Page 122
9.3.	Experimental.....	Page 123
9.4.	Results.....	Page 128
9.5.	Discussion.....	Page 138
9.6.	Conclusions.....	Page 140
10.	The effects of internal stress on coating tribology, and drill tests of coatings.....	Page 141
10.1.	Introduction.....	Page 141
10.2.	Experimental.....	Page 141
10.3.	Results.....	Page 144
10.4.	Discussion.....	Page 149
10.5.	Conclusions.....	Page 151
11.	Overview and discussion.....	Page 152
11.1.	Introduction.....	Page 152
11.2.	Hysteresis and ion chemistry.....	Page 153

11.3.	Deposition and testing of simple coatings.....	Page 156
11.4.	Development and testing of layered coatings.....	Page 159
12.	Conclusions.....	Page 165
12.1.	Introduction.....	Page 165
12.2.	Findings.....	Page 166
12.3.	Suggestions for further investigations.....	Page 167
13.	References.....	Page 168
14.	Appendix A: Optical microscopy of coating surfaces.....	Page 185
A.1:	Introduction.....	Page 185
A.2:	Experimental.....	Page 185
A.3:	Results.....	Page 186
A.4:	Discussion.....	Page 191
A.5	Conclusions.....	Page 193
15.	Appendix B: Alternate pulsing regimes, effects of pulsing during ion etching.....	Page 194
B.1	Introduction.....	Page 194
B.2	Experimental.....	Page 194
B.3	Results.....	Page 196
B.4	Discussion.....	Page 200
B.5	Conclusions.....	Page 200

	pulse rate	
B.3	Experimental array 2, designed to test the effects of pulse rate during ion etching on coating adhesion.	195
B.4	Experimental array 3, designed to test the effects of etching bias on coating adhesion	196

List of Figures: (Figures prefixed with ‘A’ or ‘B’ appear in appendices A or B respectively)

Figure: Heading: Page:

2.1	The most basic PVD system consists of a chamber which is evacuated to the level of molecular flow regime. The coating material is held in a crucible, usually composed of a refractory metal such as tantalum. The crucible is heated, by means of a high current being passed through it, and the substrate to be coated is placed within direct line of site of the coating material. The molecular flow regime ensures that the vaporised material follows straight line paths. (Image courtesy of betelco.com)	7
2.2	Diagram of a simple plasma diode. From left to right the annotated features are: The cathode; an electrode carrying a negative bias. Aston Dark Space: A region separating the cathode glow and cathode, where electrons emitted by the cathode have insufficient energy to excite gas atoms. Cathode glow: A region where electrons are colliding, and recombining, with ions emitting photons. Cathode dark space: A region of lower electron density, and so fewer collisions with ions. Negative glow: A region where accelerated electrons have gained enough energy to excite gas atoms. Faraday space: As we move along the discharge the electrons have less energy to excite gas atoms, and the negative glow gradually fades. Positive column: An extended luminous region where the electric field provides just enough energy to excite the gas atoms. [18].[19] (image courtesy of Ian Tresman)	8
2.3	The Paschen curve for five commonly used gasses. The x-axis is pressure multiplied by distance between the electrodes, the y axis is potential difference required to strike a plasma (breakdown voltage).	9
2.4	Simplified schematic of a basic sputter system	10
2.5 a & b	A cross section of a sputter magnetron, shown in figure 2.5 a. Behind the target and the backing plate are placed two groups of magnets, an inner and outer ring, with opposite poles facing the surface. This results in looped magnetic field lines extending out from the target, through the chamber space, and back into the target. These field lines trap electrons close to the target surface, which ionise the gas in the chamber much more densely close to	13

	the target surface than in the rest of the chamber. A view of the set up from above shows that this results in a concentrated ‘race track’ region of sputtering (figure 2.5 b).	
2.6	The structure of a plasma approaching an isolated surface and the corresponding change in plasma potential.	15
2.7	The zone of enhanced electron density	15
2.8	A simplified schematic of the sputter process. Positively charged ions of the working gas, in this case Argon (shown in red) are created by random events, or by electrons emitted by the negatively charged target surface. These ions are then drawn towards the target surface, gaining kinetic energy from the electric field as they accelerate. As an argon ion strikes the surface it transfers kinetic energy to the target atoms, which follows a series of dislocations. Where one of these dislocations returns to the surface with sufficient energy an atom of target material is sputtered into the body of the chamber. Image courtesy of Alacritas-Consulting.com.	18
2.9	A cross sectional diagram of the magnetic field lines emitted from a balanced magnetron. The magnetic field lines are shown in deep blue. The density of the plasma during sputtering is shown by graded colours; pink/purple for intense, yellow/green for moderate, and blue for background. The rectangular block at the bottom of the image is the magnetron and target surface itself. All the field lines that leave the targets surface return to it, giving a tightly confined plasma close to the target surface. Image courtesy of www.plasmionique.com	19
2.10	A cross sectional diagram of the filed lines and plasma density emitted from a type 1 magnetron. Magnetic field lines are shown in deep blue, plasma density is shown colour coded, purple/pink being most intense, yellow/green being moderate, and blue being back ground .In this configuration the inner ring of magnets is more powerful, and many of the field lines terminating at the inner ring extend to infinity. This results in a relatively weak, poorly confined plasma, extending into the chamber. Image courtesy of www.plasmionique.com	20
2.11	Cross sectional diagram of plasma density and magnetic field lines emitted from a type 2 unbalanced magnetron. Magnetic field lines are shown in deep blue, plasma density is shown colour coded; Black/purple/pink is most intense, yellow/green is moderate, blue is background. In this configuration the outer ring of magnets is more intense than the inner, resulting in many of the field lines that terminate at the outer ring extending away from the target. This results in a strong but ill confined plasma, stretching away from the target and into the chamber space. Image courtesy of http://www.plasmionique.com/magnet.htm .	20

2.12	A cross sectional diagram of closed field configuration multi-magnetron system. Magnetic field lines shown in red. Each magnetron has an outer magnet ring with the opposite polarity to that of the one next to it. This results in closed magnetic field surrounding the substrates in the centre, which greatly enhances plasma density. Image courtesy of pvd-coatings.co.uk	21
2.13	An idealised graphic of a system pressure hysteresis loop for a typical oxide system	24
2.14	Hysteresis curves for an aluminium oxide DC reactive sputtering system. Image adapted from material courtesy of [31].	25
2.15	Thornton structure zone model. Along the right hand axis the ratio of substrate temperature to melting/decomposition temperature of the film increases to the right. Along the left hand the working gas pressure (in millitorrs) increases to the left. In zone 1 the film structure consists of widely spaced columns of film growth. In zone T, a later addition to the model, the film consists of intertwined fibrous grains. In zone 2 the structure is of closely packed columnar grains, and in zone 3 the grains are in contact with each other, but still discernable. Beyond zone 3 the structure is fully dense and 'glass-like'. Image courtesy of [152]	28
3.1	Transition metals, comprising of the d-block, shown highlighted on the periodic table. Image courtesy of colorado.edu	33
3.2	Phase diagram for the Cr-N system.	34
4.1	Top: A simplified cross section view of the main deposition chamber of the UDP 350. Bottom: A plan view of the chamber. The chamber is portrayed with the planar (as opposed to planetary motion, see below) substrate holder in place. Sensor ports set into the chamber walls have not been depicted, for the sake of clarity.	38
4.2	Annotated photographs of the magnetrons: (1) Top view showing the magnetrons set in place in the sputter chamber wall, (2) Rear view showing the magnetron removed with the arrangement of cooling pipes, (3) with the target face removed exposing the (empty) coolant reservoir.	39
4.3	A schematic of the UDP 350 sputter system, showing the diffusion pump, main chamber, connecting feeds, main pressure gauges, Ar inlet and N ₂ (reactive gas) inlet.	40
4.4	A simplified cross section of the operation of a water cooled diffusion pump. Image courtesy of the society of vacuum coaters.	41
4.5	The fibre-optic feed through allowing egress of FISO signals from the chamber, shown set down on the workbench.	42

4.6	A simplified cross section of the Baratron capacitance manometer: As the diaphragm is deformed the capacitance of the attached capacitors changes, providing an electronic reading of pressure	43
4.7	The vertical substrate holder	44
4.8	The planetary motion substrate holder.	45
4.9	A simplified schematic of the OEM feedback loop: light of a particular frequency from the plasma travels along a fibre optic cable to the OEM. The OEM signal is passed to the process control box, which ascertains whether the intensity of the frequency the OEM is monitoring is above or below the setpoint in its memory. The process control box then signals the piezoelectric valve to open or close depending on the intensity measured	46
4.10	The TDS 3014 oscilloscope with current and voltage probes attached	47
4.11	The power line attachment, which allows the oscilloscope to safely measure high currents	48
4.12	The current probe head, with labelled components	48
4.13	A close up of the oscilloscope voltage probe head with the conducting hook extended	49
4.14	The oscilloscope voltage probe head with its earth lead.	49
5.1 a & b	Oscilloscope traces of the current (figure 5.1a) and voltage (figure 5.1b) of one channel, supplying the substrate side of the UDP 350 deposition system, of the AE Pinnacle plus power supply during pulsed operation. Pulse rate is set to 100 kHz .Substrate bias is controlled to a time averaged 100V set point	52
6.1	The Teer Coatings Limited ST3001 scratch test unit	55
6.2	The single pass scratch adhesion tests. Image courtesy of PVD-coatings.co.uk	57
6.3	An example of the initial stages of cracking around the edges of the scratch track	57
6.4	The beginning of continuous spallation around the edge of the scratch track, accompanied by intermittent spallation along the bottom of the track. Indenter motion is from right to left.	58
6.5	A typical T_{c3} for a CrN coating on tool steel. The beginning of continuous perforation of the coating at the bottom of the wear track is seen, accompanied by massive spallation around the edges of the scratch track. Stylus motion is right to left. The discolouration is caused by remnants of the cleaning solution used to remove debris.	59

6.6	The Micro Materials nano-indentation platform, without its climate controlled housing. Image courtesy of Micro Materials.	60
6.7	A simplified schematic of the nano indenter apparatus	61
6.8	The Dektak profilometer	63
6.9	A simplified diagram of the diffraction process	64
6.10	The XRD trace for table salt, with 2 theta along the x-axis and X-ray reflection intensity along the y axis. Image courtesy of universe-review.ca	66
7.1	An idealised graphic of how hysteresis behaviour is expected to present itself. Image courtesy of Alacritas Consulting.	68
7.2	Voltage probe connection to the substrate holder mechanism	69
7.3	Image of the substrate during pulsed substrate bias operation. Four points on the camera image are indicated, and were monitored over the course of one pulse	72
7.4	The change of target bias with time, for three nitrogen flow rates: Low (5 SCCM), Medium (9 SCCM) and high (12 SCCM). Conditions are standard, pulse regime is DC.	73
7.5	The change of nitrogen partial pressure with time, for three nitrogen flow rates: Low (5 SCCM), Medium (9 SCCM) and high (12 SCCM). Conditions are standard, pulse regime is DC	74
7.6	The change in target bias with time, for four nitrogen flow rates. 0, 5, 8 and 11 SCCM of nitrogen flow correspond to 100%, 70%, 50% and 45% of the full metal OEM signal respectively	75
7.7	The change in intensity of the 425 chromium plasma emission line (the basis for OEM setpoint control) with inflow of nitrogen to the system in SCCM. Conditions are standard, pulse mode is DC, and substrate bias is -65 volts.	76
7.8	The increase in nitrogen partial pressure with increasing nitrogen flow rate. Pulse regimes are: DC, 100 kHz, and 300 kHz. The substrate bias is -70 volts, and conditions are standard.	76
7.9	XRD spectra for Cr _x N coatings deposited with 1 and 5 SCCM of N ₂ inflow. Peaks relating to the presence of Cr-N compounds are labelled.	77
7.10	The change in atomic % ratio of Cr to N with reactive gas flow rate during sputtering. Three groups of coatings are shown; two were deposited with substrate bias pulsing	77

	applied at 100 kHz and 200 kHz, and one was deposited by DC sputtering.	
7.11	Target bias hysteresis curves by N ₂ inflow rate for DC and pulsed substrate bias at 100 kHz.	78
7.12	Target bias hysteresis curves by N ₂ inflow rate for 3 alternate pulsing regimes	79
7.13	Target bias hysteresis curves by full metal signal percentage	79
7.14	Substrate bias and current waveforms at 100kHz substrate bias pulse frequency -100V substrate bias.	80
7.15	Bias and current waveforms at 100 kHz substrate bias pulse frequency, -400V substrate bias	80
7.16	Bias and current waveforms at 300 kHz substrate bias pulse frequency, -500V substrate bias	81
7.17	The change in intensity of the 750 nm wavelength, at each imaging point, with time. Imaging points are shown in relation to the substrate in figure 7.3. The change in intensity at each point is compared with the voltage against time waveform for substrate bias, shown as the black trace. From left to right, top to bottom: Point one, point two, point three and point four. Target power was controlled at 500w.	81
8.1	The change in substrate current with frequency for four inflow rates of N ₂ (reactive gas in MFC set point flow control mode). Substrate bias was set at -100V	92
8.2	The change in substrate power with substrate bias for the available range of substrate bias pulsing frequencies. The UDP 350 is operated here in non-reactive mode	93
8.3	The change in substrate current with substrate bias for the available range of substrate bias pulsing frequencies. The UDP 350 is operated here in non-reactive mode	93
8.4	Variation of substrate current with substrate bias and on time (duty cycle %), at bias pulse rate of 350 kHz.	94
8.5	Variation of substrate current with substrate bias and on time (duty cycle %), at substrate bias pulse rate of 250 kHz.	94
8.6	Substrate voltage and substrate current waveforms against time, during reactive sputtering. Pulse frequency was 100 kHz, 50% on time duty cycle	95
8.7	Comparison of substrate current and bias in reactive and non-reactive sputtering, with a substrate bias set-point of -100V. Pulse frequency was 100 kHz, 50% on time duty cycle	98

8.8	Comparison of substrate bias and current waveforms to electron density (n_e), Sputtering was done in non reactive pulsed DC substrate bias mode, with a substrate bias of -70V. The red line indicates the equivalent measurement when sputtering is done in DC mode. Pulse frequency was 100 kHz, 50% on time duty cycle	97
8.9	Comparison of electron temperature to substrate current and bias waveforms, performed during pulsed substrate bias operation. The red lines and markers indicate the equivalent readings for DC operation. Pulse frequency was 100 kHz, 50% on time duty cycle	98
8.10	Comparison of ion density to substrate bias and current waveforms. Red lines indicate equivalent readings from DC operation. Pulse frequency was 100 kHz, 50% on time duty cycle	99
8.11	Electron density against time for two bias values in nonreactive mode (-70 V and -100V) and three bias values in reactive mode (-70V, -100V, and -200V). In reactive mode the nitrogen content is equivalent to that of an OEM signal of 40% FMS or 9 SCCM of N ₂ flow in MFC setpoint flow control mode. Pulse frequency was 100 kHz, 50% on time duty cycle	100
8.12	Comparison of electron temperature against time readings for reactive and non reactive sputter modes, across a range of dc substrate bias setpoints. Pulse frequency was 100 kHz, 50% on time duty cycle	101
8.13	Comparison of floating potential across a range of substrate bias setpoints, in reactive and non-reactive sputtering. Pulse frequency was 100 kHz, 50% on time duty cycle	102
8.14	Comparison of plasma potential readings, across a range of substrate bias set points, for reactive and non reactive operations. Pulse frequency was 100 kHz, 50% on time duty cycle.	103
8.15	Comparison of ion densities, for a range of substrate bias setpoints, for reactive and non reactive operation. Pulse frequency was 100 kHz, 50% on time duty cycle	104
8.16	The variation in emission with time on three wavelengths corresponding to the Ar (I) emission. Sputter mode was non reactive, with a substrate bias pulse rate of 100 kHz and a substrate bias of -200V.	105
8.17	The variation in emission with time on three wavelengths corresponding to the Cr (I) emission. Sputter mode was non reactive, with a substrate bias pulse rate of 100 kHz and a substrate bias of -200V.	106
8.18 a	The percentages of crystal planes oriented relative to the film surface. DC biased CrN samples compared to pulsed biased CrN samples top,	107 –
& b	DC biased Cr ₂ N samples compared to pulsed biased Cr ₂ N samples bottom.	108

8.19	Comparison of residual stresses between DC films and pulsed bias films	109
8.20	A comparison of the XRD traces for Cr ₂ N coatings deposited using DC and pulse substrate bias	109
8.21	Typical SEM fracture cross sections of films deposited at DC bias (left) and 350 kHz bias (right). Substrate bias was -70V.	110
8.22	The change in wear with time for pulsed and dc deposited CrN coatings at -70V and -100V substrate bias. Pulse rate was 350 kHz.	111
8.23	The L _{c3} critical loads for total CrN coating failure (L _{c3}) for dc and pulsed deposited coatings at -100 V and -70V substrate bias.	112
8.24	Variation in Cr ₂ N coating adhesion with substrate bias for two different pulse regimes at -100 V and -70 V substrate bias. Critical load given is L _{c3} , Critical load for total film failure	112
8.25	The coating hardness for CrN coatings deposited using dc and pulsed substrate bias, for bias values of -70V and -100V.	113
8.26	The coating hardness for Cr ₂ N coatings deposited using dc and pulsed substrate bias, for bias values of -70V and -100V	113
8.27	Variation in frictional coefficient with time for CrN coatings deposited using pulsed and DC sputtering. Substrate biases used were -100V and -70V	114
8.28	Average wear rates over 20 minutes for dc and pulsed CrN coatings deposited at -70V	114
8.29	Average wear rates over 20 minutes for dc and pulsed CrN coatings deposited at -70V	115
8.30	An optical micrograph of a typical wear track on a coated tool steel coupon. The coating was a 2 micron deep monolithic Cr ₂ N coating deposited at a substrate bias of -100V, with a pulse frequency of 300 kHz.	116
8.31	The change in temperature with time for two substrate bias values (-20v and -60v) and two substrate bias pulse rates (0 kHz and 175 kHz).	117
9.1	A schematic of the array 2 coatings.	125
9.2	Effect of pulse regime and layer stoichiometry on wear rate. The wear rates averaged over 20 minutes, for 3 coating architectures. Rates of wear were calculated by profilometry from 4 random transects of the wear track	128
9.3	Effect of pulse regime and layer stoichiometry on hardness. The surface hardness for 3 coating architectures. Hardness was found by nanoindentation, from a grid of 25 indents	129

	with 25 micron separations	
9.4	Effect of pulse regime and layer stoichiometry on coating adhesion. The critical loads for total failure of 3 coating architectures. The critical loads given are the averaged values of 3 scratch tracks taken at the edges and the middle of the substrate	129
9.5	Internal stress in array 1 coatings as determined by XRD peak shift and peak broadening	130
9.6	XRD trace, in Bragg Brentano mode, of sample 2a	131
9.7	Figure 9.7: SEM micrograph of coating 3a on steel coupon . A section of the coupon was extracted, cut, polished, and set into conducting resin to allow for a true cross section image to be taken. Linear features suggestive of columnar growth extend from the dc deposited CrN layer into the pulsed deposited Cr ₂ N layer for a short distance. Some delamination between the interlayer and the substrate is visible.	131
9.8	High resolution TEM image of sample 3a. Top left: wide angle view of layer 2. Top right: close up of layer 2. Bottom left: wide angle view of layer1. Bottom left: close up of layer 1. These are cross sectional views of coating sections extracted by focused ion beam milling, hence the visible structures are crystal grains, not column tops.	132
9.9	Internal stress in array 2 coatings as measured by peak shift and peak broadening	133
9.10	The abundance of the {200} in plane texture for each array 2 coating.	133
9.11	XRD spectra of sample 1b in Bragg-Brentano and glancing angle mode.	134
9.12	Variation of critical load with interlayer depth for films deposited with a bias pulse of 300kHz	135
9.13 a & b	Optical micrographs of the failure points for 50 nm interlayer coating (figure 9.13a) and 500 nm interlayer coating (figure 9.13b).	136
9.14	The changes in frictional coefficients with applied load as the scratch tests for coatings with deep and shallow interlayers progress	137
9.15	Variation in coating adhesion between coatings with a graded interlayer-coating boundary and those with an ungraded boundary	138
10.1	Wear rates for a range of coating architectures deposited during the course of this study.	142
10.2	Coating stress against sample number, as measured by peak shift and broadening of the {200} peak on XRD spectra	144

10.3	Wear rate against layer 1 depth/sample number	145
10.4	Coating adhesion, as found by single pass scratch testing, against layer 1 depth	145
10.5	Hardness, as measured by the average of 25 nanoindentations, against layer 1 depth. Error bars shown are 1 s.d.	146
10.6	The response of the array 2 coatings and three standards (Uncoated drill bits, standard CrN coating, CTiAlN coating) to drill testing. From each set of drill bits tested the minimum, maximum, and average responses are given. Standard coatings were supplied by Teers Coatings Ltd	147
10.7	SEM micrograph of the cutting edge of drill bit with coating 1b, post failure. Left, raw image, Right annotated.	148
10.8	SEM micrograph of the cutting edge of drill bit with coating 3b, post failure. Right, raw image, left annotated	149
A.1	Optical image of the surface of coating 1a. The image is somewhat overexposed due to the very smooth reflective metallic nature of the surface. The image measures 500 microns along its bottom edge.	186
A.2	Fracture cross section of coating 1a. The coating partly delaminated near the fracture, apparently lifting away sections of substrate material, visible in the bottom left hand corner.	186
A.3	Optical micrograph of coating 2a. The bright material is the coating, the darker material is the substrate. The image measures approximately 500 microns along its bottom edge.	187
A.4	SEM micrograph of the surface fractures on coating 2a	187
A.5	Optical microscope image of the surface of coating 3a. The light toned material is the coating, the darker toned areas with light centres may be short compression fractures. The image measures approximately 500 microns along its bottom edge	188
A.6	SEM image of the fracture cross section of coating 3a	188
A.7	Optical image of the surface of coating 4a. The image measures approximately 500 microns along its bottom edge	189
A.8	SEM image of the fracture cross section of coating 4a.	189
A.9	Optical microscope image of coating 5a. No substrate is visible in this image, the light and dark areas are caused by upwards buckling (telephone chord defects) of the coating. The	190

	image measures approximately 500 microns along its bottom edge.	
A.10	SEM image of the fracture cross section of coating 5a. Only the coating is visible here as the coating had delaminated away from the fracture for several millimetres in every direction	191
A.11	SEM image of a heavily delaminated section of coating 5a.	183
B.1	Top left: DC Comparison. Top right: Dual cathode pulsing. Bottom left: Target pulsing. Bottom right: Substrate pulsing. Images of the synchronously pulsed sample are unavailable as the sample suffered massive spontaneous delamination shortly after being deposited	196
B.2	Deposition rates against pulse regime	197
B.3	Mean surface deviation from average level for four films deposited under each of the four pulsing regimes.	197
B.4	Hardness values for films deposited under four pulsing regimes	198
B.5	L_{c3} Critical loads for films deposited under four pulsing regimes	198
B.6	Variation in L_{c3} with substrate bias pulse rate during ion cleaning	199
B.7	The change in coating adhesion with substrate bias during ion etching	199

Thesis Abstract:

The work described in this thesis formed part of a larger collaborative project between Manchester Metropolitan University, the University of Liverpool, and our industry partner Teer Coatings Ltd., which was entitled “Dual source pulsed plasmas for the production of ultra-high performance coatings.”

Closed field unbalanced magnetron sputtering (CFUBMS) has become a mainstay of sputter deposition techniques. However improvements and new approaches are always being sought. This project has focused on the application of one variation, pulsed substrate bias (PSB) deposition, to the reactive sputter deposition of chromium nitride. Cr_xN is of great interest to industry, as it offers similar wear and corrosion resistance to the better known TiN, but with greater thermal stability. Pulsed substrate biasing is a relatively recent technology. It potentially allows scope for improvement of coating structure, and hence tribology, through greater ion bombardment of the coating during deposition.

The initial aims of this project were: To characterise the pulsed CFUBMS system during reactive deposition of Cr_xN ; to gain an understanding of the plasma behaviour and processes during deposition; to understand the influence of the pulsed plasma over coating microstructures, and relate relevant changes in these microstructures to changes in coating tribology. With the resultant data the project then turned to identifying the strengths and weaknesses of PSB deposition, and finding means to enhance coating performance using the technique.

Plasma studies were largely undertaken at the University of Liverpool, using optical spectrometry, CCD camera imaging, and Langmuir probe measurements. Based on these findings 5 coatings were deposited at MMU, and subjected to structural and tribological tests such as scratch adhesion testing, nanoindentation, thrust washer wear testing, surface profilometry, and optical microscopy. Selected coatings were deposited onto cutting tools (twist drills) and tested to failure in a simulated industrial environment. Coating microstructure was investigated at MMU by SEM and EDS. Selected coatings were investigated by XRD at the University of Sofia, and by TEM at Oxford University.

The pulsed CFUBMS system is shown to be adequately stable to reactively sputter Cr_xN . PSB deposition is shown to increase ion bombardment at the substrate. Enhanced ion bombardment is in turn related to the growth of a denser coating, with a more ordered crystallographic structure with greater surface hardness. However the PSB approach is also shown to increase compressive stress within the coating, and potentially damage effective adhesion. As a consequence we have sought to combine the DC bias and PSB methods, as well as changes in coating stoichiometry, in a series of layered coatings. The best performing of these layered coating architectures is significantly harder wearing than standard CrN coatings, and approaches the wear resistance of CrTiAlN coatings in drill tests.

Pulsed substrate bias deposition is a potentially powerful addition to the portfolio of sputter coating techniques. Here it has been successfully applied to enhance the microstructure, tribology, and wear resistance of Cr_xN coatings.

1.1 Introduction to the project:

1.1 Project background and aims:

Many of the challenges faced by engineering and science are related to the properties of materials at their surfaces. A simple example would be the machining of high speed tool steel ingots. Saw blades consisting of a material with the mechanical and thermal properties to continuously cut tool steel over the kinds of periods of time required by industry, without failure, would need to be composed of expensive high performance alloy. Alternative cutting methods', such as laser cutting, plasma torch, or water jet cutting carry their own limitations which may render them unsuitable. In order to cut high speed tool steel with a blade of less expensive material (e.g. tool steel itself) we must look to the surface properties of the material; The working edge/face of the blade is where mechanical wear, thermal damage, and corrosion due to heat and atmospheric vapour take place. Treating the surface to improve properties can greatly extend the working life and tolerances of a blade.

One of the most common means of surface treatment is surface coating. All surface coating methods deposit a layer of material, often only microns deep, with superior surface properties to the bulk, resulting in improved performance. A great variety of coating methods and materials exist, and to give a meaningful description of each would be a considerable work in its own right, outside the scope of this text. However it can be said that thin film technologies fall into two broad categories:

1. Physical Vapour Deposition (PVD), where the coating material is transported in a reduced pressure regime from a source to the surface to be coated (referred to as the substrate) by physical means, such as a state change from solid to gas phase and back to solid.
2. Chemical Vapour Deposition (CVD), where the coating material is formed at the substrate by means of either chemical reactions between 2 or more precursors, or the decomposition of a single precursor, often at high temperatures.

This project is focused on a relatively new variant of PVD; **Pulsed Magnetron Sputtering (PMS)**. Generally, in magnetron sputtering processes the term 'pulsed' refers to the nature of the driving voltage waveform at the magnetron target, but in this project the effect of

pulsing the bias voltage at the substrate has also been studied. The two primary materials investigated here with regards to pulsed biasing are the two main phases of chromium nitride; NaCl cubic crystal structured CrN and hexagonally structured Cr₂N (dichromium nitride). Chromium nitride is a coating material of particular interest to industry, as it has similar hardness and wear resistance to the more commonly applied titanium nitride, but greater thermal stability and corrosion resistance [1,2].

The aims of the project were:

- To study the relationship between the power supply input parameters, the plasma chemistry within the chamber, and the properties of the deposited coatings.
- To test and validate the application of pulsed magnetron sputtering and pulsed substrate biasing to hard wearing Cr_xN coatings.
- To define optimum conditions for the production of Cr_xN .
- To measure the performance of PMS deposited Cr_xN coatings against those deposited by similar sputter deposition methods.

This project has taken place with the support of Teer Coatings Ltd, and as part of a larger EPSRC-funded investigation into pulsed substrate biasing primarily in collaboration with the University of Liverpool. Other collaborators include the Colorado School of Mines, the University of Oxford, the Open University, and the University of Central Lancashire.

1.2 Project Outline:

Chapter 2: Details the principles of physical vapour deposition (PVD), its application to coatings technology, and the development of the PMS system

Chapter 3: Provides a description of chromium nitride, and a description of its advantages and disadvantages as a hard wearing coating.

Chapter 4: Describes the form and function of the TEER UDP 350 deposition system, and all the modifications made to it during this project.

Chapter 5: Details the Advanced Energy Pinnacle Plus power supply, its pulsing modes, its set point control, and the application to PMS.

Chapter 6: Outlines the project plan, and details standard deposition conditions, standard substrate preparations, and the standard tribology and microstructure tests applied.

Chapter 7: Describes the effects of pulsed substrate biased sputtering on the Cr-N system plasma and the studies of the waveform delivered by the pinnacle plus power supply. The effects of reactive gas content and PSB upon stoichiometry and crystal structure in simple Cr_xN coatings are also presented.

Chapter 8: Presents observations on the influence of PSB upon ion current drawn at the substrate, and a more detailed investigation of the effects of PSB upon the sputter plasma using Langmuir probe and optical spectrometry. An array of simple Cr_xN coatings deposited under varying conditions of substrate bias and pulse rate are investigated to relate changes in microstructure to effects on tribology.

Chapter 9: Details experiments involving layering coatings by pulse regime (d.c. and PSB) and by stoichiometry. The effects upon microstructure and tribology are reported. In addition the effects of the addition of a Cr interlayer, the effects of interlayer depth, and the influence of grading boundaries between layers are reported.

Chapter 10: Presents the tribological effects of layering coatings by stoichiometry and pulse regime in tandem, and compares the effectiveness in drill tests of the coating architectures developed in this project to industry standard CrN and CrTiAlN coatings provided by Teer Coatings. SEM analysis of drill bit cutting edges post wear is presented.

Chapter 11: Discussion section.

Chapter 12: Conclusions.

References.

Appendix A: Presents preliminary evidence of the occurrence of internal stresses in Cr_xN coatings, and the effects of stoichiometry on these stresses.

Appendix B: Appendix to chapter 9: Reports the influences of PSB ion etching, and alternate pulse regimes (for example target and substrate both pulsed in phase) are reported.

1.3: Project plan:

As a research project is an exploration into the unknown a definitive plan is almost impossible. However from the beginning of the project, knowing it to have a 3 year span, a simple structure was laid out:

April 2007 to November 2007:

1: Literature review and familiarisation with the equipment, techniques and concepts in magnetron sputtering. Familiarisation with the concepts involved in producing and optimising thin hard coatings. Literature review, focussing on the approaches used by other researchers to improve the performance of thin hard transition metal nitride coatings, chiefly Ti_xN and Cr_xN .

2: Hysteresis work, characterisation of the sputter system, deposition and analysis of chromium coatings onto various substrates, deposition and analysis of simple CrN coatings onto various substrates. Knowledge of substrate preparation, introduction to basic analysis techniques such as tribological tests, SEM and XRD.

November 2007 to November 2008.

1: Work in conjunction with the plasma physics group under Professor James Bradley to gain greater understanding of the plasma processes at play in the on and off phases of the pulse. Combine this knowledge with experience of simple Cr_xN coatings to better understand the effects of pulsed plasmas and narrow the range of deposition conditions to discover optimums in terms of wear response.

2: Progress to using the effects of pulsed plasmas to deliberately influence coating performance and tailor structures to improve wear response.

November 2008 to November 2009:

1: Using the knowledge gained so far identify the optimum conditions for depositing monolithic coatings of CrN and Cr_2N . Understand the effects of pulsed plasmas on the substrate and growing film and apply this knowledge to produce novel coatings with improved wear resistance.

November 2009 to April 2010;

Knowledge transfer to Teer Coatings and begin write up.

In addition to the above goals the project was structured around quarterly meetings with the Liverpool University Plasma Physics Group, and the reports these generated.

Chapter 2: Physical vapour deposition (PVD)

2.1: Basic PVD

This project utilises magnetron sputtering techniques, which are examples of physical vapour deposition processes. Fundamentally, sputtering involves the same three stages as other PVD processes:

1. Conversion of coating material to the vapour phase.
2. Transport of the vapour flux to the surface to be coated.
3. Condensation of the vapour flux on the surface, i.e. nucleation and film growth.

In all cases these stages are performed in a vacuum. Vacuum conditions are needed as almost all materials are highly reactive at their vaporisation temperatures, hence exposure to atmospheric oxygen will result in immediate oxidation. To further improve conditions any residual gas in the coating apparatus can be replaced by an inert gas, such as argon. The pressures used may be such that any residual gas in the chamber is in free molecular flow regime (as opposed to the fluid flow regime encountered at higher pressures). Free molecular flow regime (FMFR) is reached when the density of gas particles in the chamber is low enough that the average distance travelled by a particle before a collision with another particle (known as the mean free path) is greater than the dimensions of the chamber [4,3]. However it should be noted that it is possible to sputter or evaporate materials at pressures in the high 1Pa range and at that pressure the mean free path is only a few millimetres.

The most basic PVD system, vacuum evaporation, comprises a crucible in which the coating material is held, enclosed within a vacuum chamber (Figure 2.1). The surface to be coated is placed within a direct line of sight of the coating material. Line of sight is required as under FMFR the gas phase coating particles will travel in straight lines.

The crucible is heated, usually by a high electric current, although in the case of e-beam evaporation heating is achieved by a focused beam of electrons [5]. As the coating material vaporises, monolayers of the coating material will build upon any surface with a direct line of sight to the crucible, and over time the coating will build in thickness [3].

This basic form of PVD has drawbacks, chiefly that the composition, deposition, and microstructure of the coating are difficult to control. This makes the method unsuitable for many applications, especially those involving more advanced coatings including multilayers, grading or other variations in composition and microstructure. [3].

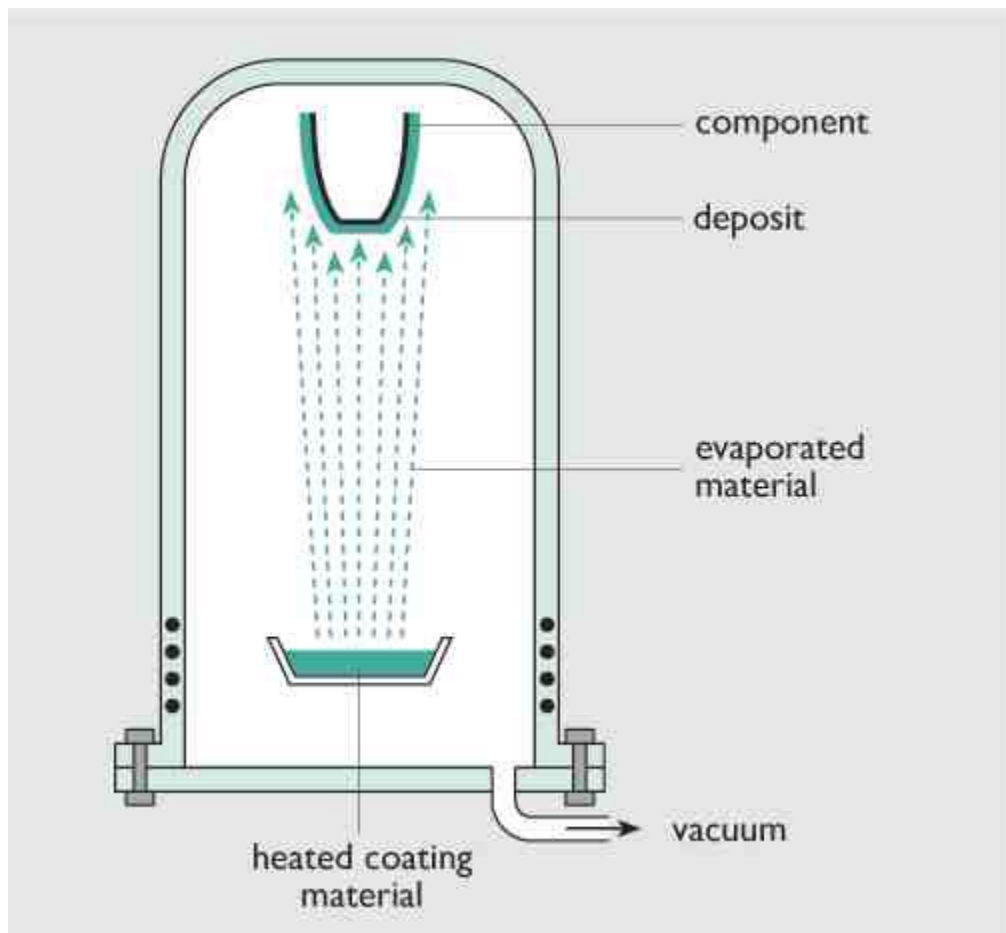


Figure 2.1: The most basic PVD system consists of a chamber which is evacuated to the level of molecular flow regime. The coating material is held in a crucible, usually composed of a refractory metal such as tantalum. The crucible is heated, by means of a high current being passed through it, and the substrate to be coated is placed within direct line of site of the coating material. The molecular flow regime ensures that the vaporised material follows straight line paths. (Image courtesy of betelco.com)

2.2 Sputter Deposition

Sputter deposition has provided a much more versatile form of PVD for many coatings applications. This process produces the vapour by means of rarefied ionised gas, known as

plasma, unlike conventional evaporation or e-beam evaporation. [3]. It is the presence of the glow discharge plasma, specifically the ion component, which provides unique opportunities to control a growing coating. Plasmas can be highly complex phenomena, and a description of the phenomena and structures that can exist within plasma would be outside the scope of this work. For further details please refer to [6]. A few plasma structures and processes relevant to the magnetron sputtering process will be described here:

Plasma:

Plasma is a mix of ionised atoms, free electrons and neutral atoms [6]. Strictly this refers to an ionised gas with an overall neutral charge, although in many real world situations this is not quite true. Plasma is generated in many natural phenomena; lightning, aurora, and the Sun are some of the most readily recognisable examples. The first artificial plasmas were created by scientists such as Irvine Langmuir in the early twentieth century. These were made by filling an evacuated glass vessel (also known as a plasma diode) with a low pressure gas and applying a high potential difference between an anode and cathode situated in the vessel. These were referred to as ‘glow discharges’. The basic structure of a glow discharge plasma is shown in figure 2.2.

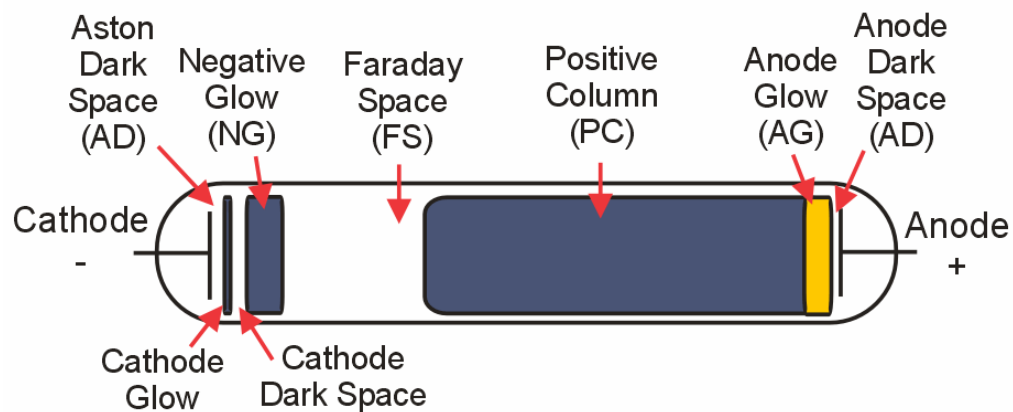


Figure 2.2: Diagram of a simple plasma diode. From left to right the annotated features are: The cathode; an electrode carrying a negative bias. Aston Dark Space: A region separating the cathode glow and cathode, where electrons emitted by the cathode have insufficient energy to excite gas atoms. Cathode glow: A region where electrons are colliding, and recombining, with ions emitting photons. Cathode dark space: A region of lower electron density, and so fewer collisions with ions. Negative glow: A region where accelerated electrons have gained enough energy to excite gas atoms. Faraday space: As we move along the discharge the electrons have less energy to excite gas atoms, and the negative glow gradually fades. Positive column:

An extended luminous region where the electric field provides just enough energy to excite the gas atoms. [18],[19] (image courtesy of Ian Tresman)

Plasma ignition:

In a gas with a potential difference applied across it a random event produces a free electron. Such random events are common, and can take many forms, such as an atom being struck by a high energy (UV, X-ray, gamma) photon, or naturally occurring alpha particle. The electron and ion thus created are then accelerated in opposite directions (towards the anode and the cathode, respectively) by merit of their opposite charges, although, due to its low mass, the electron moves so much faster that the ion can be thought of as standing still by comparison (this is known as a ‘cold’ ion)[8,13]. As the electron moves away it gains energy from the potential field, and interacts with neutral atoms. Many of these interactions will produce more ion/electron pairs, which in turn accelerate. This produces a chain reaction, and as long as the potential difference is maintained above a certain voltage (given by the Paschen curve in figure 2.3) a plasma can persist [8,13].

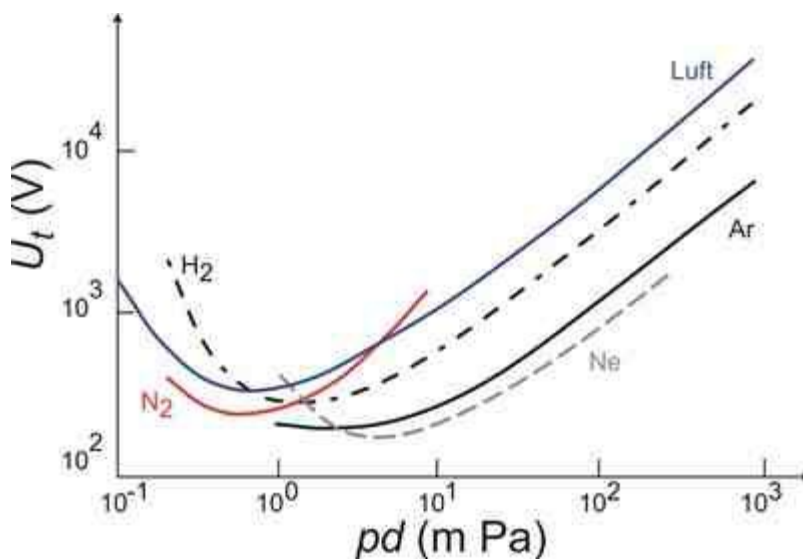
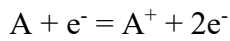


Figure 2.3: The Paschen curve for five commonly used gasses. The x-axis is pressure multiplied by distance between the electrodes, the y axis is potential difference required to strike a plasma (breakdown voltage). Image courtesy of cr4.globalspec.com.

The conditions for the chain reaction to start are that the mean free path of the particles in the chamber must be short enough that the separated electron can interact with the neutral

atoms frequently before striking a chamber wall [8,13]. As electrons are much more mobile than ions the majority of ionisation events are electron / neutral interactions. A typical neutral atom /electron interaction is written as:



Where A is the neutral atom, e^- is the electron and A^+ is the newly ionised atom. The electron impact knocks free one outer shell electron from the neutral atom, and the original electron recoils away without being captured.

2.3 Magnetron Sputtering:

Sputtering system:

In a sputter chamber the space between the anode and cathode is filled with a rarefied gas, typically argon, at pressures typically in the region of 0.1 to 10 Pa. A basic magnetron sputtering system consists of a chamber evacuated to a good quality (5×10^{-4} Pa) vacuum, which then has the working gas, usually argon, introduced. The chamber contains a 'target' plate, backed by permanent magnets, of material to be sputtered, and a substrate to be coated. Usually both of these can be actively powered or 'biased' (figure 2.4).

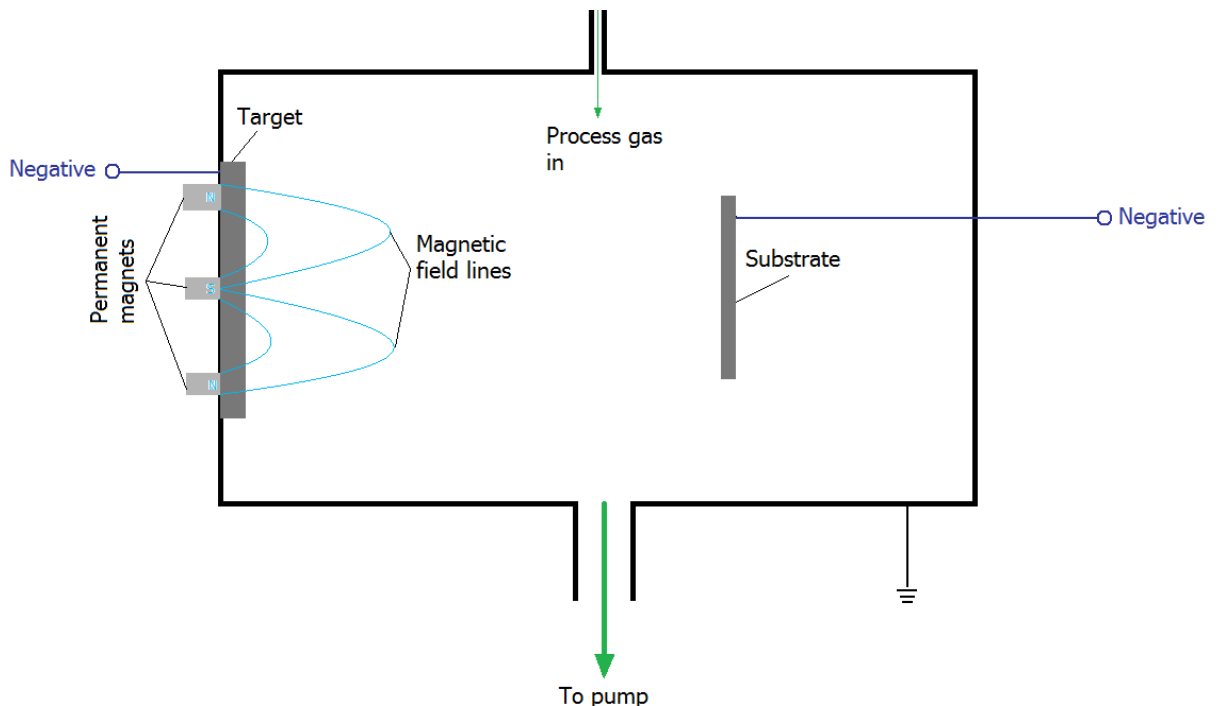


Figure 2.4: Simplified schematic of a basic sputter system.

Magnetron sputter discharge:

While a typical magnetron discharge shares many similarities with a simple glow discharge plasma there are important differences. One of the most important is that in the magnetron system both the target and substrate act as cathodes, unless deliberately biased otherwise. It is the walls of the chamber that behave as the anode, and as the primary sink for particles from the plasma. Another is that a magnetron plasma can be ignited at a much lower potential difference between anode and cathode than a glow discharge. A magnetron discharge is less uniform than a simple glow discharge; it interacts with magnetic fields from the target and contains areas of greatly enhanced electron density and ion creation.

Sputter plasma ignition:

In a magnetron sputtering system the plasma is created by applying fifty to several hundred volts between an anode and cathode. This is a significantly lower potential drop than for a plasma diode of similar dimensions. The potential difference required to ignite a plasma for any given gas is given by the Paschen curve as shown in figure 2.3. At typical sputter pressures the required potential difference to ignite the plasma is on the order of thousands of volts. The much lower $p.d$ value required for a magnetron plasma is due to the magnetic field at the sputter target: the target is backed by a double ring of permanent magnets, configured as in figure 2.5. These rings create a complete magnetic circuit, extending in front of and behind the target plate surface.

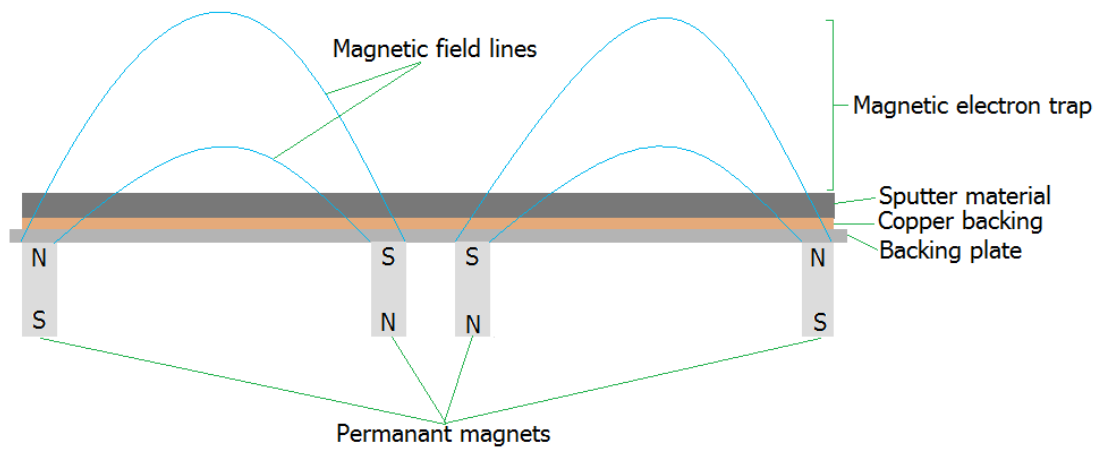


Figure 2.5a

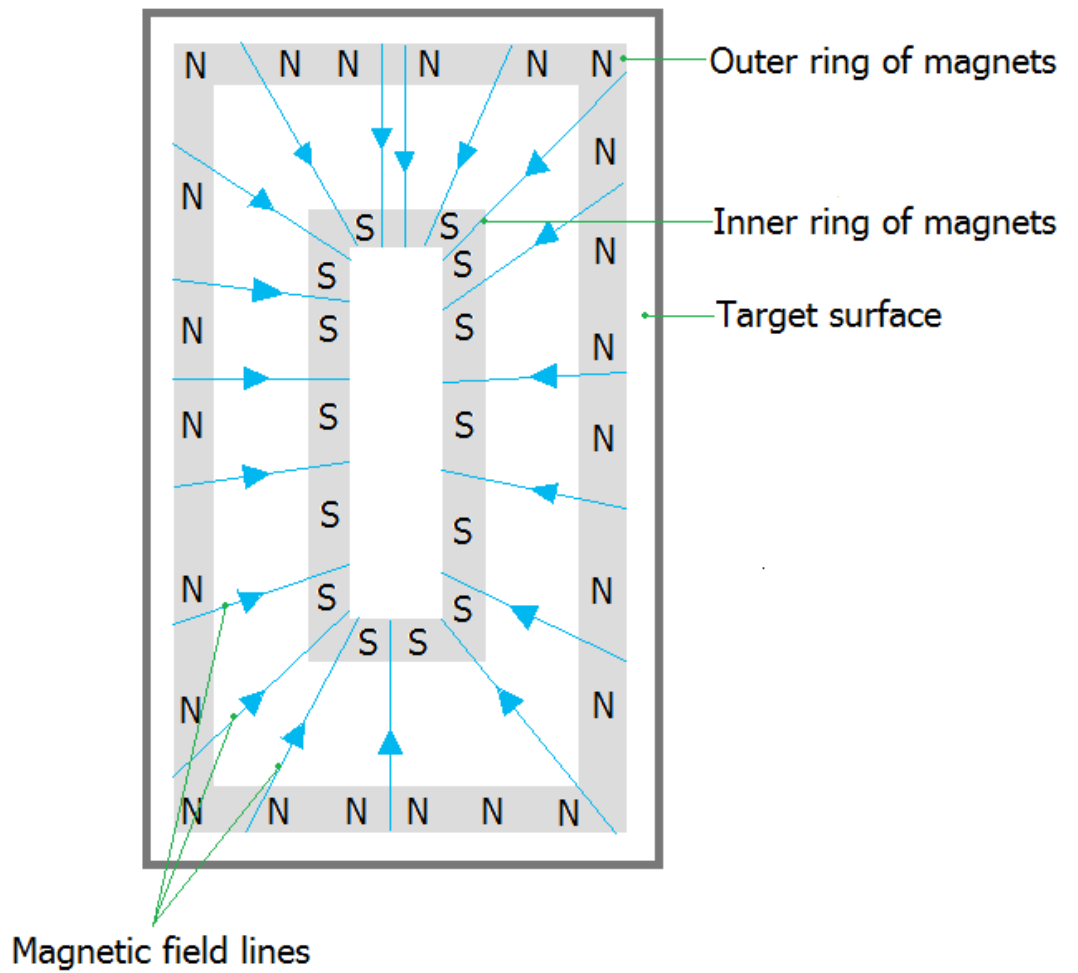


Figure 2.5b

Figure 2.5 a & b (Previous page): A cross section of a sputter magnetron, shown in figure 2.5 a. Behind the target and the backing plate are placed two groups of magnets, an inner and outer ring, with opposite poles facing the surface. This results in looped magnetic field lines extending out from the target, through the chamber space, and back into the target. These field lines trap electrons close to the target surface, which ionise the gas in the chamber much more densely close to the target surface than in the rest of the chamber. A view of the set up from above shows that this results in a concentrated 'race track' region of sputtering (figure 2.5 b).

Hall current:

Where a charged particle, such as an electron, is in motion in a volume containing a magnetic field line the particle will follow a spiral path around the field line, with a radius of:

$$r = v / z$$

Where r is the Larmor radius, v is the particle's tangential velocity, and z is the period of gyration about the field line.

Where a charged particle is in motion in a region containing a magnetic field with some component of an electric field perpendicular to the magnetic field the charged particle will drift in a direction perpendicular to both fields with a velocity known as the Hall drift velocity.

The force felt by the particle is given by:

$$F = q[E + (v \times B)]$$

Where F is the force experienced by a moving charge in a magnetic field, q is the value of the charge, v is the charge velocity, E is the electric field strength and B is the magnetic field strength.

In a magnetron magnetic trap the mass drift of electrons gives rise to a Hall current, moving along the racetrack above the magnetron surface. The electrons in fact follow a 'hopping' motion as they move along the field lines and drift simultaneously.

The magnitude of the Hall current density is given by:

$$J_H = (e \times n \times E) / B$$

Where J_H is current density and n is plasma density.

As electrons are very low in mass (and hence inertia) it is much harder for an electron to move across a magnetic field line than follow it. This confines free electrons close to the target, at a much higher density than the bulk plasma. Neutral atom ionisation in this region is far more likely, allowing the sputter plasma to ignite and be maintained at lower potential differences.

Sputter plasma charge and structures:

Technically the electrical charge of a plasma is neutral overall, as there are an equal number of positive and negative charge carriers. However due to the loss of electrons to the chamber walls or other earthed surfaces the bulk plasma will often acquire a low positive potential in real world situations. This occurs as negative charge carriers (electrons) are many times lighter than positive charge carriers (ions) and at a given temperature / kinetic energy will move much faster, leaving the plasma ions behind. This can be shown by considering an electron-ion pair in a simple plasma:

For both drift and diffusion the flux of electrons is far greater than that of ions. As electrons leave the plasma the bulk plasma becomes positively charged, restraining the loss of electrons. This is known as ambipolar diffusion. As electrons reach the earthed chamber walls they are lost to the system. However if the surface upon which they impinge is electrically isolated from earth, then that surface will acquire a net negative charge, known as the floating potential. This is usually of the order of several tens of volts. Surfaces that acquire this potential will repel further electrons, and accelerate ions towards themselves. The density of electrons falls more rapidly than that of ions, creating a dark region filled with ions accelerating towards the negatively charged surface. Typically this region is around 1 mm deep, and is referred to as a Debye or dark 'sheath' as it does not emit light. As the potential drop across the sheath is quite large it effectively shields the surface from the electrical effects of the bulk plasma. Plasmas also contain a deeper region adjacent to the sheath known as the 'presheath', across which a much smaller potential drop occurs (figure 2.6).

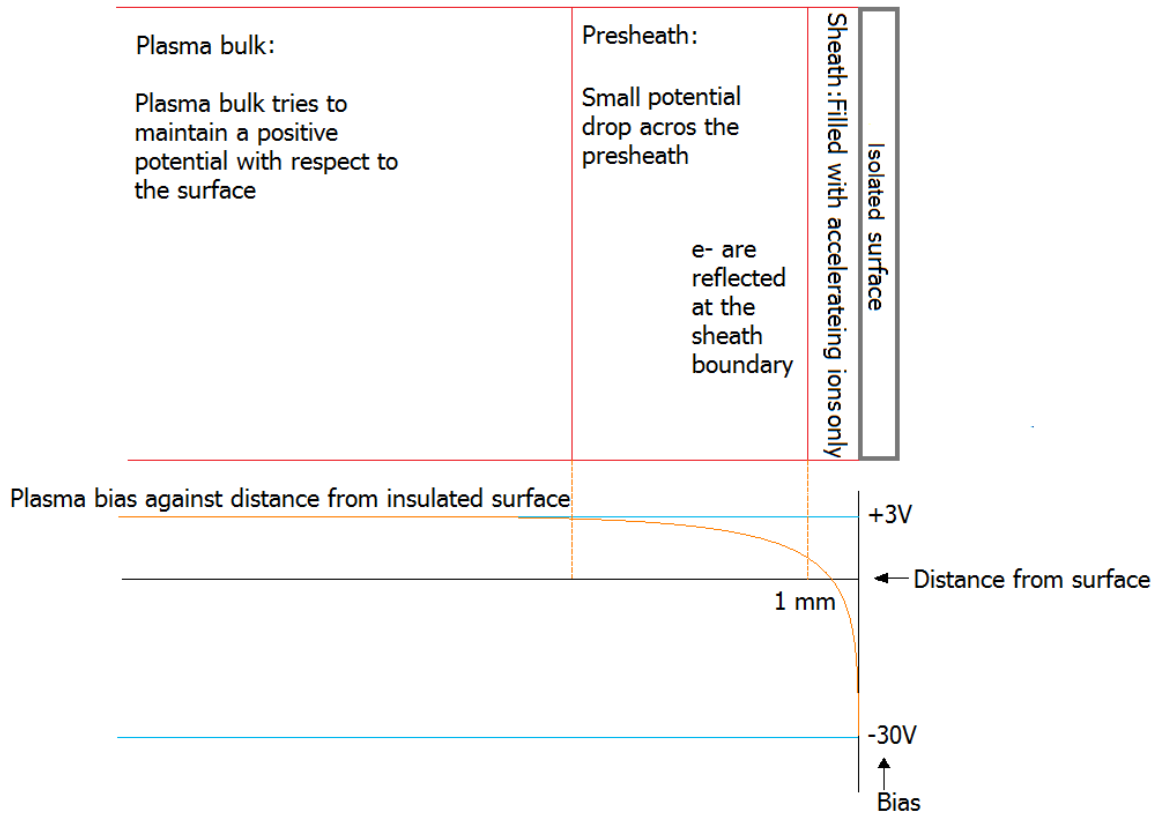


Figure 2.6: The structure of a plasma approaching an isolated surface and the corresponding change in plasma potential.

As mentioned above a double ring of magnets is used to create a ring of higher electron density lying with its long axis parallel to the target surface (figure 2.7), allowing a lower ignition voltage of the plasma discharge.

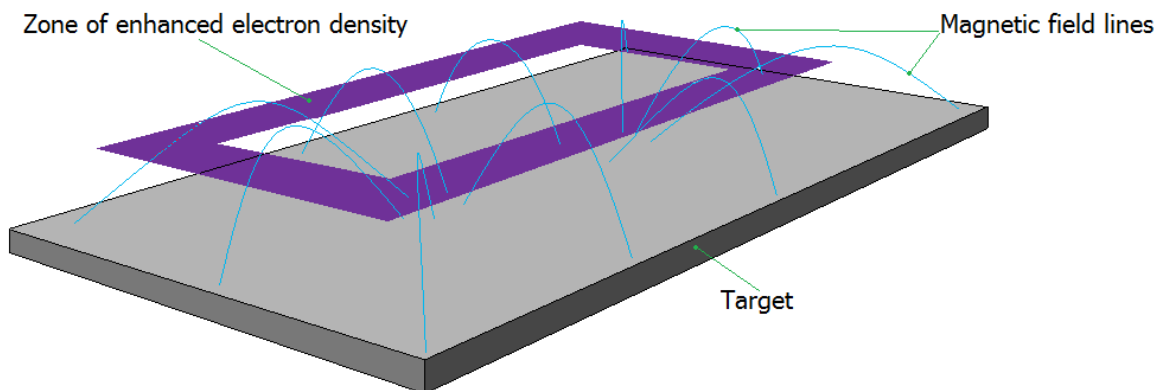


Figure 2.7: The zone of enhanced electron density.

Once the plasma is ignited the ring of higher electron density persists, creating a region of much higher ionisation close to the target surface. As ions, having greater inertia, are not confined to the magnetic field lines they are free to fall out of the plasma under the cathode bias and sputter the target surface. This causes a ring of greatly enhanced sputtering at the target (remember the electrons, which cause the ionisation, are following hopping motions in a ring around the target and above its surface), known as the race track. This approach is used as the basic sputter process is not, ordinarily, a practical means for growing coatings. An unconfined plasma in a vacuum chamber will be extremely rarefied and evenly distributed, and so sputtering will take place across every surface in the chamber. Hence the species sputtered from the target will be little more numerous than those sputtered from the chamber walls and other surfaces in the chamber. Even if the target material comprised the entire chamber and every surface therein, the rate of sputtering would be extremely low. Thus it is necessary to confine the sputtering close to the target so that the majority occurs at the surface of the target.

Plasma optical emission:

The radiation emitted by the plasma is the result of energy being lost from ions excited by collisions with other ions, free electrons or neutral species. These collisions result in free electrons recombining with ions, and so giving up energy in the form of radiation, as well as ions being thermally excited by collisions. This process is important, as the intensity and frequency of the radiation can be used to determine the species present in the plasma, and their concentration, as well as information on their spatial distribution [8,9].

Pulsed sputter plasmas:

Pulsed d.c. magnetron sputtering is a relatively new development, first developed to suppress arcing during the deposition of dielectric materials, but which has been shown to have other beneficial effects. In particular the pulsed system generates a greater flux of higher energy ions, which can be used to improve coating properties as the coatings grow. In the pulsed d.c. system, bias is provided to the substrate as an approximately square waveform. This leads to a rapidly (in the mid kHz region) increasing and decreasing plasma current, and a simultaneously growing and collapsing sheath at the substrate. During the off phase of the cycle the cathode bias overshoots and becomes positive,

forcing the plasma to acquire a much larger positive potential (30 V or so) in order to keep ions and electrons from flowing out of the plasma. This high potential leads to very energetic ions, in the case of the AE power supplies where the overshoot can reach 100 V, with energies up to 100 eV! At the beginning of the on phase electrons have been observed with energies in the region of 20 eV, resulting in greater ionisation of the sputter gas.

Magnetron sputtering process at the target:

This method of converting solid material to vapour carries several advantages; it is possible to adjust the rate of sputtering and hence deposition precisely [21], and it is possible to sputter materials with high vapour pressures that would be impractical to vaporise in bulk.

The material to be sputtered (the target) is made the cathode in the system and this is where the positively charged ions will be drawn, gaining a high kinetic energy from the electric field. In a simple sputtering system the majority of impacts are not in fact ion impacts, but are due to neutral gas atoms which have been thermally excited by ions. Thus ion energy is still a dominant controlling factor on gas particle impacts at the substrate [22]. As the incoming particles strike the target they transfer kinetic energy to the target. On the macro scale the effect of this is to heat the target. On the atomic scale each impinging ion produces a chain of dislocations in the targets atoms, and where the energy of the incoming ion is great enough the chain of dislocations may end in a target atom being ejected from the target and into the chamber space (Figure 2.8) [22]. Typically this occurs when the energy transferred normal to the surface is greater than three times the surface binding energy [23] [24], typically of the order of tens of eV [25]. This value is known as the sputter threshold. The exact binding energy at the surface is, in the case of a crystalline target, partly dependent on the orientation of the crystal structure relative to the surface [24]. As a result of the differing surface properties of different materials each material has its own sputter yield. Sputter yield (s) is given by:

$$S = \text{Number sputtered atoms} / \text{number of incident ions}$$

Sputter yield increases as the d electron shells of the target material are filled.

Consequently the more closed a material's electronic structure, the higher its yield is likely to be [26].

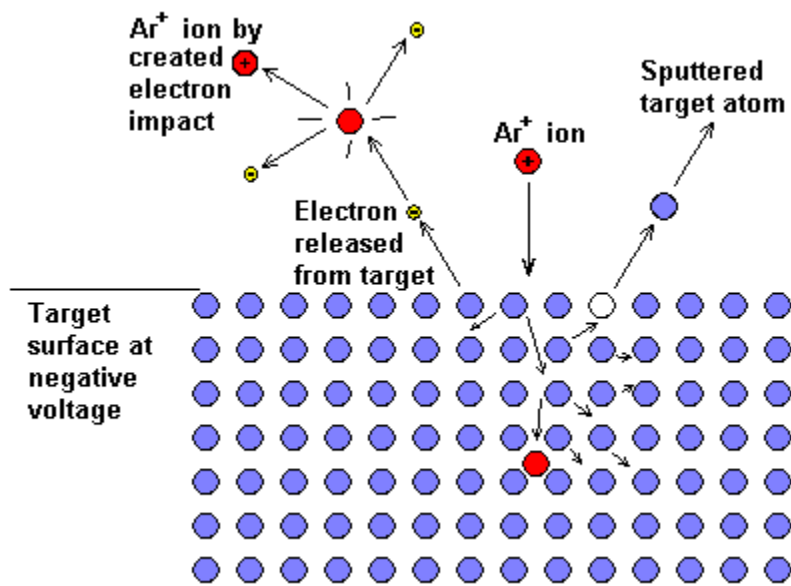


Figure 2.8: A simplified schematic of the sputter process. Positively charged ions of the working gas, in this case Argon (shown in red) are created by random events, or by electrons emitted by the negatively charged target surface. These ions are then drawn towards the target surface, gaining kinetic energy from the electric field as they accelerate. As an argon ion strikes the surface it transfers kinetic energy to the target atoms, which follows a series of dislocations. Where one of these dislocations returns to the surface with sufficient energy an atom of target material is sputtered into the body of the chamber. Image courtesy of Alacritas-Consulting.com.

Sputtered particles will arrive at the surface to be coated with a wide range of energies. The energy of sputtered neutral species will be chiefly determined by how much the sputter threshold is exceeded, and by the density of the gas in the chamber, as this affects the mean free path and hence the number of gas phase collisions neutral species undergo.

The surface to be coated (the substrate) is typically placed in front of the cathode, although all parts of the chamber with a line of sight to the target will receive a coating of the target material. The substrate holder can be (usually) negatively biased. This allows for a mechanism to control the energies of the arriving ions more precisely, by adjusting the bias voltage at the substrate. In the majority of d.c. sputter systems the percentage of coating atoms ionised is around 1%. However impinging ions of both the working gas and the sputtered material can have a significant effect on the structure and properties of the near surface substrate, and the growing film itself.

Configurations for planar magnetrons:

There are many possible configurations of polarity and field strength available to designers of planar sputter targets/magnetrons:

1. Balanced configuration

In a balanced configuration the outer and inner rings of magnets are of approximately equal strength, and all the field lines are closed loops leaving and returning to the target surface. The plasma is tightly confined to the target surface, as shown in figure 2.9. This limits the ability of the system to bombard the substrate with ions, and the ability of any reactive gasses (see later section) to interact with the plasma [28]. Hence this configuration is seldom used today.

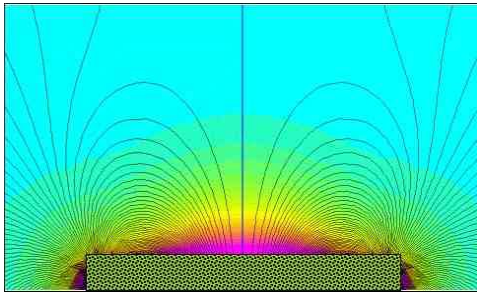


Figure 2.9: A cross sectional diagram of the magnetic field lines emitted from a balanced magnetron. The magnetic field lines are shown in deep blue. The density of the plasma during sputtering is shown by graded colours; pink/purple for intense, yellow/green for moderate, and blue for background. The rectangular block at the bottom of the image is the magnetron and target surface itself. All the field lines that leave the targets surface return to it, giving a tightly confined plasma close to the target surface. Image courtesy of www.plasmionique.com

2. Unbalanced configuration Type 1

In a type 1 unbalanced configuration the central ring of magnets is more powerful than the outer ring. This results in some of the magnetic field lines from the inner ring extending

away from the magnetron and towards the chamber walls, as shown in figure 2.10. This results in lower electron and ion densities near the target than in the above mode, and higher densities deeper into the chamber [28] [29].

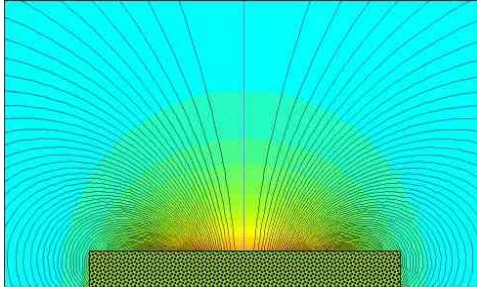


Figure 2.10: A cross sectional diagram of the field lines and plasma density emitted from a type 1 magnetron. Magnetic field lines are shown in deep blue, plasma density is shown colour coded, purple/pink being most intense, yellow/green being moderate, and blue being back ground .In this configuration the inner ring of magnets is more powerful, and many of the field lines terminating at the inner ring extend to infinity. This results in a relatively weak, poorly confined plasma, extending into the chamber. Image courtesy of www.plasmionique.com.

3. Unbalanced configuration type 2

In a type 2 unbalanced configuration the outer ring of magnets is more powerful, resulting in some of the field lines from the edge extending away into the chamber space towards the substrate, as shown in figure 2.11. As a result electrons will follow these field lines away from the target surface, generating ions in the region of the substrate. This configuration results in much greater ion bombardment of the substrate [29] [28].

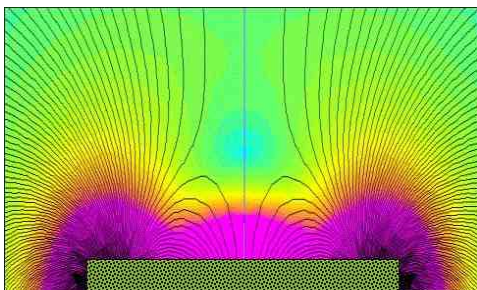


Figure 2.11: Cross sectional diagram of plasma density and magnetic field lines emitted from a type 2 unbalanced magnetron. Magnetic field lines are shown in deep blue, plasma density is shown colour coded;

Black/purple/pink is most intense, yellow/green is moderate, blue is background. In this configuration the outer ring of magnets is more intense than the inner, resulting in many of the field lines that terminate at the outer ring extending away from the target. This results in a strong but ill confined plasma, stretching away from the target and into the chamber space. Image courtesy of <http://www.plasmionique.com/magnet.htm>.

4. Closed field configuration:

In a closed field magnetron there are an even number of sputter targets, with their magnets arranged such that the field lines emitted by each one join with the field lines of the target adjacent, as shown in figure 2.12. This results in a much denser plasma, and hence ion bombardment, close to the substrate [29].

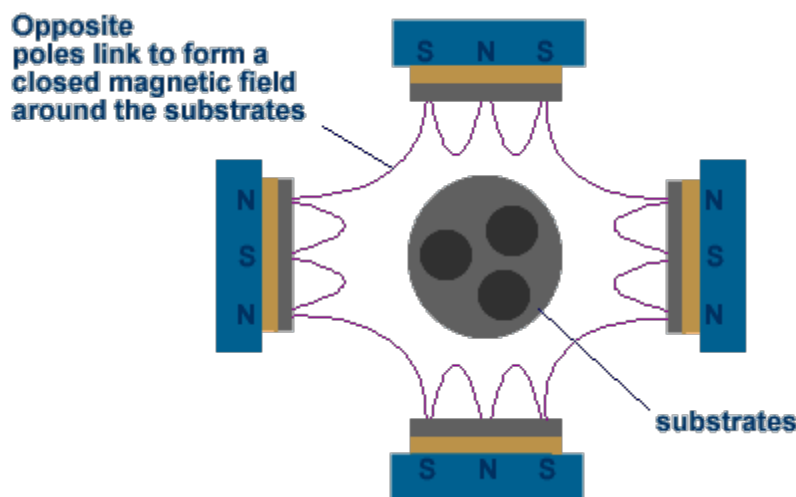


Figure 2.12: A cross sectional diagram of closed field configuration multi-magnetron system. Magnetic field lines shown in purple. Each magnetron has an outer magnet ring with the opposite polarity to that of the one next to it. This results in closed magnetic field surrounding the substrates in the centre, which greatly enhances plasma density. Image courtesy of pvd-coatings.co.uk

Other magnetron configurations:

There are many possible configurations of magnetic field and target surface which could be used. Planar circular or rectangular geometries are the most prevalent, as they are relatively easy to construct, however some of the most common alternative geometries are listed below:

1. Hollow cathode magnetron:

A hollow cathode magnetron is built by adding a cylinder of target material to the planar magnetron surface. This cylinder confines the working gas, giving a smaller mean free path in the vicinity of the target. Advantages of this approach include better target material utilisation at lower pressures, the ability to maintain sputtering at lower pressures than a planar magnetron, and improved directionality of the sputtered material [14].

2. Cylindrical post magnetron:

This configuration consists of a target shaped as a cylindrical post, surrounded on all sides of the curved surface by a cylindrical anode, so that the electric field extends radially from the cylinder's axis. The magnetic field is applied parallel to the cylinder's axis, so that electrons emitted by the anode are immediately confined in a cylindrical sheath close to the target's surface. This results in a dense, uniform, plasma close to the target, which provides a much more efficient target utilisation. However the plasma density is not uniform along the direction of the cylinder's axis, and so over time the target surface will begin to take on a concave outer face [15].

3. Powder sputtering:

The powder sputtering process is identical to that of the planar system, but the solid target face is replaced with a hollowed out trough, in which a powder is placed. The trough is placed face up, such that the powder is held in place by gravity. This form of sputtering is often used in research, as it allows for great flexibility of the target material, and allows for chemically novel coatings, such as YBCO high temperature superconductors, to be deposited.

2.4 Reactive sputtering:

Reactive sputtering involves introducing a gas other than the working gas into the chamber, in order to react with the sputtered material as it moves through the chamber and/or at the substrate surface. This process provides a simple means of depositing oxide/nitride films by allowing the gaseous and solid phase components to be introduced to

the chamber separately. PVD of solid compound materials, by contrast, is a low rate process, due to the relatively low sputter yields of most compounds compared to metals, and often suffers from problems due to decomposition of the compound into simpler molecules, resulting in sub-stoichiometric films.

Reactive sputtering does have downfalls however. The most commonly encountered is target poisoning. When the reactive gas is introduced it will react with the target material as readily as it reacts with the vapour phase and film material. Hence a layer of oxide or nitride will begin to accumulate at the target, and where the poisoned material has significantly different electrical, thermal, and sputtering (i.e. a different sputter yield) properties than the pure target material this can disrupt the sputtering process.

Hysteresis behaviour in reactive sputtering:

As the reactive gas content of the sputtering atmosphere increases the deposited film will begin to form compounds by the reaction of the target material and the reactive gas (oxides in the case of oxygen as reactive gas, nitrides in the case of nitrogen etc). At sufficiently high reactive gas content the entire deposited coating will be a compound of the reactive gas. At still higher reactive gas contents the compound will begin to form on the target surface, and probably disrupt the sputter process. This process of compound growth on the target will continue even if the inflow of reactive gas is reduced. The compound growth will not stop until the reactive gas content of the chamber drops sufficiently that clean metal surface can be exposed by the sputtering at the target. This is generally referred to as hysteresis.

The two regimes of target sputtering, metallic and compound coating can be seen easily in many systems if a plot of flow rate against chamber pressure is made, as shown in figure 2.13.

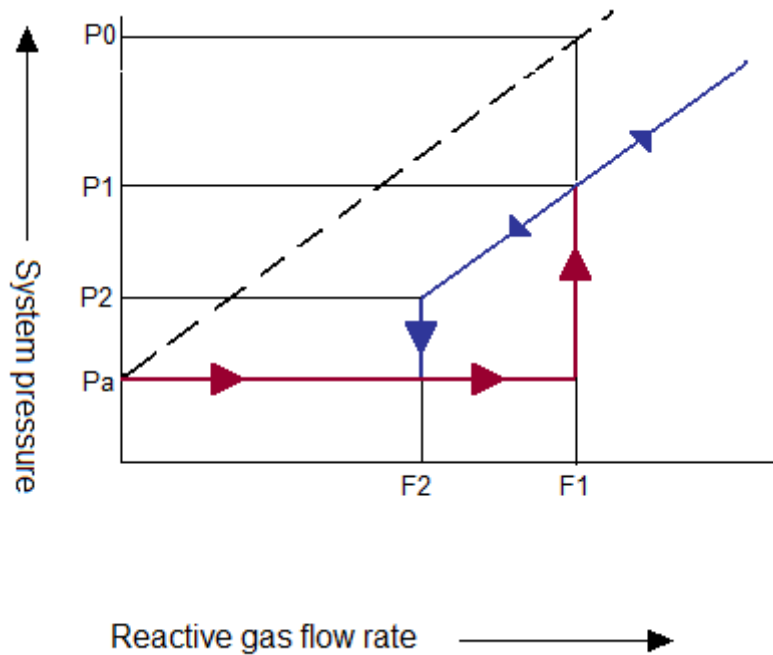


Figure 2.13: An idealised graphic of a system pressure hysteresis loop for a typical oxide system.

A constant pressure (P_a) is maintained by the inflow of process gas (Ar typically) and the pumping speed of the chamber pump. The broken black line represents the increase in chamber pressure if the Ar flow were to be increased linearly, following the relation:

$$P = Q/S$$

Where P is chamber pressure, Q is flow rate of the Ar and S is total pumping speed from the chamber.

The Maroon/blue curve represents two states of the sputter system: the maroon section represents the system before target poisoning occurs, where the formation of reactive gas compounds effectively getters reactive gas out of the system, and consequently the chamber pressure is insensitive to reactive gas flow rate below a certain point. The blue section represents the system after the point of target poisoning has occurred, where the gettering effect is no longer sufficient to remove all the reactive gas from the sputter atmosphere. In this section the chamber pressure rises and falls linearly with reactive gas flow rate, offset from the black dashed line by $P_0 - P_1$ [30].

The transition from the maroon to blue section occurs at reactive gas flow rate F_1 . At F_1 compound starts to grow on the target surface, in almost all cases reducing the sputter yield. Deposition rates also show a hysteresis like effect. The presence of compound

material on the target will usually have an effect on other system parameters, such as target bias and current. Figure 2.14 below shows a real hysteresis curve for an aluminium – oxygen d.c. system.

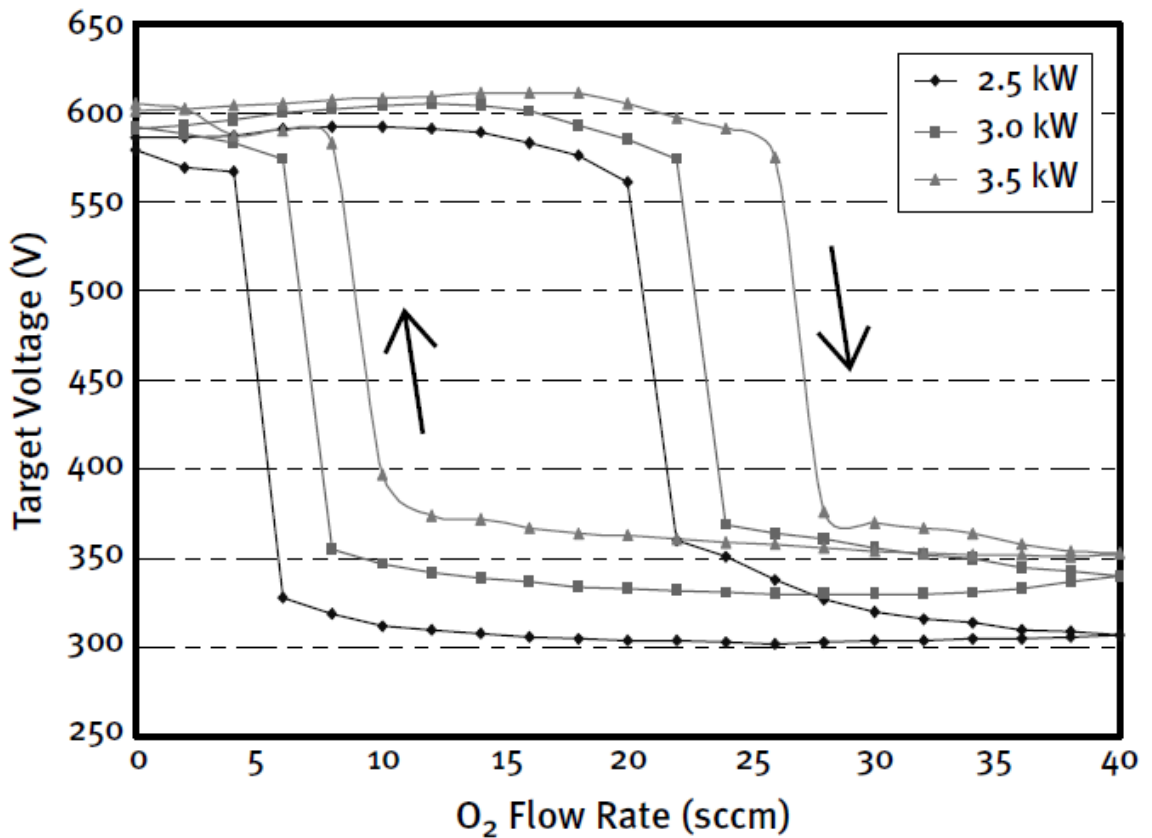


Figure 2.14: Hysteresis curves for an aluminium oxide d.c. reactive sputtering system. Image adapted from material courtesy of [31].

The magnitude of the hysteresis observed is partly dependent on the pumping speed of the system. It has been shown that above a certain rate of pumping there is no hysteresis effect [32] as the reactive gas is removed from the chamber before it can react. It has also been shown that moving the reactive gas inlet in relation to the pump inlet can decrease the width of the hysteresis curve [33].

2.5 Film Growth:

The growth of a PVD film happens in stages [34], the length of each stage depending mainly on the energy of the incoming adatoms, the binding energy between the adatoms and the substrate, the sticking coefficient between adatoms and substrate, the temperature of the substrate, and the rate of arrival of the coating atoms at the surface [35] [36].

First stage:

Atoms that arrive at the substrate are referred to as adatoms. The mobility of adatoms depends on the substrate temperature as a proportion of the melting point of the adatom material. If the substrate is relatively hot, the adatoms to arrive at the substrate are relatively mobile across the surface, and will remain so until they encounter a surface dislocation with a higher than average binding energy. Such a defect could be a pre-existing surface feature, such as where a screw dislocation reaches the surface, a step between surface monolayers, or could be a defect introduced to the crystal structure by the impact of a high energy ion. An adatom which becomes caught in such a defect then provides a nucleation site for other adatoms to join together. If the substrate surface is relatively cold, adatoms tend to stick where they land, which can lead to columnar coating structures [37].

Second stage:

Small islands of adatoms form around the nucleation sites (Volmer-Weber growth pattern [38]). These islands are preferential sites for further adatoms to come to rest, both those moving across the surface and those approaching from the coating source. This results in several effects; the islands grow three dimensionally, with new monolayers forming on the upper surface of the island well before the substrate has a complete monolayer across its surface. The steps between the island monolayers provide still better sites for nucleation, so as the island grows in size it develops a step pyramid structure. As the islands are dynamic structures with adatoms constantly joining and leaving, the smaller islands, which have a smaller perimeter and upper surface to gain new adatoms, will tend to lose atoms, and grow more slowly, than the larger ones [39]. In the Stranski – Krastanov model [40] islands do not begin to form until after the initial monolayers have been deposited, as the adatoms are more greatly attracted to the substrate surface than each other.

Third stage:

As a result the surface quickly becomes dominated by relatively large multilayer island structures which continue to grow until they meet at the edges. In cases where the substrate surface is cold, adatoms with incoming energies near the sputtering threshold will not move more than two atomic radii unless thermal energy is supplied by the substrate. In this case the islands will grow more rapidly in the vertical, and will form many long thin columns. As this 'forest' reduces the potential angles of approach for incoming adatoms to reach the surface the inter column gaps will not fill in, with atoms attaching themselves to the tops and sides of columns instead [41].

This results in widely separated columnar growth, where the film consists of columns of film material separated by voids. These films will tend to be porous and have poor mechanical properties.

Fourth stage:

The above leads to many modes of film growth. These range from one where the growing film is relatively smooth and featureless, to one where the surface has at least one complete monolayer, with pyramid structures of further growing monolayers sitting on top, to one where the film is growing as a series of separated columns. Intermediate to these possible stages is a spectrum of film structures, ranging from narrow widely separated columns, to columnar structures in contact with each other, to fully dense films with a 'glassy' structure. In order to model the possible growth modes for a film we use a **Structure Zone Model (SZM)**. The most widely used of these is the Thornton SZM, as shown in Figure 2.15, although refinements of this have resulted in more complete pictures of films growth, such as the Kelly and Arnell SZM [17] [42].

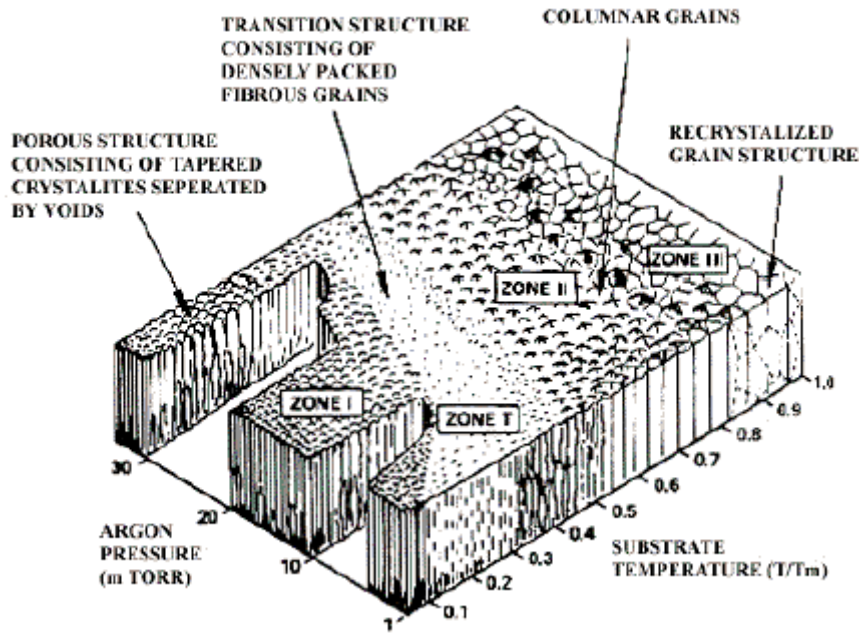


Figure 2.15: Thornton structure zone model. Along the right hand axis the ratio of substrate temperature to melting/decomposition temperature of the film increases to the right. Along the left hand the working gas pressure (in millitorrs) increases to the left. In zone 1 the film structure consists of widely spaced columns of film growth. In zone T, a later addition to the model, the film consists of intertwined fibrous grains. In zone 2 the structure is of closely packed columnar grains, and in zone 3 the grains are in contact with each other, but still discernable. Beyond zone 3 the structure is fully dense and 'glass-like'. Image courtesy of [152]

2.6 Effects of ion bombardment on the growing film:

Ion bombardment is the major process which gives magnetron sputter deposition advantages over thermal deposition [43]. Ion bombardment provides a means of pre-treating the substrate prior to deposition, and controlling film growth as deposition progresses. As a means of pre-treatment it generally serves two purposes;

- 1) To remove unwanted material such as surface oxides, nitrides, and organic contamination from the substrate, referred to generally as ion etching [65]. In conjunction with chemical and mechanical cleaning techniques such as acid etching and ultrasound bathing this allows for the growth of homogeneous films which are better bonded to the surface, and which provide a more even cover against, e.g., corrosion. Reactive gas ions can be more efficient at removing organic compounds,

as they decompose contaminants chemically, whereas the working gas will only decompose the contaminants thermally. However reactive gas ions will also tend to react with the substrate, and lead to unwanted oxides or nitrides on the substrate surface.

- 2) Ion etching can also be used to expose sub-surface features in the bulk, by removing surface layers.

The prepared surface can then be subjected to ion bombardment in order to tailor the surface properties to be optimum for the growing film. Perhaps the most important function of ion bombardment in this context is to disrupt the surface and near surface crystal structure by implantation [44]. This leads to surface defects, which make ideal nucleation sites for the first wave of adatoms, and promotes denser film structures, and better adhesion.

As a means of controlling film growth ion bombardment affects both film composition and structure, and so can serve a number of useful roles:

By the same mechanism as during ion pre-treatment, ion-surface interactions will tend to remove contaminants in the film. This promotes a more ordered and homogeneous structure, decreases the occurrence of large voids, and improves inter-layer adhesion in multilayer coatings. Ion bombardment also influences the microstructure of the growing film in a number of ways. As noted in the above section, the final microstructure of a growing film is heavily influenced by the mobility of adatoms moving across its surface. One means of influencing adatom mobility is ion bombardment. Unlike neutral species of evaporated coating material, ions (of reactive gas, working gas, and target material) will accelerate over the distance of the Debye sheath, and a negative bias voltage applied to the substrate will substantially increase the incident ion energy at the film. Hence ion bombardment can add considerable kinetic/thermal energy to the substrate, and to the adatoms at the surface, allowing them to diffuse further before coming to rest at a nucleation site or as part of a growing island [45]. As detailed above this will affect film structure, which will in turn affect mechanical, electrical, and optical properties. The flux of ions at the substrate also influences the density of implanted working/reactive gas atoms in the growing film. These atoms displace coating atoms, introducing defects into the film's crystal structure, which introduces residual compressive stress into the film as it

grows [46]. Implanted ions can also affect the chemical composition of the film. Depending on the energy of an impacting ion it may also cause further dislocations around the site of impact, local melting and re-crystallisation of the film structure, amorphisation of the film crystals, and re-sputtering.

Ion bombardment, enhanced through a negative bias voltage, will result in many ions having sufficient energies to cause a 'thermal spike' when they strike the substrate surface. In this energy regime the impact of the ion delivers enough kinetic/thermal energy to animate many atoms in the volume of the bulk surrounding the impact site. After the impact the animated bulk briefly resembles a tiny bubble of highly compressed gas phase material. Roughly 10^{-11} seconds after impact the temperature around the impact of a 100 keV Xe ion may exceed 10000 degrees Kelvin and pressures of ten thousand bar [47]. Material is ejected from this region, by thermal mechanisms as opposed to dislocation chains. The fluid region will cool and re-crystallise rapidly, which may lead to a locally different crystal orientation, the removal of impurities or implanted ions by out gassing, or in the case of a compound film, chemical alteration by dissociation and out-gassing of one or more components. Thermal spikes can reduce residual stress, as they will anneal out dislocations.

Residual stress in sputtered films:

Residual stress is an important parameter of PVD coatings, as a film with a high degree of internal stress will be closer to the elastic limit and generally more prone to delaminating. Generally residual stress scales with the ratio of ions to neutral atoms arriving at the substrate, and with the square root of ion energy. In transition metal nitride films defect density decreases with the energy of the impinging ions at low substrate temperatures, until at a critical substrate bias minimum defect density is reached. Beyond this critical substrate bias, defect density increases with substrate bias [49]. Although residual stress is largely the result of ion implantation and dislocations, high energy ion bombardment can reduce residual stress. This is due to film/substrate heating, which will tend to anneal out dislocations, so defect density falls as substrate temperature rises. [50]

Re-sputtering:

Re-sputtering occurs where the impact of energetic ions on the film causes sputtering of the film material itself. This can be a problem for materials with high sputter yields as the

film will only continue to grow and increase density while the re-sputtering rate is below the rate at which new material nucleates on the substrate. However the ion energy must be high for re-sputtered material to be entirely lost to the film. Atoms at regions of high curvature, such as at the tip of a spike, or on the corner of a step, are most vulnerable to this, as they have fewer bonds with the bulk material. If ion energy is close to the sputter threshold of the film material the re-sputtered atoms may then return to the surface at a different point with enough energy to mobilize atoms surrounding the impact point. This has the beneficial effect of smoothing surface topography.

Re-sputtering can also modify surface chemistry if one component of a compound film has a different sputter yield than the others, and by the same method it may be used to remove near surface impurities.

For PVD coatings of certain materials, for example copper, where ions have energies between 1 keV and tens of keV the re-sputtering process can actually induce the formation of surface structures. This process is relatively poorly understood.

Thermal spike regime impacts can be a major source of re-sputtering at the substrate, as not only are high energy ions involved but thermal desorption of material may continue for some time following the initial impact.

3: Cr_xN

3.1 Chromium nitride; a transition metal nitride.

The transition metals are all members of the d-block of the periodic table, shown in figure 3.1 excluding the group 12 elements and scandium, yttrium, lanthanum and actinium, which are assigned to different groups. The formal IUPAC definition is: "an element whose atom has an incomplete d sub-shell, or which can give rise to cations with an incomplete d sub-shell."

Transition metal nitrides based on elements early in the d-block tend towards high hardness, good thermal properties and low susceptibility to corrosion. Their physical and electronic properties can embrace those of metals and ceramics. These properties make transition metal nitrides of great interest to science and industry, especially in the field of hard coatings, but also in the areas of semiconductor research, optical properties, and diffusion barriers [51]. Nitrides of chromium and titanium have been particularly well studied due to their wide range of industrial applications.

Nitrogen forms compounds with all the early d-block elements, tending towards simple face centred cubic (fcc), body centred cubic (bcc) close packed hexagonal (cph) or simple hexagonal (hex) structures, similar to those of the metals themselves. In later d-block elements the structures are more complex. The type of structure likely to be formed can be found by Hagg's rule, which states that the structure will be simple if the ratio of the radii of the non-metal atoms to that of the metal atoms is less than 0.59 [52]. For chromium nitride this ratio is 0.55469, the ratio of the radii of the nitrogen atom (71 picometers) to the chromium atom (128 picometers).

IA 1	IIA 2		IIIB 3	IVB 4	VB 5	VIB 6	VII 7	VIII 8	VIII 9	VIII 10	IB 11	IIB 12	IIIA 13	IVA 14	VA 15	VIA 16	VIIA 17	VIIIA 18
H	He												B	C	N	O	F	Ne
Li	Be												Al	Si	P	S	Cl	Ar
Na	Mg												Ga	Ge	As	Se	Br	Kr
K	Ca	Sc	Ti	V	Cr	Mn	Fe	Co	Ni	Cu	Zn		In	Sn	Sb	Te	I	Xe
Cs	Sr	Y	Zr	Nb	Mo	Tc	Ru	Rh	Pd	Ag	Cd		Tl	Pb	Bi	Po	At	Rn
Rb	Ba	La	Hf	Ta	W	Re	Os	Ir	Pt	Au	Hg							
Fr	Ra	Ac	Rf	Db	Sg	Bh	Hs	Mt	Ds									
		lanthanides																
		Ce	Pr	Nd	Pm	Sm	Eu	Gd	Tb	Dy	Ho	Er	Tm	Yb	Lu			
		actinides																
		Th	Pa	U	Np	Pu	Am	Cm	Bk	Cf	Es	Fm	Md	No	Lr			

Figure 3.1: Transition metals, comprising of the d-block, shown highlighted on the periodic table. Image courtesy of simplychemistry.org.

Chromium falls into column six of the first d-block row (figure 3.1). As a solid it forms a simple bcc structure, has a silver-grey colour, and has long been of interest to industry due to its high hardness, high melting point, and good corrosion resistance.

Chromium nitride forms two main crystalline structures, governed chiefly by the abundance of nitrogen during deposition. A nitrogen rich film will form cubic structured CrN, nitrogen poor films will form mixed phase, or Cr₂N (di-chromium nitride) only, with a hexagonal structure. It is likely that even when the coating stoichiometry is correct for CrN (mass percentages of 79% Cr and 21% N) some Cr₂N is present [53]. A phase diagram for chromium nitride is presented as figure 3.2. Each of the main crystalline forms will be examined in turn:

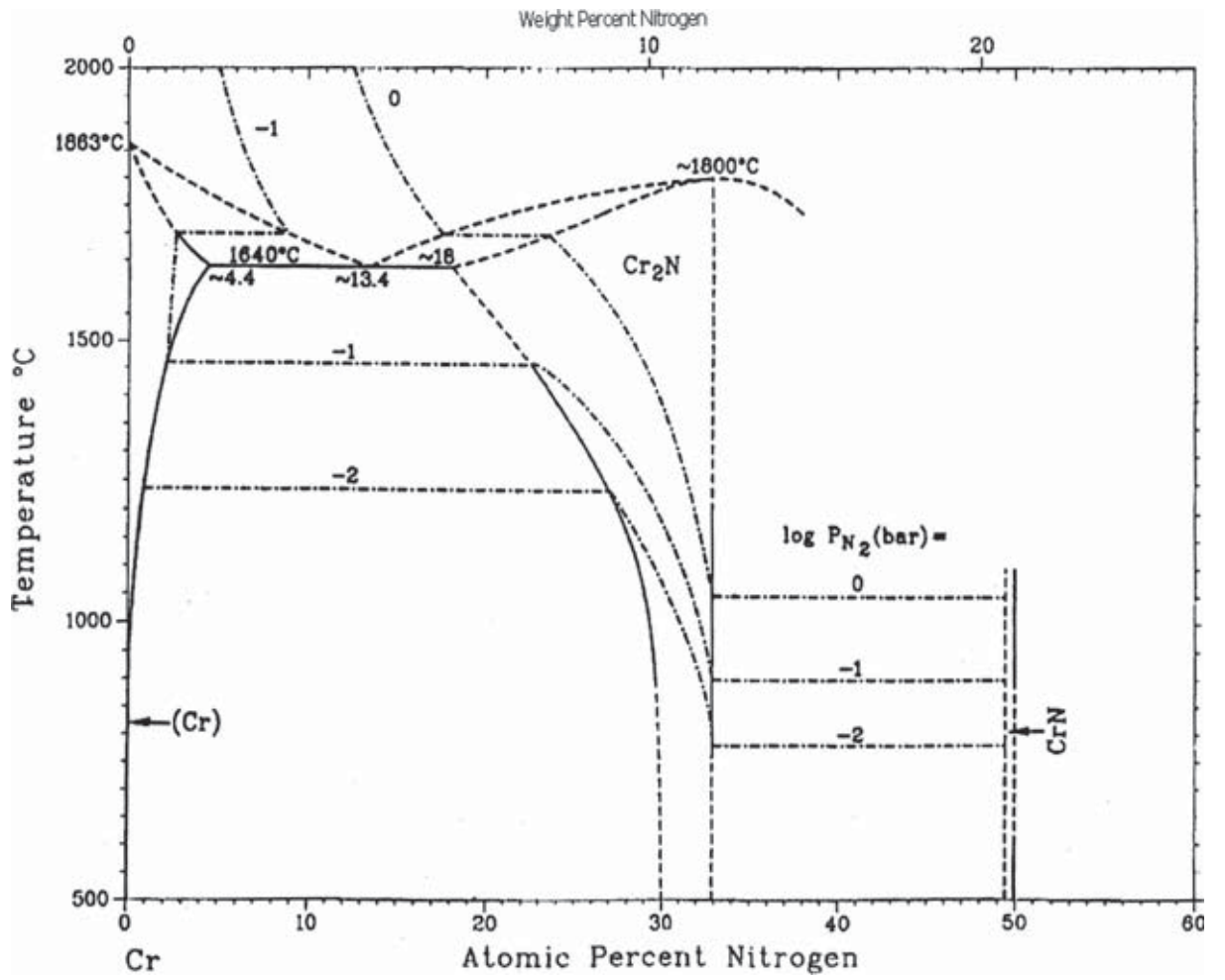


Figure 3.2: Phase diagram for the Cr-N system.

3.2 CrN:

This is a grey compound which is an fcc crystalline solid at room temperature. The crystal structure is an octahedral 6 co-ordinate system, as in NaCl. The nitrogen atoms occupy the interstitial gaps between the chromium atoms. This provides a chemically stable coating, with a thermal decomposition point of 2045 Kelvin, an excellent resistance to corrosion, low internal stress and a single crystal hardness of approximately 22 GPa [54] within 100nm of the surface. CrN can be either a semi-conductor or a conductor, and experiences a transition between the two states at 260 Kelvin. As a powder or polycrystalline solid CrN can be identified by XRD: the five strongest powder crystal lines for both CrN and Cr₂N are given in table 3.3. Previous work done by G.A Zhang, and more recently by Costel Constantin [55], demonstrates that epitaxially grown CrN can show semiconductor properties.

Table 3.1: The five most intense crystallographic planes as registered by Bragg-Brentano XRD of powder samples. Source: Joint Committee on Powder Diffraction Standards.

Chemical formula	{h,k,l}	% intensity	d-spacing (angstroms)
CrN	200	100	2.068
CrN	220	80	1.463
CrN	111	80	2.39
CrN	311	60	1.463
CrN	400	30	1.034
Cr ₂ N	111	100	2.1
Cr ₂ N	110	25	2.35
Cr ₂ N	112	25	1.63
Cr ₂ N	002	25	2.22
Cr ₂ N	221	25	1.38

3.3 Cr₂N :

Cr₂N is similar in appearance to CrN. The crystal structure is simple hexagonal. This material is highly corrosion resistant, with good mechanical properties. The reported single crystal hardness is in the region of 28 GPa [56].

3.4 Applications of Cr_xN:

Applications of chromium nitride coatings fall into two categories: Decorative and hard wearing.

Chromium nitride is suitable for decorative applications as it has the appearance of metallic silver when the nitrogen content is relatively low. When the nitrogen content is high the coating appears a grey colour and can be used as part of a pallet of possible surface colourings. It has relatively low internal stress (when deposited by conventional sputtering), it has high hardness and wear resistance, making it a durable and long lasting pigment.

As a hard wearing coating chromium nitride most often finds application in dry machining environments. This is due to its higher thermal stability and lower internal stress than TiN, its good low friction qualities, and its excellent mechanical properties (high hardness, very low wear rate etc). These allow a very thin (1 to 5 microns) layer of CrN to be deposited but still have a significant impact on a tool piece or working face life span, which is an advantage with high tolerance parts. Chromium nitride does not produce significant fragments as a result of wear, and the addition of a chromium adhesion interlayer promotes extremely high adhesion with most kinds of steel [57] [58]. A high corrosion resistance also provides a defence against the effects of atmospheric vapour. A further example of a chromium nitride application would be a coating for piston rings in an internal combustion engine.

4: UDP 350 deposition system:

The deposition system used is based on the Teer Coatings unbalanced magnetron deposition system. This is a relatively small system, and is a common piece of equipment for laboratories, although not for industrial scale deposition:

4.1: System overview.

The UDP 350 is a versatile system, which can be configured for up to 3 magnetrons, in closed or open field operation. A simplified diagram of the system is given in figure 4.1. The substrate holder base allows for a number of compatible substrate holders to be used. There are three equidistantly spaced ports on the chamber walls suitable for 300mm x 100mm rectangular magnetrons, as shown in figure 4.2. The magnetrons are water cooled, and have magnetic fields generated by two layers of magnets: ferrous and rare earth alloy. All joints in the vacuum system are sealed using polyurethane ‘O’ rings, compressed in place by external clamps.

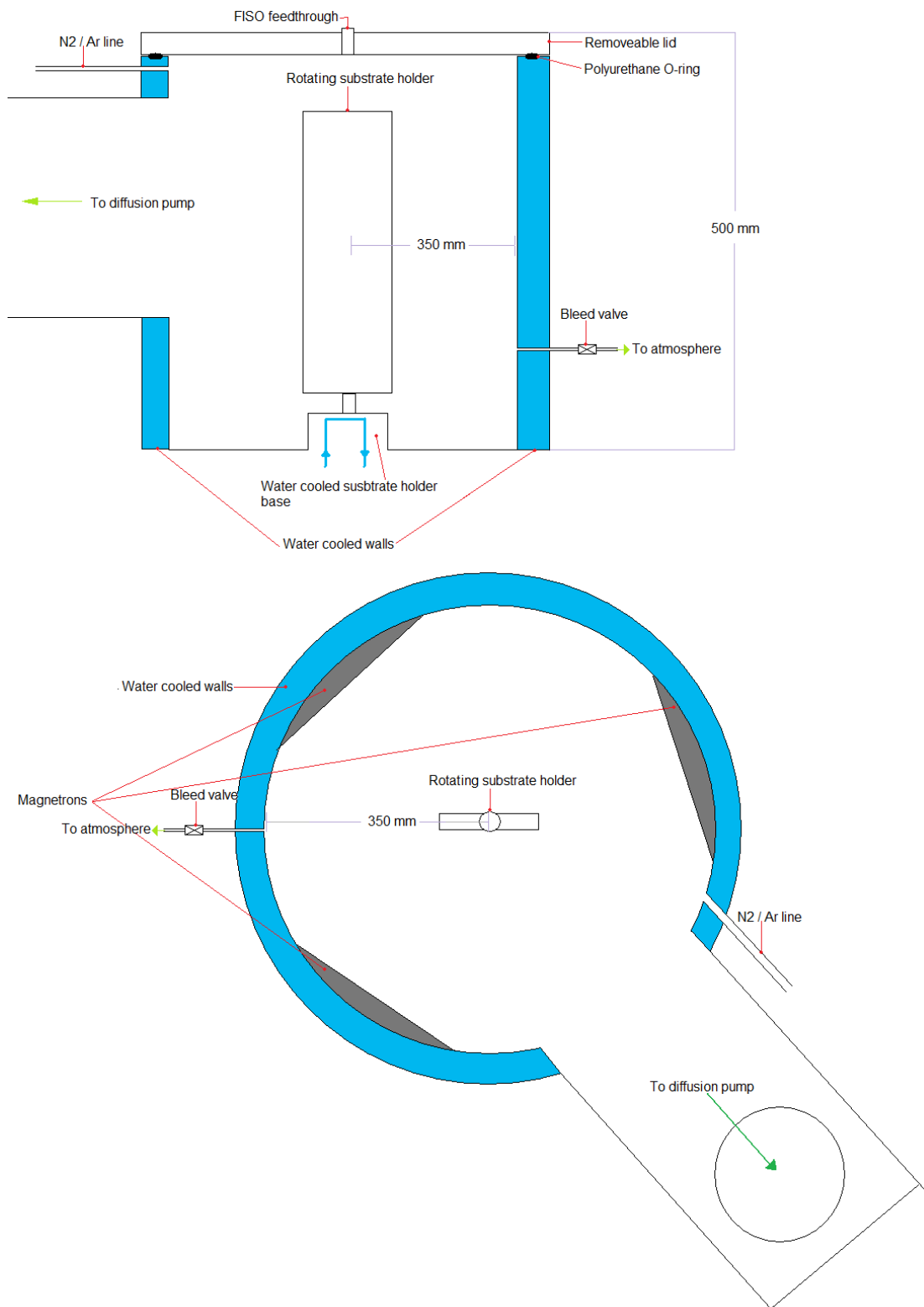


Figure 4.1: Top: A simplified cross section view of the main deposition chamber of the UDP 350. Bottom: A plan view of the chamber. The chamber is portrayed with the planar (as opposed to planetary motion, see below) substrate holder in place. Sensor ports set into the chamber walls have not been depicted, for the sake of clarity.

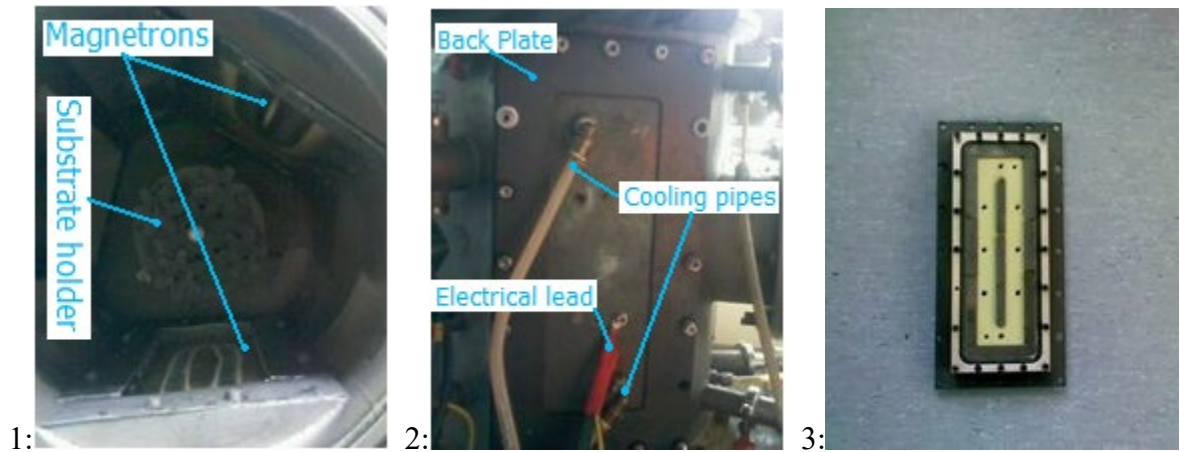


Figure 4.2: Annotated photographs of the magnetrons: (1) Top view showing the magnetrons set in place in the sputter chamber wall, (2) Rear view showing the magnetron removed with the arrangement of cooling pipes, (3) with the target face removed exposing the (empty) coolant reservoir.

The system operates as a closed field unbalanced system (see section 2.3). In a purpose built system the magnetron targets would sit opposite each other, however as this is an older design that has been adapted, the magnetron faces are inclined to each other at approximately 60 degrees.

4.2: Vacuum system:

The main vacuum chamber is a cylindrical stainless steel tube measuring 350mm in radius and 500 mm in height. A vacuum system diagram is given in figure 4.3. The wall of the chamber is water cooled, and the substrate holder is placed in the centre. The holder is mounted on a bearing set into the chamber floor, allowing it to be rotated by a motor external to the chamber. The substrate holders can be interchanged, allowing for a variety of configurations to be emplaced. The base of the substrate holder is water cooled to protect the bearings and seals. The chamber wall houses up to three magnetrons, equidistantly spaced. For the purposes of this project only two were installed, with the third space being blanked. The chamber is accessed by removing the top lid. The main chamber is roughed to low vacuum by a 40 m³/hr Edwards rotary pump and brought to a high vacuum in the region of 5x 10⁻⁴ Pa by an Edwards diffusion pump. Base pressures in the region of 1 x 10⁻⁴ Pa can be achieved with sufficient pumping time. The standard procedure for reaching base pressure is as follows: The system begins with the high

vacuum valve and valves 1 and 2 closed. The chamber is sealed, and valve 1 is opened allowing the rotary pump to evacuate the main chamber to a low vacuum. Chamber pressure is monitored by a thermal Pirani gauge. At this point the Baratron gauge is sealed, to maintain it at vacuum. When the main chamber pressure is brought to below 10 Pa valve 1 is closed and valve 2 is opened, followed by the high vacuum valve. This allows the diffusion pump to bring the main chamber to base pressure and avoids contaminating the main chamber. At the same time the Baratron and Penning gauges are switched on. Once diffusion pumping has begun the chamber will typically take 2 to 3 hours to reach base pressure.

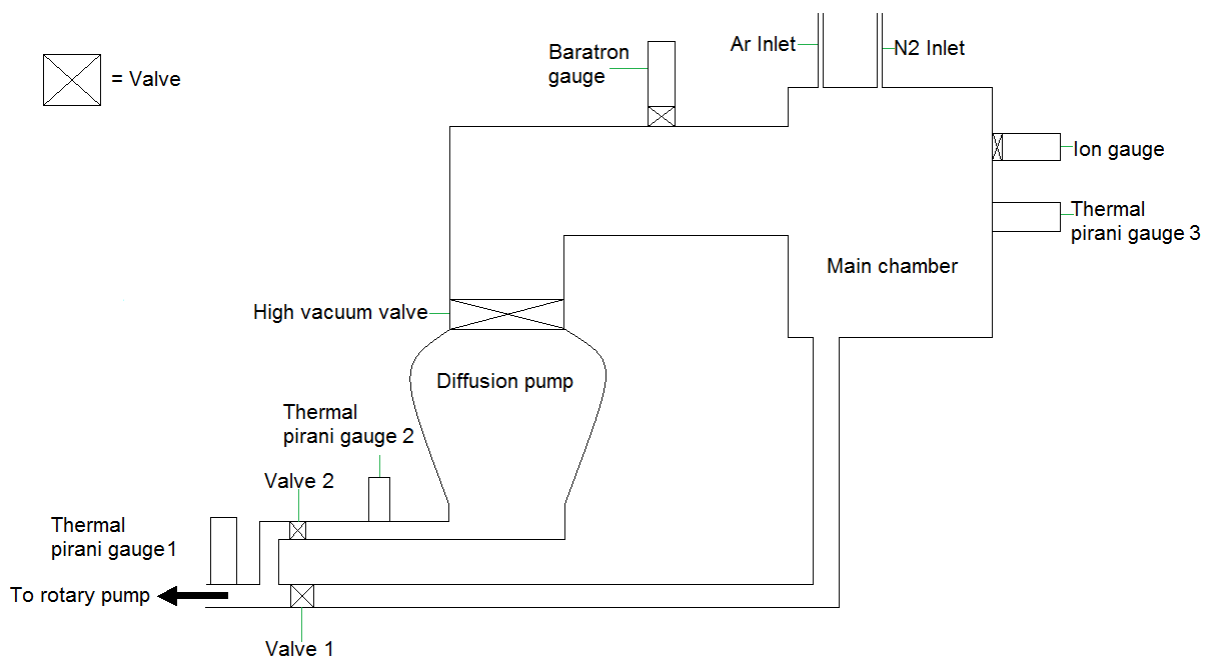


Figure 4.3: A schematic of the UDP 350 sputter system, showing the diffusion pump, main chamber, connecting feeds, main pressure gauges, Ar inlet and N₂ (reactive gas) inlet.

4.3: Rotary pump:

The rotary pump used is a two stage 40 m³/hr Edwards rotary pump. The pump has a dual usage. With the system in roughing mode (valve 2 closed, high vacuum valve closed, valve 1 open) the pump acts to bring the pressure of the chamber to below 10 Pa. In backing mode (valve 1 closed, high vacuum valve open, valve 2 open) the rotary pump serves to remove exhaust gases from the outlet of the diffusion pump.

4.4: Diffusion pump:

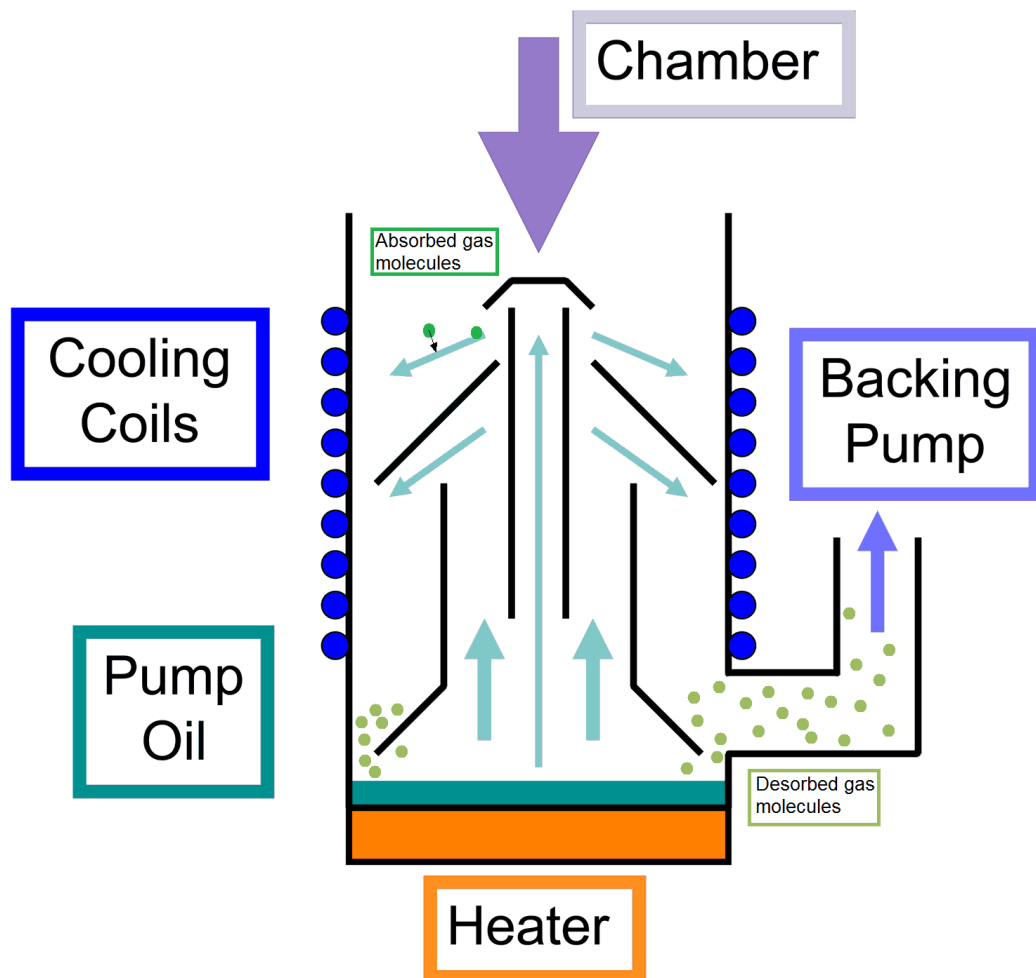


Fig 4.4: A simplified cross section of the operation of a water cooled diffusion pump. Image courtesy of the society of vacuum coaters.

The diffusion pump is a high vacuum pump, not intended for use at atmospheric pressures. Its operation is shown in figure 4.4. The operation of the diffusion pump consists of a base filled with oil heated by an electrical heater. The evaporated oil is drawn up the centre of the pump body, and is sprayed at a 45 degree angle out of nozzles around the central core, creating a series of ‘umbrellas’ of supersonic oil travelling away from the inlet and towards the cooled walls of the pump. Upon striking the wall the oil condenses and travels back down the pump under gravity. When hot the oil chemically absorbs the chamber gas entering the pump through the inlet, and as it cools this gas is released. The function of the oil is to carry the gas in chemisorbed form down the pump towards the outlet where it collects at pressures high enough to be pumped away by the rotary pump. Diffusion pumps

are extremely simple and therefore durable devices, allowing residual gas pressures in the region of 10 Pa to be reduced to the region of 0.0005 Pa over a 24 hour period. Although not ultra high vacuum this is more than adequate for the purposes of PVD. The chief drawback of diffusion pumping, the migration of hydrocarbon (oil) contaminants into the main chamber, can be simply mitigated by a swing valve partially closed placed along the tube lining the pump inlet and the main chamber, or can be almost entirely eliminated by the addition of a liquid nitrogen cooled trap at the inlet mouth.

4.5: Temperature sensors:

Temperature was measured by means of a FISO technologies fibre optic temperature probe which was passed through an optical feed through (figure 4.5) in the lid of the chamber.

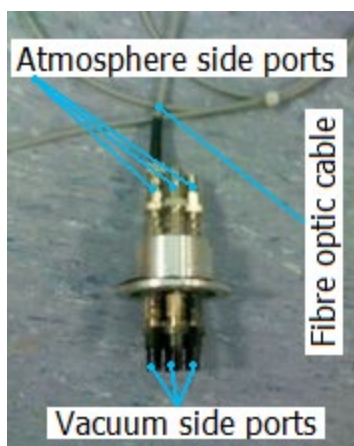


Figure 4.5: The fibre-optic feed through allowing egress of FISO signals from the chamber, shown set down on the workbench.

The interferometer at the probe tip has a time resolution of below 1 second and a temperature resolution of ± 1 degree Kelvin. As the fibre optic probes were only guaranteed up to 350 degrees Celsius, a temperature that might be exceeded by the substrate, the temperature monitoring runs were performed separately, so that sputtering could be ceased when the temperature reached damaging levels.

4.6: Pressure sensors:

The vacuum system is connected to three types of pressure sensors:

- Baratron capacitance manometer:

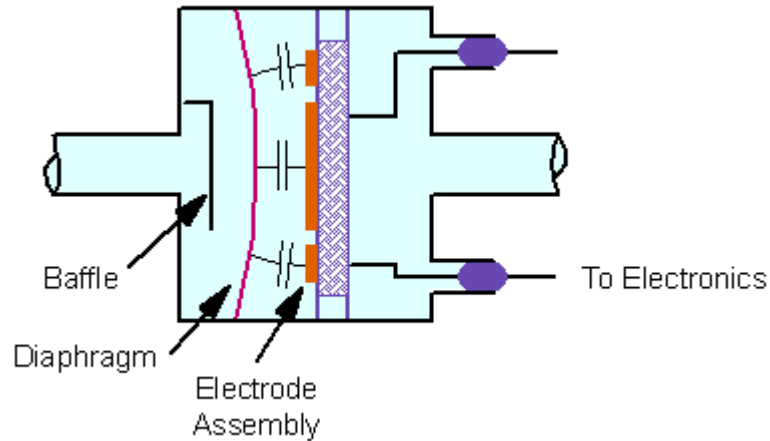


Figure 4.6: A simplified cross section of the Baratron capacitance manometer: As the diaphragm is deformed the capacitance of the attached capacitors changes, providing an electronic reading of pressure.

This is an electromechanical sensor which measures gas pressure by the amount it distorts a flexible membrane. This membrane makes up one plate of a simple capacitor, which changes its capacitance as the membrane distorts, allowing direct measurement of pressure, irrespective of gas type.

- Penning gauge:

This is a 'cold cathode' ionisation gauge. It measures pressure by the ease of ionisation of the chamber gas. Chamber gas is ionised by electrons emitted from a plasma, and the ions are collected by a conducting grid. The probability of a collision between an electron and a gas particle is proportional to the gas particle density. The pressure is determined by the magnitude of the collected ion current.

- Thermal Pirani gauge:

These gauges measure pressure by the transmission of heat away from a filament exposed to the chamber conditions. As the primary methods of thermal energy transmission are

conduction and convection at atmospheric pressure the efficiency of thermal energy transmission can be used to monitor pressure.

4.7: Substrate holder:

The substrate holder is located in the centre of the main chamber, and consists of a vertical rectangular section of aluminium, mounted onto an electrically isolated base (figure 4.7). The base is water cooled, and covered with a cylindrical shield to prevent accumulation of unwanted sputter deposits and potential electrical bridging between the holder and the chamber floor. The upright substrate holder is pierced with a grid pattern of holes which allow a variety of substrates to be held in place by means of screws, washers and bolts:



Figure 4.7: The vertical substrate holder.

The substrate holder base can be rotated by a motor set just below the chamber floor, which is controlled by a panel on the front right hand section of the rig.

A planetary motion substrate holder was used when we required 360 degree coverage of the substrate, such as might be used for coating a drill bit:

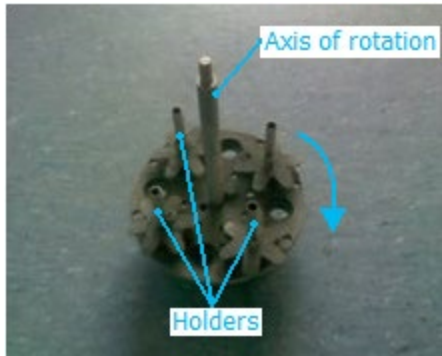


Figure 4.8: The planetary motion substrate holder.

This consisted of four freely turning supports for a cylindrical substrate, spaced equidistantly around the substrate holder base (figure 4.8). Each place has a series of ‘petals’ at the bottom, which move with the substrate. An electrically isolated pin and rod arrangement attaches to the base in such a way that it remains still whilst the holder assembly rotates, and as the assembly rotates the pin strikes the petals at the base of each substrate causing them to turn. Over the course of a deposition run, this results in an even exposure to the flux of sputtered target material for each substrate position.

4.8: Magnetrons:

The magnetrons used are rectangular in configuration, taking chromium targets measuring 300mm x 100mm. These are bonded to copper backing plates and are water cooled (figure 4.2), the backing plate making one wall of a reservoir through which chilled water is pumped. Behind the reservoir are located two layers of magnets, providing the magnetrons field. The layer closest to the target surface consists of ferrite magnets. The second layer uses stronger rare earth magnets.

4.9: Optical Emissions Monitoring (OEM) system:

A schematic of the OEM feedback loop is given in figure 4.9. Control of reactive gas (nitrogen) flow was achieved by using either a mass flow controller, or an optical emissions monitoring (OEM) feedback loop.

This system consists of a tuneable optical emission monitor (monochromator), provided with a view directly through the widest part of the race track, by means of a fibre optic cable attached to a window in the chamber lid. This OEM is linked to a reactive gas flow control box [59], which allows for the input of a setpoint value for the signal received, in arbitrary units. The control box is in turn linked to a piezo electric valve on the nitrogen feedline, which opens and closes, via PID control, to maintain the inflow of reactive gas at such a level that the OEM maintains the signal at the preset level.

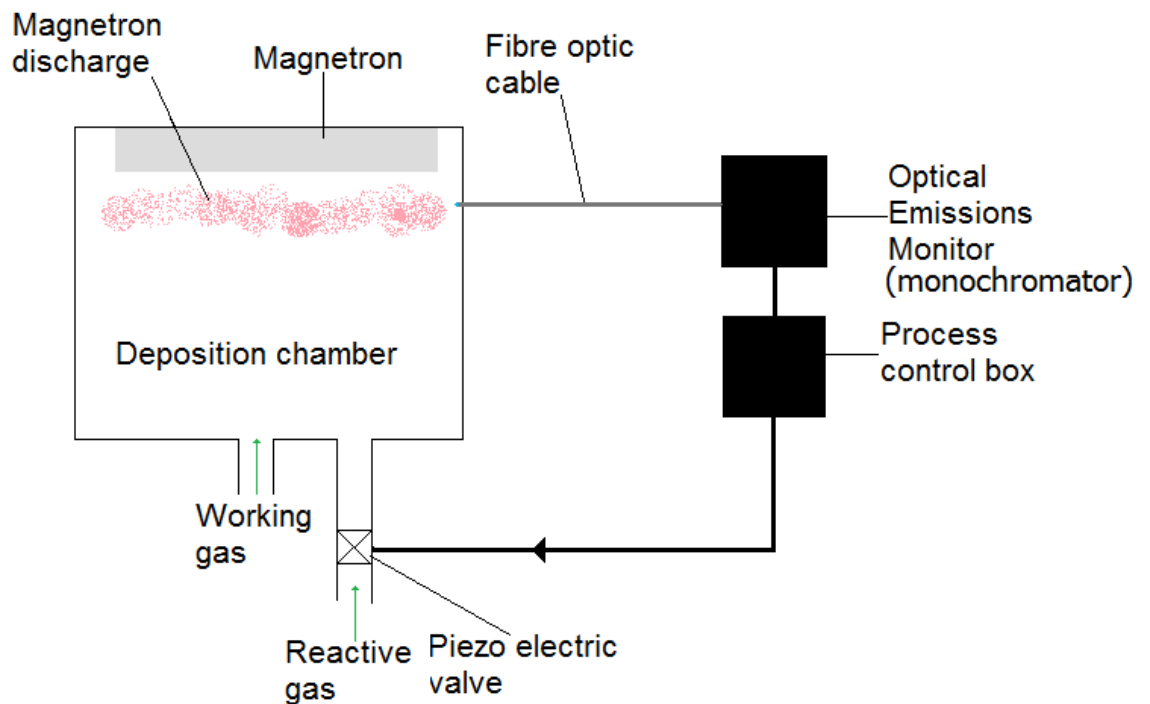


Figure 4.9: A simplified schematic of the OEM feedback loop: light of a particular frequency from the plasma travels along a fibre optic cable to the OEM. The OEM signal is passed to the process control box, which ascertains whether the intensity of the frequency the OEM is monitoring is above or below the setpoint in its memory. The process control box then signals the piezoelectric valve to open or close depending on the intensity measured.

4.10: Gas inlets and flow control:

Both reactive gas and working gas (nitrogen and argon, respectively) enter the chamber through a single inlet on the chamber wall, located between the two magnetrons. Ten centimetres from the entry point the pipe splits, with one side going to the argon source and one to the nitrogen source. The argon flow into the chamber is controlled by an MKS

mass flow controller, with a maximum flow rate of 100 SCCM. The controller is calibrated for nitrogen, so the flow rates were calculated using a 1.39 gas correction factor of N₂ to Ar flow for thermal mass flow controllers. The reactive gas flow is controlled by an OEM feedback loop as described above.

4.11: Oscilloscope:

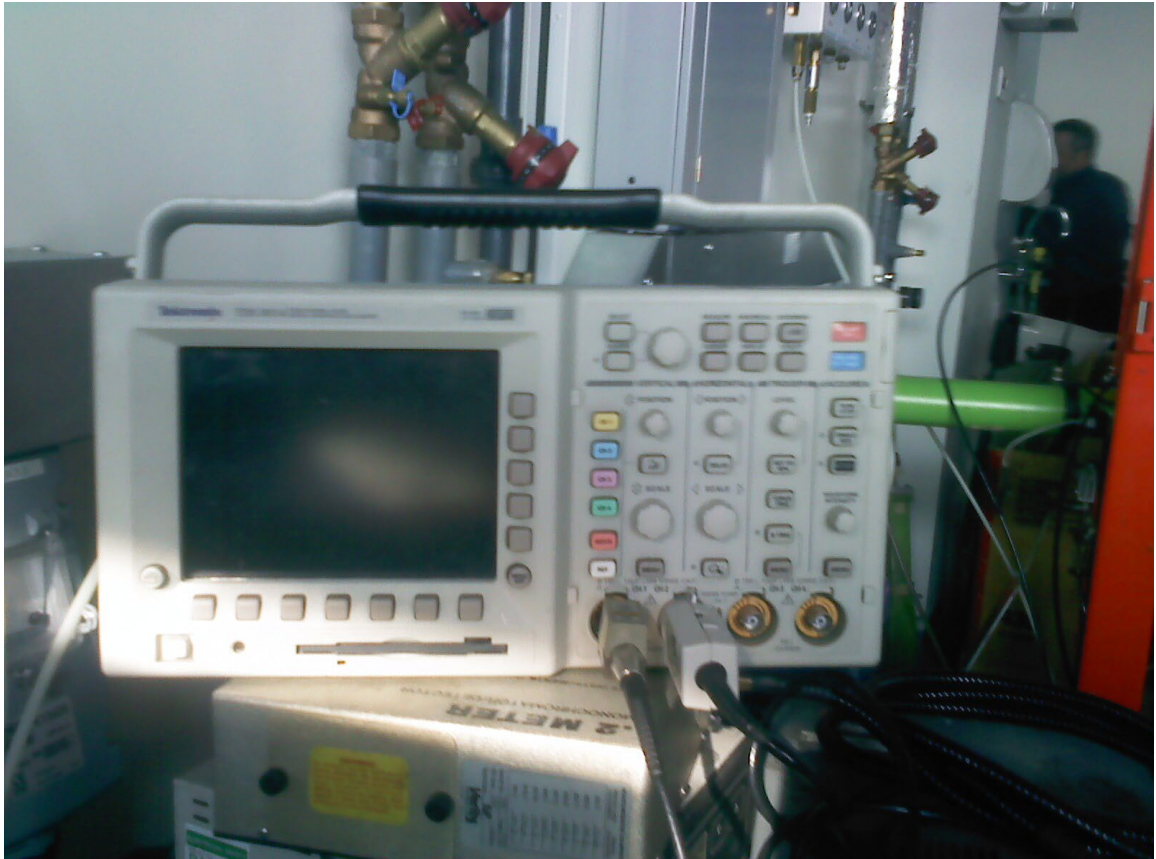


Figure 4.10: The TDS 3014 oscilloscope with current and voltage probes attached.

The oscilloscope used in all these investigations was a four channel TDS 3014 (shown in figure 4.10). This model accepts both current and voltage probes, and will automatically calculate power based upon these readings. Current probes are applied to the system using a current measurement box (shown in figure 4.11). This consists of a hollow metal chamber with connectors for the power cables at either end of its long axis.

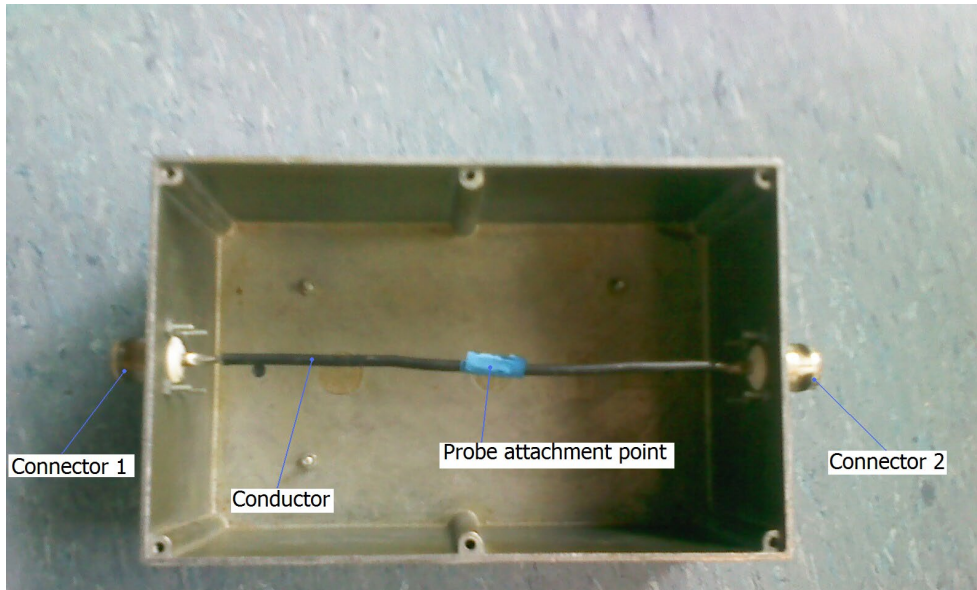


Figure 4.11: The power line attachment, which allows the oscilloscope to safely measure high currents. A length of exposed conductor runs between the two connectors and the current probe (shown in figure 4.11) clips around it.



Figure 4.12: The current probe head, with labelled components.

The voltage probe consists of a retractable conducting hook in a plastic housing, and is earthed using a crocodile clip arrangement (figures 4.12 and 4.13).

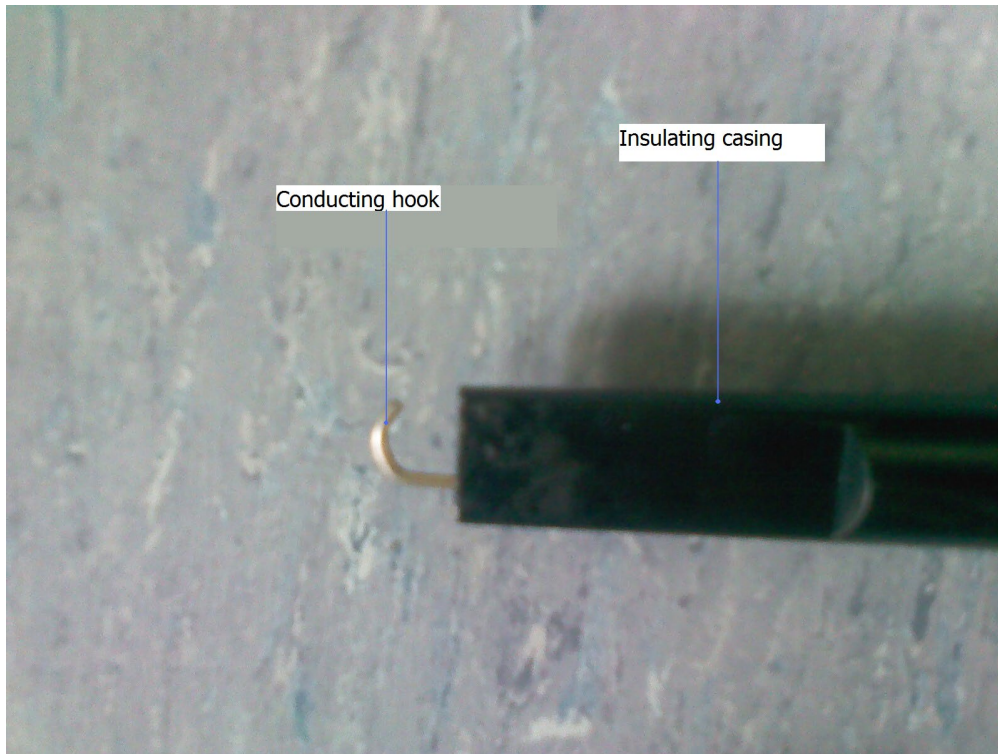


Figure 4.13: A close up of the oscilloscope voltage probe head with the conducting hook extended.



Figure 4.14: The oscilloscope voltage probe head with its earth lead.

While the current probe can only be attached safely where there is a suitable and safe section of appropriate diameter connector, the voltage probe can be attached at numerous points on the system. In this project the voltage probe was connected to the point where the power cables entered the base of the substrate holder (shown in chapter 7, figure 7.2) and to the back of the magnetron.

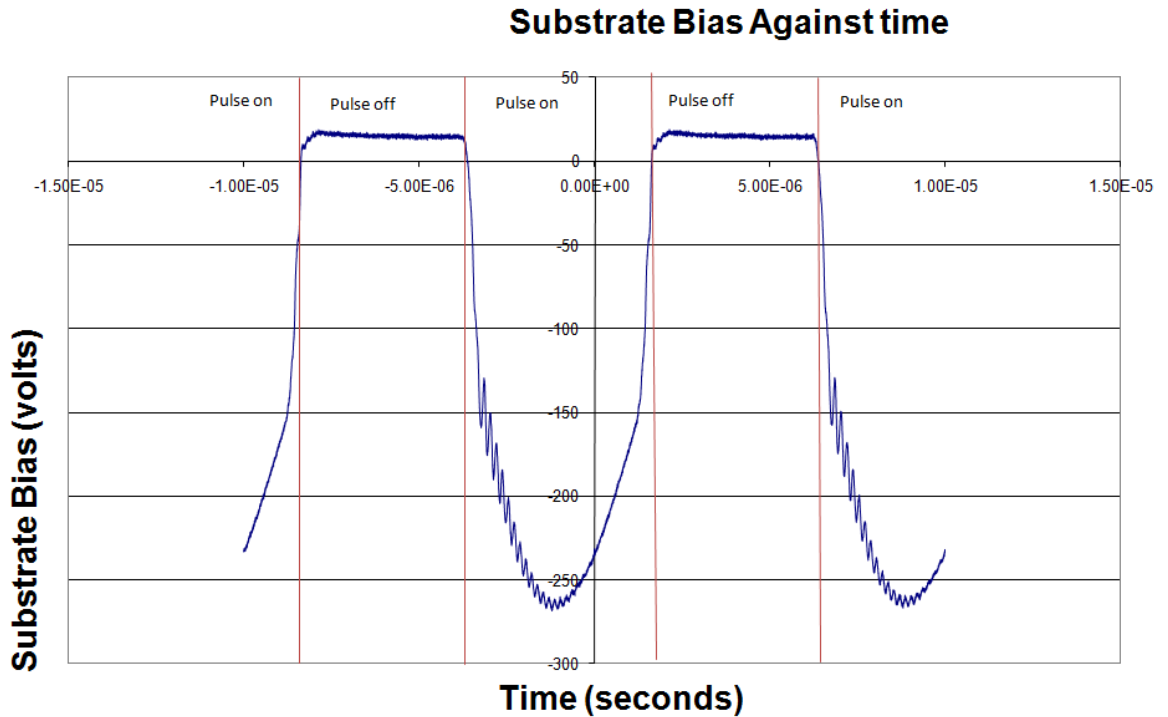


Figure 5.1b

Figure 5.1 a & b; Oscilloscope traces of the current (figure 5.1a) and voltage (figure 5.1b) of one channel, supplying the substrate side of the UDP 350 deposition system, of the AE Pinnacle plus power supply during pulsed operation. Pulse rate is set to 100 kHz .Substrate bias is controlled to a time averaged 100V set point.

Alternate pulsing regimes:

Where both are active the two channels can be related to each other in three different ways: Both waveforms can be in phase with each other (synchronous pulsing), they can be offset by 180 degrees (dual cathode pulsing), and they can float with no set relation to each other (asynchronous pulsing). This work has focused on pulsing applied to the substrate bias only. Hence the following pulsing regimes are referred to as the 'alternate regimes':

- Target pulsing:

In this regime pulsing is applied to the target only. The substrate channel operates as a d.c. channel. Sputtering conditions are as standard. Target pulsing mode and substrate pulsing mode are both applied using the asynchronous setting which allows the pulse rate of each channel to be set independently.

- Simultaneous substrate and target pulsing with no fixed phase relationship.

In this mode pulsing was again applied to both substrate bias and target power, and the waveforms are allowed to propagate with no fixed relationship to each other. This is set up using the asynchronous setting.

- Simultaneous in-phase substrate and target pulsing.

In this regime d.c. pulsing is applied to both the substrate and the target, at the same rate, and the two waveforms are applied in-phase with each other. This is set using the synchronous setting. The conditions are otherwise standard.

- Simultaneous 180 degrees out of phase substrate and target pulsing.

In this mode both the target power and substrate bias are pulsed, such that the waveforms are 180 degrees out of phase with each other. As a 50% duty cycle was used in all investigations, this essentially meant that while one side is being powered the other is in its off time. This is set up using the dual cathode setting.

Duty cycle:

The on time of the pulse can be varied from 10% up to 90%, in most cases. However as the longest pulse the unit can deliver is 5 microseconds the possible on time for frequencies lower than 100 kHz is limited.

Chapter 6

6.1 Standard preparations:

Preparation of substrates for deposition:

Substrates, both tool steel coupons and (111) surface textured Si wafers, were first cleaned in an ultrasonic bath, in three stages. Each stage involved cleaning for 40 minutes in a different solvent: first acetone, then methanol, then ethanol. Following ultrasound treatment the substrates were placed in the vacuum chamber which was reduced to base pressure, and then backfilled with a 2 Pa Ar sputtering atmosphere. The substrates were then subjected to between 1 and 5 minutes of ion etching, using a target current of 0.3 amps, and a substrate bias of -650 volts.

Preparation of coatings for tribological tests:

Coatings were not cleaned in an ultrasound bath to avoid possible cavitations, but were immersed in methanol for ten minutes and then gently cleaned using optical wipes which leave no fibres behind.

Preparation of coatings for SEM work:

Coatings were prepared as for tribological tests, but a second stage of cleaning using ethanol was included to minimise residue.

Preparation of coatings for TEM work (include FIB milling):

In order to extract a sample of suitable cross sectional thickness for TEM imaging the coating was cleaned as in 6.2 and then placed in Oxford University's Focussed Ion Beam Milling facility. This technique uses a focused beam of ions to sputter away sections of coating, allowing samples only tens of microns across to be extracted. It is described in detail by Gnauck et al [148]. Using FIB, a section of the coating was extracted, and attached to a copper TEM grid by applying a small quantity of tungsten hexacarbonyl gas to the chamber and using the ion beam to decompose it in the vicinity of the required join, depositing the tungsten. This is a low pressure CVD process.

6.2: Standard deposition conditions:

The standard deposition conditions were in part based upon previous work at MMU [60] [61] [62] on increasing the density, crystallographic structure, and wear resistance of TiN coatings. These suggested that a substrate bias in the range of -20V to -100V, and a target power of 0.5 to 2 kW, would provide a dense coating in zone T or zone 2 of the Thornton structure zone model. Characterisation of the coatings (detailed in later chapters) suggested that an optimum region in terms of coating adhesion and hardness, as well as minimising columnar growth, lies in the region of -50 to -80 volts substrate bias, and 1kW of target power. The sputtering pressure was approximately 0.2 Pa

6.3: Standard tribological tests:

Scratch adhesion test:

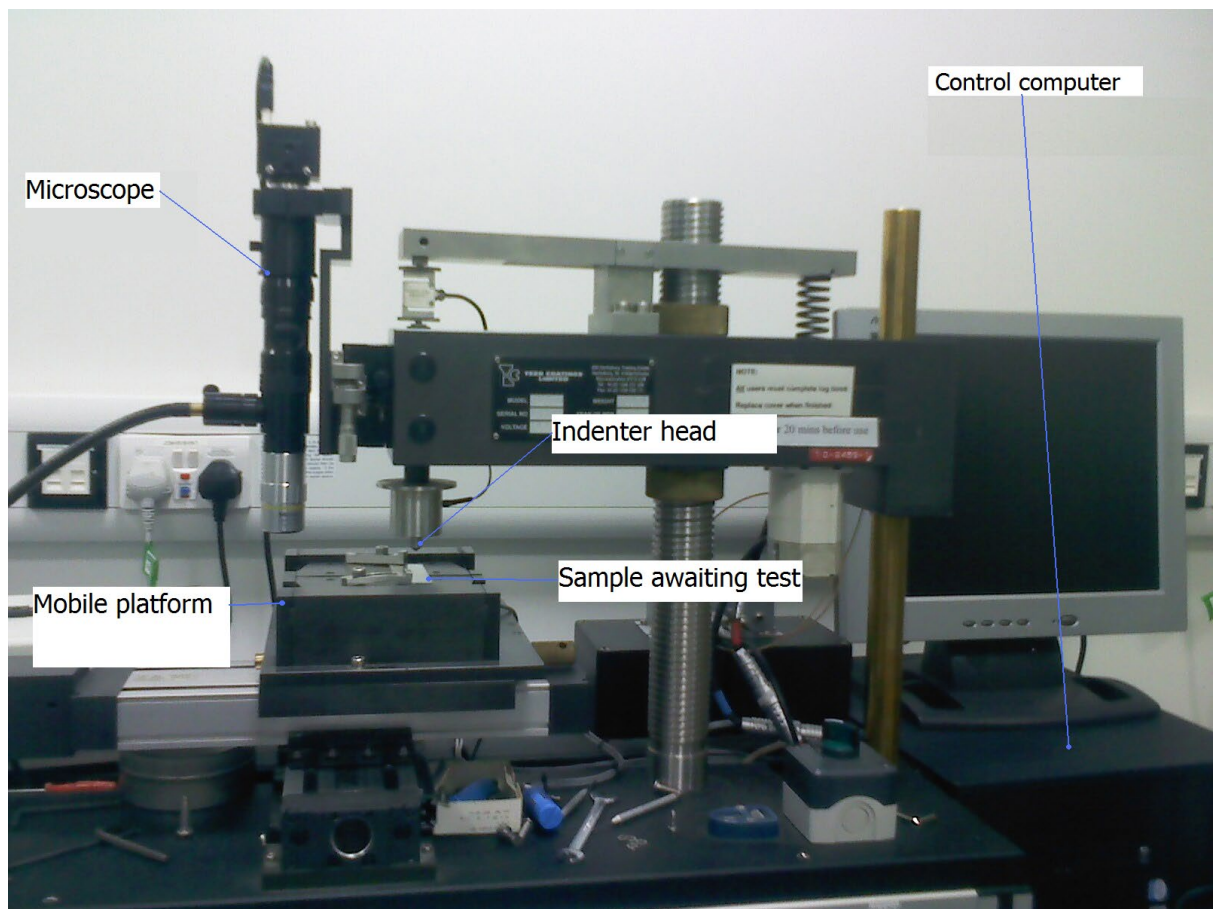


Figure 6.1: The Teer Coatings Limited ST3001 scratch test unit.

One of the fundamental coating properties is the ‘adhesion’ - the interfacial forces- between the bulk material of the coating and the substrate. Scratch adhesion testing is a means of evaluating the adhesion of a coating to a given substrate. The results require interpretation, and a number of possible failure modes can occur, either consecutively or concurrently. For the purposes of this text a simplified overview of the effects of scratch adhesion testing of thin hard coatings is presented. A more detailed view is presented by K.L.Mittal [63].

For all of the scratch tests in this work a Teer Coatings Limited ST3001 scratch tester (shown in figure 6.1) was used. The process of scratch adhesion testing is as follows:

- 1) A layer of coating is deposited onto a polished substrate small enough to fit into the testing platform.
- 2) A diamond tipped stylus with a 200 micron radius is brought into contact with the coating surface.
- 3) The stylus is dragged across the coating surface (as shown in figure 6.2) at a fixed rate with steadily increasing pressure perpendicular to the coating surface, leaving a scratch track in the coating.
- 4) As the stylus moves a number of measurements are made: The friction coefficient between the stylus tip and the coating, and the acoustic emissions associated with the movement across the coating are the chief measurements of interest.
- 5) After the scratch is completed the scratch track is examined under an optical microscope. The computer controlled movement of the sample holder allows the position of acoustic emission events, changes in frictional coefficient etc to be matched to positions along the scratch track.

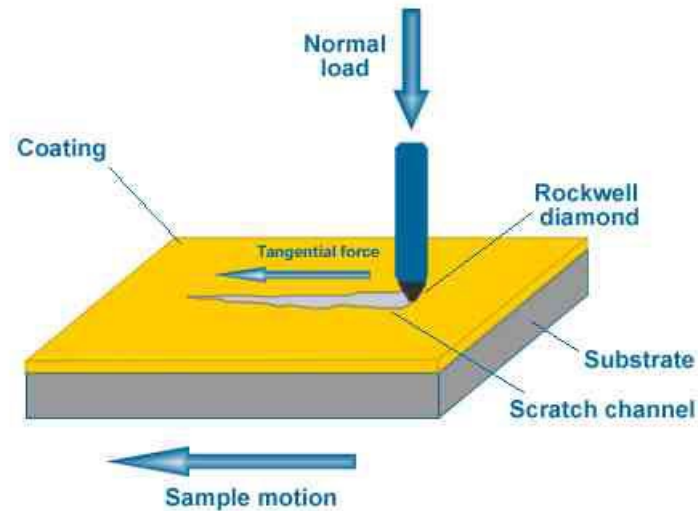


Figure 6.2: The single pass scratch adhesion tests. Image courtesy of PVD-coatings.co.uk

Analysis of the scratch track under the optical microscope, accompanied by the measurements taken during the formation of the scratch track, forms the basis of the adhesion analysis. Acoustic emissions and changes in frictional coefficient serve to point out locations on the scratch track where events relating to coating adhesion may have occurred. These events are then verified by the optical microscope. Typically three critical loads normal to the coating surface are determined:

- L_{c1} : This is the normal force at which the first continuous cracking of the coating occurs, as shown in figure 6.3. This may be accompanied by intermittent spallation outside the scratch track or along the bottom of the scratch track.

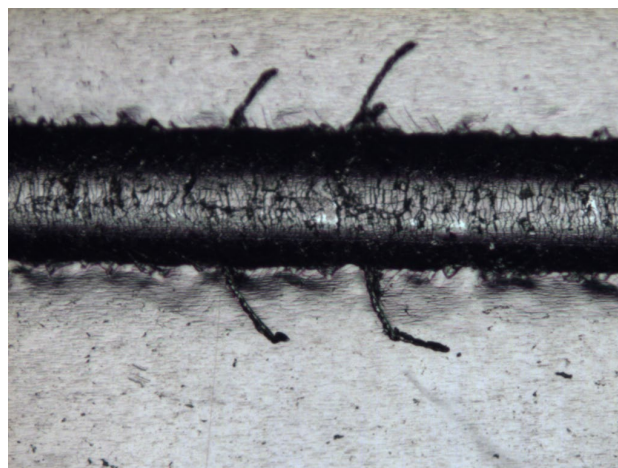


Figure 6.3; An example of the initial stages of cracking around the edges of the scratch track.

- L_{c2} : This is the normal force at which the first continuous spallation of the coating outside of the scratch track occurs, as shown in figure 6.4. This may be accompanied by intermittent spallation and/or ductile perforation along the bottom of the scratch track. Cracking along the bottom of the scratch track will usually accompany this stage. This commonly represents the first occurrence of failure of the interfacial bond between coating and substrate, due to stress transmitted through the coating-substrate interface ahead of, and to the sides of the indenter.



Figure 6.4: The beginning of continuous spallation around the edge of the scratch track, accompanied by intermittent spallation along the bottom of the track. Indenter motion is from right to left.

- L_{c3} : This is the normal force needed to cause total failure of coating adhesion. This can manifest in a number of ways (shown in figure 6.5): Continuous ductile perforation of the coating along the bottom of the scratch, total spallation of the coating inside and outside of the scratch track, or a combination of the two.

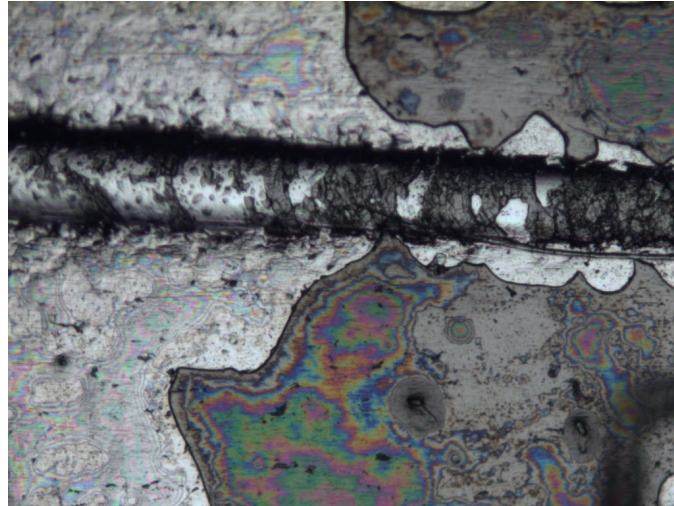


Figure 6.5: A typical L_{c3} for a CrN coating on tool steel. The beginning of continuous perforation of the coating at the bottom of the wear track is seen, accompanied by massive spallation around the edges of the scratch track. Stylus motion is right to left. The discolouration is caused by remnants of the cleaning solution used to remove debris.

Nanoindentation tests:

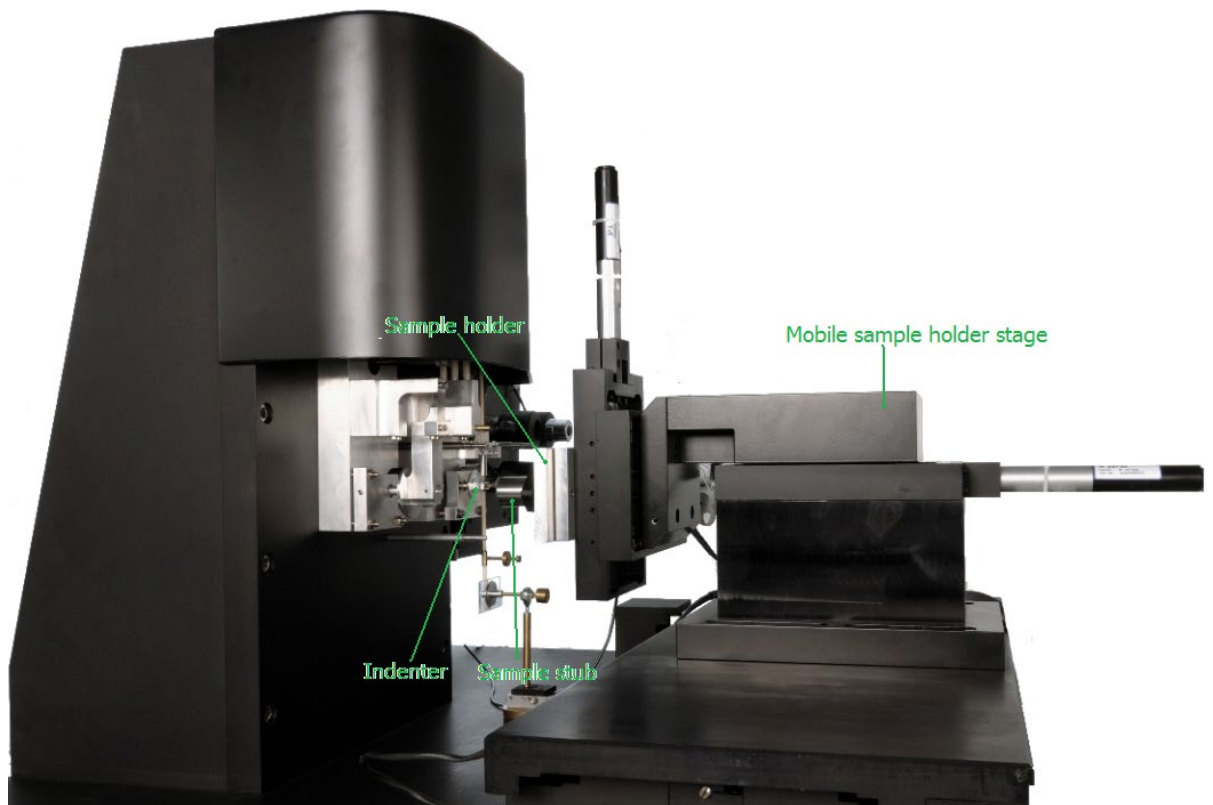


Figure 6.6; The Micro Materials nano-indentation platform, without its climate controlled housing. Image courtesy of Micro Materials.

Nano indentation is a relatively new means of measuring coating properties, chiefly surface hardness and elastic modulus. All surface hardness measurements in this project were carried out with a Micro Materials Nano-Test platform, shown in figure 6.6). Samples are thoroughly cleaned and any residue removed. They are then securely fastened to an aluminium stub which is held tightly in place on the apparatus by a screw. Using a lever system controlled by a solenoid (figure 6.7) an indenter is brought into contact with the coating surface. The indenter is then pushed into the coating with incrementally increasing force, and its displacement measured. When a preset maximum load is reached the force is removed in increments, and the indenter displacement again measured with each step. This produces a force against displacement hysteresis curve, from which the hardness and elastic modulus of the coating can be estimated to a depth of up to approximately 10% of coating thickness.

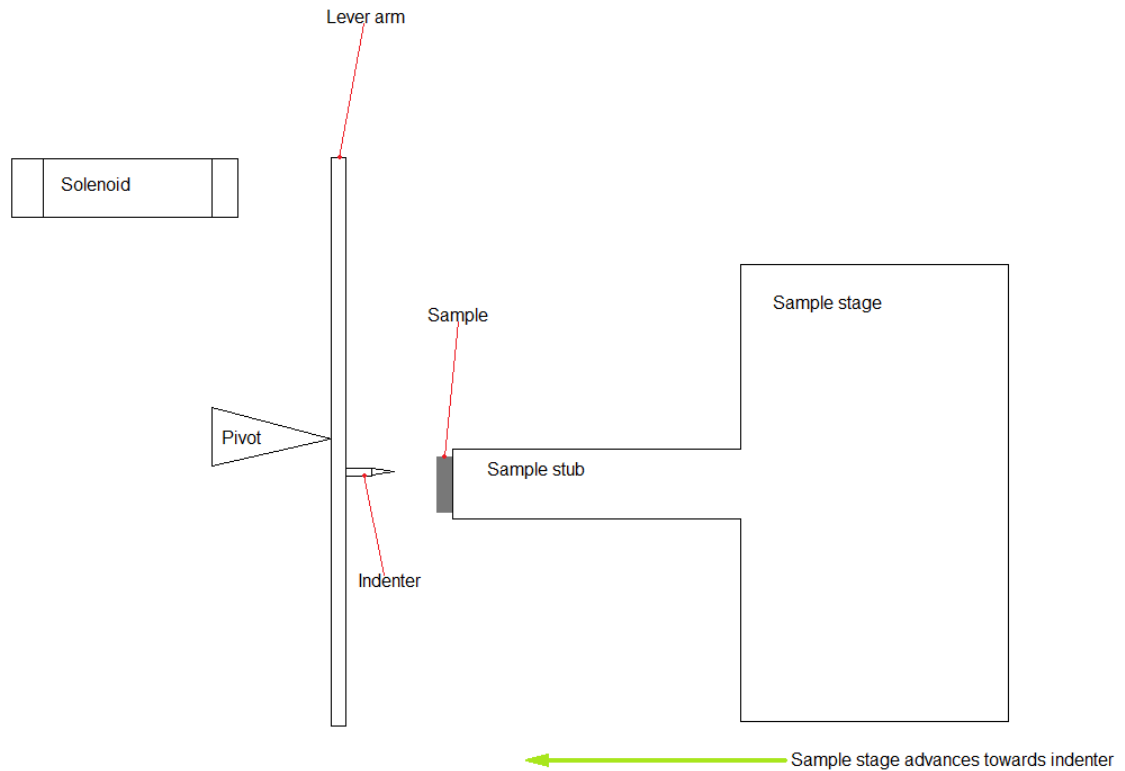


Figure 6.7: A simplified schematic of the nano indenter apparatus.

Typically multiple indents are made in a grid pattern, and the averaged values of these measurements taken. In order to obtain a realistic average across a reasonable area of coating our standard indent grid was 25 indents in a 5 x 5 grid, with a separation of 20 microns. The indentation mechanism is housed in a climate controlled case.

Thrust washer wear test:

The thrust washer wear test is one of the best laboratory tests available for simulating ‘real world’ wear and tear. It is especially useful in estimating coating response to wear over large areas [155]. The test piece, a flat coupon of coated material, sits in a sample holder, while an annular washer of some material of exceedingly high wear resistance is held against it with a pre set load. The washer is then rotated at a fixed rate and the turning force between the mating faces is recorded by a transducer [153]. For this project the washer was made of tungsten carbide, with an inner radius of 12mm and an outer radius of 15mm. The standard interfacial force was 300N. The sample holder had some freedom of movement about the horizontal plane, and was connected to lever arm, which was connected to the force - voltage transducer. This allowed a basic measure of the frictional force being

developed at the interface between washer and sample to be recorded by a simple datalogger. The thrust washer test is often used in conjunction with profilometry to measure the rate of wear; by periodically pausing the thrust washer test the profilometer can be used to develop a real time measurement of the wear track.

In a real world situation contact is not even across the two mated surfaces. Contact occurs where high points of topography, referred to as 'asperities', contact each other near their tips. As a first approximation the interaction between the two faces may be modelled as the bonding and debonding of the tips of asperities. However this only truly applies under vacuum conditions: Further complicating the situation are the effects of atmosphere: under sea level room temperature conditions a layer of adsorbed water vapour and organic contaminants from the atmosphere builds up on almost every surface. Many surfaces will also react with atmospheric oxygen under heat produced by friction to produce an oxide 'glaze' with different frictional and wear properties to the bulk coating [154]. For these reasons the thrust washer tester is limited by the ability to reproduce the ambient conditions under which real world wear will take place, as well as by the maximum speed of the rotating face.

Profilometry:

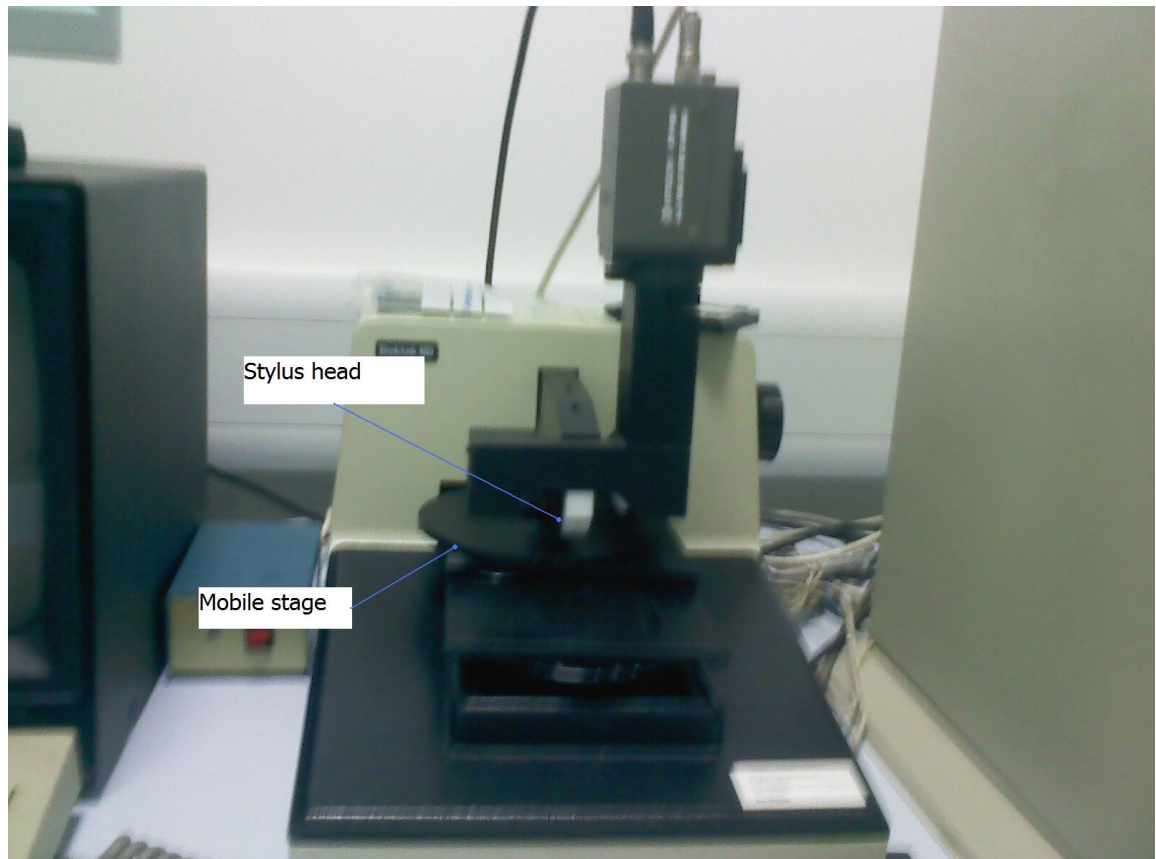


Figure 6.8: The Dektak profilometer.

Profilometry is a standard test for measuring the topography of a surface at small scales. A fine pointed probe or stylus is brought into contact with the sample surface, with negligible force. It is then dragged across the surface at a fixed rate, and its vertical displacement is recorded via a transducer. This allows topography along the stylus track to be measured.

Bragg-Brentano mode and glancing angle mode X-ray Diffraction:

X-ray diffraction is a technique for identifying materials by the diffraction patterns produced when the sample is exposed to a beam of x-rays: The incoming x-ray photons are scattered off the electron shells of the atoms making up the sample. Where the atoms are arranged in a regular fashion, as in a crystalline material, the photons scattered off different crystal planes will experience constructive or destructive interference depending on the angle of the incoming x-ray beam (see figure 6.9). By varying the angle of incidence a pattern of peaks and troughs in intensity (or diffraction pattern) with incident angle can be built up. Every crystalline substance produces a unique diffraction pattern, which can be

used as a fingerprint to identify it. Compounds produce unique patterns independently of their constituent elements. Around 50,000 inorganic crystalline materials have had their diffraction patterns recorded for reference.

However, the diffraction pattern can tell us more than simply which compound or element is present. Consider a beam of approximately parallel x-rays with identical wavelength and phase from an emitter striking planes of atom in a crystal:

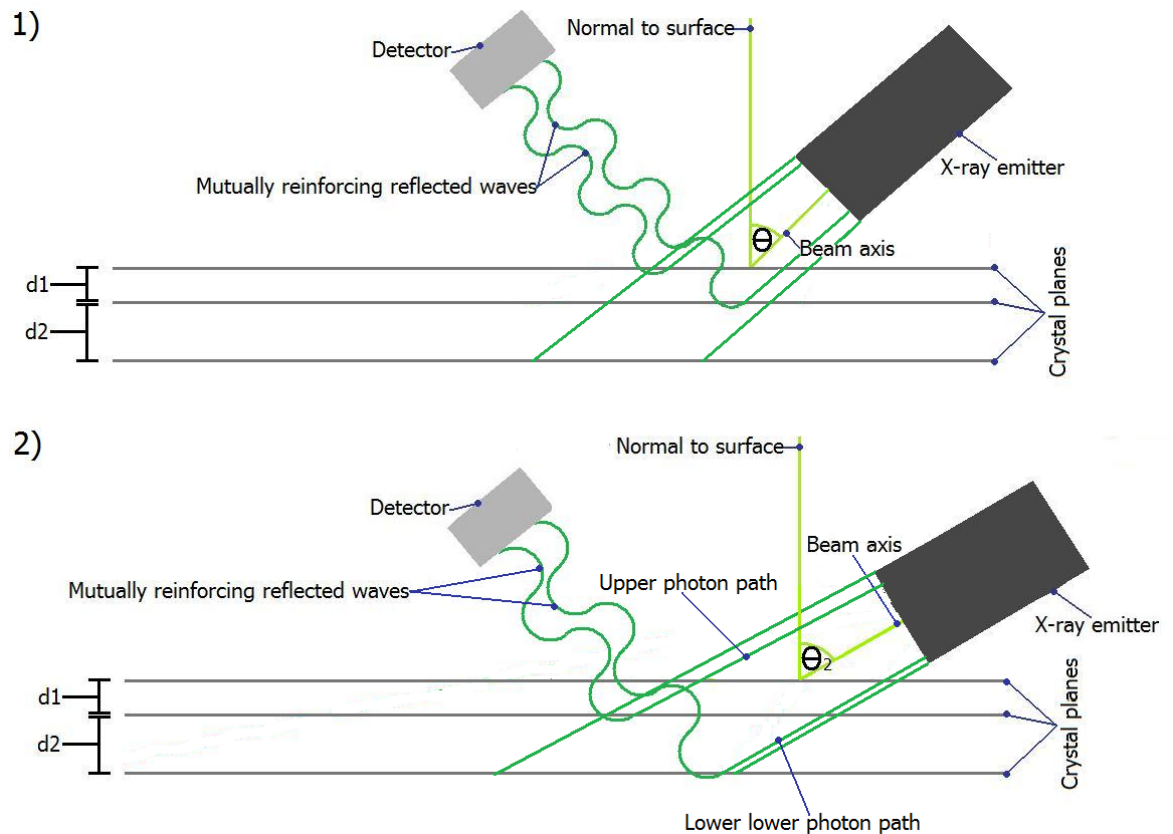


Figure 6.9 : A simplified diagram of the diffraction process:

- 1) X-ray photons are scattered off different crystal planes. The lower photon path is $2d_1\sin\theta_1$ longer than the upper. Constructive interference (mutually reinforcing wave peaks and troughs) occurs when this length is equal to an integer multiple of the wavelength. At the angle θ this is true for the path difference between photons reaching the upper and mid crystal planes, but not for any other planes; hence the reflection seen at angle θ is unique to of crystal planes with a separation d_1
- 2) The angle of the beam changes to θ_2 . Now the difference in path length equalling an integer multiple of the wavelength is between photons striking the mid and lower planes, and no other. This is because the photons travelling the lower path traverse an extra distance of $2d_2\sin\theta_2$, which is equal to an integer multiple of the photon wavelength. Hence the reflection at angle θ_2 is indicative of crystal plane separation d_2 .

The two parallel beams make an angle Θ with the crystal planes. To get constructive interference the difference in path length between beam 1 and beam 2 must be a whole number of wavelengths. This is known as Bragg's law:

$$n\lambda = 2d \sin \theta,$$

Where n is an integer, λ is the wavelength of incident wave, d is the spacing between the planes in the atomic lattice, and θ is the angle between the incident ray and the scattering planes.

This can then be re-arranged to give:

$$\sin \theta = \lambda / 2d$$

Hence the separation between crystal planes that will produce constructively interfering reflections can be expressed as a function of 2θ . The angle θ can be manipulated by moving the X-ray source with respect to the surface along an arc with its centre of radius at the samples surface midpoint, allowing the X-ray emission to scan for different crystal plane separations. This is usually shown as a XRD pattern (shown in figure 6.10).

XRD Pattern of NaCl Powder

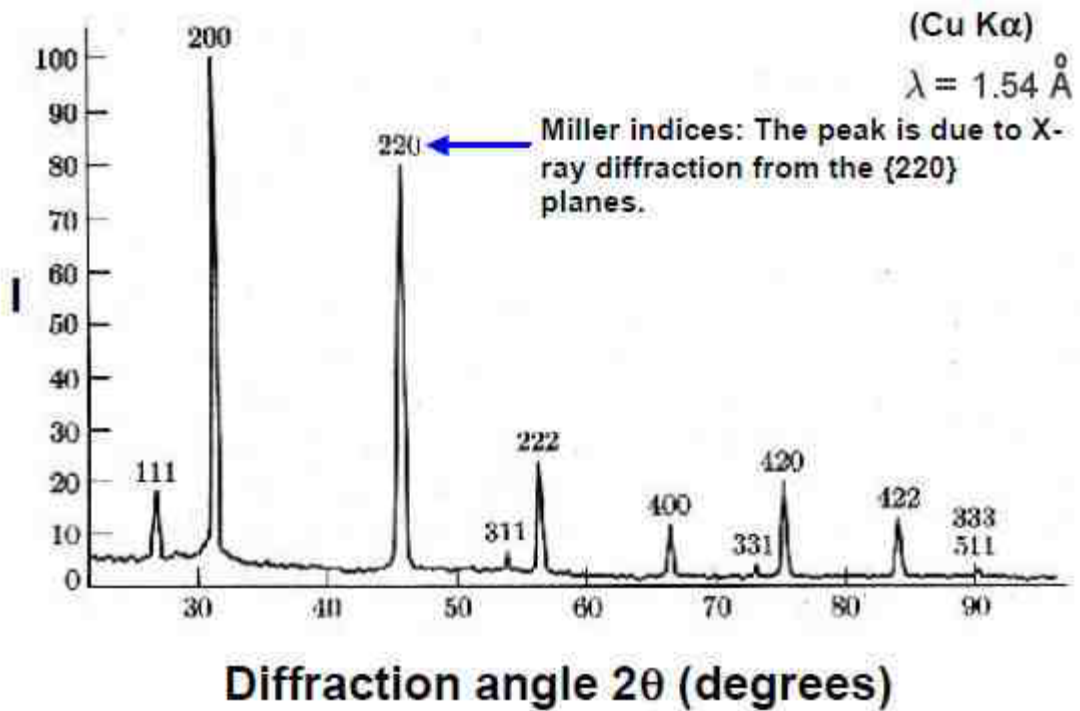


Figure 6.10 : The XRD trace for table salt, with 2θ along the x-axis and X-ray reflection intensity along the y axis. Image courtesy of universe-review.ca

The different spacing (referred to as d-spacing from Bragg's law) correspond to the quantities of different lattice spacing oriented parallel to the surface of the sample, allowing a measure of the crystalline orientation to be taken.

The reference patterns are produced from a powdered sample of the material, producing a diffraction pattern in which crystal planes are randomly oriented.

Chapter 7: System characterisation

7.1 Introduction:

Characterisation of a system is a vital foundation for further work. Here characterisation is taken to mean the system's response to various modes of operation, and the various sputtering parameters, in terms of basic physical readings (such as temperature and pressure) and the effects upon system biases, currents, and powers. It is also important to understand the relationships between true values of these and those given by the power supply, which only provides time averaged values.

This, coupled with observations of the plasma, provides insight into the plasma processes, which are at the beginning of understanding the coating growth. Depositing a series of simple coating samples as well begins to give a first look at how the system responds to reactive gas and substrate bias pulsing.

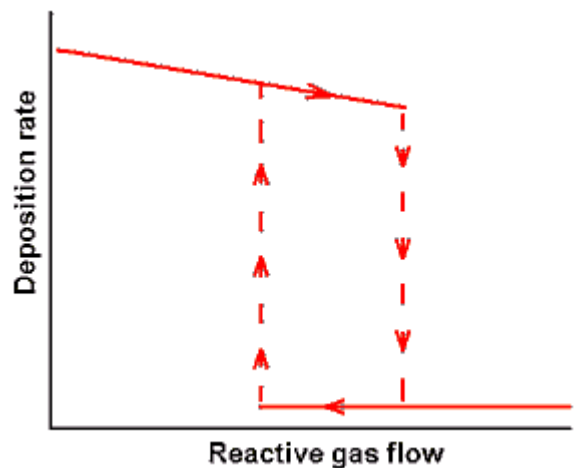
One of the most important phenomena in reactive sputtering is target poisoning, as described in Chapter 2. In order to locate the conditions under which target poisoning occurs, reactive sputter systems are characterised by running a series of hysteresis loops, where the reactive gas content of the chamber is brought up to a maximum value, and then reduced back to zero, in incremental steps.

7.2: Recapping hysteresis theory:

As previously described in Chapter 2, target hysteresis is a form of positive feedback loop: The reactive gas poisons the target, which reduces the sputter rate at the target, and increases target poisoning. This means that at certain critical points the target's behaviour, most importantly the rate of sputtering from it, can change drastically with only a tiny additional increase in reactive gas content. It is important to identify these transition points, and to do this a 'hysteresis loop' is performed. Once identified the reactive gas flow rate can be managed by systems such as plasma or optical emission monitoring (OEM) [66]. Hysteresis behaviour is investigated by increasing then decreasing the flow of reactive gas into the chamber whilst monitoring chamber conditions and power supply readings (target voltage, target current, reactive gas partial pressure, OEM readings). These changes are

made in incremental steps, with a period of fifteen minutes between each step to allow the system to stabilise. As described earlier the ‘return’ leg does not recover to previous high values (due to the build up of compound on the target taking time to sputter away due to a poorer sputtering rate) until the reactive gas flow has dropped to below the initial transition point. Figure 7.1 is an example of a hysteresis curve for deposition rate versus reactive gas flow into the sputter chamber, such as for a typical oxide system. Other system parameters closely related to target conductivity and composition also undergo hysteresis, most notably target bias and current. These may be appropriate measures of hysteresis where the difference in cathode bias between the poisoned and clean target is sufficiently large [67]. Hysteresis refers to any system where the relationship between two parameters follows different paths when the parameters are increasing and decreasing. The size of the area enclosed by the ‘out’ and ‘back’ curves (i.e. increasing and decreasing reactive gas flow) indicates the magnitude of the hysteresis effect (e.g. in terms of target bias). In the case of reactive sputter deposition there is often a point at which the ‘out’ leg of target bias curve drops dramatically (as in most oxide systems); this is an indicator [68] of the point at which target poisoning covers the complete surface of the target. The exact behaviour depends on relative secondary electron coefficient of the target material –in some cases the target bias may *increase* as target poisoning takes hold.

Right fig 7.1. An idealised graphic of how hysteresis behaviour is expected to present itself. Image courtesy of Alacritas Consulting.



With the Pinnacle Plus power supply, which is capable of continuous d.c. or pulsed d.c operation, the hysteresis must be investigated across the available range of frequencies (d.c. and 100 kHz to 350 kHz), and the various alternate operating modes (dual cathode, asynchronous etc). This allows the conditions inside the rig to be indentified for reactive sputtering at maximum deposition rate with minimal target poisoning.

Characterisation was broken down by mode of operation: Hysteresis studies were performed at D.C, 100 kHz, 200 kHz, 300 kHz, and 350 kHz. Hysteresis studies were also

performed in the alternate pulsing regimes described in Chapter 5. A 50% duty cycle was used throughout.

Plasma characterisation:

An initial optical characterisation of the sputter plasma using a Ti target, in d.c. and pulsed mode of operation without any reactive gas present, was performed using a Andori Star DH520 camera focused on the volume immediately in front of the substrate (specifically 4 spots near the substrate, shown in figure 7.3) which sits 11 cm from the target, and along the line adjoining their centre points), using a 750nm (Ar (1) line) centre wavelength filter.

7.3: Experimental:

In each of the investigations the following system properties were monitored and plotted against nitrogen flow rate and substrate bias frequency: chamber pressure, reactive gas partial pressure, working gas partial pressure, target voltage, target current, substrate current, substrate power, plasma OEM signal intensity (taken as a percentage of the 425 nm line intensity at **Full Metal Signal**) referred to as FMS%. Substrate bias, power, current, and target bias power, and current were measured both by the power supply readings, and by an oscilloscope attached to the main power cable to the substrate/target by the arrangements shown in figure 7.2 and in Chapter 4.

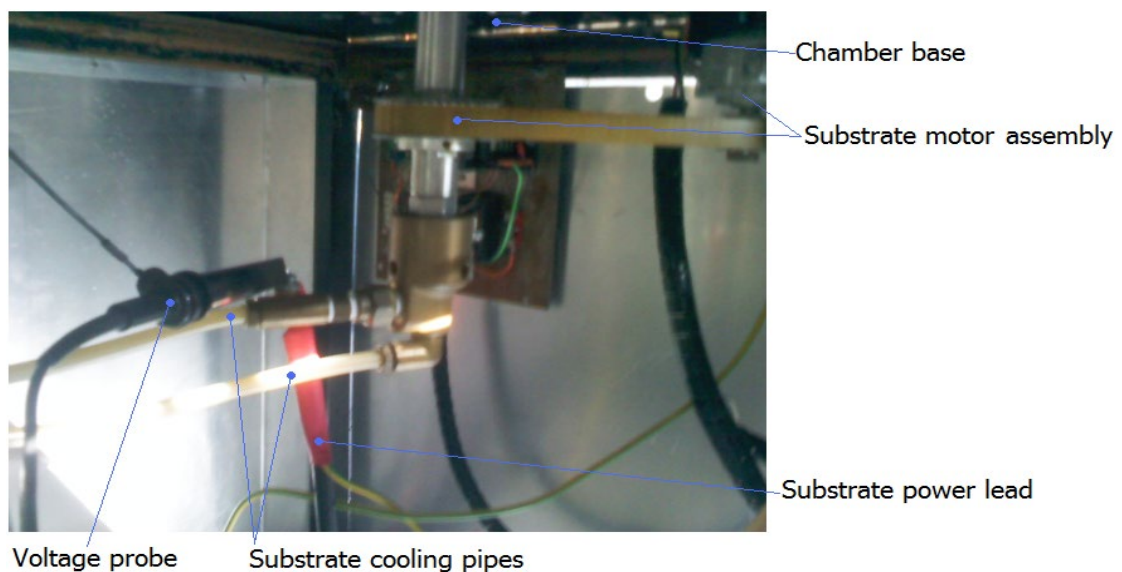


Figure 7.2 : Voltage probe connection to the substrate holder mechanism.

The natural change in chamber conditions over time was first measured. This does not apply where an active control system such as OEM feedback is in use, but was a useful indicator of system stability for the hysteresis studies which followed. The reactive gas line was re-routed through a mass flow controller and controlled using a fixed set-point value. Chamber conditions were monitored over a period of one hour, or until they reached a stable value, with readings taken every 5 minutes. Where a stable value was reached by a system parameter in substantially less than an hour the experiment was redone with a higher time resolution (for example 30 seconds).

Hysteresis studies began with d.c. only sputtering, at standard conditions. In d.c. mode the UDP 350 operates as would a normal closed field magnetron system. This is also the mode in which the effects of substrate bias, target power and gas partial pressure are easiest to unravel without the interference of possible pulsing effects.

The UDP 350 rig was set up to run with the flow of reactive gas into the chamber controlled by an MKS mass flow controller. The chamber was pumped down to an initial base pressure of 1×10^{-3} Pa. The process gas (argon) was then introduced at a fixed flow rate of 10 SCCM, giving a working gas pressure of 0.2Pa. Conditions were standard, and the d.c. substrate bias was set at -100 volts. Standard settings were applied to all variables except nitrogen flow rate, and were kept constant throughout the experiments. Beginning at zero SCCM of nitrogen, the flow rate was increased in steps of either 1 or 0.5 SCCM up to 15 SCCM. After each increase the rig was given five minutes to find equilibrium before any readings were taken. Points on the graph of particular interest were then further investigated using increments of 0.2 SCCM. Nitrogen partial pressure was simply estimated by subtracting the measured pressure of the argon working gas (taken before the reactive gas was introduced) from the total measured chamber pressure.

This was our standard procedure for hysteresis experiments. Following the investigation of the d.c. curve the experiment was repeated with a pulsed substrate bias at frequencies of 100, 200, 300 and 350 kHz. Hysteresis loops were also performed in the alternate pulsing modes, as listed in Chapter 5.

Variations in target bias and coating composition and crystallography with working gas and reactive gas pressure have been investigated in the past by others [69][70], though not in conjunction with pulsed substrate biasing and other pulsing regimes prior to this project.

It has been established by Shah et al (2010) that changes in chamber pressure (with constant ratio of working gas to reactive gas) cause changes in crystallographic orientation in the d.c. case. In light of this, working gas pressure has been kept constant throughout to ensure any crystallographic changes seen are due to pulsing or working gas/reactive gas ratio effects.

The above experiments were performed using the time averaged readings from the Pinnacle Plus power supply. In order to interpret these results it is necessary to understand the relationship between the power supply readouts and the time resolved measurements as provided by a Tektronix TDS 3014 oscilloscope. The oscilloscope was connected to the electrical channels for the substrate and the target, as shown in figures 4.11 and 7.2, by current and voltage probes. The oscilloscope was used to directly measure the waveform supplied by the Pinnacle Plus. Traces of the waveforms for bias and current were directly measured, and recorded in both time resolved and time averaged modes. Traces were taken for the full range of pulsing rates. Substrate bias was varied from -50 to -650 volts, and reactive gas was not introduced into the system. All other variables were as standard.

These experiments were followed by the deposition of coatings at a range of nitrogen flow rates and OEM signal percentages, from 0 SCCM of nitrogen flow or 100% full metal signal, to a fully poisoned target (40% signal). In order to identify the best CrN forming region on the curve coating composition were studied by XRD (Seifert & Co. using Cu K α radiation in the Bragg–Brentano mode) and by EDX. Deposition conditions and substrate cleaning were standard, as described in Chapter 6.

In addition the intensity of the plasma emission in front of the substrate during sputtering of a Ti target was imaged. This was done during pulsed substrate bias operation (at a target power of 500W, a substrate bias of -100V, and a substrate bias pulse frequency of 100 kHz) and d.c. substrate bias operation. The imaging was carried out using an Andori Star DH520 camera, and a filter with a centre wavelength of 750nm. This wavelength corresponds to the Ar (I) emission line. Four points were selected (as shown in figure 7.3) and the change in intensity of the 750 nm wavelength was recorded over a whole pulse cycle, to ascertain how the plasma evolves with the changing waveform.

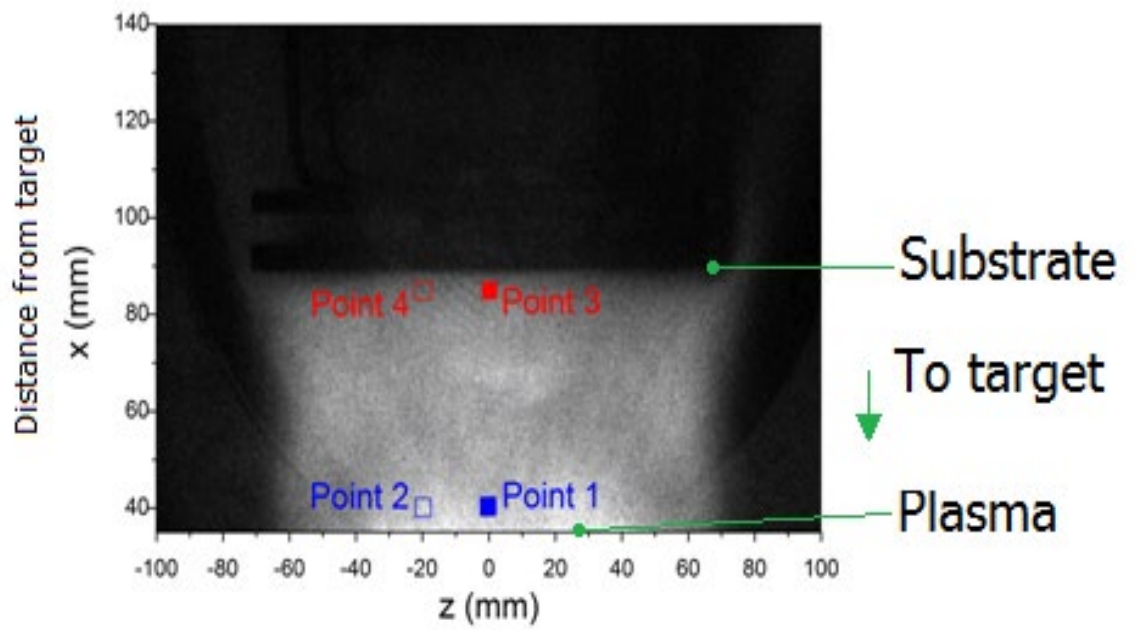


Fig 7.3: Image of the substrate during pulsed substrate bias operation. Four points on the camera image are indicated, and were monitored over the course of one pulse.

7.4: Results:

Change in global parameters with time:

Change with time of the pulsed substrate bias Cr-N system was measured, to provide information on overall system stability. No parameters were changed from their starting settings in these experiments – the system was simply allowed to run:

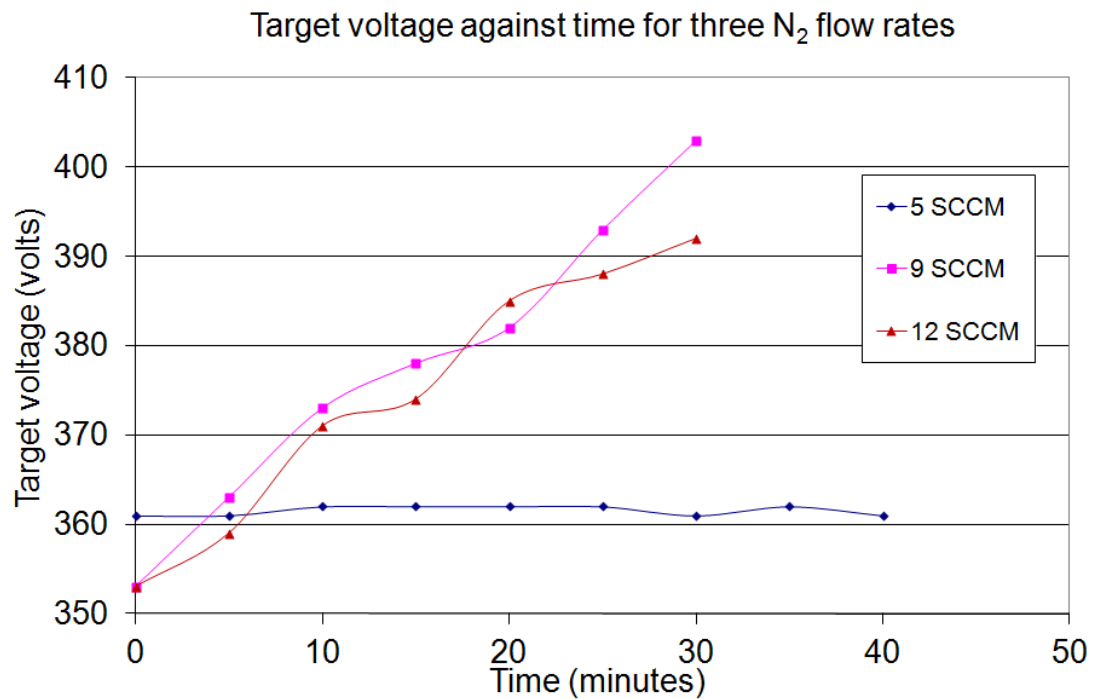


Fig 7.4: The change of target bias with time, for three nitrogen flow rates: Low (5 SCCM), Medium (9 SCCM) and high (12 SCCM). Conditions are standard, pulse regime is d.c.

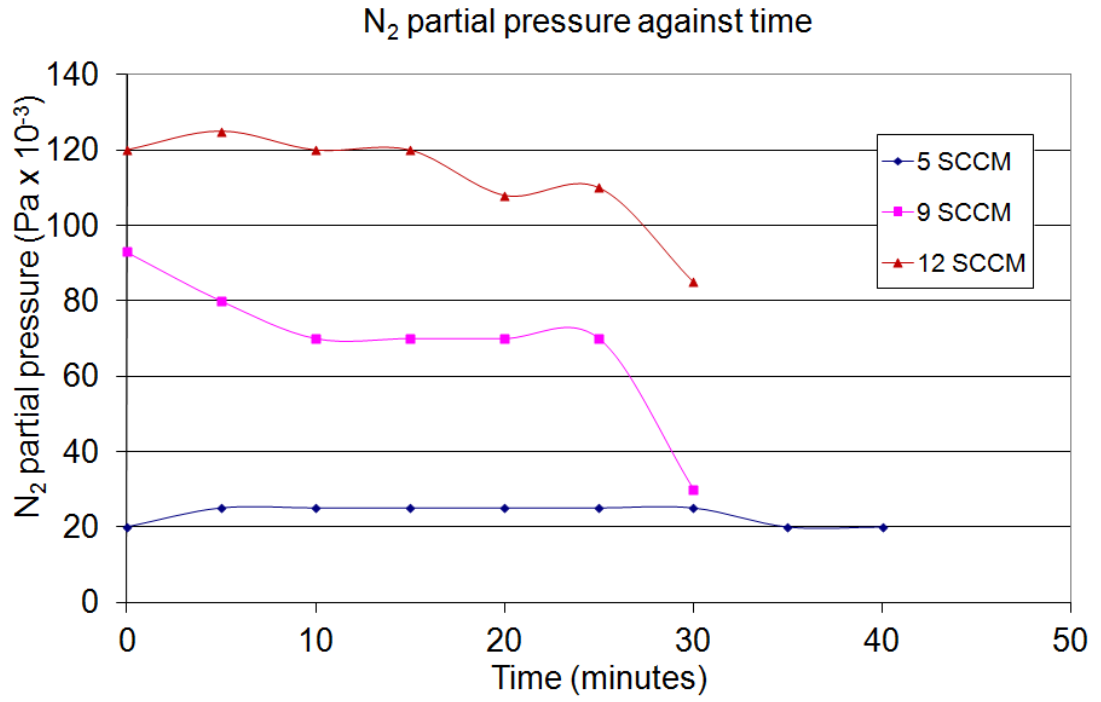


Fig 7.5: The change of nitrogen partial pressure with time, for three nitrogen flow rates: Low (5 SCCM), Medium (9 SCCM) and high (12 SCCM). Conditions are standard, pulse regime is d.c.

Change in global parameters with pulsing frequency:

The second stage in system characterisation was to establish the relationships between various global parameters, and their effect on the crystallography and stoichiometry of simple deposited coatings:

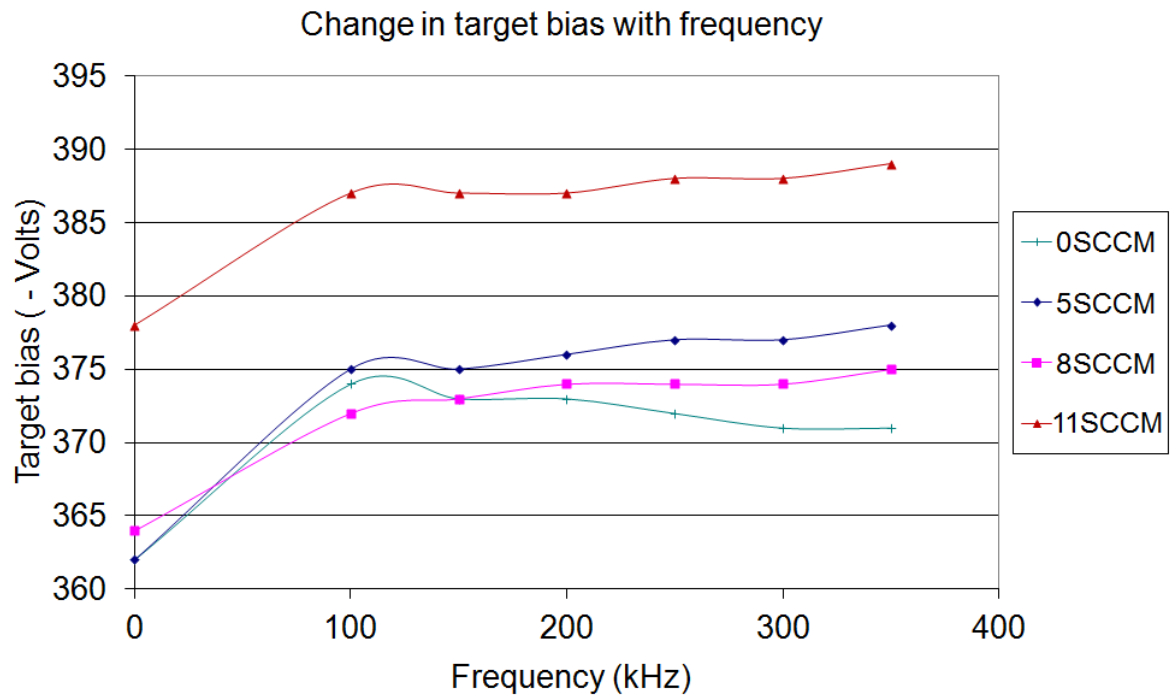


Figure 7.6: The change in target bias with time, for four nitrogen flow rates. 0, 5, 8 and 11 SCCM of nitrogen flow correspond to 100%, 70%, 50% and 45% of the full metal OEM signal respectively.

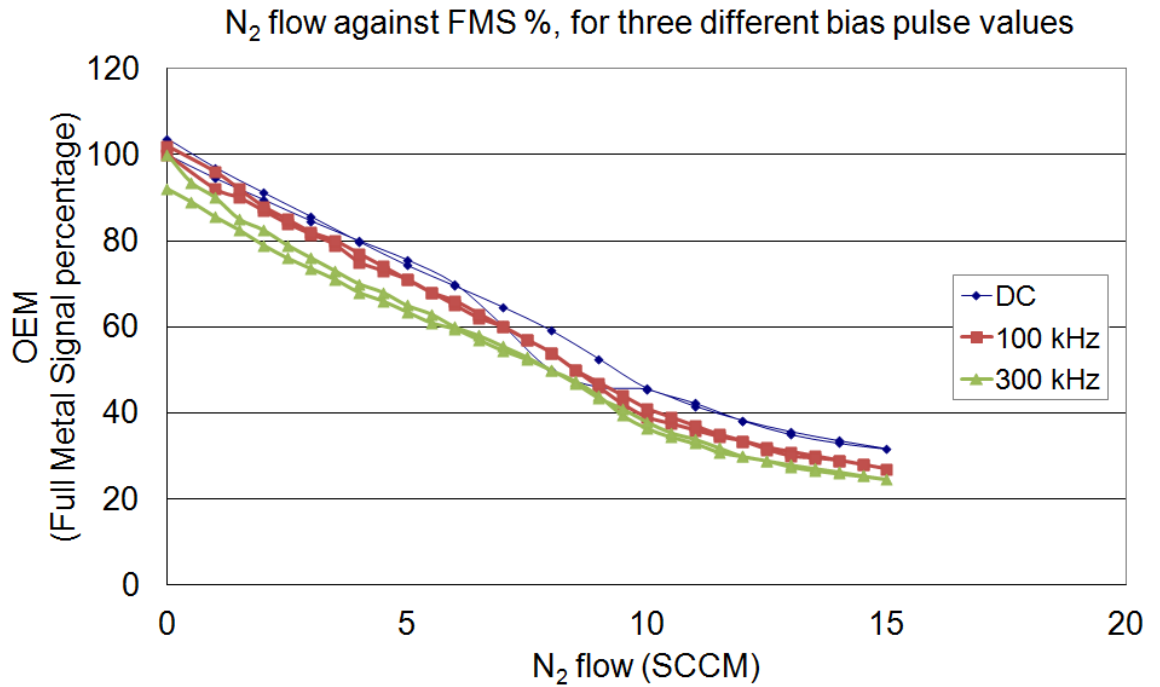


Fig 7.7: The change in intensity of the 425 chromium plasma emission line (the basis for OEM setpoint control) with inflow of nitrogen to the system in SCCM. Conditions are standard, pulse mode is d.c., and substrate bias is -65 volts.

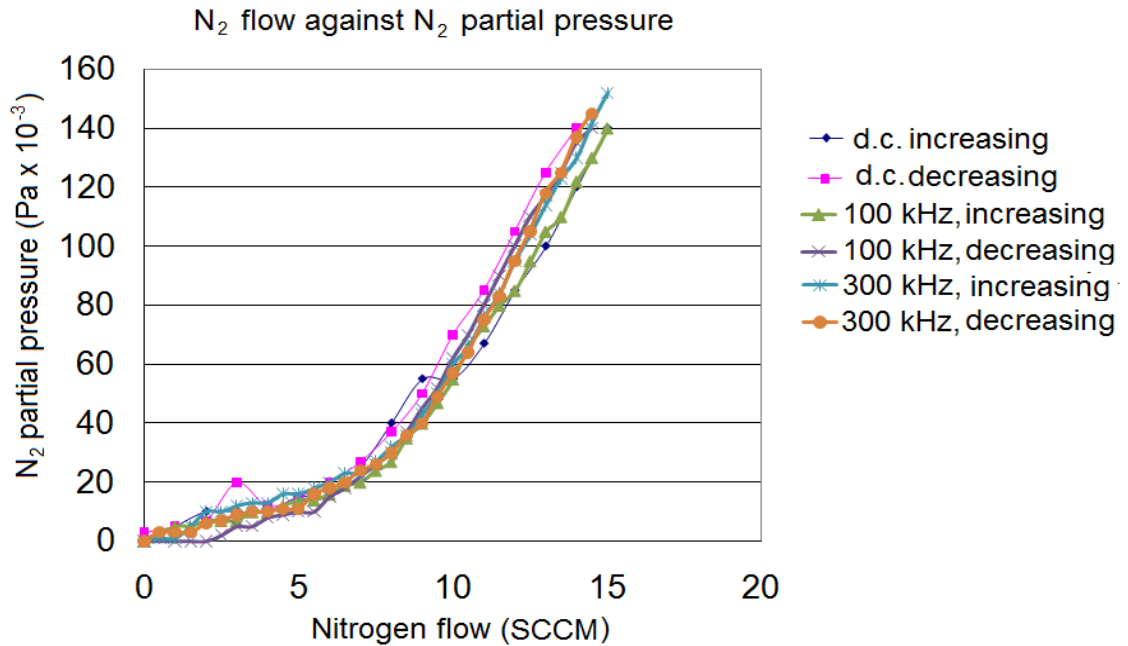


Fig 7.8: The increase in nitrogen partial pressure with increasing nitrogen flow rate. Pulse regimes are: d.c., 100 kHz, and 300 kHz. The substrate bias is -70 volts, and conditions are standard.

XRD analysis of films shows peaks associated with cubic CrN at each setting, suggesting that this is the thermodynamically preferred phase (Fig. 7.9). Peaks probably relating to the Cr₂N {111} were observed below 6 SCCM of N₂ flow.

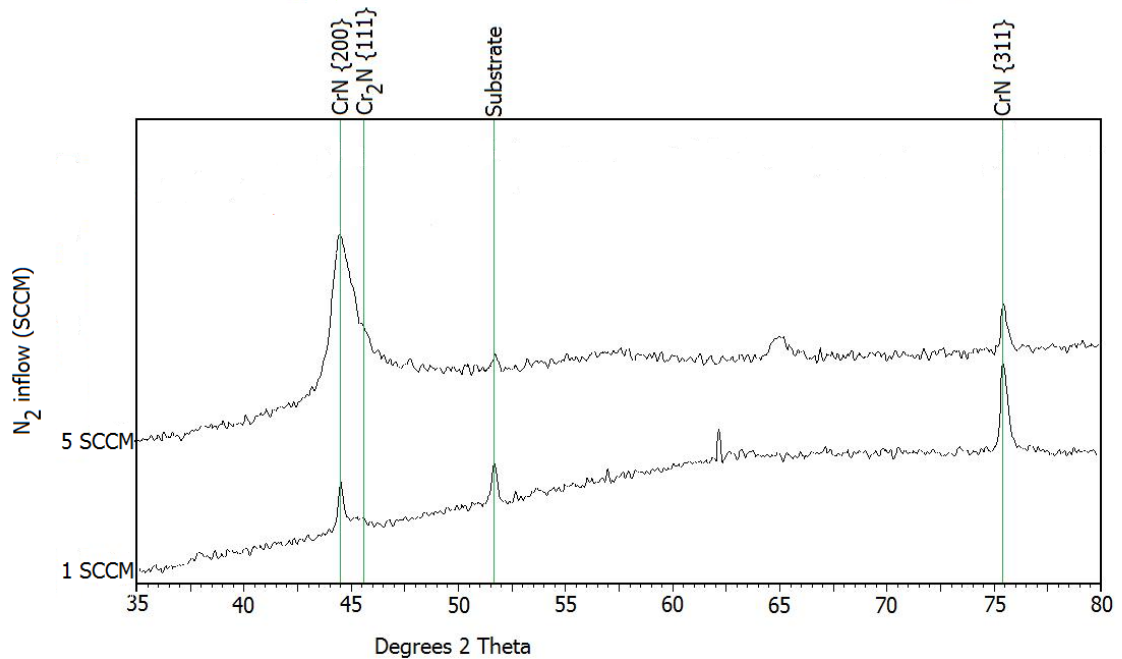


Figure 7.9: XRD spectra for Cr_xN coatings deposited with 1 and 5 SCCM of N₂ inflow. Peaks relating to the presence of Cr-N compounds are labelled.

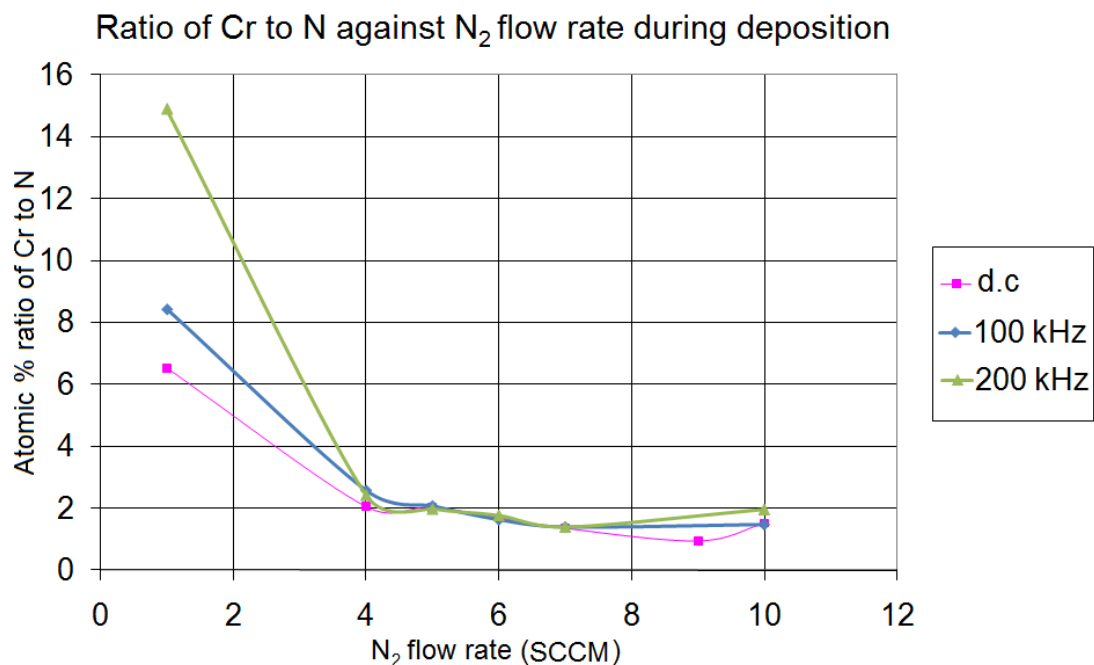


Figure 7.10: The change in atomic % ratio of Cr to N with reactive gas flow rate during sputtering. Three groups of coatings are shown; two were deposited with substrate bias pulsing applied at 100 kHz and 200 kHz, and one was deposited by d.c. sputtering.

Hysteresis loops:

Hysteresis loops were performed to find the onset point of target poisoning, its degree, and the ability of the system to recover. Several pulsing regimes were investigated, with d.c. as a comparison:

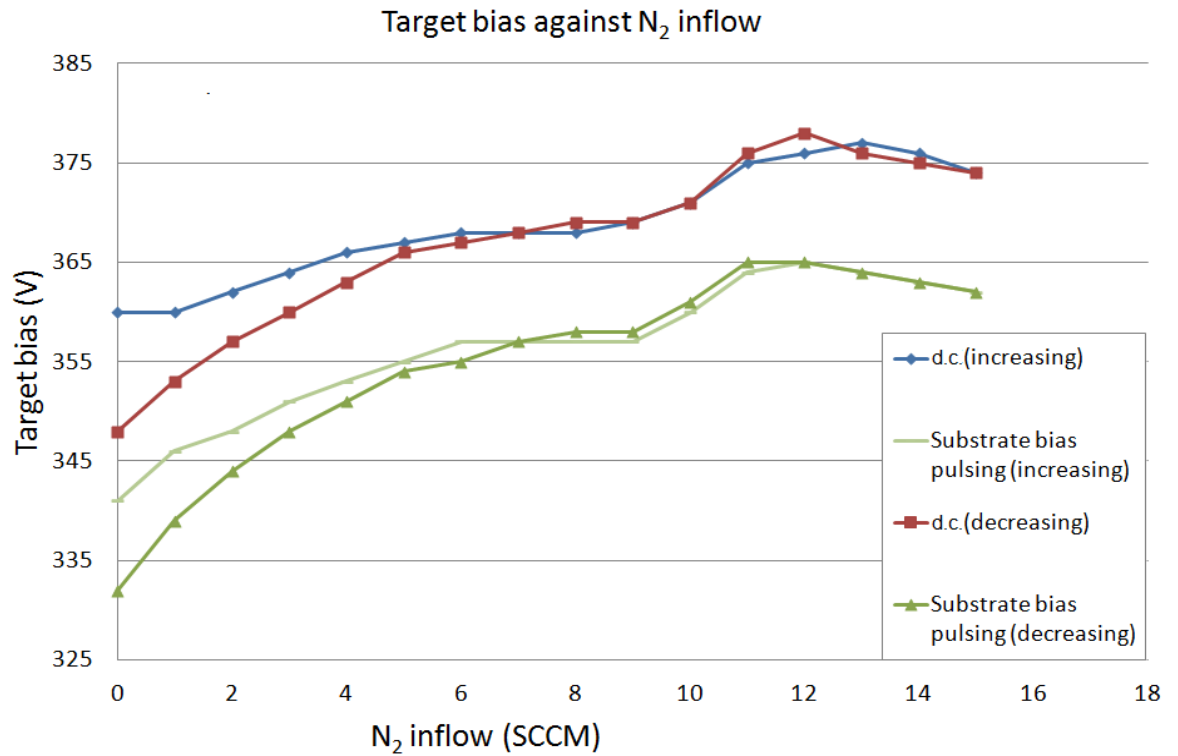


Fig 7.11 Target bias hysteresis curves by N₂ inflow rate for D.C and pulsed substrate bias at 100 kHz.

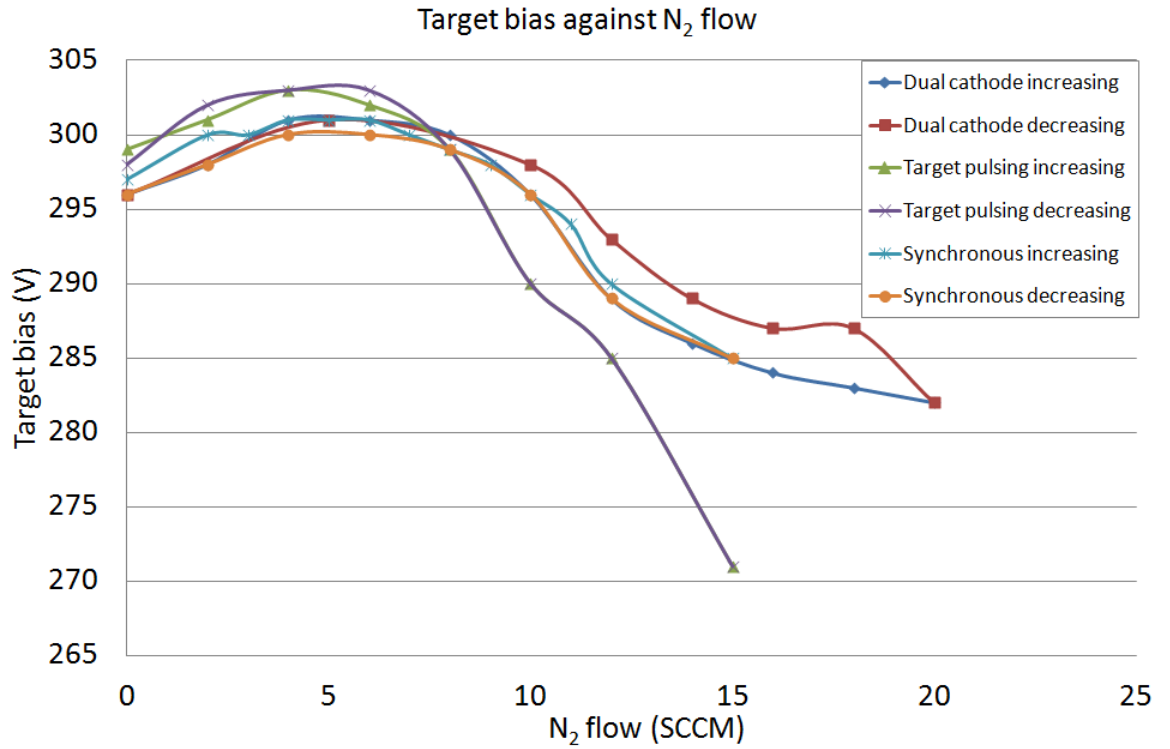


Figure 7.12: Target bias hysteresis curves by N₂ inflow rate for 3 alternate pulsing regimes.

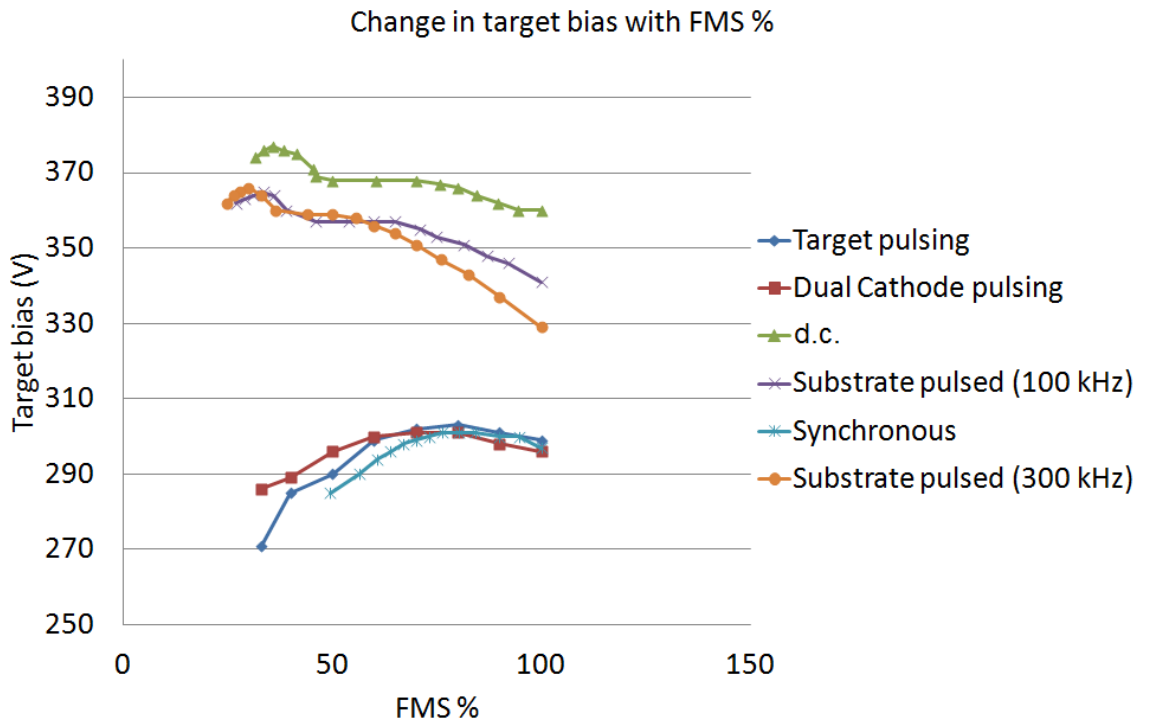


Figure 7.13: Target bias hysteresis curves by full metal signal percentage.

Waveforms and initial plasma analysis:

Using the TDS 3014 oscilloscope the voltage and current wave forms generated by the power supply were measured, and compared to the change in intensity of the 750 nm Ar(1) emission line over the course of a cycle:

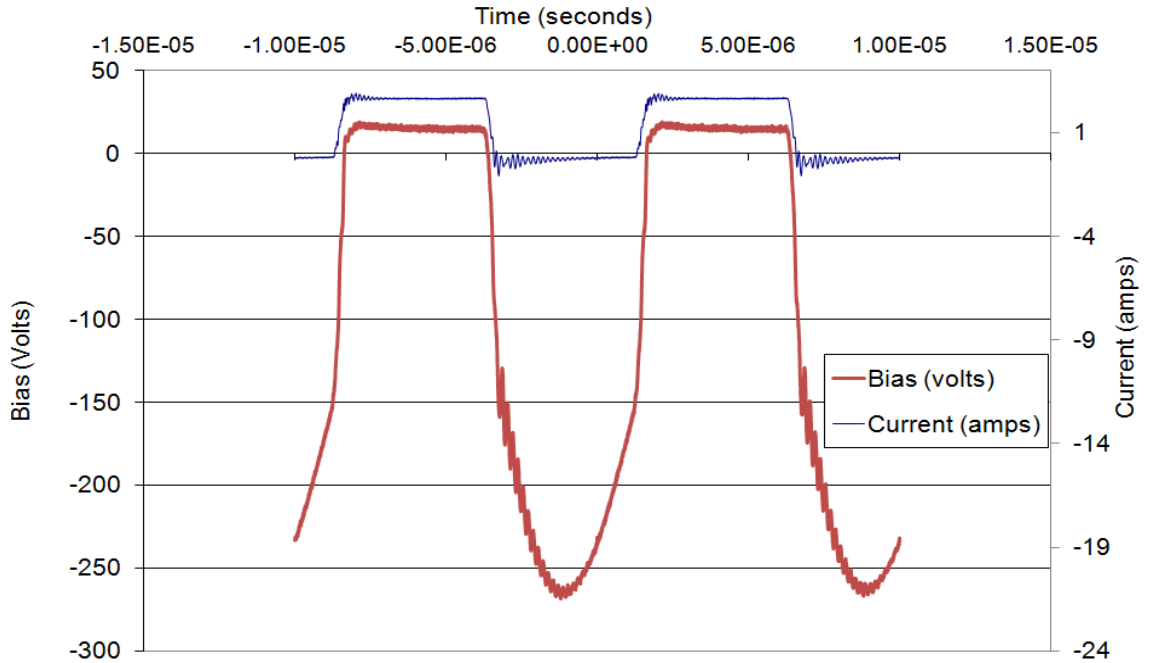
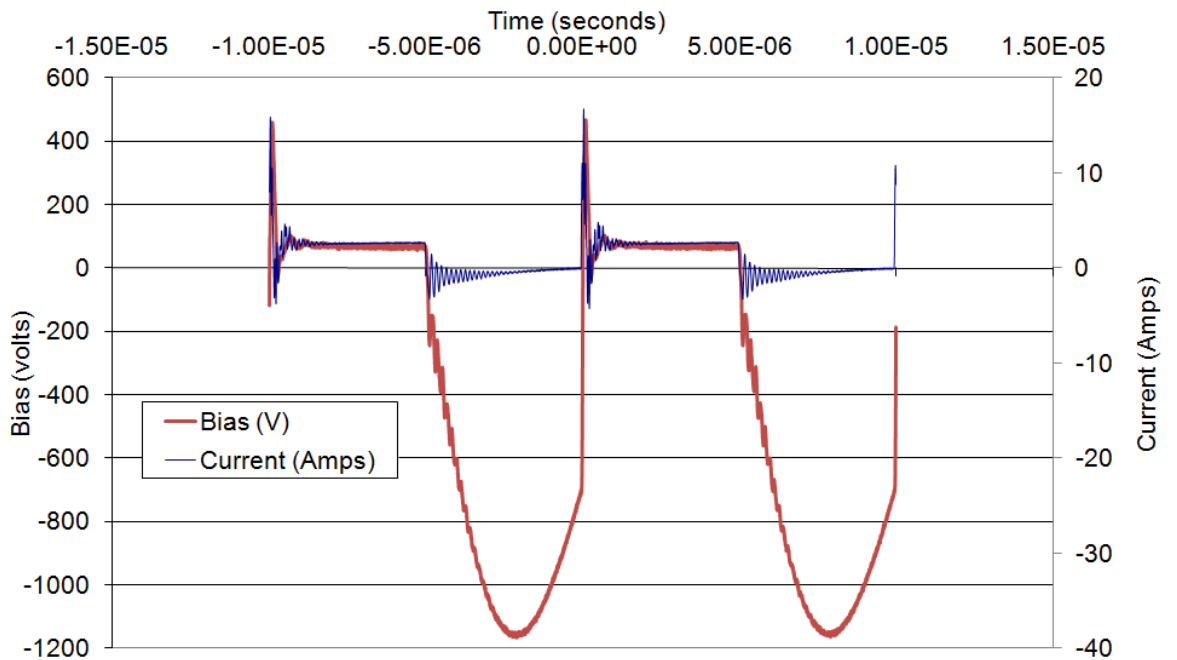
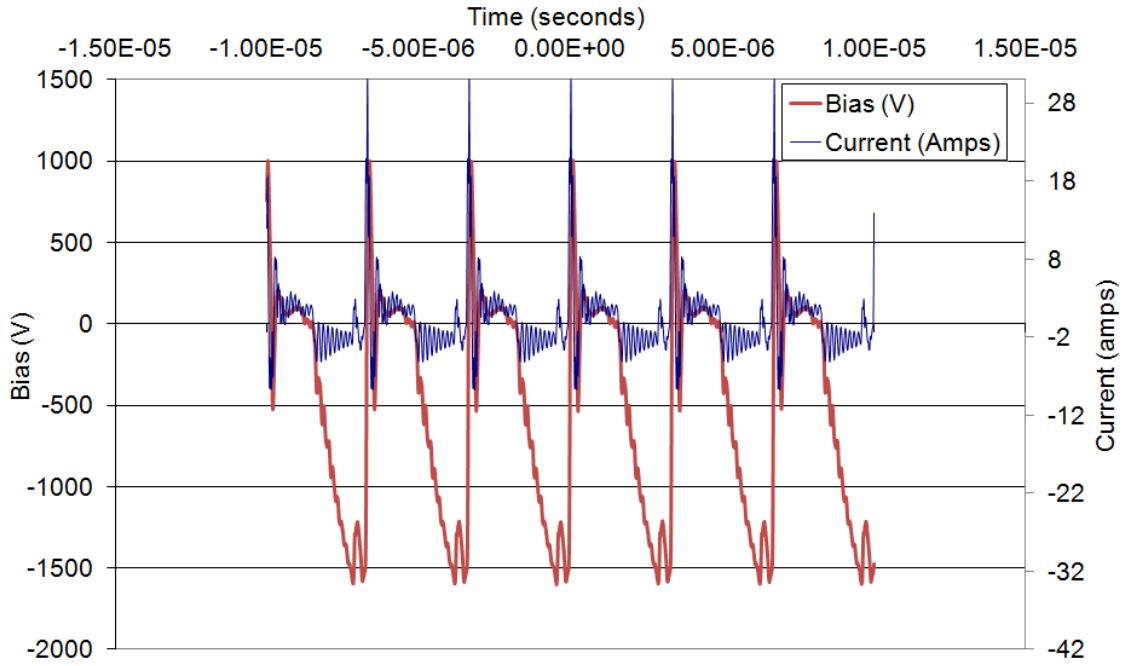


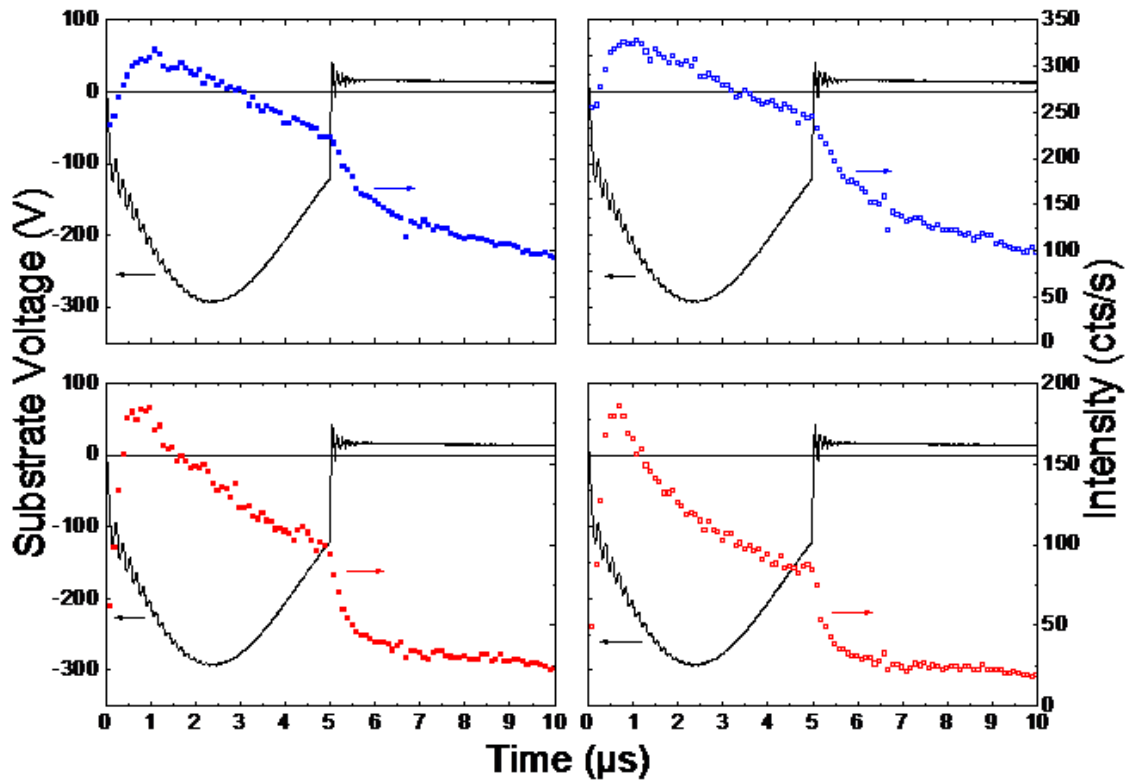
Figure 7.14: Substrate bias and current waveforms at 100kHz substrate bias pulse frequency -100V substrate bias.



7.15: Bias and current waveforms at 100 kHz substrate bias pulse frequency, -400V substrate bias.



7.16: Bias and current waveforms at 300 kHz substrate bias pulse frequency, -500V substrate bias.



7.17: The change in intensity of the 750 nm wavelength, at each imaging point, with time. Imaging points are shown in relation to the substrate in figure 7.3. The change in intensity at each point is compared with the voltage against time waveform for substrate bias, shown as the black trace. From left to right, top to bottom: Point one, point two, point three and point four. Target power was controlled at 500w.

7.5: Discussion:

The progression of individual global system parameters with time, when all other global parameters are kept constant, reveals the stability of the system: At N₂ flow rates above 5 SCCM (equivalent to 70% FMS or below) the target voltage increases at a steady rate, whereas for a 5 SCCM flow rate (equivalent to a 70% FMS) the target voltage remains constant (figure 7.4). However in all cases N₂ partial pressure remains constant until 25 to 30 minutes whereupon it drops sharply in the nitrogen rich atmospheres (9 and 12 SCCM of N₂ flow), and more shallowly in the nitrogen poor (5 SCCM of N₂ flow) atmosphere (figure 7.5). This suggests that the target poisoning is at least equalled by the sputtering of material off the target surface at 5 SCCM. At higher nitrogen flow rates poisoning exceeds the sputtering rate and the target is becoming steadily more saturated with nitrogen as time progresses. Where reactive gas flow and substrate bias are constant target bias increases with substrate bias pulse rate between 0 and 100 kHz and thereafter remains level, for the available range of reactive gas flow rates (figure 7.6).

The hysteresis experiments performed show little sign of conventional hysteresis behaviour.

The variation in target bias with increasing and decreasing nitrogen flow rate for the Cr–N system is shown in Fig.7.11 for d.c. and two substrate bias pulse rates, and in and 7.12 for the alternate pulsing regimes. The ‘out’ leg of each curve is shown with respect to OEM signal in figure 7.13. There is little evidence of true hysteresis behaviour (compared to many oxide systems). However, the data does show some interesting trends. In both pulsed substrate bias mode and d.c. substrate bias mode there appear to be two maxima in the target voltage levels at approximately 5–6 and 10–11 SCCM of nitrogen, respectively. Target bias drops after the second maxima, around 12 SCCM. N₂ partial pressure (shown in figure 7.8) rises at 0.03×10^{-1} Pa per SCCM then knees at approximately the point where target bias begins to climb towards the second maxima (8 to 10 SCCM). From there it rises at 0.14×10^{-1} Pa per SCCM. This suggests gettering may be removing nitrogen below 8 SCCM, and becomes saturated above this point. This is consistent with the composition of coatings deposited above 8 SCCM which are more nitrogen rich (figure 7.10).

In the pulsed mode the OEM signal (for chromium 425 nm line plasma emission) drops linearly until the 8 to 10 SCCM point (figure 7.7), where there appears to be a gentle 'knee' followed by a slightly slower rate of decrease that tails off. Taken together with the above data this suggests that additional N₂ is being gettered less effectively at 8 SCCM, and a new equilibrium is reached at the 10 SCCM point. These findings are consistent across the range of measured substrate pulse values, and suggest that this point represents the true region of target poisoning.

The double maxima and the change in stoichiometry and crystal structure observed agree with other published results [71]. Changes in the phase of chromium nitride being formed may be related to the onset of target poisoning [75]. OEM signal intensity is observed to drop by between 50% and 30% upon initiation of pulsing. This is constant across all the available pulsing regimes and must be compensated for during deposition. At a set nitrogen content this does not appear to have an influence on coating composition or structure.

Features on the pulsed substrate bias hysteresis loop have been shown to match with the formation of different phases of chromium nitride [72]. From Han et al: "The initial positive slope on the target bias vs. N₂ flow curve corresponds to a mixed phase Cr₂N + Cr, The top of the first maxima corresponds to stoichiometric Cr₂N, and the majority of the 'saddle' between the maxima corresponds to mixed phase CrN + Cr₂N, and the second maxima onwards corresponds to stoichiometric CrN". The hysteresis findings in this study correspond closely with Hans work, suggesting that the features seen in our hysteresis studies do indeed match with different phases of chromium nitride. It therefore seems likely that the shape of the hysteresis loop is due to the build up of material on the target surface changing from mixed phase CrN / Cr₂N / Cr to mixed phase CrN / Cr₂N to single phase CrN. XRD spectra (figure 7.9) show that CrN is the dominant nitride phase in all cases, however some Cr₂N may be present at lower N₂ inflow rates.

Hysteresis studies performed in the alternate regimes also show little signs of true hysteresis. However the 'double maxima' pattern is apparently absent. Instead the system appears to move smoothly towards target poisoning. There is little variation between the alternate pulsing regime curves. The sole common factor between them is the presence of target pulsing. Target pulsing is not applied during d.c. or pulsed substrate bias operation, hence it may be that the effects of target pulsing are strong enough to dominate all the

alternate pulse regime hysteresis curves. It is also worth noting that the voltage signal is a time averaged signal and may be damping some of the variations.

Oscilloscope analysis of the current waveforms show significant overshoots during the on/off and off/on transitions in the driving voltage waveform. This becomes more and more significant at higher substrate biases and pulse rates, and is eventually accompanied by ringing (figures 7.14 to 7.16) The relationship between the waveforms and the time averaged power supply readings is clearly complex. There is an almost constant positive voltage during the off time, accompanied by a high negative current, presumably electrons.

The change in plasma emission intensity of the 750 nm wavelength, at four selected points (A,B,C and D as shown in figure 7.3) shows that Ar (I) emission intensity is greater closer to the target, and intensity is highest when the bias is applied to the target (figure 7.17). This may be due to secondary electron emission from the target. When the bias is off the intensity does not instantly dissipate but decays after an initial sharp drop.

The overall lack of hysteresis behaviour suggests that Cr / N reactive deposition may be easier to manage than many oxide systems. However the changes in readings over time show active control is still needed. The cause of the unexpected lack of hysteresis behaviour is not readily apparent, and is consistent across the available range of pulse rates. The alternate pulse regimes also show a lack of obvious hysteresis. This suggests that the secondary electron yields are similar between clean and poisoned targets, as suggested by the work of G.G. Fuentes et al and others [73] [74]. It has been shown that the relationship between the contamination layer on the target and the target bias can be complex, by Depla et al [75], however in this case one seems to be a good indicator of the other.

Chapter 8: Influence of the pulsed substrate biasing on deposition and coating performance.

8.1: Introduction:

An understanding of the plasma processes allows for a better grasp of the growth and structure of the Cr_xN coatings. As described in previous chapters the kinetic energy and rate of arrival of metal vapour ions, working gas ions, reactive gas ions, and neutral species largely determines the internal stresses, re-sputtering rate, and crystallographic alignment of a growing film. It has previously been hypothesised that, because a second discharge is initiated at the substrate during pulsed d.c. biasing operation, the ion current drawn at the substrate is not limited to the saturation ion current generated by the magnetron discharge [81] [82] [83]. Therefore determining the effect of pulsed d.c. substrate bias operation on the flux of incoming particles at the substrate is an important step in controlling film properties. The effects of target pulsing and other alternate pulsing regimes were also investigated. Four experimental arrays were designed; two looking at the effects of various settings on system parameters, one for investigation of substrate heating, and one studying simple CrN coatings. The plasma was also investigated directly by optical imaging, spectrometry, and Langmuir probe investigations with the kind help of the Plasma Physics Group at Liverpool University

A major aim of this project was to verify the reality of the apparent observed increase in substrate current drawn during pulsed substrate bias operation. To date, the physical effects at the substrate and growing film have been taken as an indirect indication of the existence of a greater ion current. The chief effect expected due to increased current is greater substrate heating [84], which was monitored by a FISO Technologies Inc fibre optic temperature probe. Substrate bias was also expected to have an influence. Changes to the crystal structure and internal stresses were expected based on the work of other investigators [85]. Due to the relatively short period of time the FISO probe can be operated in contact with the substrate without exceeding the maximum safe temperature, temperature measurements were carried out separately to the deposition runs.

8.2: Experimental.

Initially two arrays of simple experiments were performed, aimed at establishing the magnitude of the observed increase in current, and any associated effects on system parameters during pulsed substrate biasing. In the first experimental array the time averaged readings from the power supply were taken, as well as oscilloscope readings from the channel connected to the substrate. The chamber was evacuated as normal and Ar then introduced to a pressure of 0.1 Pa. Substrate bias was held at -100V, target power at 1kW. Substrate bias pulsing was systematically varied from 100 kHz to 350 kHz in increments of 50 kHz, with 15 minute pauses between each increment to allow the system to settle, and the substrate temperature to reach equilibrium. A d.c. run was also included. After each increment and settling period the following system parameters were recorded: Substrate bias, substrate current, substrate power, target bias, target current, target power, chamber pressure and OEM signal strength. This was carried out with no reactive gas in the system, and then with reactive gas flows of 5, 8, and 11 SCCM of nitrogen.

Table 8.1: Array 1: Combinations of reactive gas inflow rate and substrate bias pulse rate to determine the magnitude of the increased substrate current.

Substrate bias pulse rate (kHz)	Reactive gas flow (SCCM)
0	0
100	0
150	0
200	0
250	0
300	0
350	0

0	5
100	5
150	5
200	5
250	5
300	5
350	5
0	8
100	8
150	8
200	8
250	8
300	8
350	8
0	11
100	11
150	11
200	11
250	11
300	11
350	11

For the second experimental array the same procedure as for the first was used without reactive gas, across a range of bias voltages from -70V to -200V.

Table 8.2: Array 2: Combinations of substrate bias and substrate bias pulse rate to determine the magnitude of the increased substrate current.

Substrate bias pulse rate (kHz)	Substrate bias (-V)
0	70
0	100
0	200

100	70
100	100
100	200
150	70
150	100
150	200
200	70
200	100
200	200

300	70
300	100

300	200
350	70
350	100
350	200

To investigate the first findings in more detail the plasma was imaged and probed directly. With the kind help of Dr Bernd Liebig of Liverpool University, sputtering plasmas were studied during d.c. and pulsed substrate bias operation. Studies were carried out, both with no reactive gas, and with a reactive gas level equivalent to an OEM signal of 40% FMS. A chromium target was used, with a target power of 1 kW and a substrate bias of -70V, -100V and -200V. The -200V runs were included to exaggerate any subtle effects. Investigations used optical imaging with an Andori Star camera, optical spectrometry using a DH520, spectrometer LOT Oriel MS260i spectrometer, and Langmuir probe measurements using a probe with a 100 micron diameter by 4.9 mm length tungsten wire tip. These measurements were made in the region above the centre point of the substrate, which aligns with the centre point of the target, 1 cm from the substrate surface and 10 cm from the target surface. These measurements were time resolved with respect to the substrate bias waveform, allowing specific events in the plasma to be correlated with features of the wave. Optical spectrometry was performed at a higher bias, -200V, in order to exaggerate any hard to detect effects.

In order to confirm that the observed increases in saturation limit of the ion current were not an artefact of the instrumentation, an array of Cr_xN coatings were deposited onto {111} surface texture silicon, at a range of pulse regimes and substrate bias levels. The substrates were cleaned in an ultrasound bath using acetone, methanol, and ethanol, for 20 minutes each. They were ion etched at a target current of 0.3 amps and a substrate bias of -650V prior to deposition. Where bias pulsing was applied during deposition it was also applied during etching. Each substrate was partly masked to allow a depth measurement to be performed by profilometry. Concurrently tool steel coupons, polished to a mirror finish, were coated. During deposition the OEM turndown signal was held constant at 40% of FMS. The silicon wafers were then fractured and the surfaces and cross sections examined

by SEM. EDS was used to measure Cr and N contents. 1 cm by 1 cm Sections of the coated tool coupons were extracted, and Bragg-Brentano mode XRD was applied to measure crystal orientation. XRD peak shift measurements were used to estimate internal stress. Glancing angle mode XRD was used as a comparison to screen for oxide contamination. As the greater ion current would influence both defect density and resputtering rate, the microstructure, orientation, and internal stress were also expected to be influenced [86] [87]. Using the coated steel coupons, the hardness and adhesion were measured using nanoindentation and scratch adhesion testing, respectively, according to standard testing procedures described in earlier chapters. Each coating was deposited to a thickness of 1.5 μm , as measured by masking a section of substrate and performing profilometry of the edge of the masked area, post deposition.

Table 8.3: Array 3: Conditions for the deposition of Cr_xN coatings for tribological and microstructural analysis.

Substrate Bias	Pulsing frequency	Sample number	FMS signal %
-70V	d.c.	Sample 1	40
-70V	350kHz	Sample 2	40
-100V	d.c.	Sample 3	40
-100V	350kHz	Sample 4	40
-70V	d.c.	Sample5	60
-70V	350 kHz	Sample6	60

This range of bias values is known to be conducive to good coating properties in transition metal nitrides [88-90]. Coatings were deposited in both d.c. and pulsed substrate bias regimes. Array 4 and the subsequent experiments were subjected to tribological tests.

While critical load and hardness can be good indicators of coating performance they are not necessarily representative of the real wear environment a coating is likely to experience. Selected coatings from array 3 were applied concurrently to 3 tool steel coupons, which were each wear tested for 20 minutes, in combination with profilometry

measurements: Every five minutes the wear test was paused and five randomly chosen transects of the wear track were taken (using the Dektak profilometer) to measure the progression of wear at the surface. At the same time the frictional coefficient at the coating-thrust washer interface was measured. Average values for each set of 3 coupons were used. Coatings were also imaged using optical microscopy, to provide data on the type of coating failure occurring.

A third means of investigating the ion current delivered at the substrate is substrate heating. This indicates the total energy being delivered to the substrate, and is expected to be influenced by both substrate bias pulse rate and substrate bias. Heating was measured using the FISO probe for a period of 30 minutes. As the combination of substrate bias over 60V and pulse rate over 175 kHz produced temperatures that exceeded the FISO safe operating temperature within minutes the array is limited to these values of bias and pulsing.

Table 8.4: Array 4: Power supply settings used for runs to determine the influence of substrate bias and substrate bias pulse rate on substrate heating.

Substrate bias (v)	Bias pulse rate (kHz)
-20	0
-20	175
-60	0
-60	175

8.3: Results:

The first two experimental arrays established the increase in substrate current with pulsed substrate biasing. The effects of other global parameters, such as duty cycle and reactive gas content, on substrate current during pulsed operation were also investigated.

Array 1:

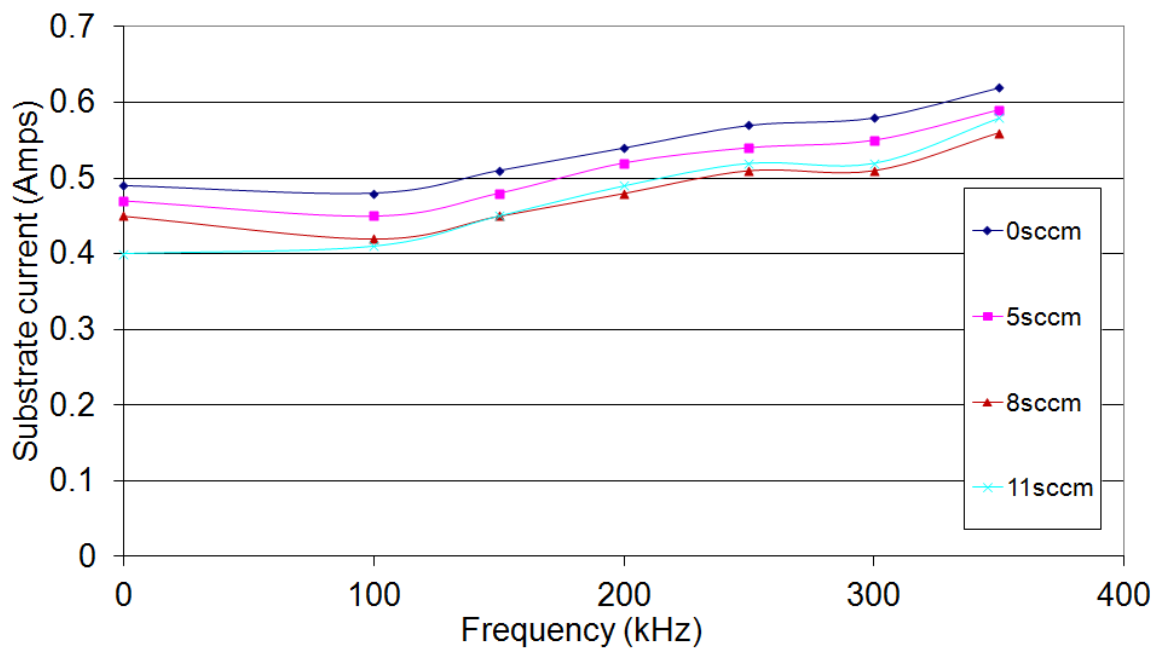


Figure 8.1: The change in substrate current with frequency for four inflow rates of N₂ (reactive gas in MFC set point flow control mode). Substrate bias was set at -100V.

Array 2:

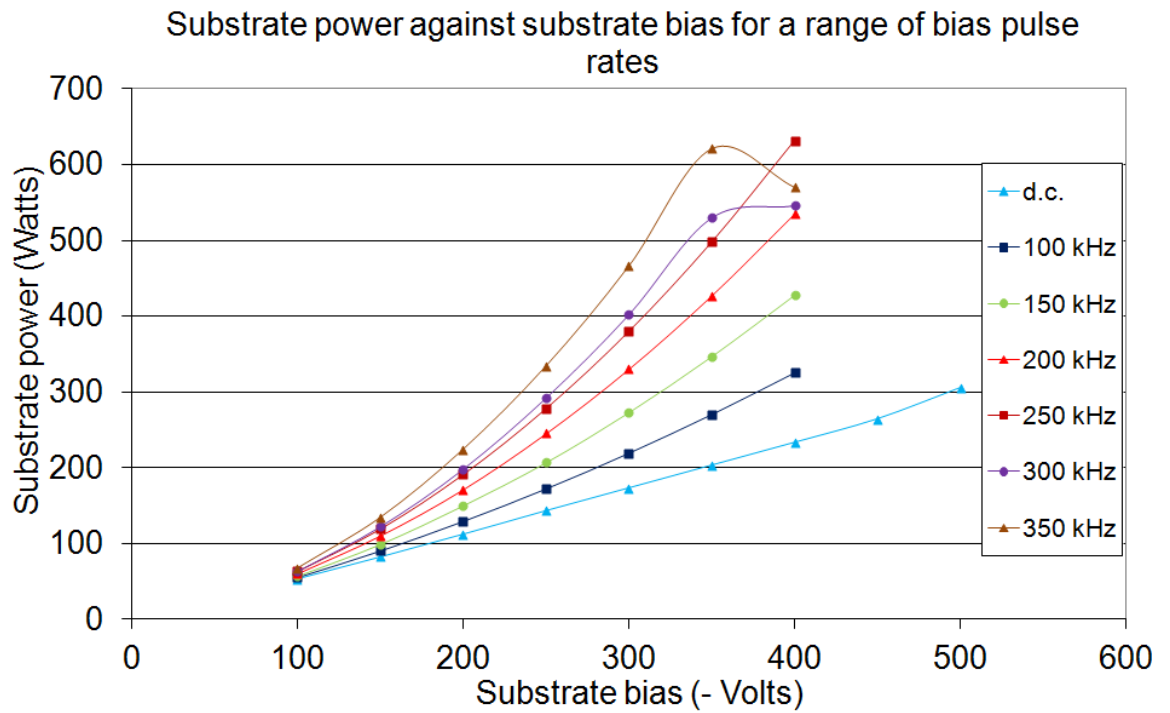


Figure 8.2: The change in substrate power with substrate bias for the available range of substrate bias pulsing frequencies. The UDP 350 is operated here in non-reactive mode.

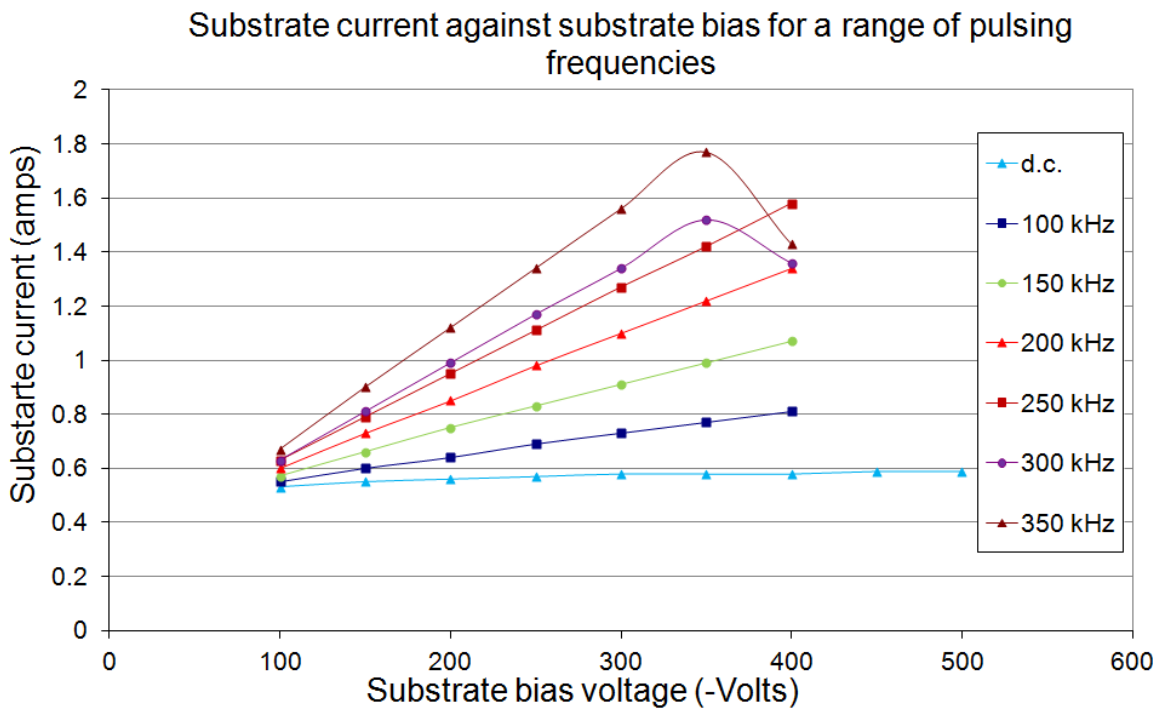


Figure 8.3: The change in substrate current with substrate bias for the available range of substrate bias pulsing frequencies. The UDP 350 is operated here in non-reactive mode.

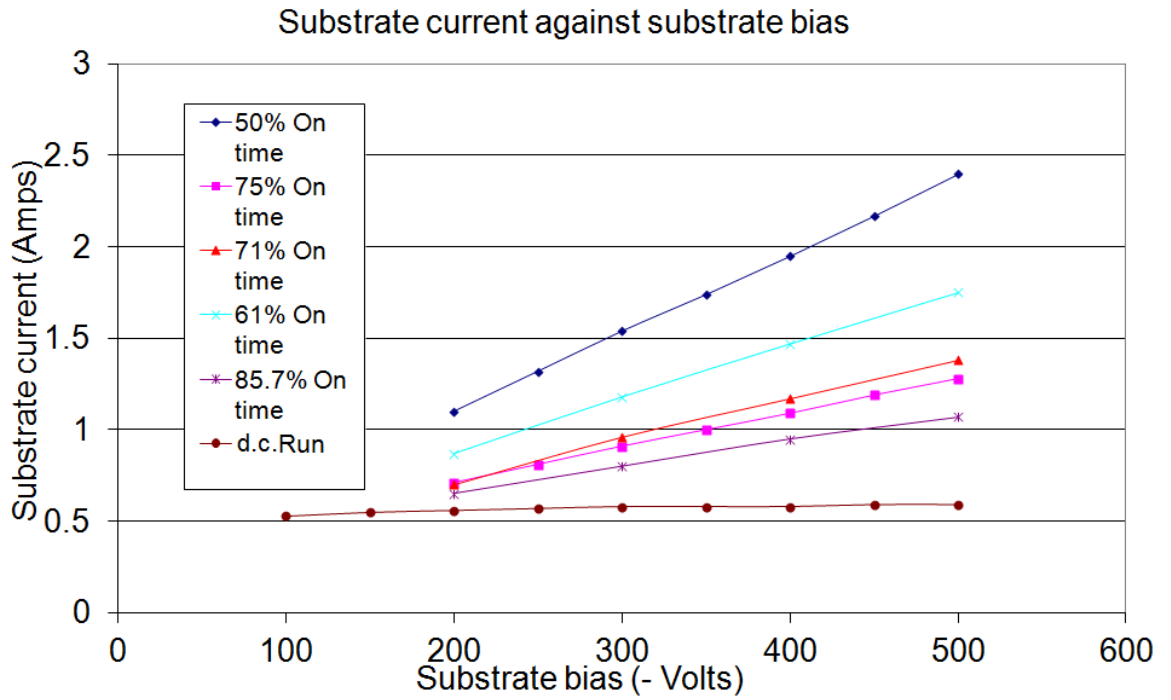


Figure 8.4: Variation of substrate current with substrate bias and on time (duty cycle %), at bias pulse rate of 350 kHz.

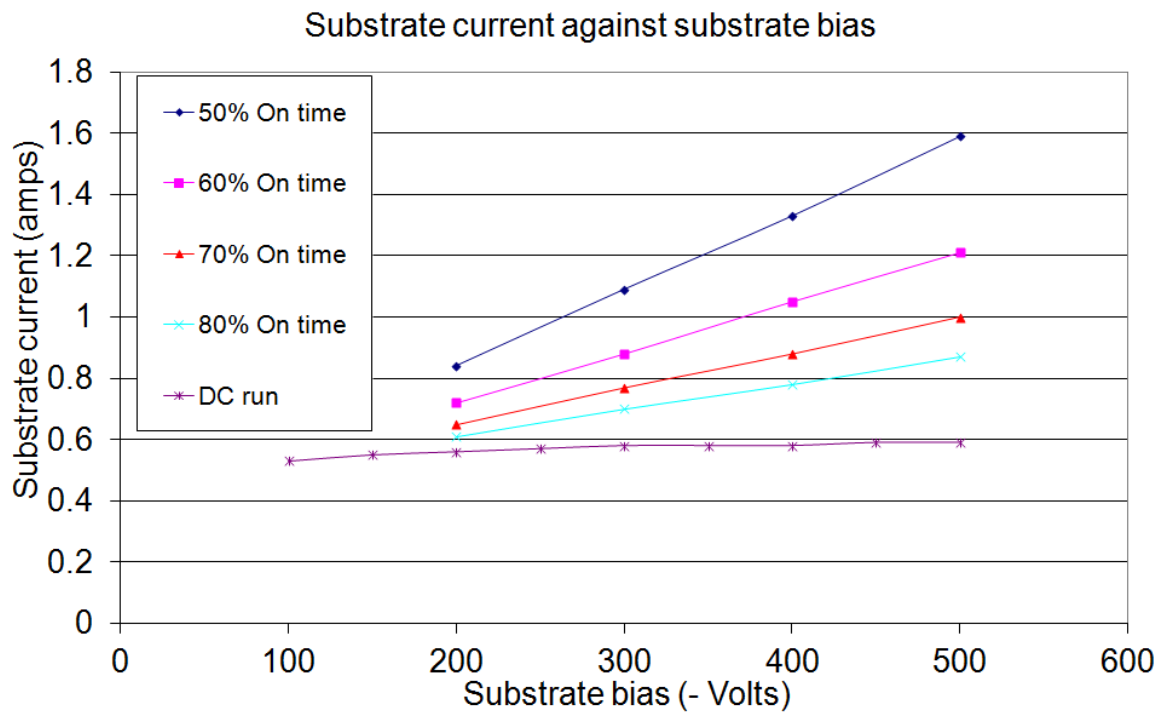


Figure 8.5: Variation of substrate current with substrate bias and on time (duty cycle %), at substrate bias pulse rate of 250 kHz.

Substrate bias and current waveforms:

The effects of reactive gas content on the pulsed substrate bias waveform were investigated. For oscilloscope measurements of the substrate bias and current, $t=0$ was taken as being the beginning of the voltage ramp for the substrate bias.

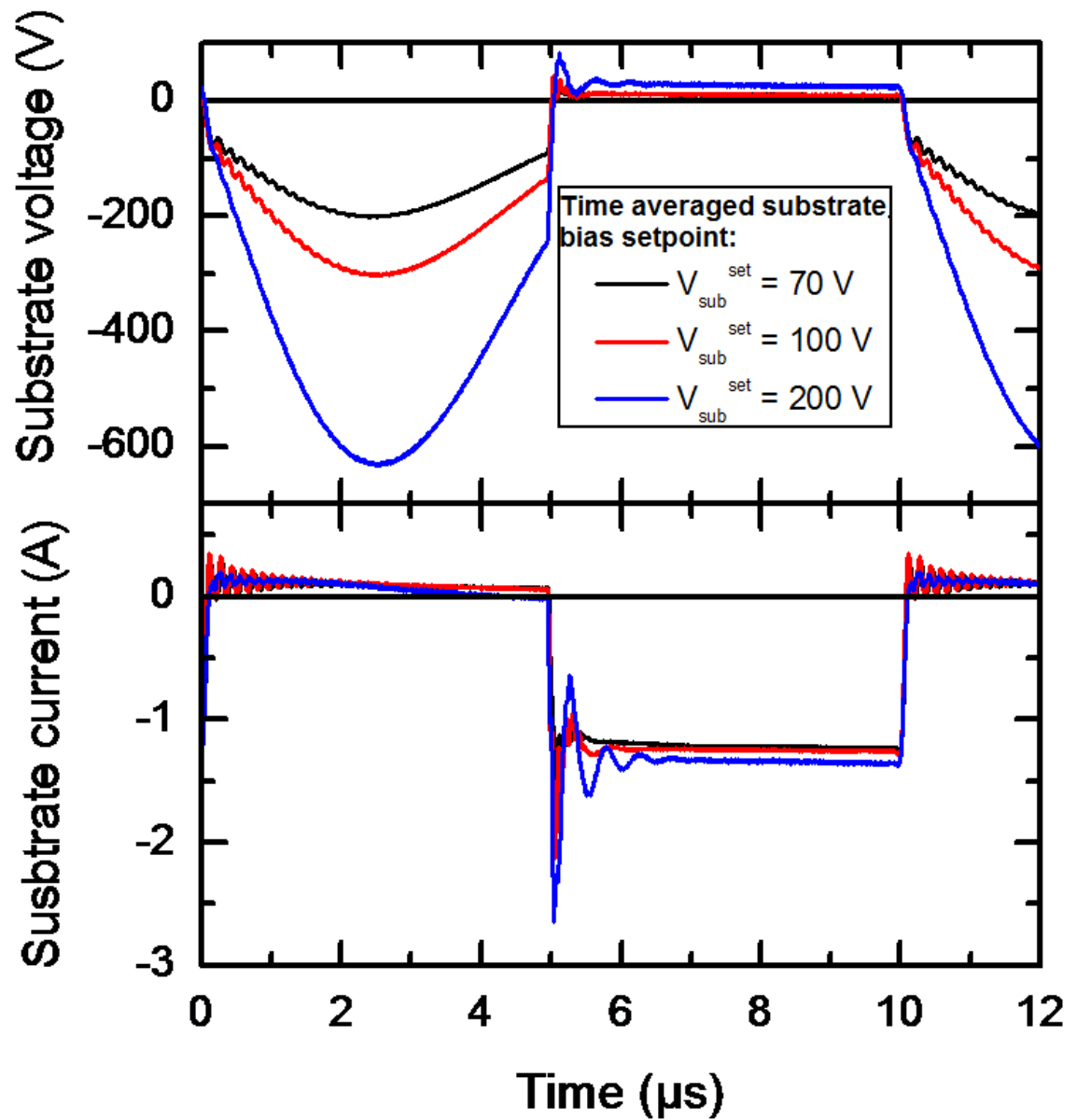


Figure 8.6: Substrate voltage and substrate current waveforms against time, during reactive sputtering. Pulse frequency was 100 kHz, 50% on time duty cycle

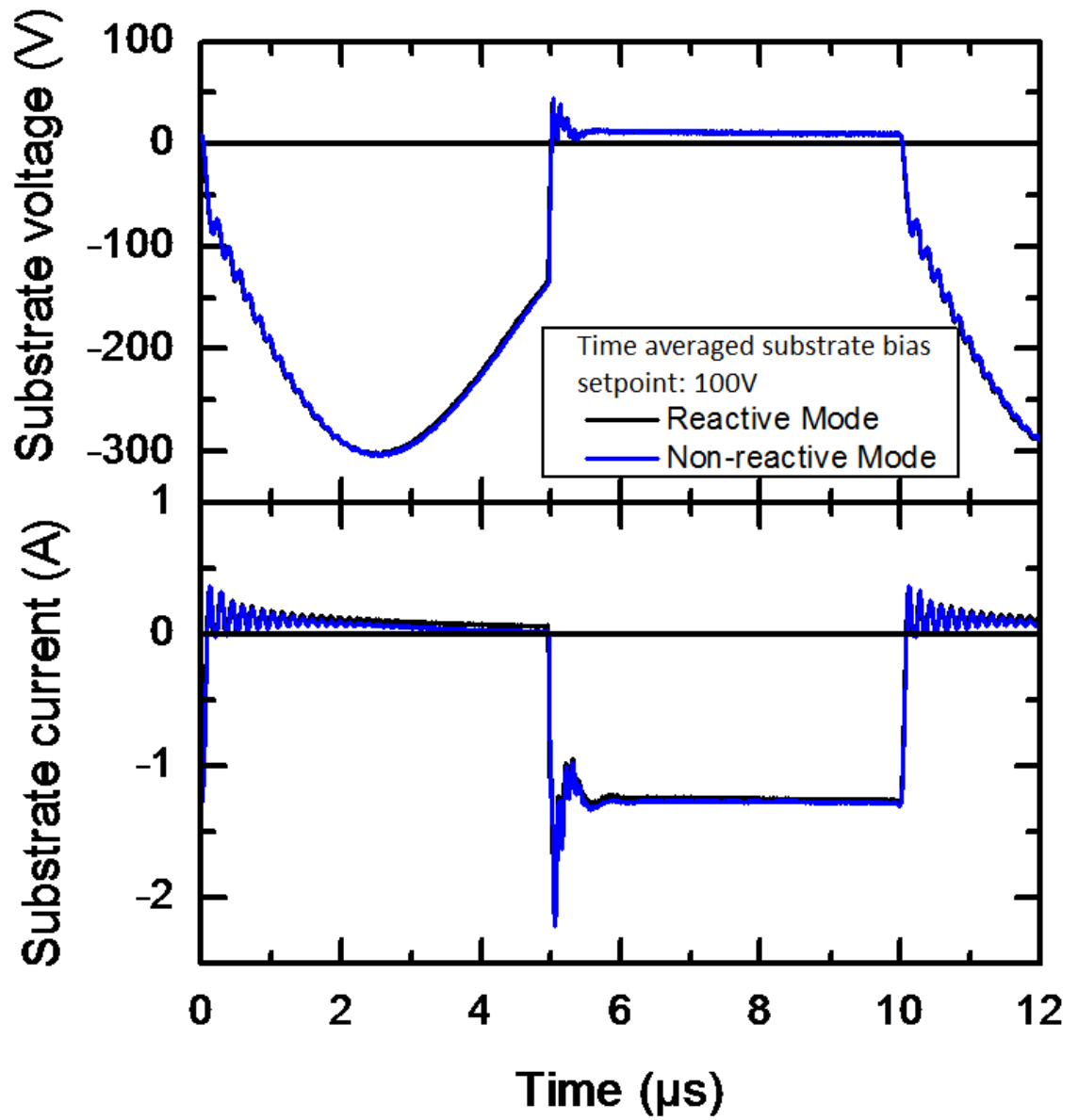


Figure 8.7: Comparison of substrate current and bias in reactive and non-reactive sputtering, with a substrate bias set-point of -100V. Pulse frequency was 100 kHz, 50% on time duty cycle

Langmuir probe results:

Using the Langmuir probe plasma characteristics, such as ion temperature, ion density, and overall plasma bias, were investigated as they changed with the pulse cycle.

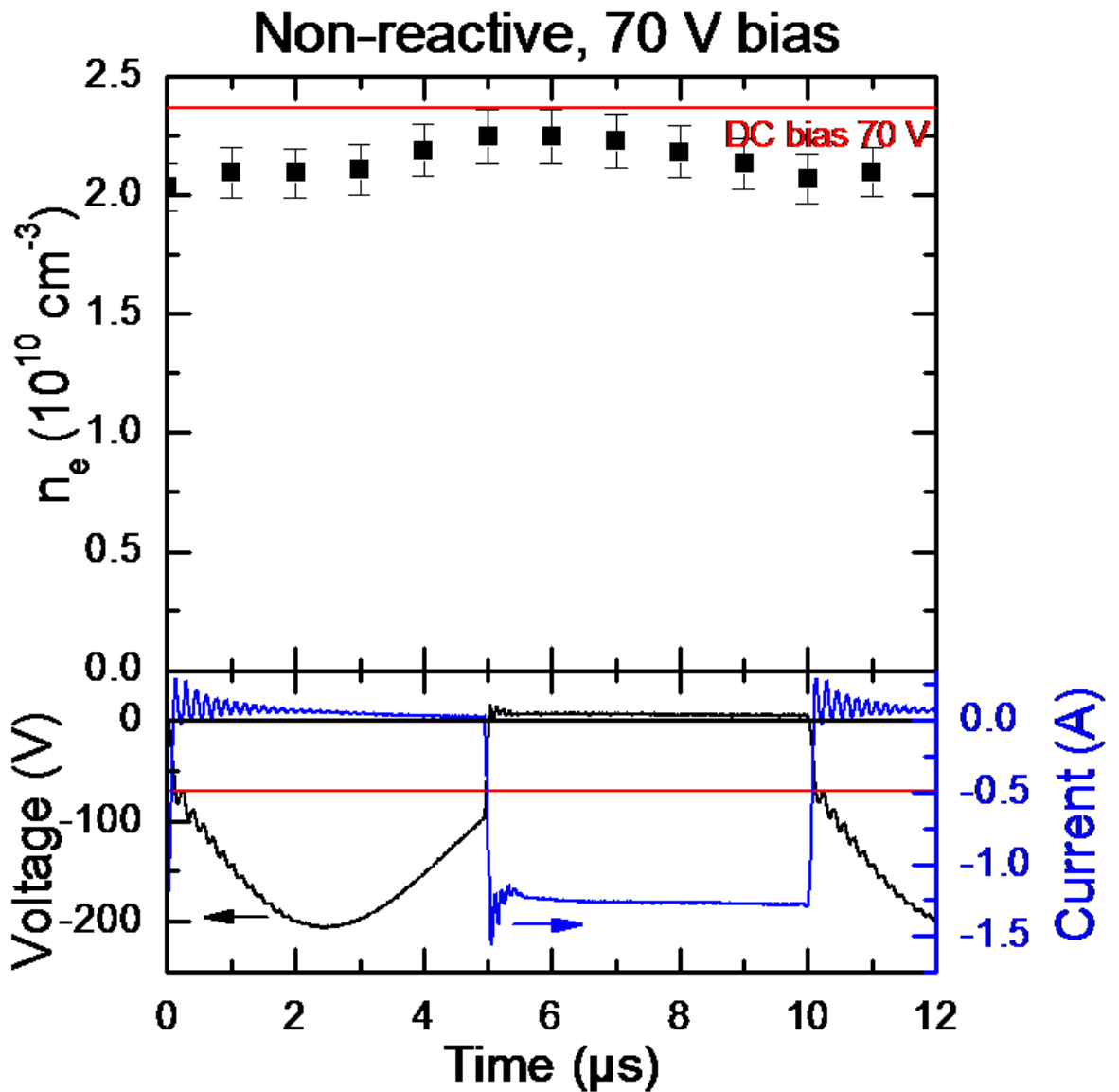


Figure 8.8 : Comparison of substrate bias and current waveforms to electron density (n_e), Sputtering was done in non reactive pulsed d.c. substrate bias mode, with a time averaged substrate bias setpoint of -70V. The red line indicates the equivalent measurement when sputtering is done in d.c. mode. Pulse frequency was 100 kHz, 50% on time duty cycle

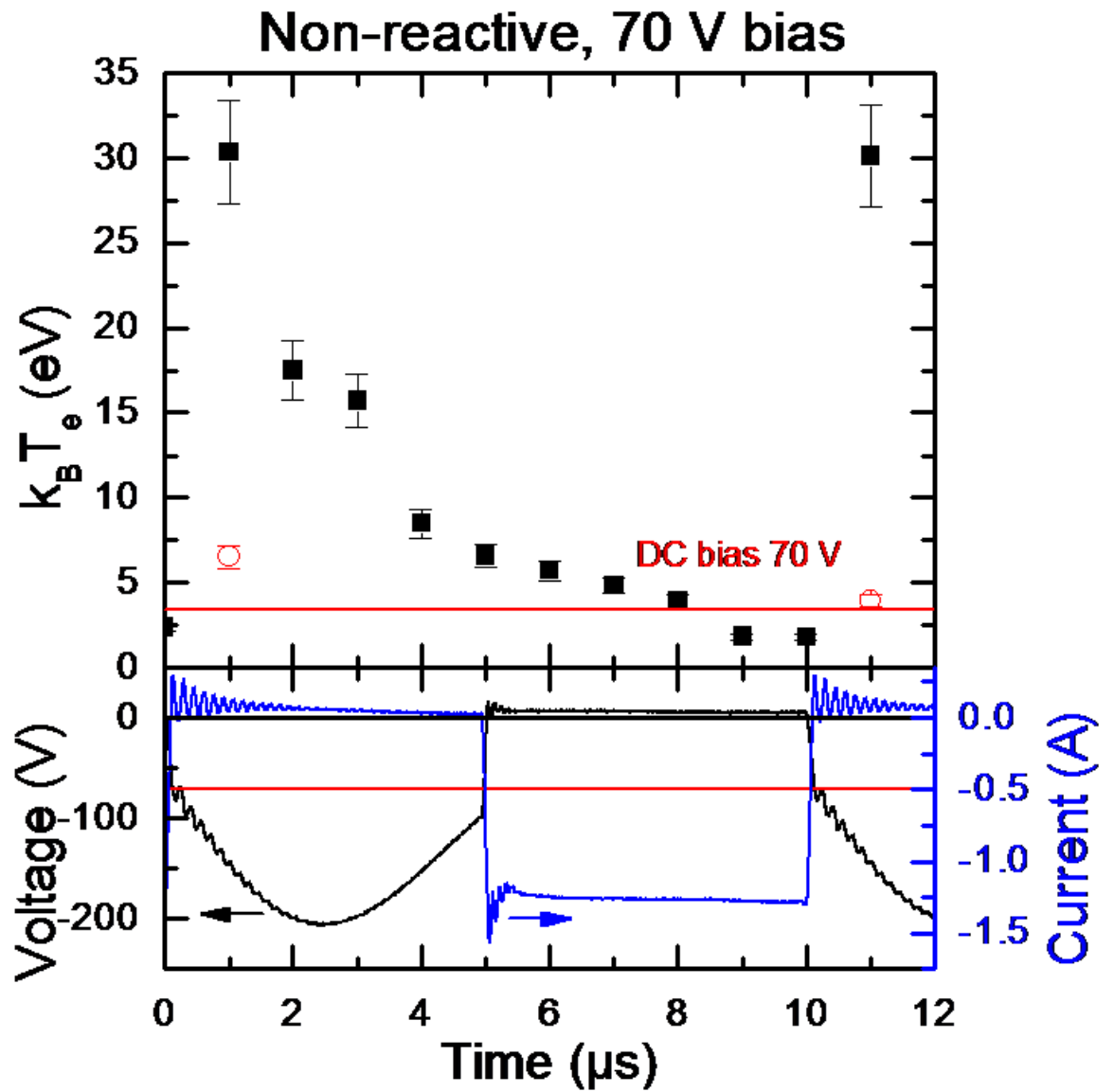


Figure 8.9: Comparison of electron temperature to substrate current and bias waveforms, performed during pulsed substrate bias operation. Sputtering was done in non reactive pulsed d.c. substrate bias mode, with a time averaged substrate bias setpoint of -70V. The red lines and markers indicate the equivalent readings for d.c. operation. Pulse frequency was 100 kHz, 50% on time duty cycle. K_B is the Boltzmann constant.

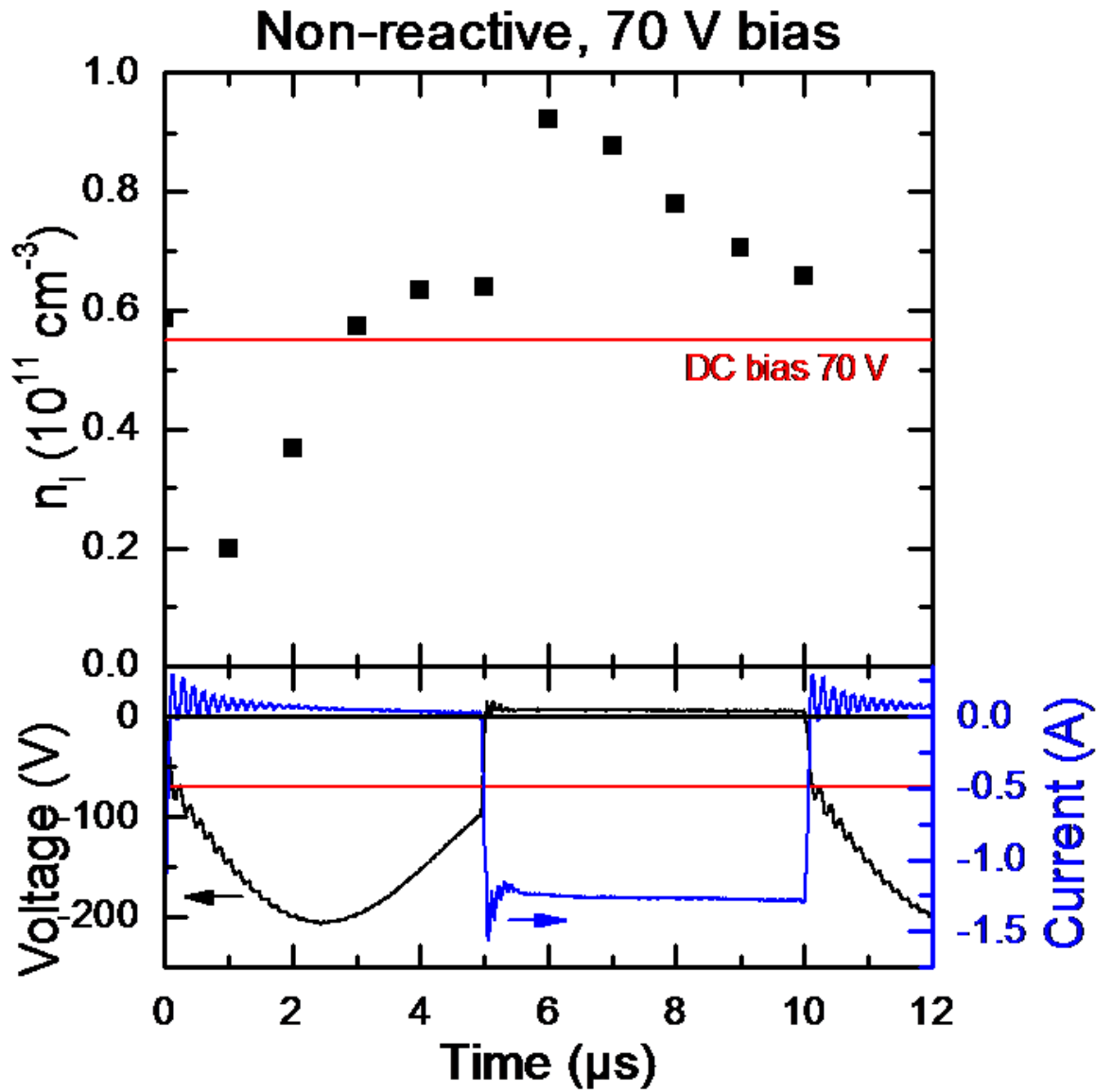


Figure 8.10: Comparison of ion density to substrate bias and current waveforms. Red lines indicate equivalent readings from d.c. operation. Sputtering was done in non reactive pulsed d.c. substrate bias mode, with a time averaged substrate bias setpoint of -70V. Pulse frequency was 100 kHz, 50% on time duty cycle

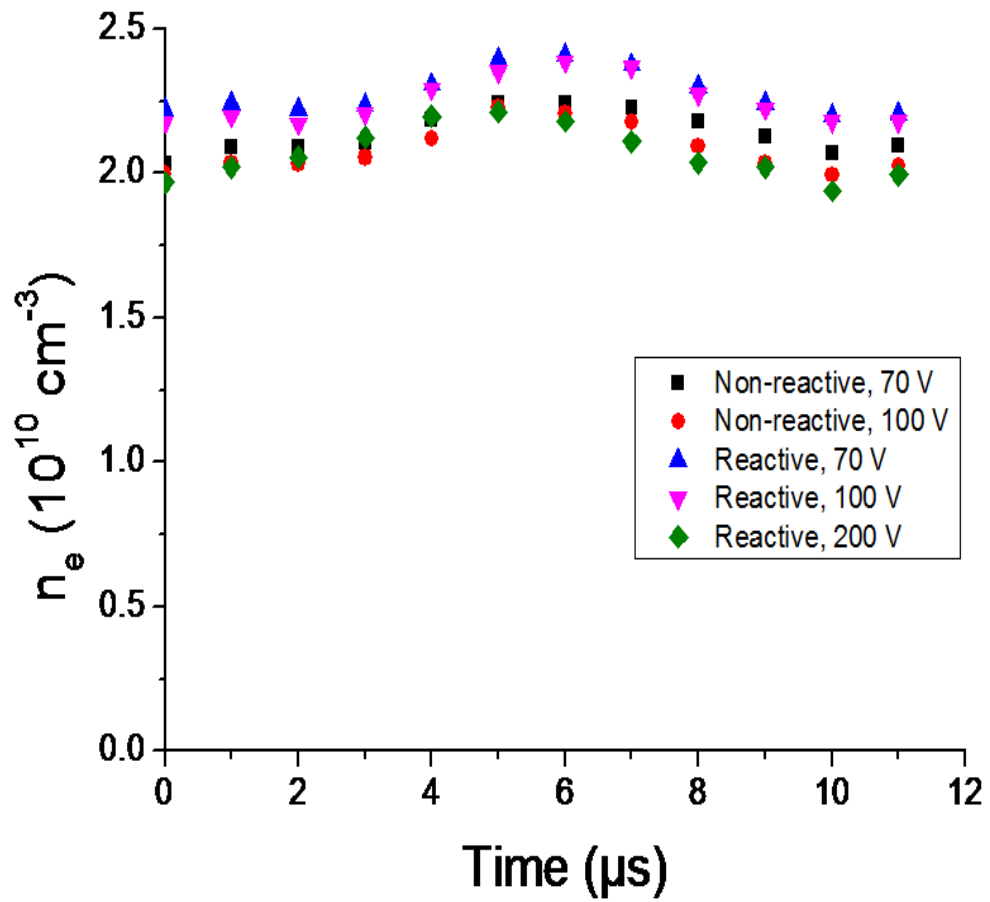


Figure 8.11: Electron density against time for two time averaged substrate bias setpoint values in nonreactive mode (-70 V and -100V) and three bias values in reactive mode (-70V, -100V, and -200V). In reactive mode the nitrogen content is equivalent to that of an OEM signal of 40% FMS or 9 SCCM of N₂ flow in MFC setpoint flow control mode. Pulse frequency was 100 kHz, 50% on time duty cycle

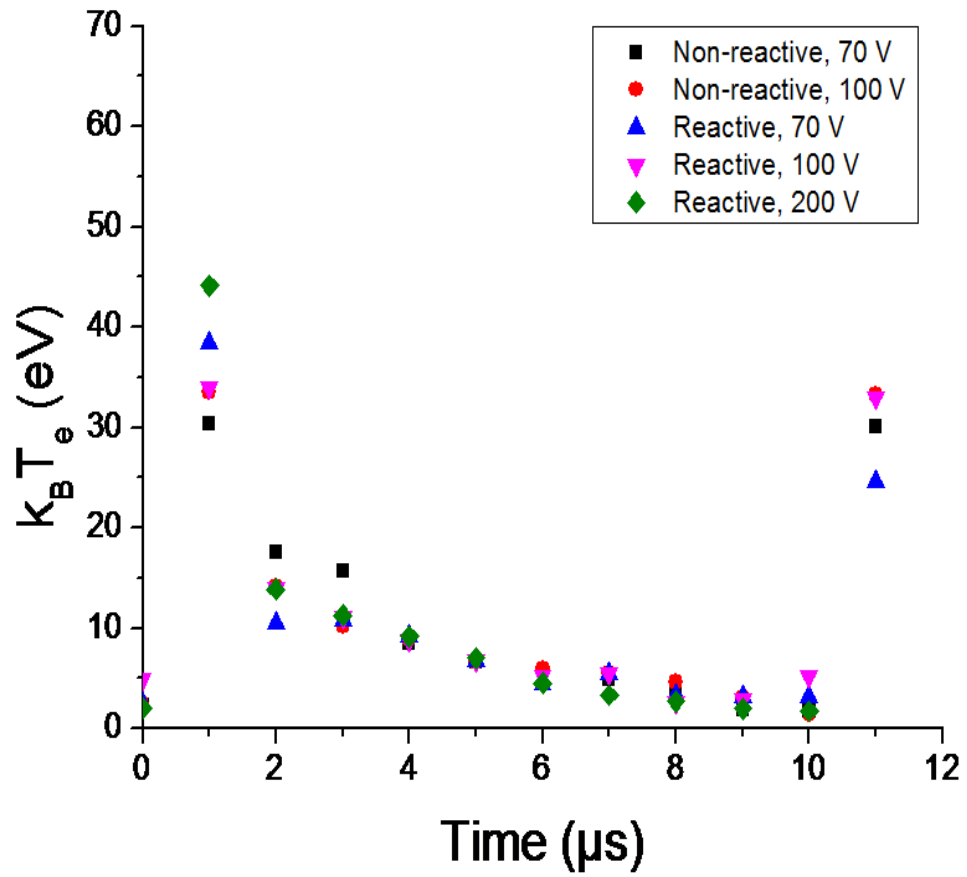


Figure 8.12: Comparison of electron temperature against time readings for reactive and non reactive sputter modes, across a range of time averaged substrate bias setpoints. Pulse frequency was 100 kHz, 50% on time duty cycle. K_B is the Boltzmann constant.

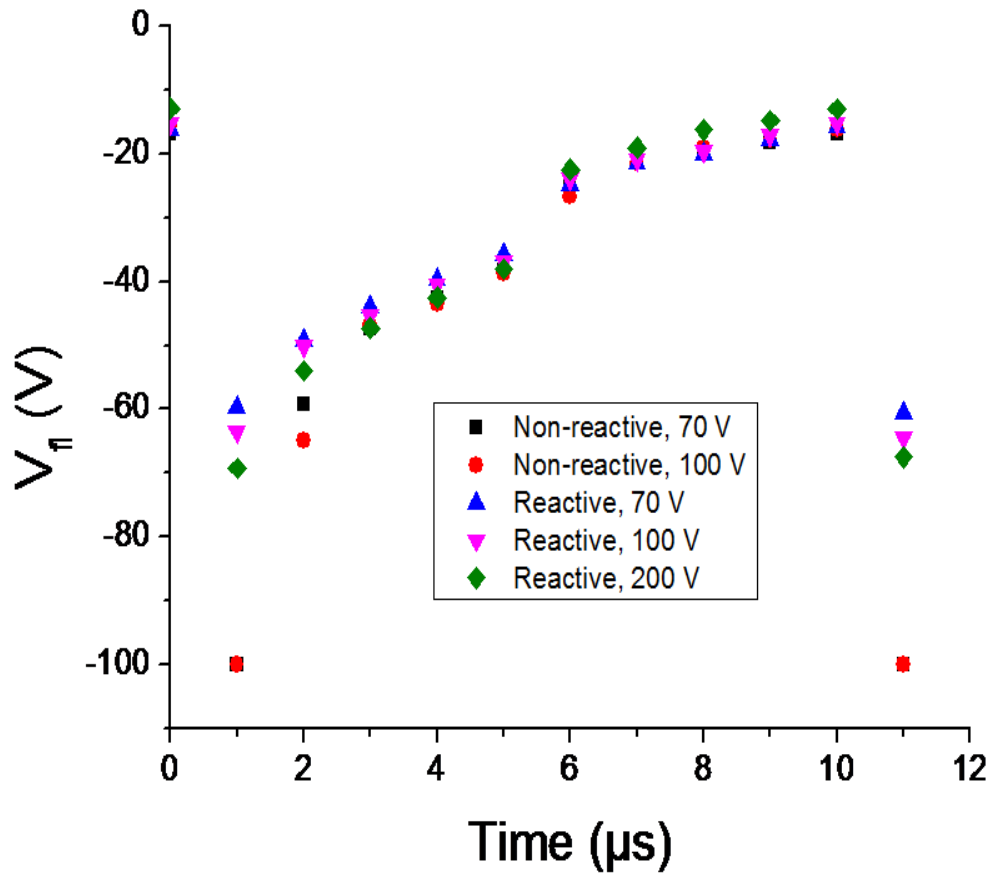


Figure 8.13: Comparison of floating potential across a range of time averaged substrate bias setpoints, in reactive and non-reactive sputtering. Pulse frequency was 100 kHz, 50% on time duty cycle

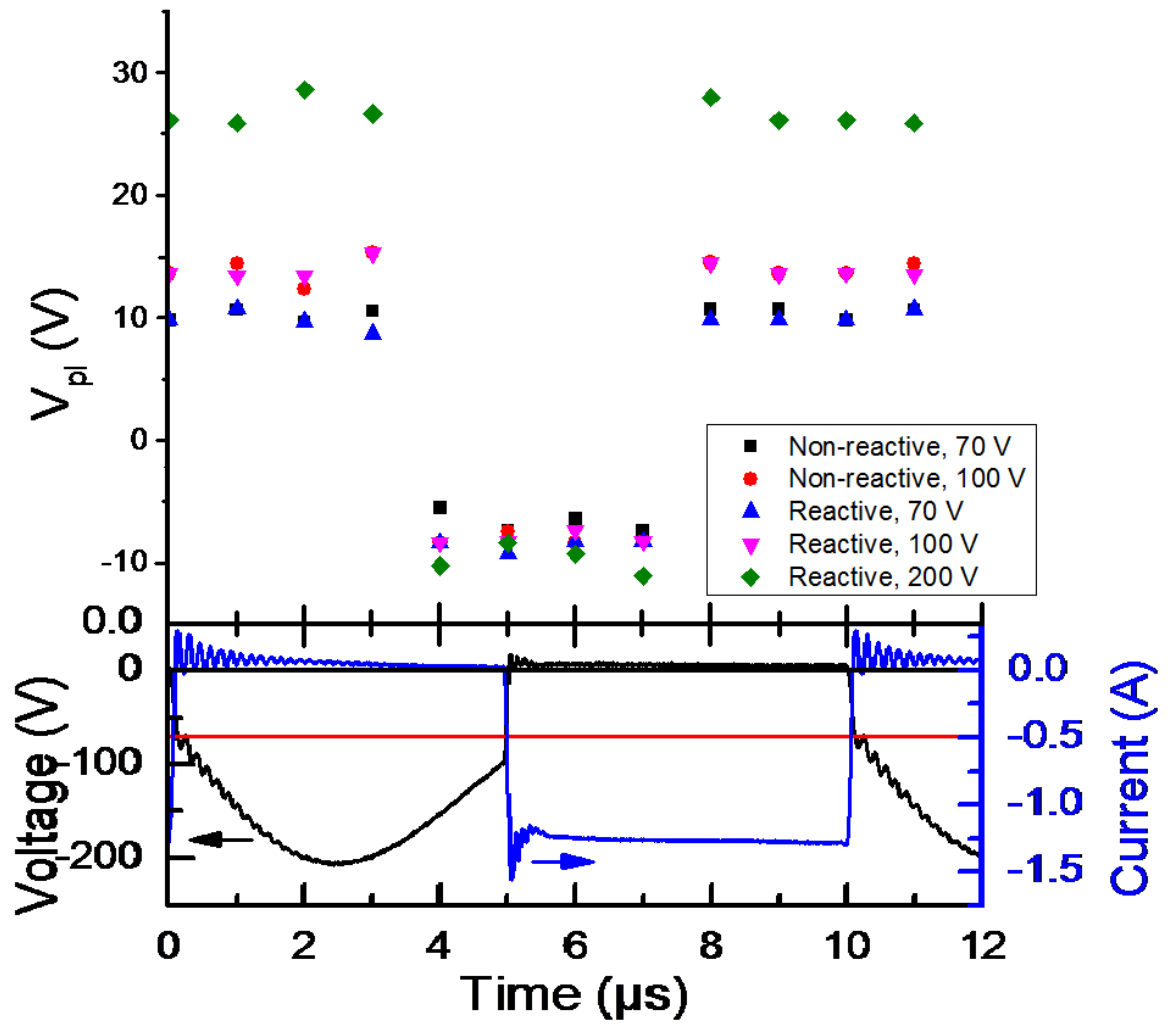


Figure 8.14: Comparison of plasma potential readings, across a range of time averaged substrate bias set points, for reactive and non reactive operations. Pulse frequency was 100 kHz, 50% on time duty cycle.

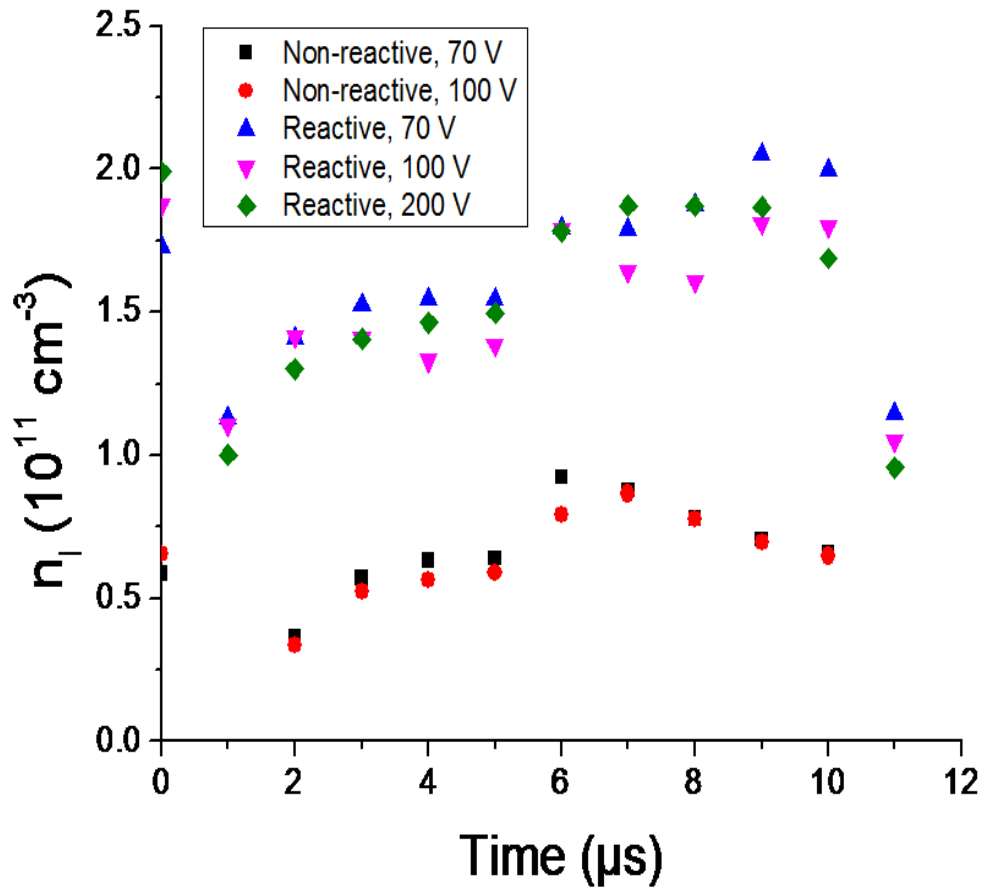


Figure 8.15: Comparison of ion densities, for a range of time averaged substrate bias setpoints, for reactive and non reactive operation. Pulse frequency was 100 kHz, 50% on time duty cycle

Optical emission spectrometry:

The intensity of various emission lines of interest were investigated as they changed with the pulse cycle.

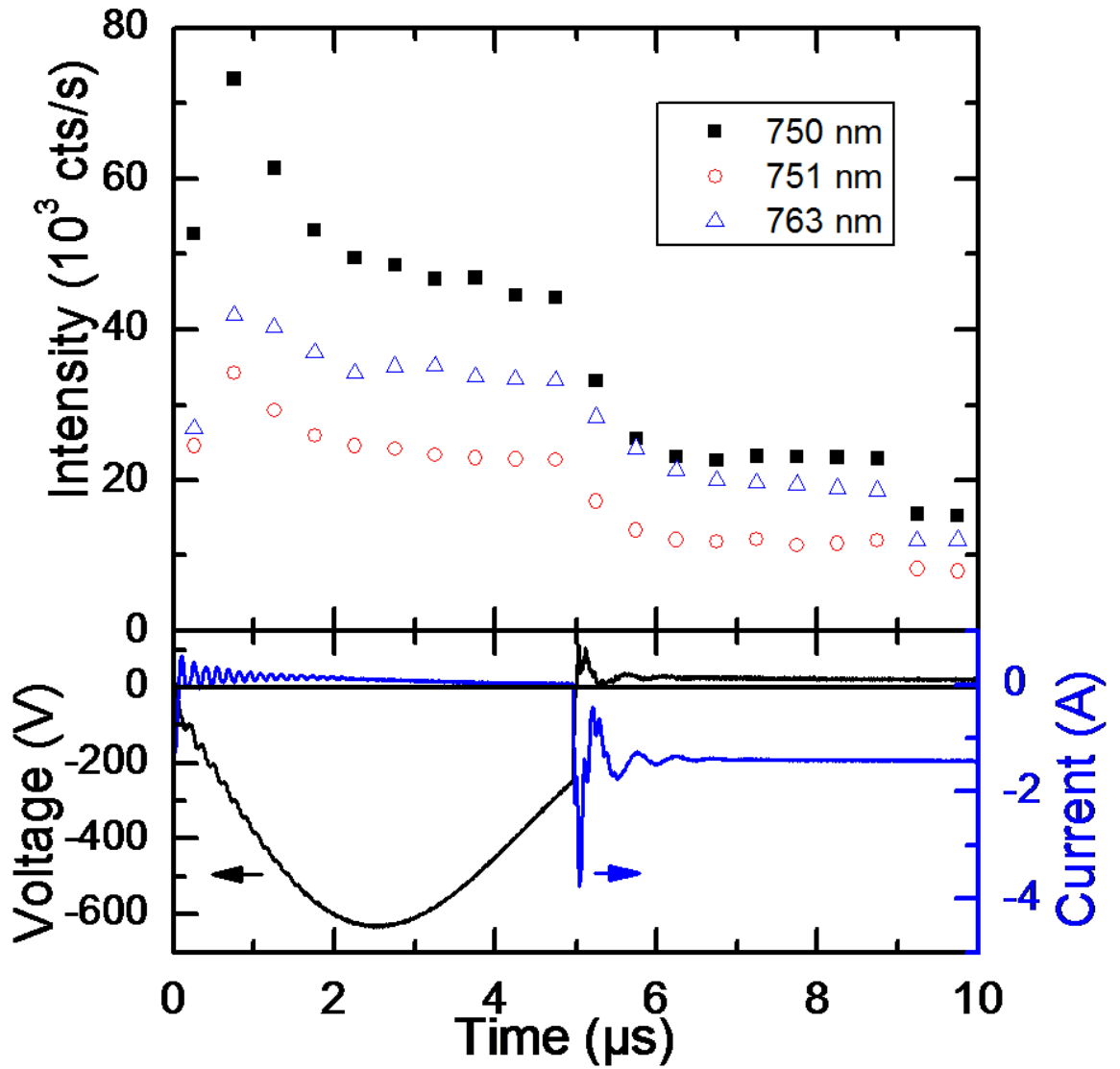


Figure 8.16: The variation in emission with time on three wavelengths corresponding to the Ar (I) emission. Sputter mode was non reactive, with a substrate bias pulse rate of 100 kHz and a time averaged substrate bias setpoint of -200V.

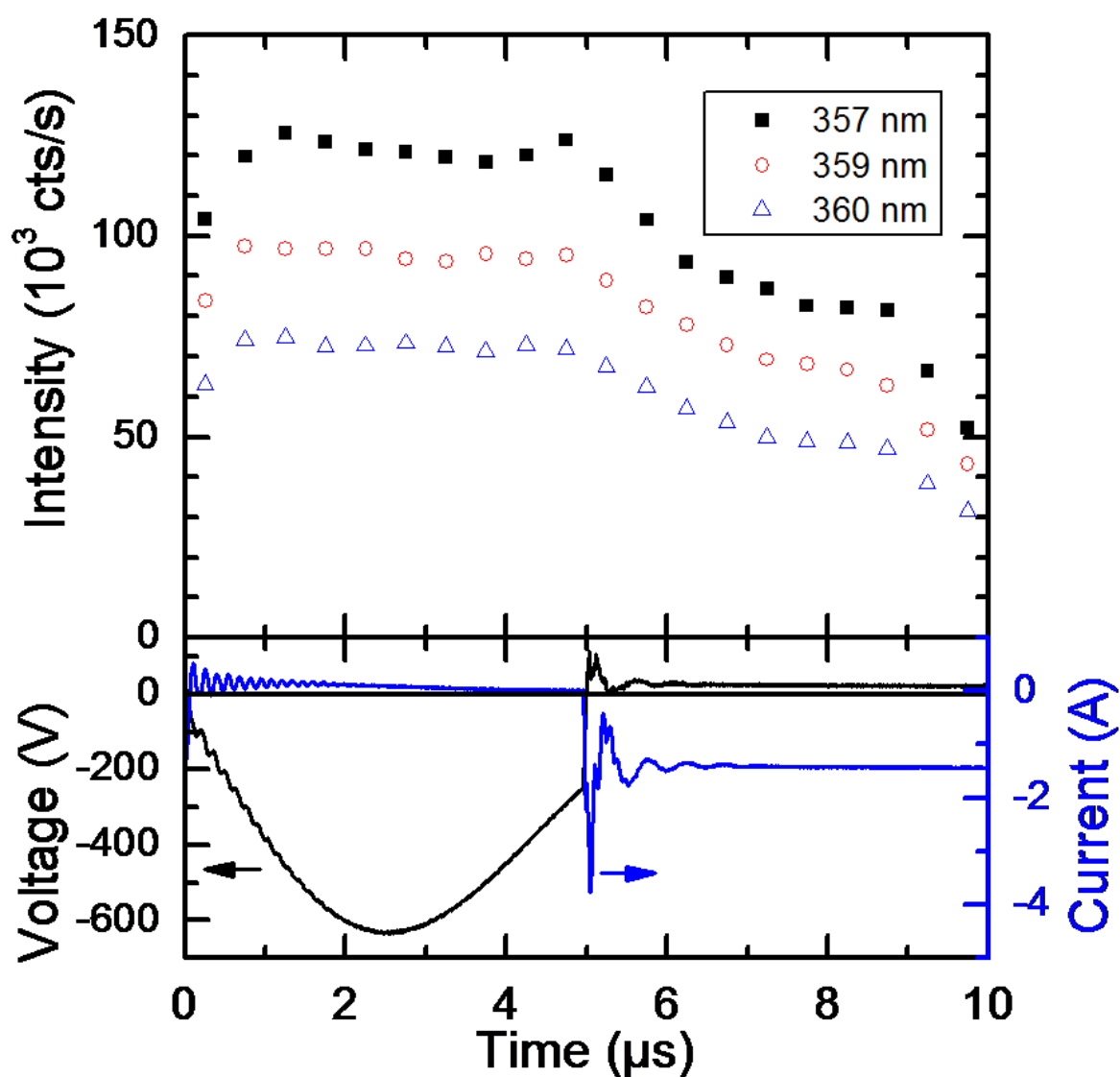


Figure 8.17: The variation in emission with time on three wavelengths corresponding to the Cr (I) emission. Sputter mode was non reactive, with a substrate bias pulse rate of 100 kHz and a time averaged substrate bias setpoint of -200V.

Array 3: Microstructure:

The array 3 coatings were examined by XRD, SEM micrographs of fracture cross sections, and EDS.

XRD data show the films have a strong {111} orientation. Comparison between the glancing angle and Bragg-Brentano mode spectra reveals a surface layer of oxides.

XRD analyses of the coatings deposited during runs with a d.c. bias of -70 V confirm the presence of {111} and {200} peaks, characteristic of CrN (figure 8.19). Both these results are also seen in equivalent films deposited at a pulse frequency of 350 kHz.

As shown in figure 8.18a, the (-70V) D.C. biased CrN coatings showed a {220} peak which is absent from the 350 kHz biased equivalent film. This indicates pulsed biasing leads to a more highly oriented CrN film compared to d.c. Both the d.c. and pulsed biased (-70V) Cr₂N coatings showed a strong {221} orientation, as well as smaller amounts of {200} {112} and {111}. The pulsed coating shows a slightly stronger {221} orientation.

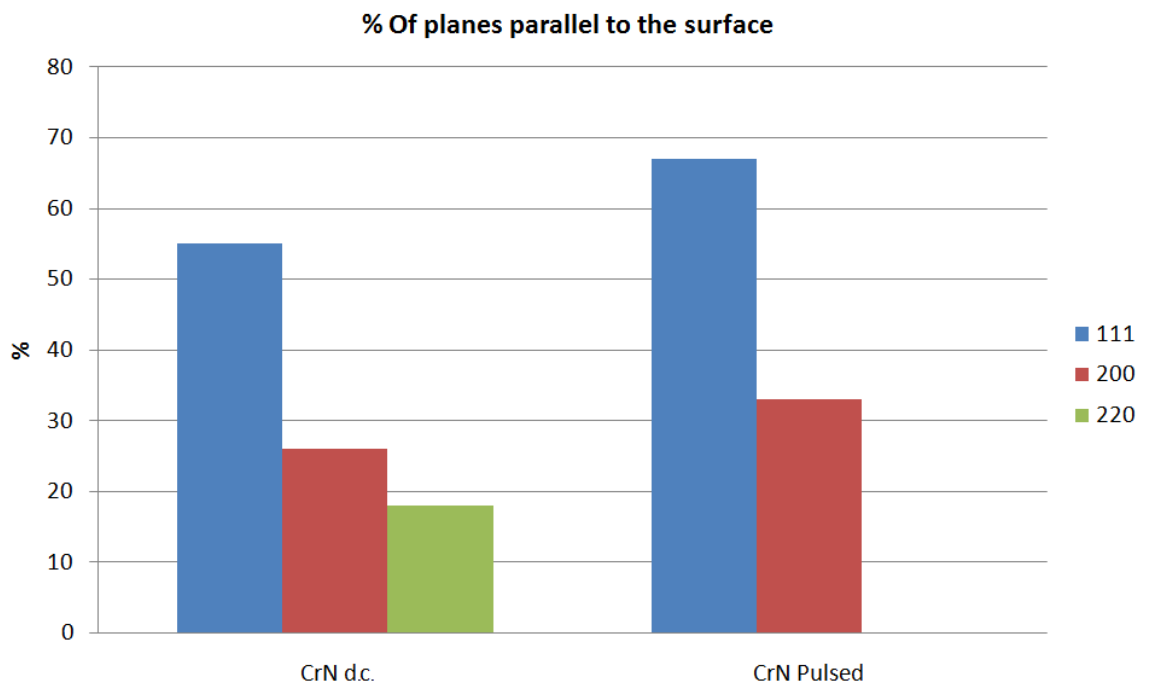


Figure 8.18a

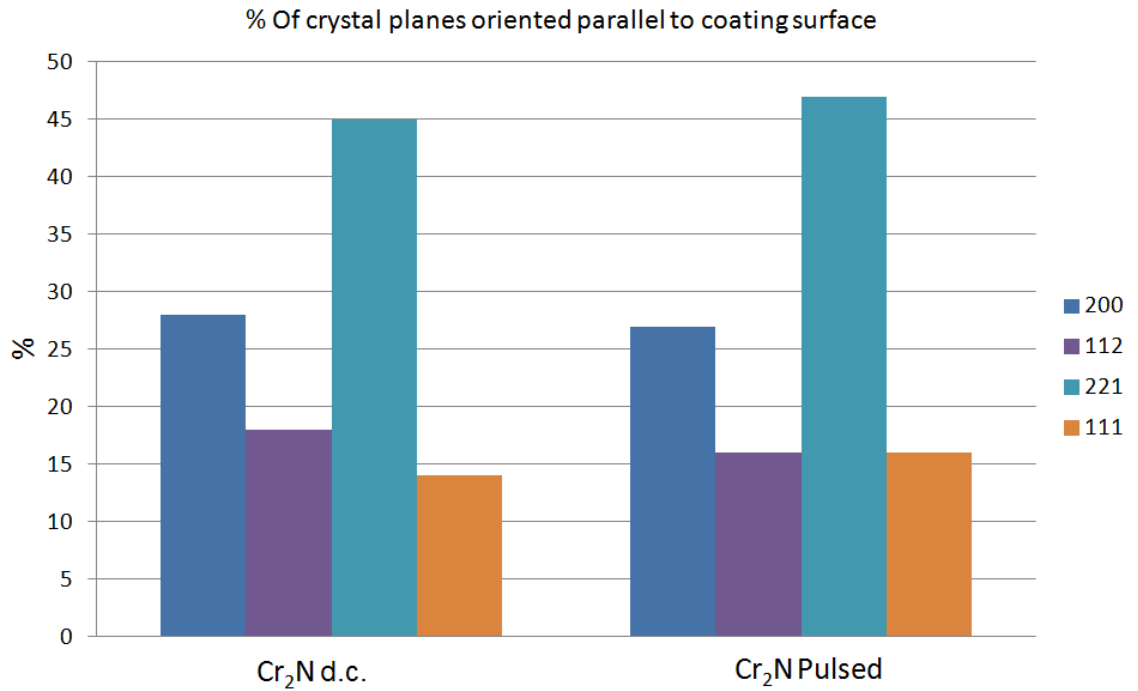


Figure 8.18b

Figures 8.18a and b: The percentages of crystal planes oriented relative to the film surface. D.C. biased CrN samples compared to pulsed biased CrN samples top, d.c biased Cr₂N samples compared to pulsed biased Cr₂N samples bottom.

All the films showed compressive residual stress, as determined by XRD peak shift of the {111} peak. The maximum stress was found in the pulsed substrate bias samples, and the minimum in d.c. samples.

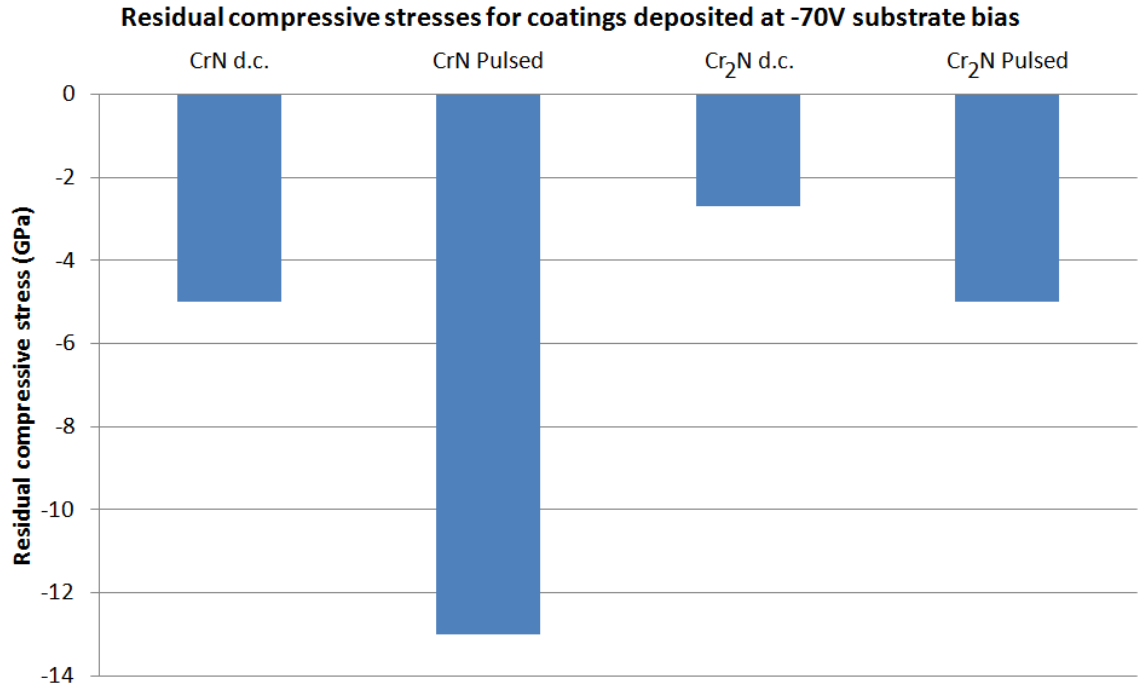


Figure 8.19: Comparison of residual stresses between d.c. films and pulsed bias films.

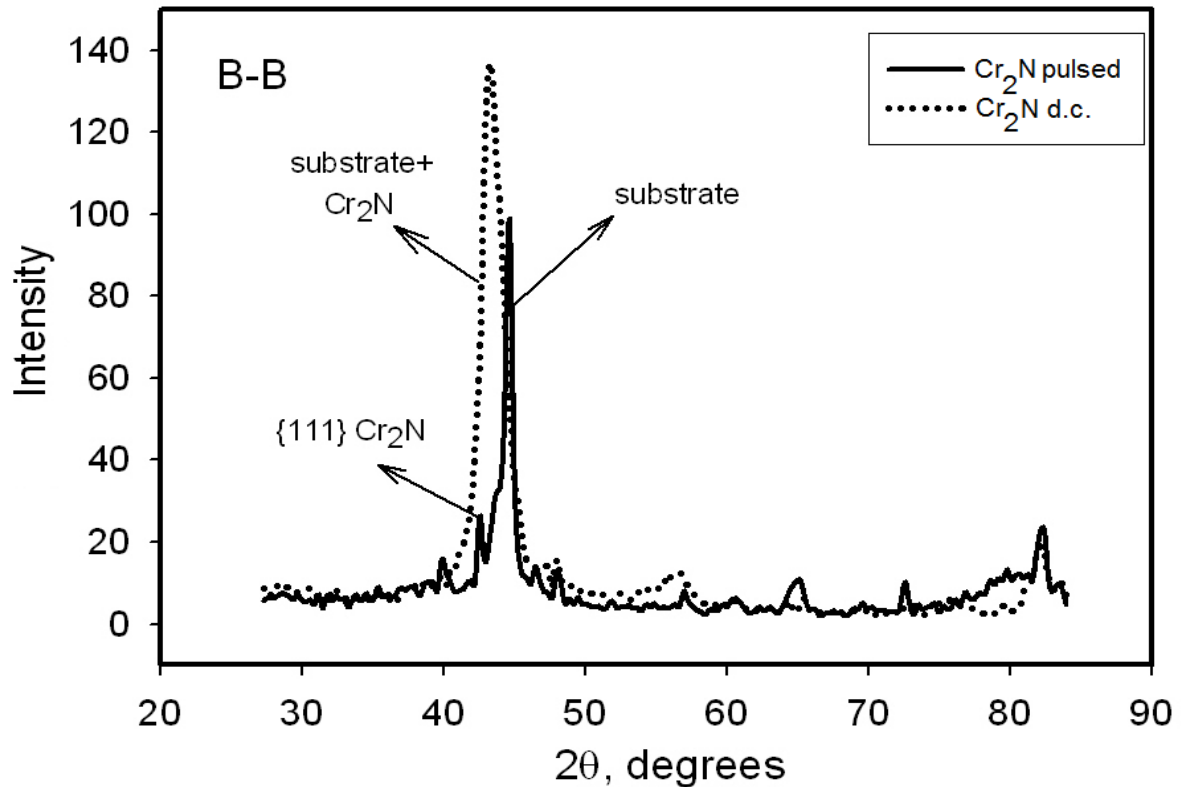


Figure 8.20: A comparison of the XRD traces for Cr₂N coatings deposited using D.C. and pulse substrate bias. The traces given are examples used for visualization.

In Cr₂N coatings a weak halo in the XRD spectra for the d.c. sample at 35-50° indicates a small amorphous phase. The pulsed only deposited coatings show a more pronounced halo at 45-50° and 80-85° indicating a greater amorphous content.

Coatings were fractured for analysis by SEM. Figures 8.21 compare SEM micrographs of fracture sections of coatings deposited at d.c. bias and 350kHz bias. These coatings were all deposited with a -70V substrate bias. These figures indicate that the coatings have dense or dense columnar microstructures. The majority of films show a smooth glass like structure. Some films show vertical patterning that may be evidence of a dense columnar structure, however there are no signs of distinct column tops on the film surfaces suggesting these patterns are artefacts of the fracture. There appears to be no variation in structure due to bias pulsing, however some d.c. deposited coatings were thicker than their pulsed deposited counterparts.

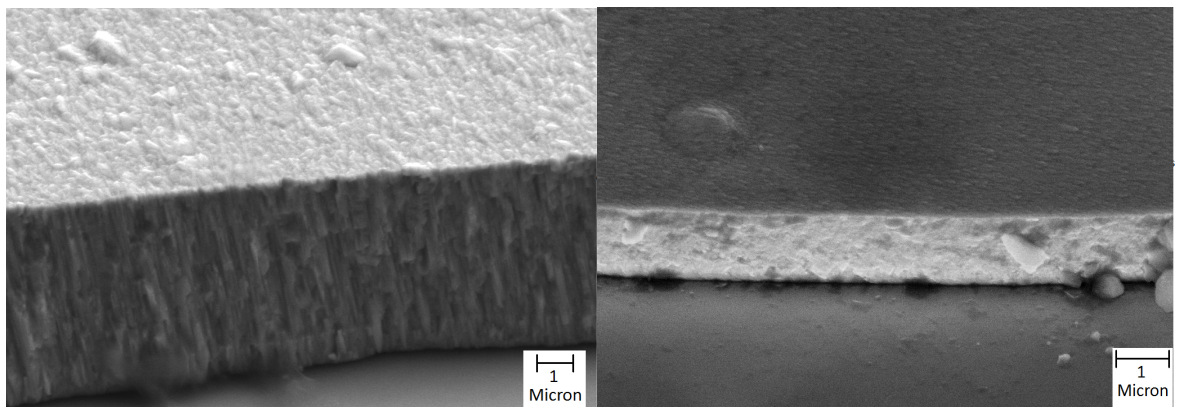


Figure 8.21: Typical SEM fracture cross sections of films deposited at d.c. bias (left) and 350 kHz bias (right). Substrate bias was -70V.

Array 3: Tribology:

The array 3 coatings were tested using our standard tribological tests, in order to relate changes in microstructure to changes in coating properties. Selected coatings were also examined by optical microscopy

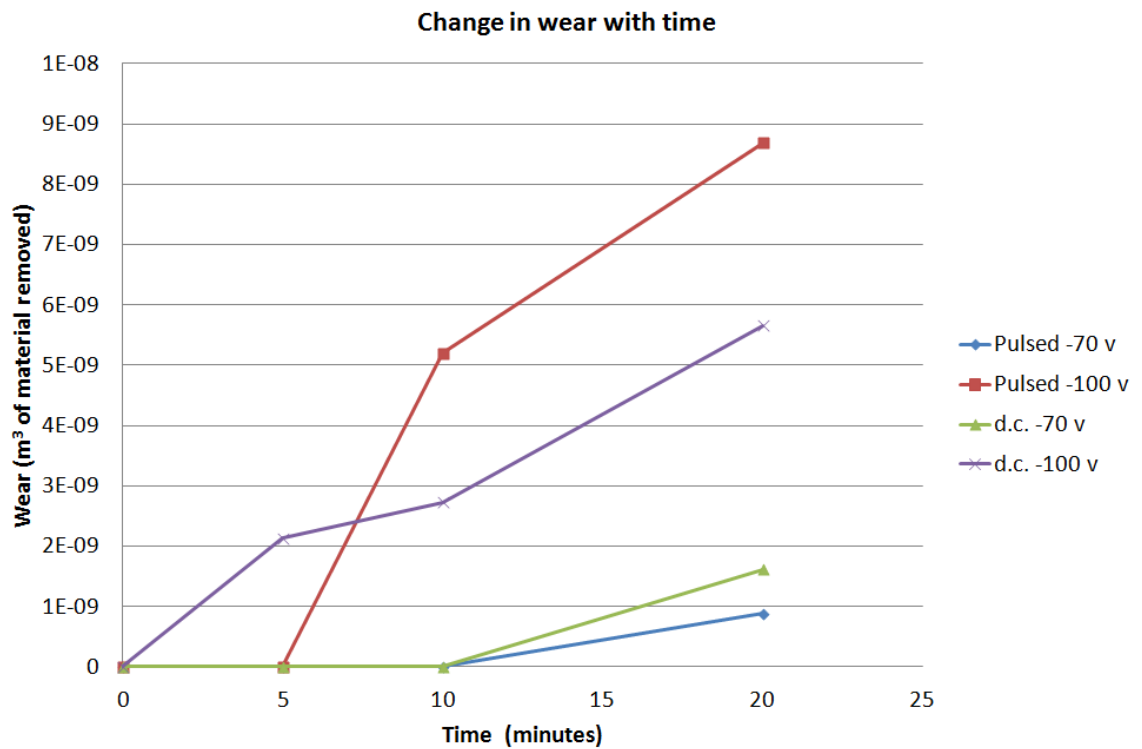


Figure 8.22: The change in wear with time for pulsed and d.c. deposited CrN coatings at -70V and -100V substrate bias. The main observed mechanism for coating wear was delamination. Pulse rate was 350 kHz.

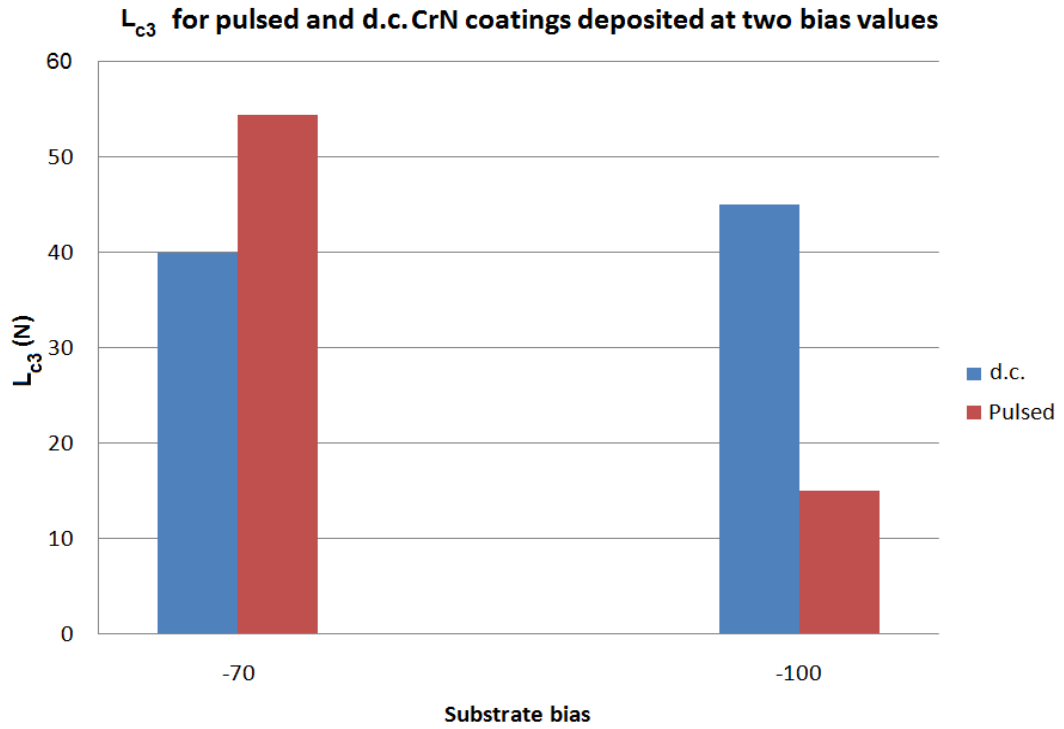


Figure 8.23: The L_{c3} critical loads for total CrN coating failure (L_{c3}) for d.c. and pulsed deposited coatings at -100 V and -70V substrate bias.

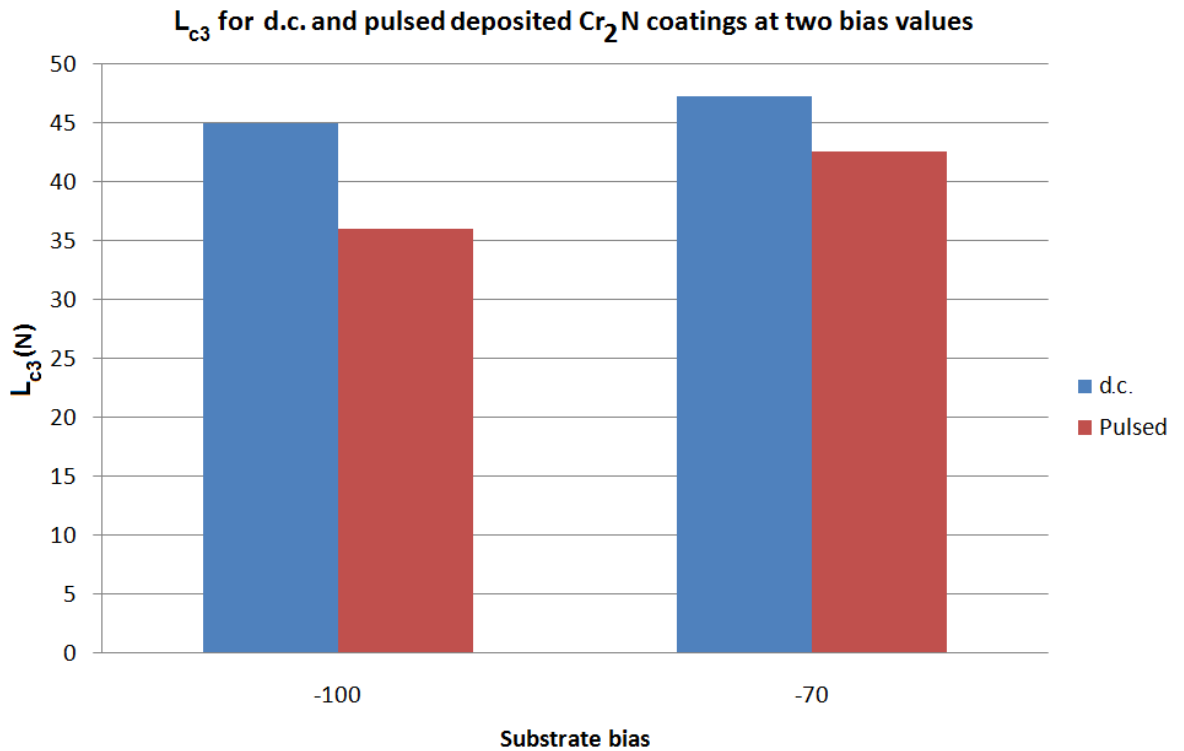


Figure 8.24: Variation in Cr_2N coating adhesion with substrate bias for two different pulse regimes at -100 V and -70 V substrate bias. Critical load given is L_{c3} , Critical load for total film failure

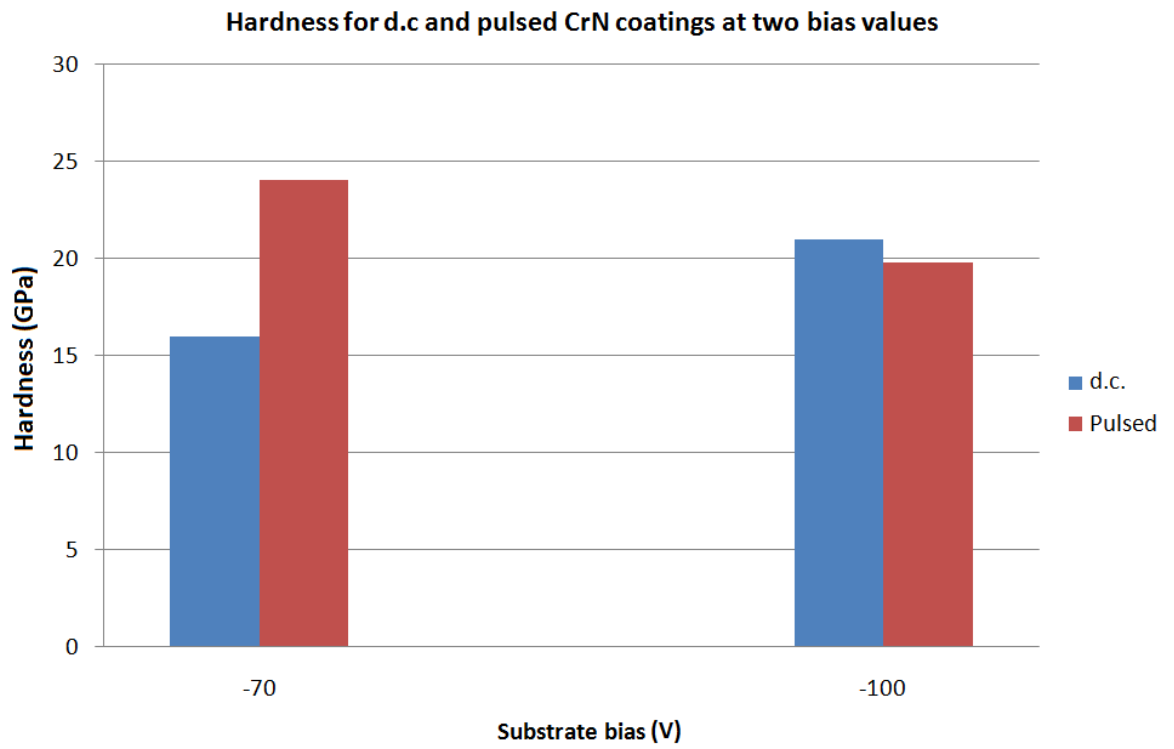


Figure 8.25: The coating hardness for CrN coatings deposited using d.c. and pulsed substrate bias, for bias values of -70V and -100V.

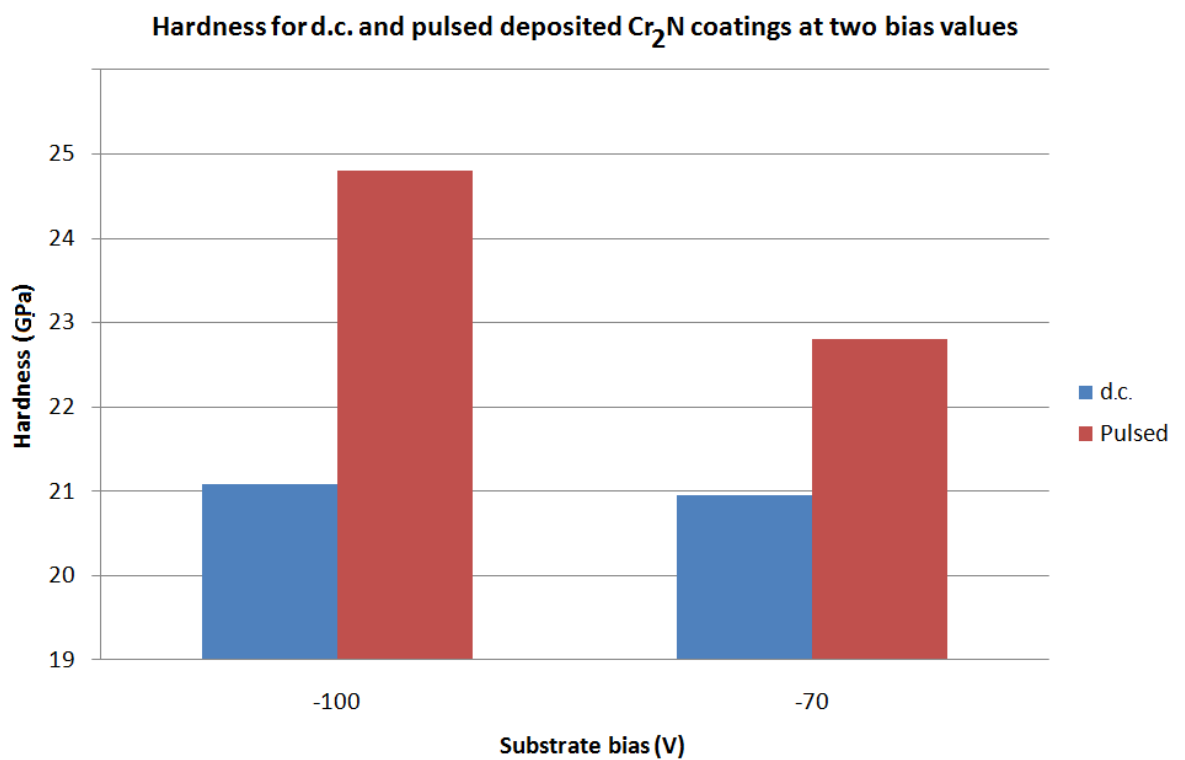


Figure 8.26: The coating hardness for Cr₂N coatings deposited using d.c. and pulsed substrate bias, for bias values of -70V and -100V.

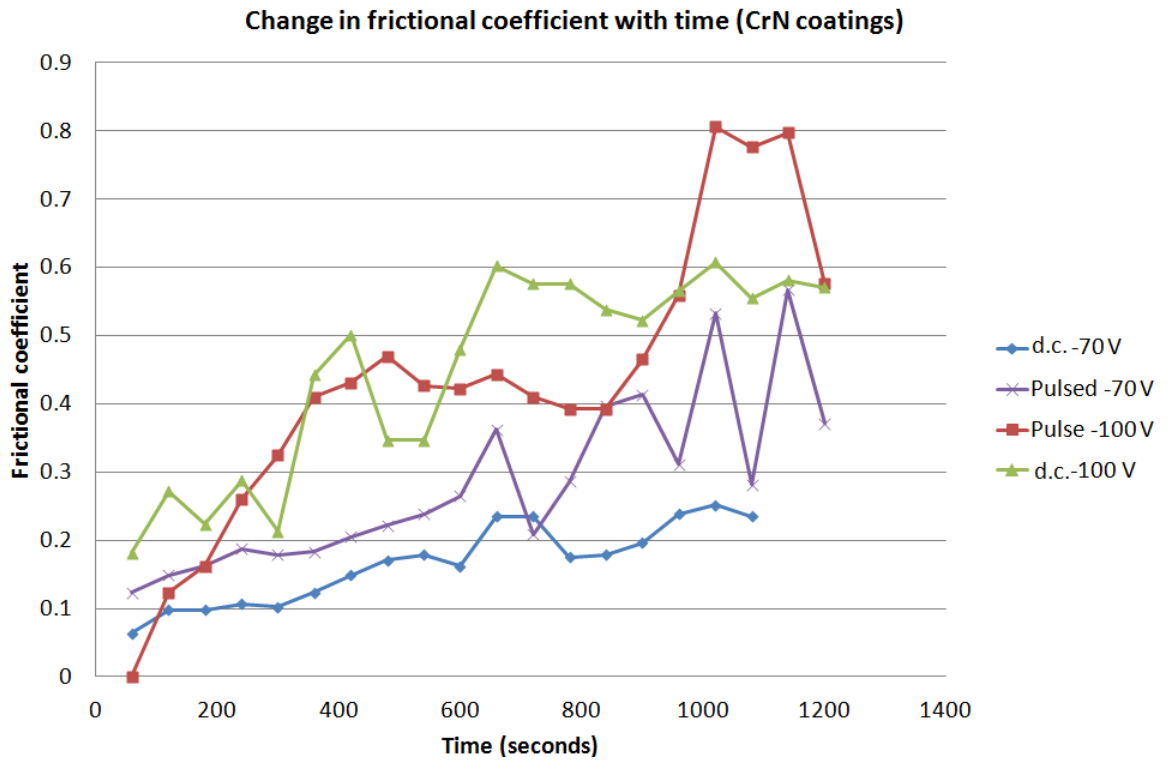


Figure 8.27: Variation in frictional coefficient with time for CrN coatings deposited using pulsed and d.c. sputtering. Substrate biases used were -100V and -70V.

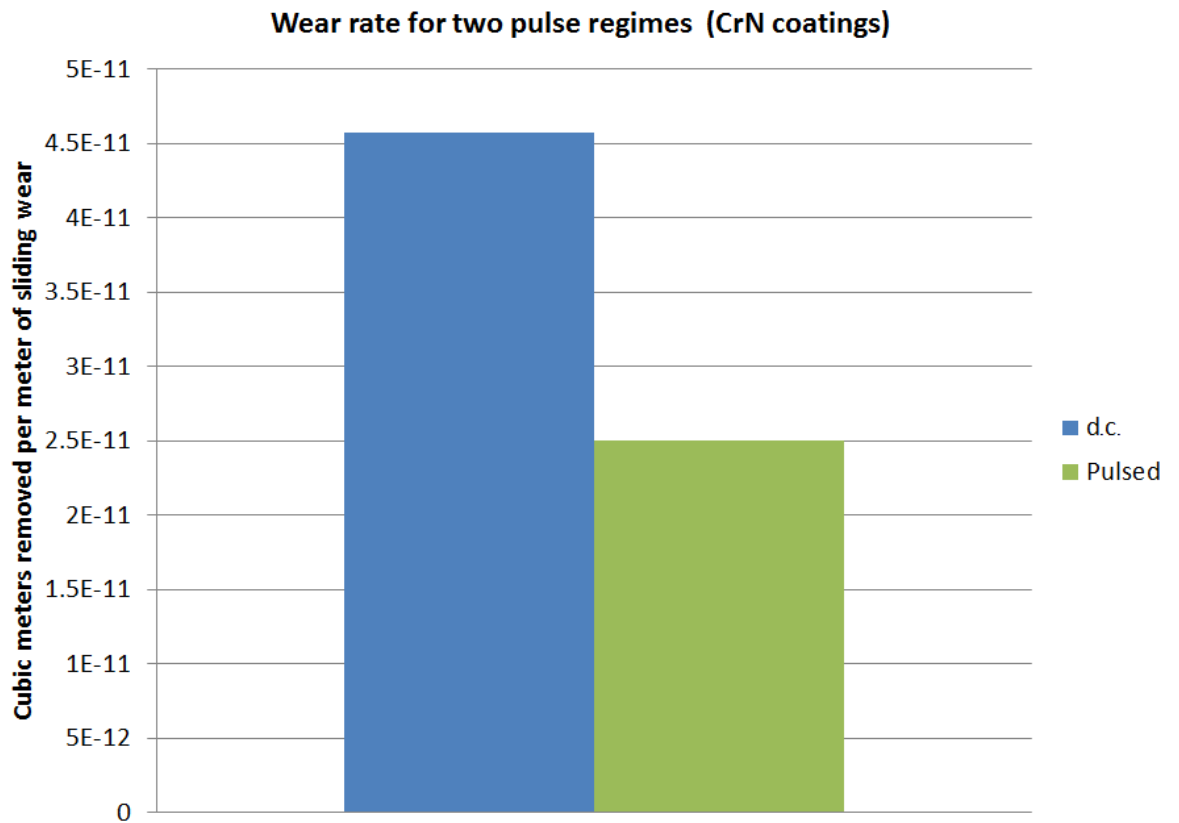


Figure 8.28: Average wear rates over 20 minutes for d.c. and pulsed CrN coatings deposited at -70V.

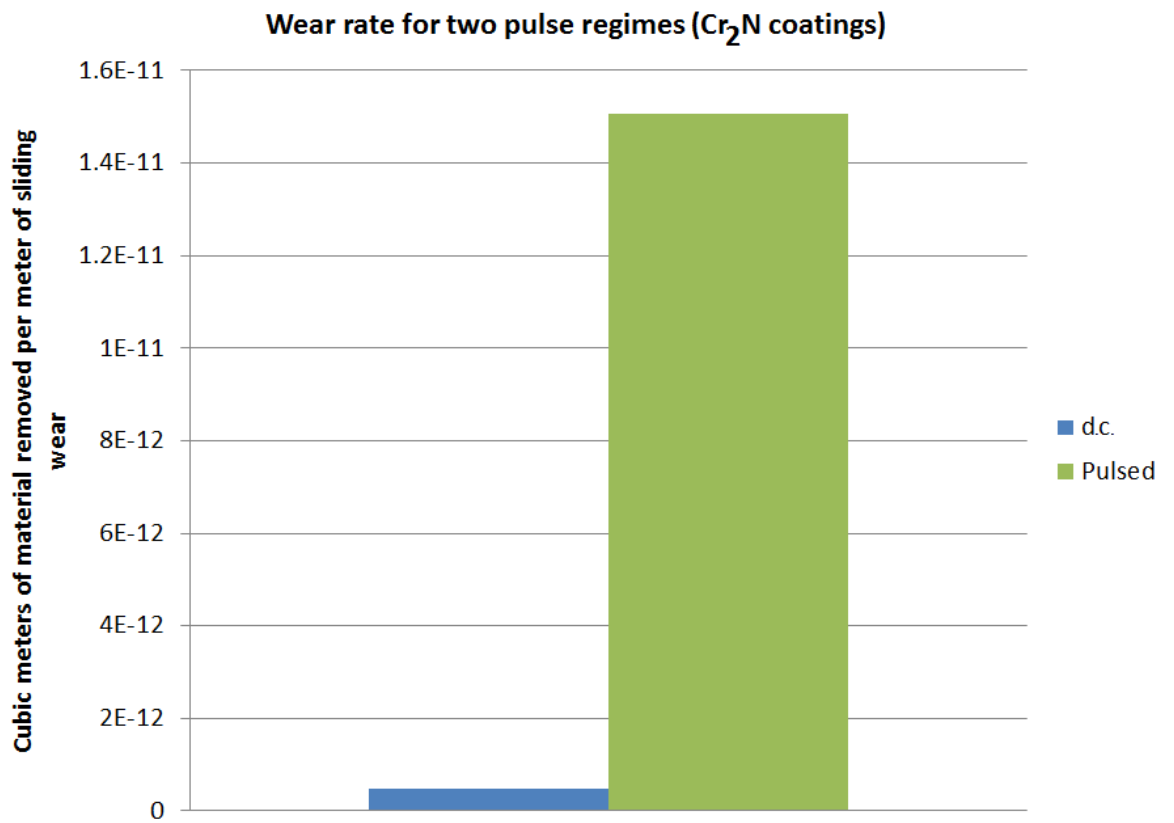


Figure 8.29: Average wear rates over 20 minutes for d.c. and pulsed Cr₂N coatings deposited at -70V.

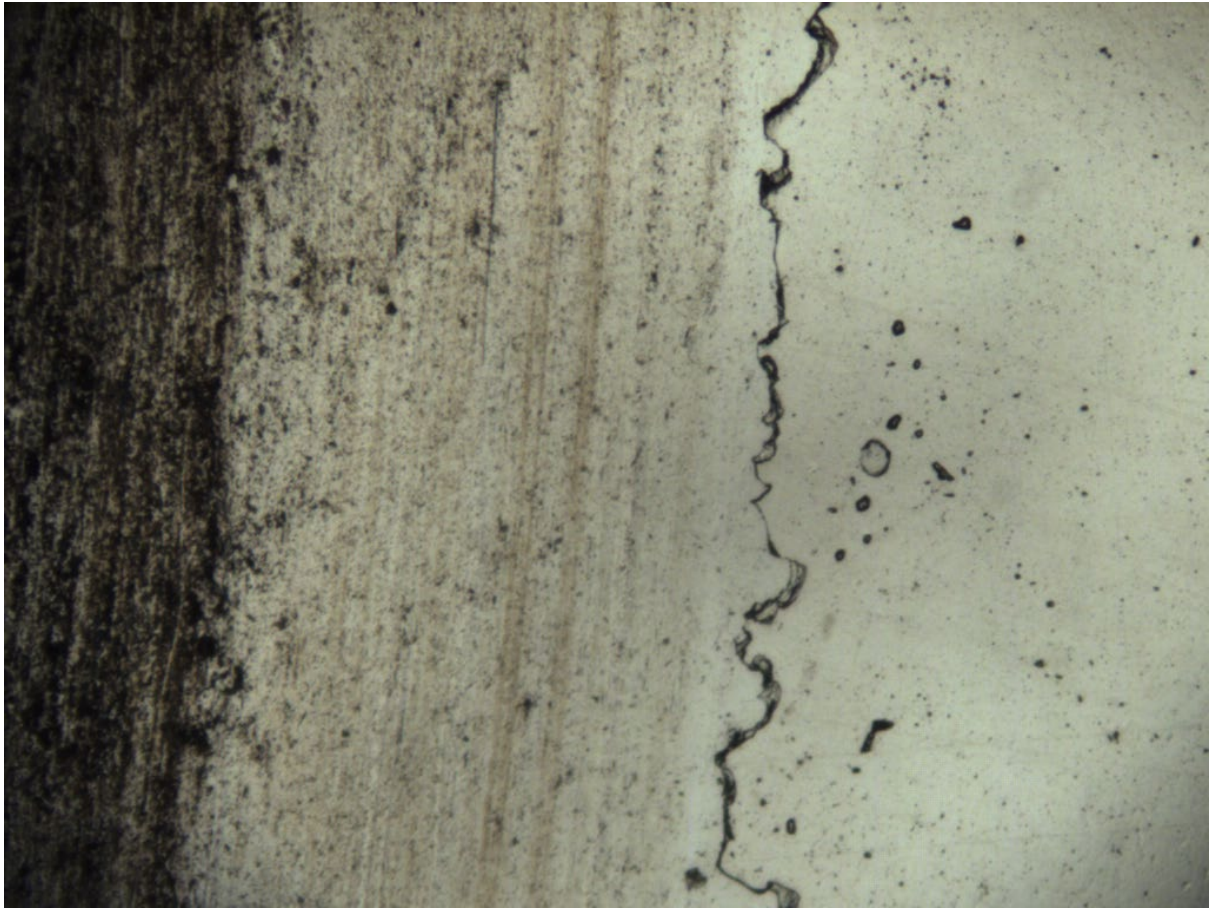


Figure 8.30: An optical micrograph of a typical wear track on a coated tool steel coupon. The coating was a 2 micron deep monolithic Cr₂N coating deposited at a substrate bias of -100V, with a pulse frequency of 300 kHz. The striated area to the left is the exposed steel substrate.

Array 4:

The change in substrate temperature with time during pulsed and d.c. deposition was measured using a FISO fibre optic temperature probe.

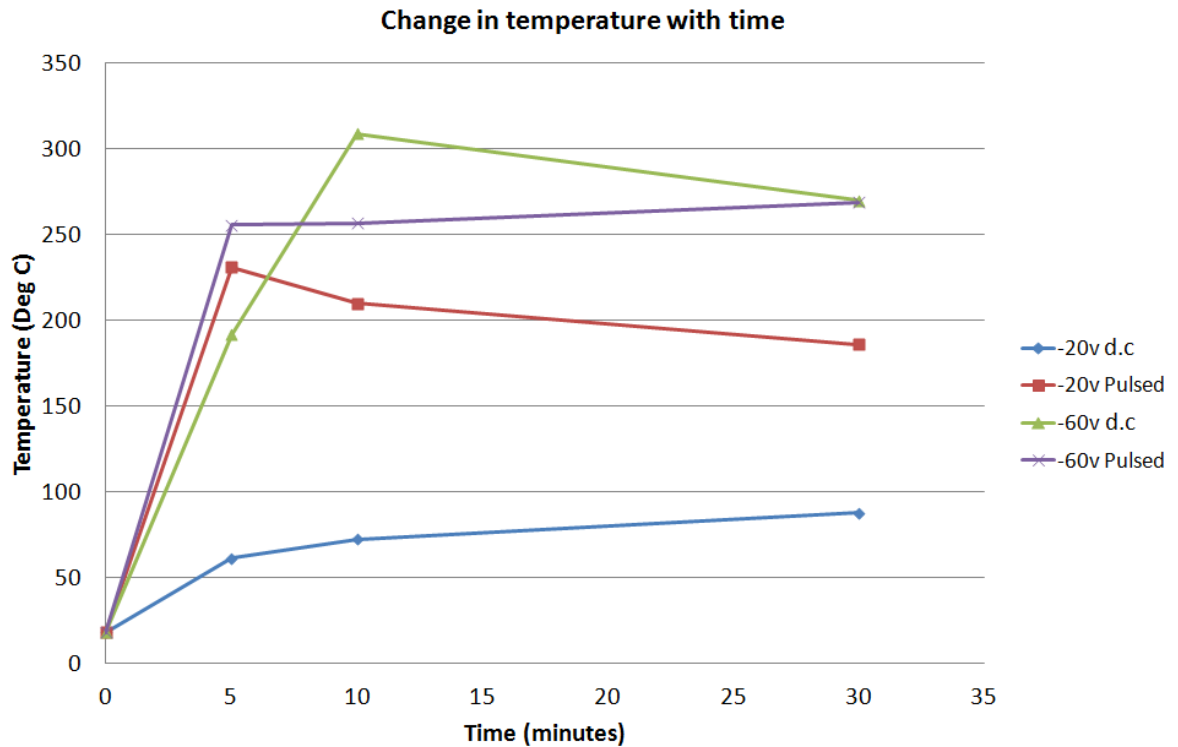


Figure 8.31: The change in substrate temperature with time for two substrate bias values (-20v and -60v) and two substrate bias pulse rates (0 kHz and 175 kHz).

8.4: Discussion:

The AE power supply readings show a greatly increased time averaged current drawn at the substrate during pulsed d.c. biasing, either from increased ion bombardment or increased electron current drawn from the substrate. The current available increases with both pulse rate and substrate bias (figures 8.2 and 8.3), and decreases slightly with increasing reactive gas content of the chamber (figure 8.1). The current also increases with increasing off time (figures 8.4 and 8.5). This suggests that pulsing increases the current drawn, though the power supply readings should not be taken in isolation from more direct measurements. Oscilloscope measurements of the waveform show greater substrate current overshoot, and ringing, as time averaged substrate bias set point increases (figure 8.6).

There are no observable differences between the reactive deposition and non reactive deposition waveforms at a given time averaged set point bias (figure 8.7).

The Langmuir probe measurements provide greater insight: Electron density remains almost constant, with a slight increase between 4 μs and 7 μs , roughly coincident with the end of the pulse (figures 8.8 and 8.11), behaviour consistent between reactive and non reactive modes and showing little variation with substrate bias. The electron density is generally lower biasing at -100V than for biasing the substrate with -70V.

Electron temperature; Langmuir probe measurements show highly energetic, suprathermal, electrons present in the first microsecond after the pulse initiation (figure 8.9 and 8.12). These then cool to form a group of electrons with an elevated temperature, which further cools conventionally. This indicates a secondary electron emission at the substrate due to high energy ions, and fits well with the initially high substrate currents due to positive ions and secondary electrons.

There is a strongly negative potential at the beginning of the pulse (below our -100V detection limit), which then increases to more positive values (figure 8.13), with a significant step at the end of the on time. This follows well with the observed electron temperature. This behaviour is similar in both reactive and non reactive cases.

The plasma potential (figure 8.14) shows positive values of +10 V, but for the period 4 μs to 7 μs , coinciding with the small rise in electron temperature, it becomes negative, with values in the region of -5 to -12 volts. Curiously it appears to be varying slightly offset with respect to the on/off transitions. In d.c. mode the plasma has a potential of -10V. This is contrary to expectations that the d.c. plasma potential should be a low positive value, higher than ground. The positive plasma potential suggests there may be some influence happening from the sheath, although imaging suggests sheath movement is very small – possibly below the limits of detection. Quasi neutrality would suggest an excess of electrons for negative plasma potential, and a small maximum is measured. Plasma potential increases with negative substrate bias, and is independent of plasma composition.

Ion density (figures 8.10 and 8.15) is around 4 times that of electron density, and is low at the beginning of the pulse, followed by a steady increase. This may indicate ionisation occurring near the substrate by injection of energetic electrons. At the point of substrate

bias reversal there is an abrupt jump to higher values, followed by a shallow decrease in the non reactive cases, and a shallow increase in the reactive cases. Ion density is higher for all the reactive runs. This is curious as monatomic nitrogen has a higher ionisation threshold to argon (14.53 eV), and diatomic nitrogen has a threshold in the region of 16 eV.

Spectrometry shows an initial increase in Ar(I) emission (figure 8.16) after the start of the pulse, followed by a decay, relating to the initial increase and decay of electron temperature. Cr(I) emission (figure 8.17) rises less steeply, and stays constant within the on time. Cr (I) emission has a much smaller influence on electron temperature as its excitation threshold is much lower than for Ar (I) (3.4 eV versus 13 eV). Cr(I) emission initially also shows a slower decay than Ar(I) during the off time. Both species show a decrease in intensity towards the end of the off time, consistent with the low electron temperature.

The films analysed so far demonstrate dense structures ranging from the glass-like to dense columnar (figure 8.21). The porous columnar structure is not observed with obvious column heads on the film surface, and so may be an artefact of the fracturing. This would make all the films smooth in texture. SEM cross sections suggest that some d.c. coatings may be thicker than their pulsed deposited counterparts, possibly indicating greater levels of re-sputtering. XRD analysis (courtesy of Sofia University in Bulgaria), of sections of coated steel coupons, show that CrN stoichiometry films deposited by pulsed substrate bias are more oriented, i.e., have a stronger texture (figure 8.17), and both CrN and Cr₂N films have a higher internal (compressive) stress (figure 8.19). This suggests that the higher ion current observed in previous work, attributed to the ignition of a second plasma discharge in front of the substrate, is influencing film growth and structure.

Tribological tests show that for CrN coatings an increase in substrate bias has a greater overall influence on wear (Figure 8.22) and frictional coefficient against a tungsten carbide washer (figure 8.27) than the application of pulsing. However the application of pulsing has an influence on wear rates and friction coefficients at a given substrate bias; at -70V the application of pulsing appears to produce a lower average wear rate over 20 minutes (figure 8.28), whereas at -100V the application of pulsing increases wear rate.

At -70V, applying pulsing increases the critical load of CrN coatings but at higher bias values it significantly decreases it (figure 8.23). CrN hardness is slightly increased by pulsing at -70V but reduced at -100V (figure 8.25).

Cr₂N behaves differently under pulsing than CrN; at both high and low substrate bias the application of pulsing increases hardness but decreases critical load (figures 8.26 and 8.24). Average wear rate increases dramatically under bias pulsing for Cr₂N coatings (figure 8.29), suggesting that adhesive failure is the main mechanism of coating failure under these circumstances. This is supported by optical micrographs of the wear track (figure 8.30) which shows the wear track has a sharp, ragged, edge. Profilometry measurements show this edge to be an abrupt step with a height corresponding to the depth of the coating. Smaller features near the wear track edge appear to be pits with a depth identical to that of the coating. This suggests that, where it has failed, the coating has failed at the substrate-coating boundary and delaminated. It is likely that some amount of the measured wear rate is on the steel substrate, following coating failure.

Measurements of substrate heating (figure 8.31) show that the initial rise in temperature is steepest with substrate bias pulsing applied for both values of substrate bias. However there is a significant difference between the low -20V substrate bias tests and the -60V tests: In the -20V case the pulsed bias run also produced a much higher maximum temperature, whereas in the -60V case the d.c. maximum temperature was higher. The difference in the initial rate of rise was also much larger in the -20V case.

8.5: Conclusion:

The effects of the pulsed d.c. substrate bias sputtering mode on the sputter plasma have been investigated using time averaged power supply readings, Langmuir probe, optical imaging, and optical emissions spectrometry. A significant rise in time averaged current and power at the substrate is observed for high biases and high substrate bias pulse rates. Langmuir probe measurements suggest that a second group of supra thermal electrons are present in the plasma near the beginning of the pulse, and then decay back into the normal thermal electron group. These supra thermal electrons are indicative of secondary electron emission at the substrate due to impinging high energy ions. Sheath movement with the

pulse is almost non-existent (to within the limits of detection— it must collapse and reform as the voltage switches polarity), and the effects of higher substrate bias are to exaggerate events already occurring at lower bias values, as opposed to initiating new plasma events. Overall the influence of reactive gas presence on the plasma is quite small.

Coating microstructure is more ordered in pulsed deposited coatings, and internal stress is significantly higher. Coating structure is more 'glass like' and less columnar when pulsed bias deposited. Coating wear appears to be more influenced by substrate bias than by pulsing in CrN coatings, and pulsing significantly increases wear rate in Cr₂N coating. The effects of pulsing on adhesion and hardness depend on substrate bias in CrN coatings, but increase hardness and decrease adhesion in all tested Cr₂N coatings. The main mechanism of coating failure appears to be loss of adhesion leading to delaminating. This is probably mainly due to the increased internal stress in pulsed deposited coatings. We have begun to identify a region of optimum performance for Cr-N coating deposition, and these results suggest potential for bias pulsing to be used to improve wear performance for both phases of chromium nitride: Bias pulsing can be used to produce a real increase in hardness but has potentially damaging effects on adhesion. It appears that pulsed substrate bias deposition produces real changes in coating properties and microstructure, as well as plasma behaviour, strongly indicating that the increase in ion current is not an instrument artefact.

Chapter 9: Pulsed substrate bias deposition as part of layered coating architectures.

9.1: Introduction:

In order to further the project goal of improving the properties of pulsed bias deposited Cr_xN coatings, the effects of various coating architectures were investigated. The possible advantages of modifying the interlayer depth and the effects of grading the boundary between the interlayer and the main coating were also examined.

Layered coatings were deposited across a range of sputtering conditions, and then analysed by XRD, SEM, EDX, AFM, and standard tribological tests in order to produce a clear picture of the effects on stoichiometry and pulse regime on crystal structures and resulting tribology. Selected coatings were imaged by high resolution TEM, with the kind help of Oxford University. Following this, layering techniques with the potential to control coating stress were investigated [91], using SEM, EDS and XRD to investigate structure, composition, and internal stress.

9.2: Substrate preparation, deposition conditions, and analytical techniques:

Chromium nitride coatings were deposited using a Teer Coatings Ltd. UDP 350 closed field unbalanced magnetron sputtering system, which has been described in detail in Chapter 2. Standard conditions were applied throughout. Coatings were deposited onto 50 mm diameter tool steel (Rockwell C hardness 56) and silicon wafer substrates, which had been polished to a mirror finish using a polishing wheel and 1.5 micron diamond paste. Array 2 was an exception to this where only Si wafer substrates were used. Tool steel substrates were used for scratch testing and nano-indentation, silicon wafers were used for microstructural analysis. The tool steel and {111} silicon wafer substrates were cleaned for 40 minutes in acetone, then methanol, then ethanol using an ultrasonic bath, and ion etched at a target current of 0.3A and a d.c. substrate bias of -650V for five minutes prior to deposition. Apart from array 3, where interlayer depth was varied, a 250nm chromium interlayer was sputtered onto the substrate with no pulsing. Each array was repeated three times and an average value for each data point given, except in the case of TEM analysis where limited time allowed only for a small number of investigations.

The coatings were characterised in terms of their structures and composition using Bragg-Brentano X-ray diffraction analysis, EDX, scanning electron microscopy (SEM, Zeiss Supra 40) and, for selected coatings, transmission electron microscopy. The surface hardness of the coatings was measured by nano-indentation using a Micro Materials Nanotest 100 indenter; 25 indentations in a grid with 25 micron separations were made at a load of 50mN and a mean value for hardness and elastic modulus taken. A Berkovich indenter with a 25 nanometre diameter tip was used. The adhesion of the coatings was characterised by single pass scratch testing. The critical load for total failure was taken as cohesive spallation inside and outside the wear track, or ductile perforation of the film within the wear track.

Selected coatings on tool steel were cut, polished, and acid etched before being set into a conductive resin to provide a SEM cross section.

9.3: Experimental:

Array 1: Layering methods:

The effects of varying both pulse regime and stoichiometry through the coating thickness were investigated. Layering, or grading, has been shown to be effective in modifying coating properties [92]. Three coatings were deposited with various combinations of stoichiometry and pulse regime. Previous results (Chapter 8) suggest that d.c. substrate bias produces generally better adhesion, and pulsed substrate bias produces generally better hardness. Hence the focus was on d.c. deposition followed by pulsed deposition. These were analysed by XRD, and cross section images were taken by SEM. XRD was applied in Bragg-Brentano mode to reveal crystal structure and texture, and in glancing angle mode to screen for surface contaminants (i.e. surface oxidation). Coating 3a was studied using Oxford University's high resolution TEM. Micrographs were taken highlighting the changes in coating structure between pulsed Cr₂N and d.c. CrN deposition regimes. Coatings were deposited to a thickness of 1.75 microns, using standard conditions, a substrate bias of -65V, and a pulse rate of 250 kHz where applicable. Each layer was 750 nm deep, and a 250 nm Cr interlayer was included between layer 1 and the substrate.

Table 9.1: Experimental array 1, designed to contrast the microstructural properties of a range of possible simple coating architectures.

Sample number	Layer 1 description	Layer 2 description	General coating description
1a	d.c. Substrate bias, 40% FMS	Pulsed d.c. substrate bias, 40% FMS	Multilayer, High nitrogen content
2a	d.c. Substrate bias, 60% FMS	Pulsed d.c. substrate bias, 60% FMS	Multilayer, Low nitrogen content
3a	d.c. Substrate bias, 40% FMS	Pulsed d.c. substrate bias, 60% FMS	Multi Stoichiometry, Multi pulse regime

Array 2: Stress control:

Array 2 investigated the potential of layering to mitigate or control internal stress.

Interlayering and layered coating structures have produced reductions in coating stress for other investigators [93], although many of these approaches tend to focus on multi material deposition, e.g. layers of titanium nitride and tungsten [94]. Following the results of array 1; array 2 coatings were deposited in a set layering pattern based on sample 1a from that array. The coatings were deposited using a substrate bias of -65 V. The first layer deposited was a d.c. deposited 250 nm thick Cr interlayer. This was followed by a d.c. deposited high N layer, using an OEM signal of 40% of FMS. Lastly a 250 kHz lower N layer was deposited, with an OEM signal of 60% FMS. The coatings were all deposited to a depth of 2 microns. The variable was the relative thickness of the two bulk coating layers, to reveal possible stress mechanisms at work in this particular architecture. The substrates used were (111) surface textured silicon wafer and tool steel coupons, for XRD analysis and tribological testing, respectively. A cross section of the coating design is shown in figure 9.1:



Figure 9.1: A schematic of the array 2 coatings.

With the kind assistance of Prof Ivanka Iordanova of the University of Sofia, XRD was performed in both glancing angle and Bragg-Brentano mode to reveal both the CrN phase and Cr₂N phase crystal structures. Internal stresses were analysed from the XRD traces by centroid peak displacement of the {200} peak, using the equation:

$$\sigma_1 + \sigma_2 = \frac{E}{\nu} .ctg\theta^{st} .(\theta^{coat.} - \theta^{st})$$

Where: $\sigma_1 + \sigma_2$ (the sum of the parallel to the surface principal stresses); $E=200\text{GPa}$ (Young's modulus); $\nu = 0.21$ (Poisson's ratio); θ^{st} - the Bragg angle for {200} CrN from the standard JCPDS file; $\theta^{coat.}$ - the experimentally evaluated centroid (via fit with Pseudo-Voigt) of the {200} peak.

Table 9.2: Experimental array 2, designed to evaluate the effects of the relative depths of layer 1 and layer 2 on coating internal stress and micro tribology. Layer 1 is a d.c. deposited nitrogen rich layer. Layer 2 is a pulsed d.c. deposited nitrogen poor layer.

Sample number	Layer 1 depth (nanometers)	Layer 2 depth (nanometers)	Ratio layer 1 thickness to layer 2 thickness
1b	350	950	0.368
2b	500	800	0.625
3b	600	600	1
4b	850	450	1.8
5b	1000	200	5.5

Array 3: Influence of interlayer depth:

Investigations have shown that the influence of interlayers and interlayer depth on coating adhesion is significant [95-97]. To find if this holds true for pulsed substrate bias deposited coatings, four coatings of nitrogen rich (40% of FMS) chromium nitride were deposited with interlayer depths of 50nm, 250 nm, 350 nm and 500 nm, and analysed by our standard tribological techniques. The deposition conditions were standard, with a substrate bias of -65V. The interlayer was deposited with d.c. substrate bias and the bulk coating with a bias pulse frequency of 300 kHz. The substrates were circular tool steel coupons. The conditions for the array are listed in Table 3. These coatings were investigated by single pass scratch testing.

Table 9.3: Array 3 coatings. Designed to test the effects of interlayer depth and the application of pulsed substrate biasing to interlayer deposition.

Sample number	Interlayer depth (nm)	Bias setting during interlayer deposition
1c	50	d.c.
2c	250	d.c.
3c	300	d.c.
4c	500	d.c.

Array 4: Influence of grading:

Array 4 investigated the effects of grading the interlayer / bulk film boundary, comparing four coatings with both CrN (40% FMS) and Cr₂N (60% FMS) bulk Stoichiometry. Grading of layer boundaries or interfaces in coatings has been demonstrated [98] [99] to improve coating adhesion. The Cr interlayer was deposited to a depth of 300 nm using a -70 V d.c. substrate bias, followed by the bulk layers using a 300 kHz bias pulse rate. Two coatings had the reactive gas introduced in a graded fashion over ten minutes in increments of ten percent of the difference between 100% FMS and the final signal (so 60% FMS downturn = 4% FMS steps). The bias pulsing was introduced following the final OEM

signal adjustment. Two coatings were not graded, with the bias pulsing introduced following the introduction of the reactive gas. The substrates were circular tool steel coupons. Scratch adhesion testing was applied.

Table 9.4: Experimental array 4, designed to evaluate the effects of stepped grading of the interlayer – coating boundary on coating adhesion.

Sample number	Bulk FMS %	Grading types
1d	40	10% steps
2d	60	10% steps
3d	40	No grading
4d	60	No grading

9.4 Results:

Array 1: Tribology:

The tribology of array 1 coatings was investigated using our standard tribological tests.

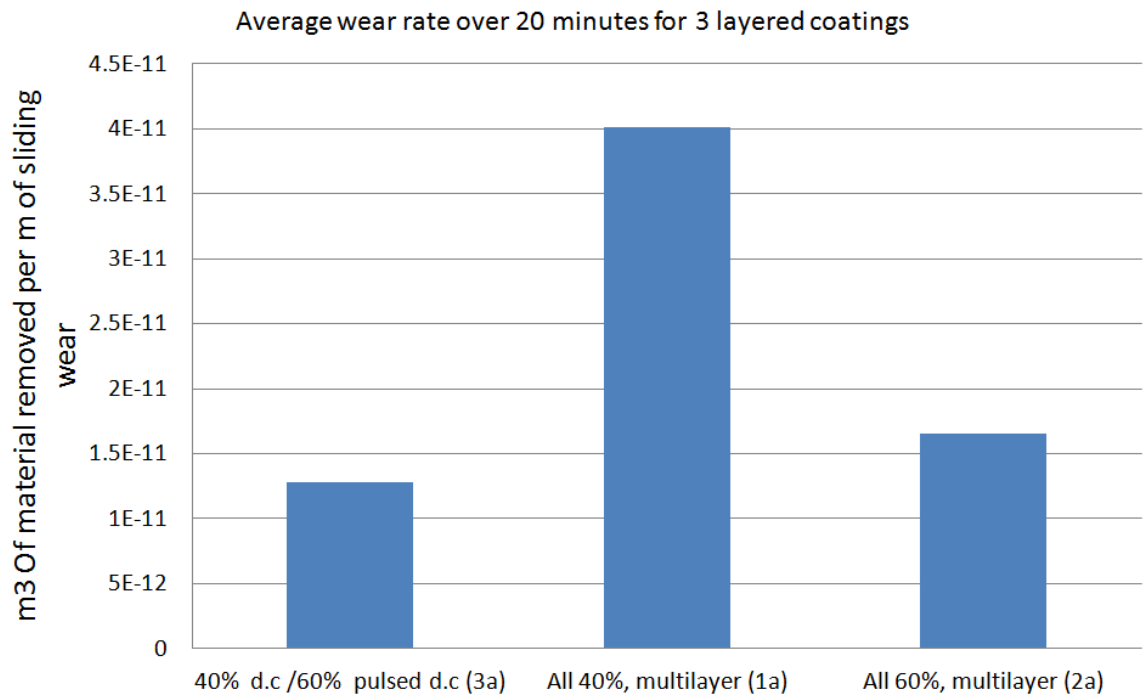


Figure 9.2: Effect of pulse regime and layer stoichiometry on wear rate. The wear rates averaged over 20 minutes, for 3 coating architectures. Rates of wear were calculated by profilometry from 4 random transects of the wear track.

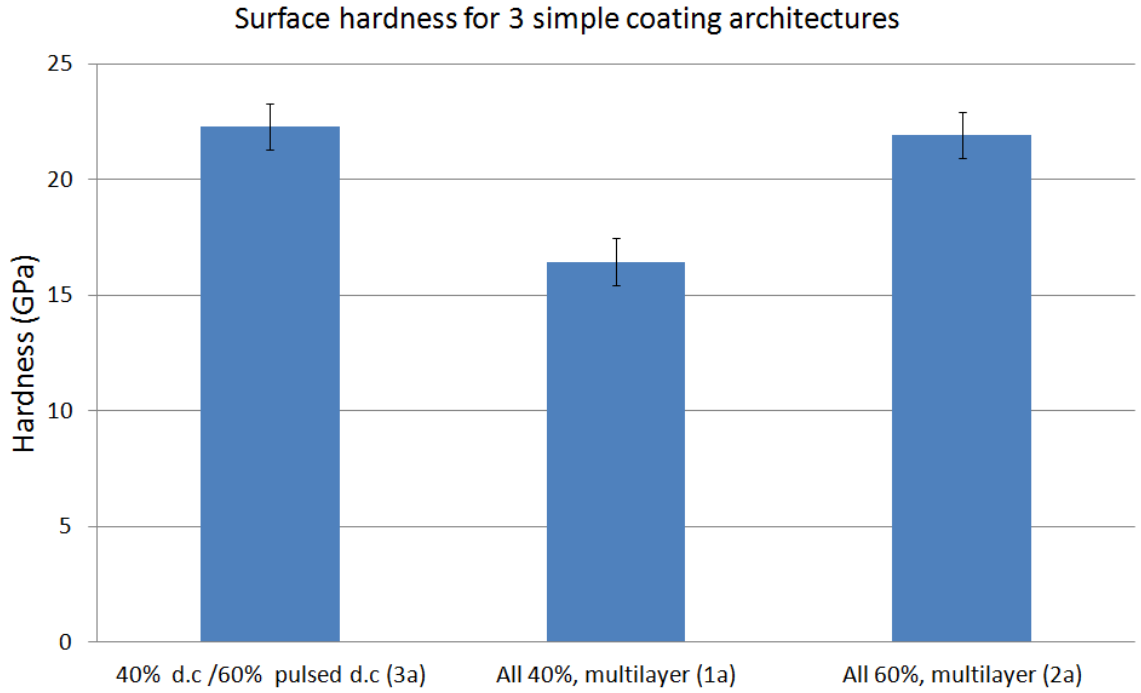


Figure 9.3: Effect of pulse regime and layer stoichiometry on hardness. The surface hardness for 3 coating architectures. Hardness was found by nanoindentation, from a grid of 25 indents with 25 micron separations.

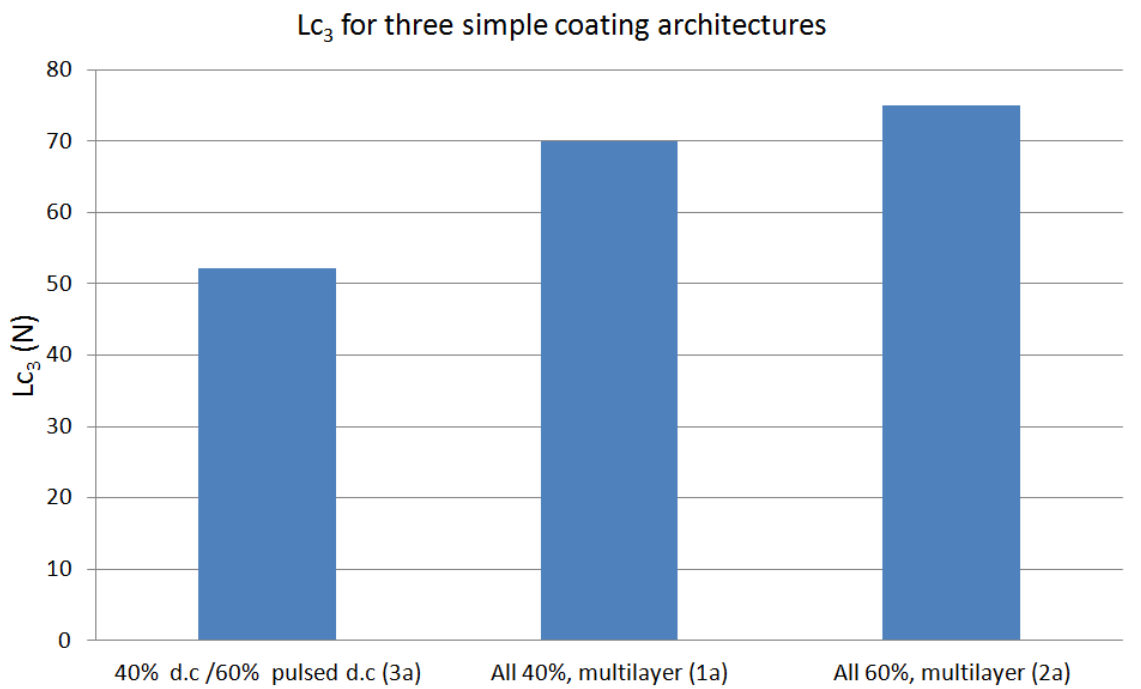


Figure 9.4: Effect of pulse regime and layer stoichiometry on coating adhesion. The critical loads for total failure of 3 coating architectures. The critical loads given are the averaged values of 3 scratch tracks taken at the edges and the middle of the substrate.

Array 1: Microstructure:

The microstructure of the array 1 coatings was investigated using XRD, SEM fracture cross section imaging, and TEM imaging for selected coatings..

Due to the dual phase nature of the array 1 coatings, separating the CrN and Cr₂N phases was not a trivial task. It should be noted that the upper layer will mask the lower layer in XRD analysis. All coatings showed a polycrystalline structure. Coatings 1a and 3a showed peaks indicating the presence of both CrN and Cr₂N. Coating 2a showed only a Cr₂N structure. The crystallographic texture appeared poorly defined in coatings 2a and 1a. In coating 3a the CrN and Cr₂N textures were similar to those found for the d.c. CrN and pulsed Cr₂N coatings examined in Chapter 8. In coating 1a the residual stresses in both phases are compressive and much higher in the Cr₂N phase. In coating 3a the stresses in the Cr₂N are tensile while in the CrN they are compressive which results in an average compressive stress with an absolute value much less than the observed in the other coatings. In coating 2a the internal stress is higher than in coatings deposited by either pulsed substrate bias deposition or d.c. deposition alone (see Chapter 8 for these values).

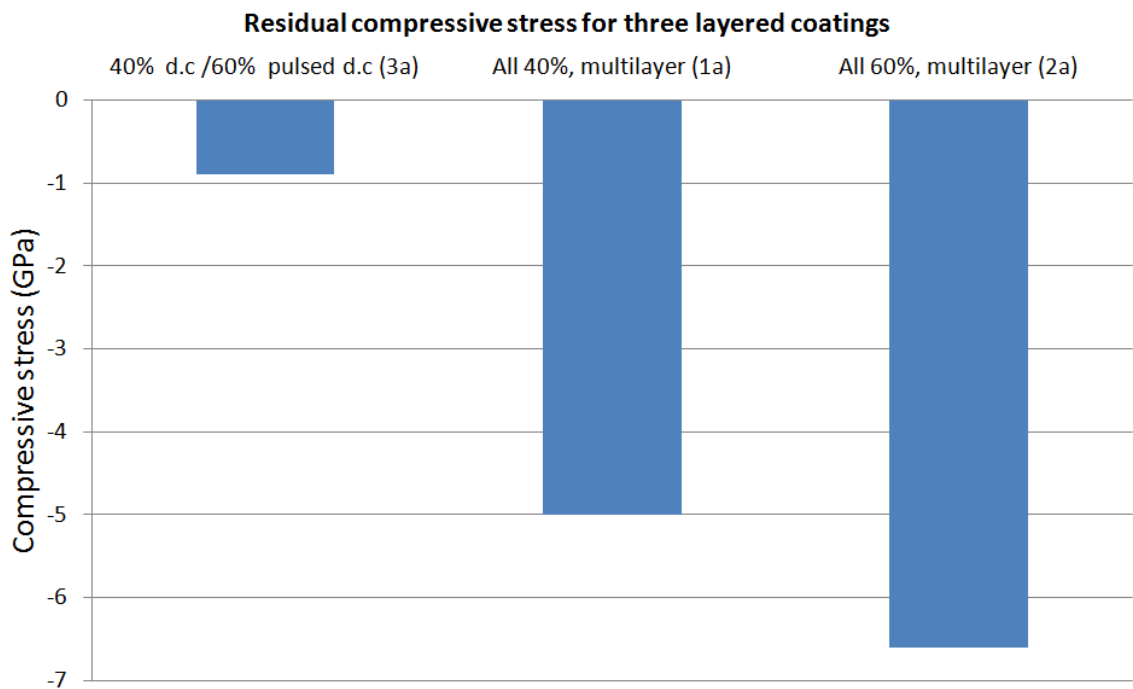


Figure 9.5: Internal stress in array 1 coatings as determined by XRD peak shift.

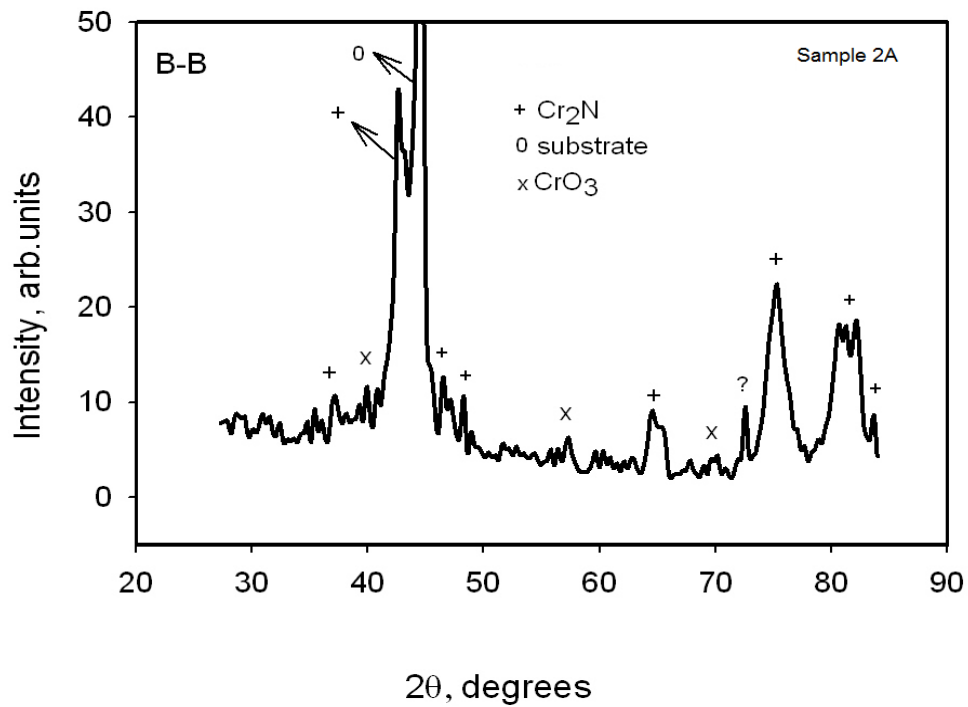


Figure 9.6: Example XRD trace, in Bragg Brentano mode, of sample 2a.

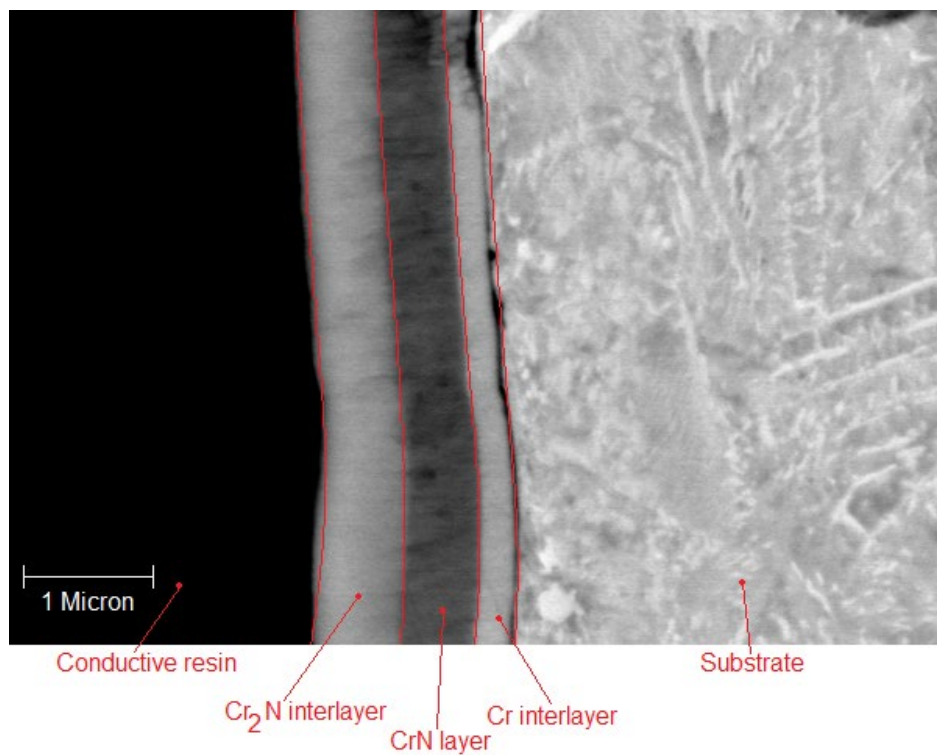


Figure 9.7: SEM micrograph of coating 3a on steel coupon . A section of the coupon was extracted, cut, polished, and set into conducting resin to allow for a true cross section image to be taken. Linear features suggestive of columnar growth extend from the d.c. deposited CrN layer into the pulsed deposited Cr₂N layer for a short distance. Some delamination between the interlayer and the substrate is visible.

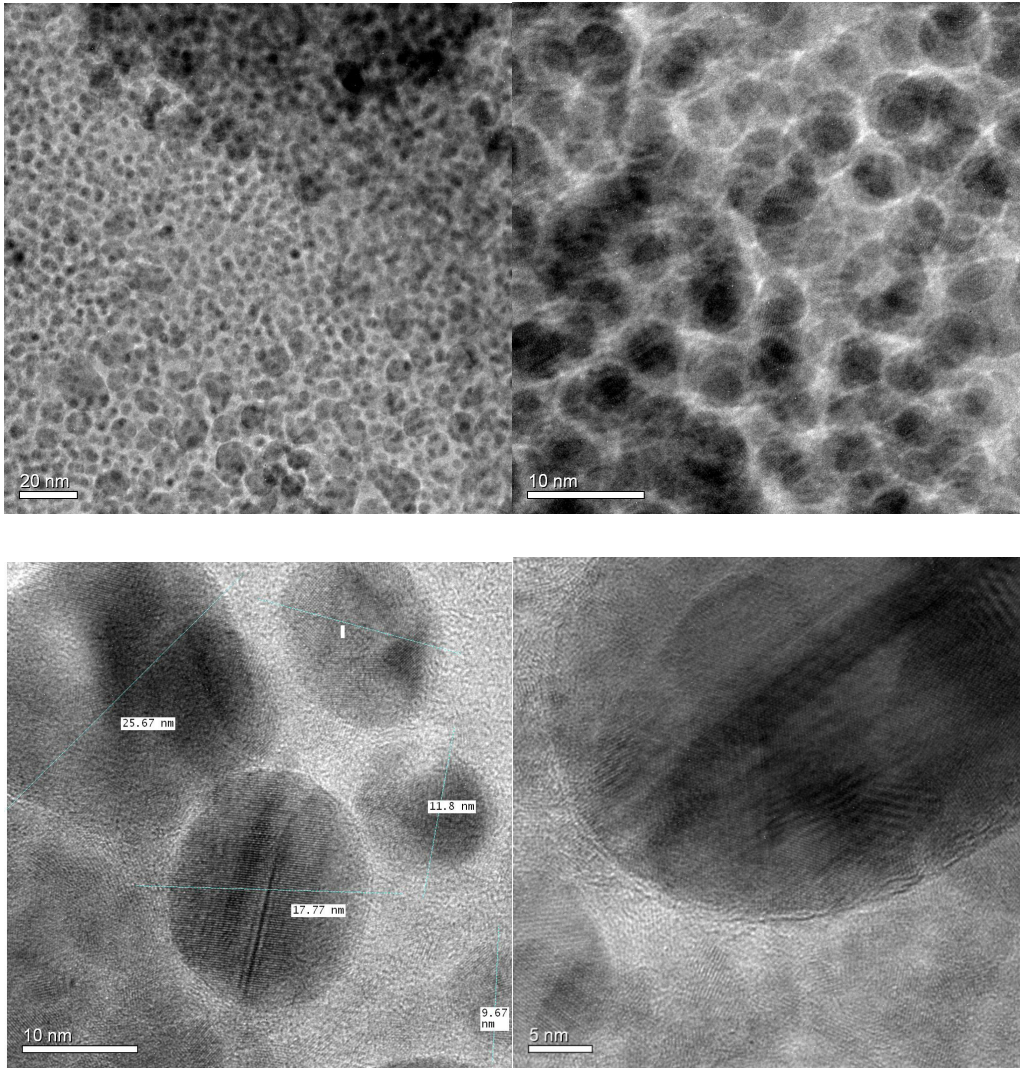


Figure 9.8: High resolution TEM image of sample 3a. Top left: wide angle view of layer 2. Top right: close up of layer 2. Bottom left: wide angle view of layer 1. Bottom right: close up of layer 1. These are cross sectional views of coating sections extracted by focused ion beam milling, hence the visible structures are crystal grains, not column tops.

Array 2:

The crystallography and intrinsic stress of the array 2 coatings was examined using XRD.

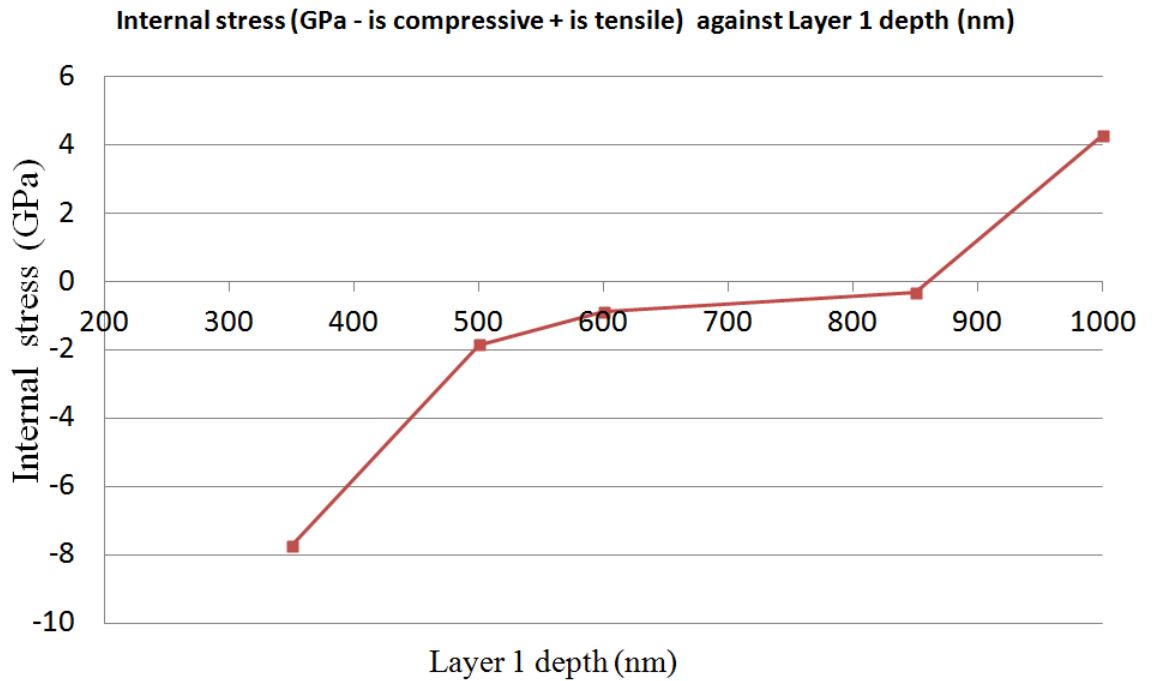


Figure 9.9: Internal stress in array 2 coatings as measured by centroid peak shift.

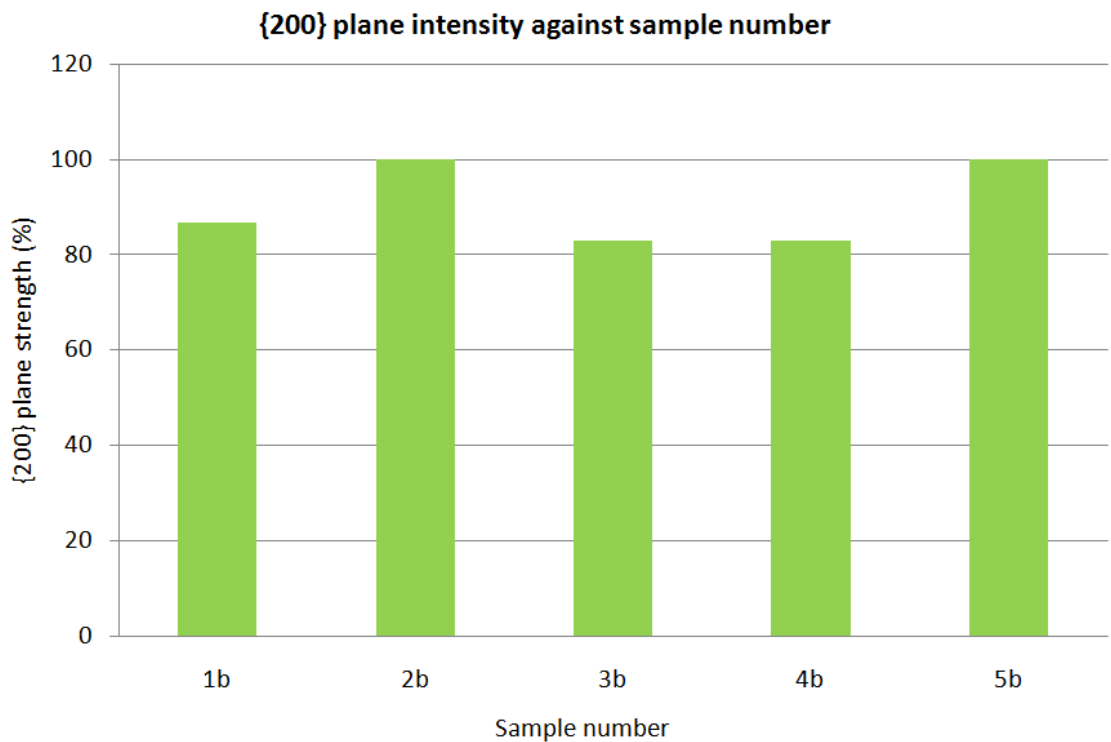


Figure 9.10: The abundance of the {200} in plane texture for each array 2 coating.

Peaks consistent with the presence of both CrN and Cr₂N are seen with polycrystalline Cr₂N being the dominant phase. In all the array 2 coatings a very strong {200} in plane texture has been formed. In the coatings 1b, 3b and 4b {200} very weak peaks namely {220} {311} and {111} are available in the B-B patterns, making up from 13% to 17% of the total texture. This means that for these coatings the {200} in-plane texture, although strongly predominating, is weaker than that observed in coatings 2b, and 5b. In coatings 2b and 5b the {200} is the only peak registered from the CrN phase which points out that within experimental accuracy ($\pm 5\%$) almost all the CrN crystals are oriented so that their {200} planes are parallel to the coating surface.

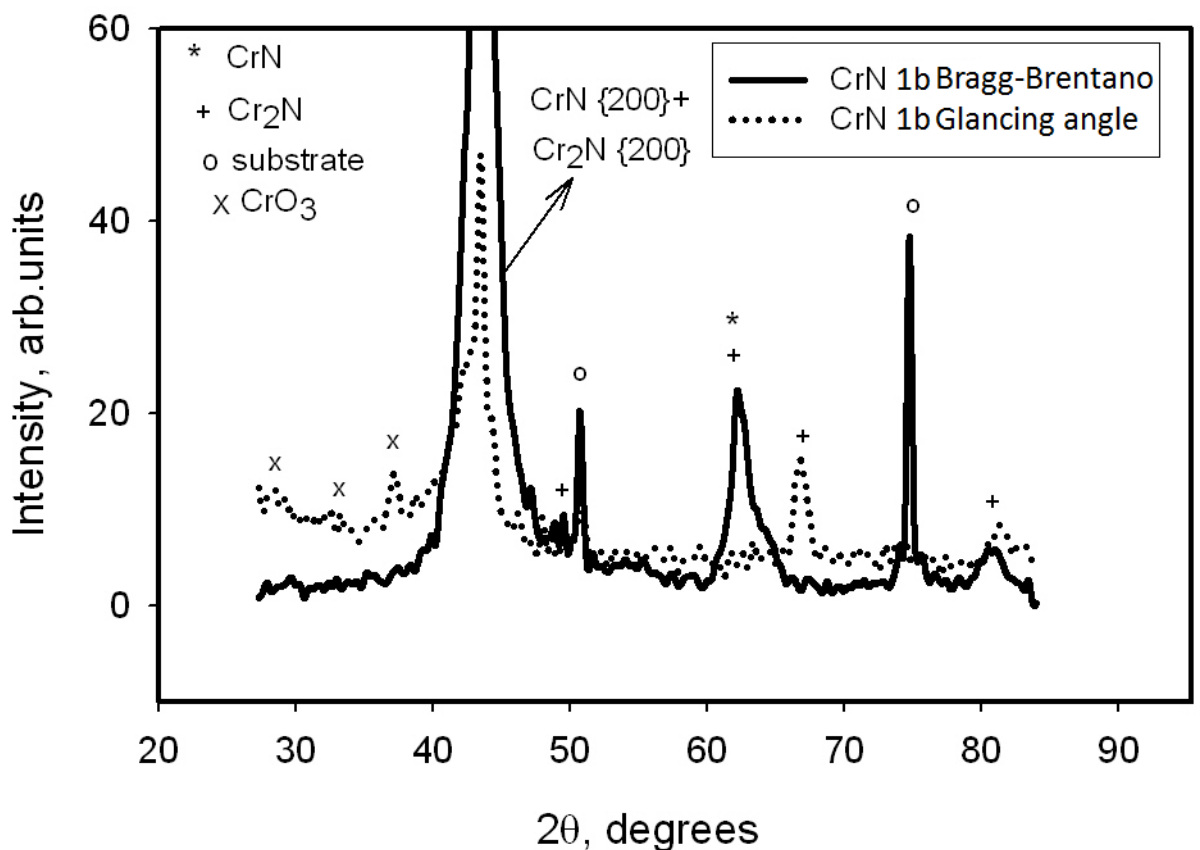


Figure 9.11: Example XRD spectra of sample 1b in Bragg-Brentano and glancing angle mode.

XRD spectra were taken in Bragg-Brentano mode, and in glancing angle mode, in order to screen for the presence of oxides. Oxide peaks were found to be present in the glancing angle spectra, but not the Bragg-Brentano mode pattern, as shown in figure 9.10. This demonstrates that the oxide material is only present on the surface of the coating and not in the bulk.

Array 3:

The change in critical load for total coating failure (L_{c3}) with interlayer depth was investigated, using scratch adhesion testing, and failure modes along the scratch tracks were investigated by optical microscopy.

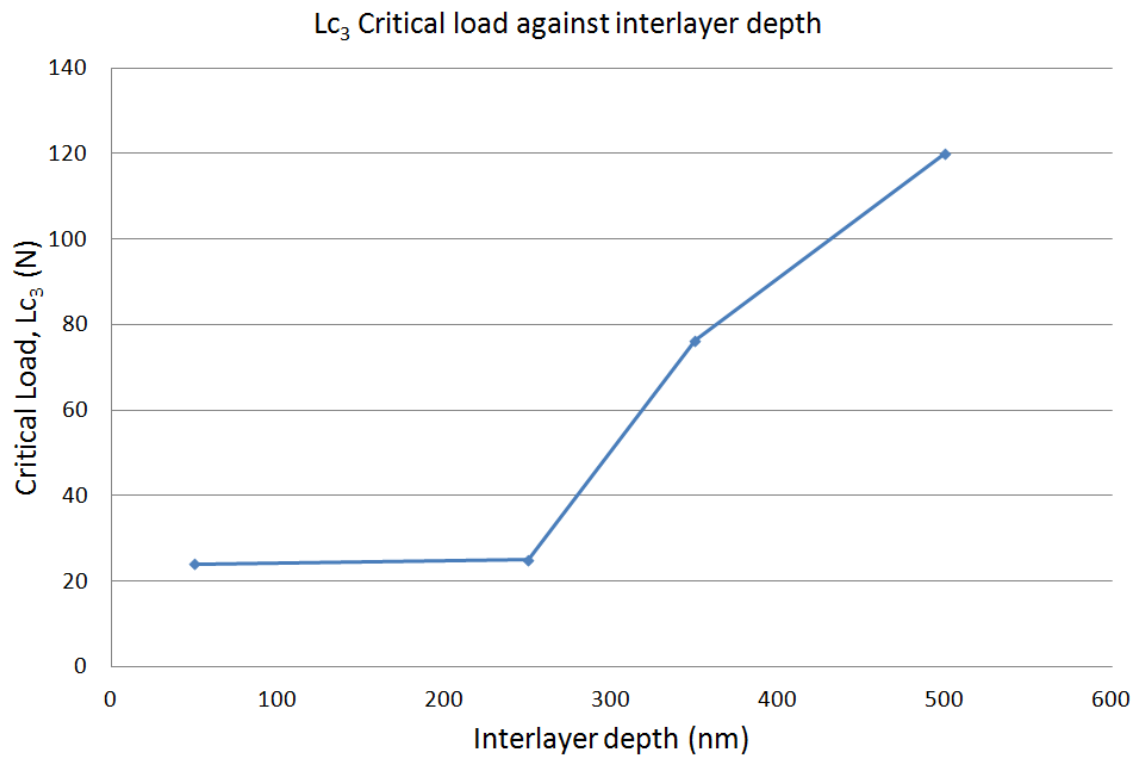


Figure 9.12: Variation of critical load with interlayer depth for films deposited with a bias pulse of 300kHz

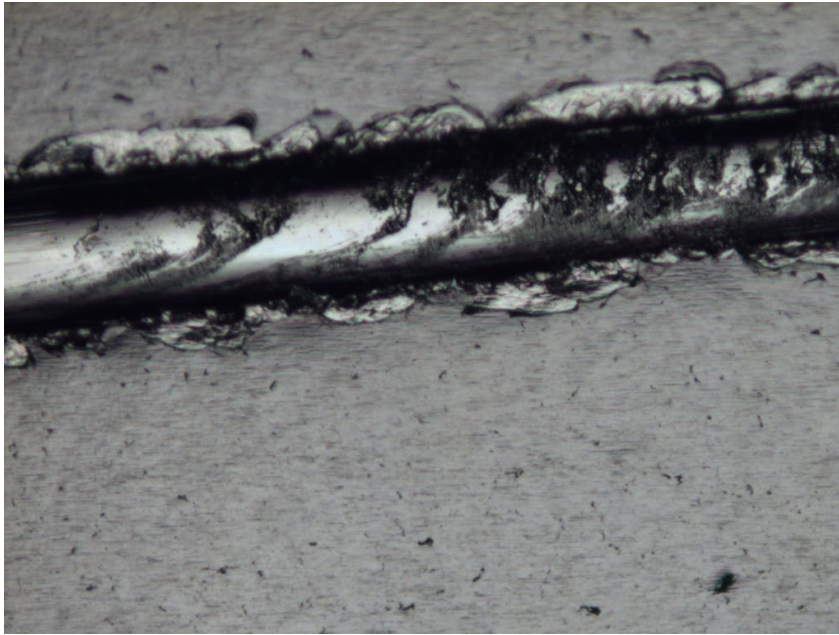


Figure 9.13a

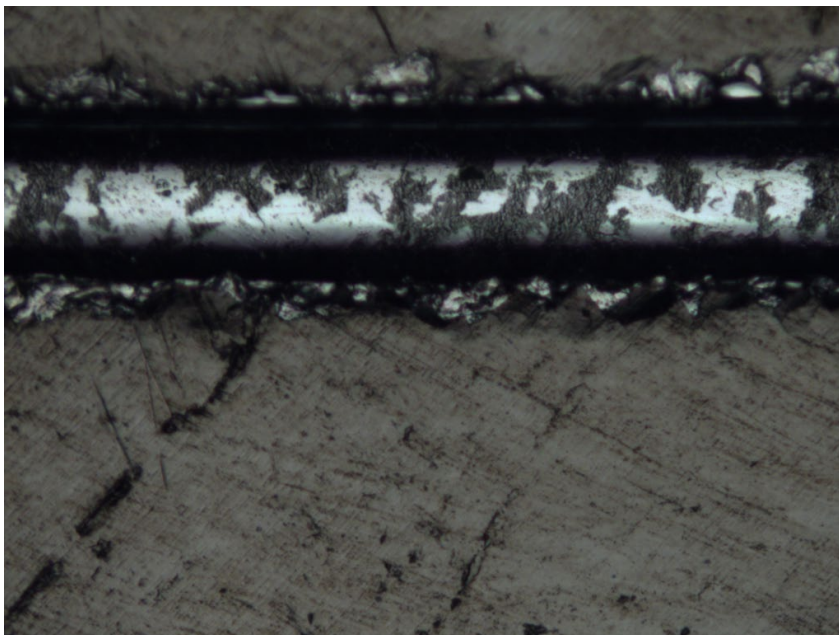


Figure 9.13b

Figures 9.13 a, and 9.13 b: Optical micrographs of the failure points for 50 nm interlayer coating (figure 9.13a) and 500 nm interlayer coating (figure 9.13b).

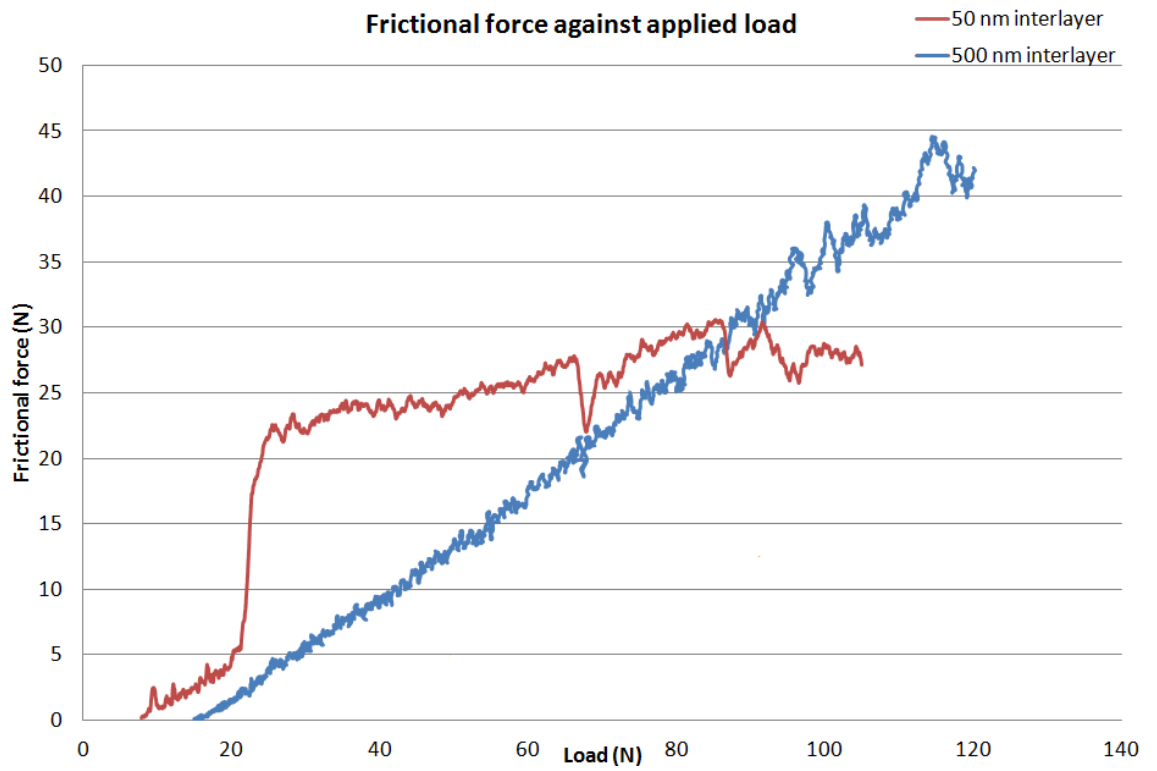


Figure 9.14: The changes in frictional coefficients with applied load, as the scratch tests for coatings with deep and shallow interlayers progress.

Array 4:

The change in critical load for total coating failure (L_{c3}) with the application of interlayer-coating grading was investigated, using scratch adhesion testing.

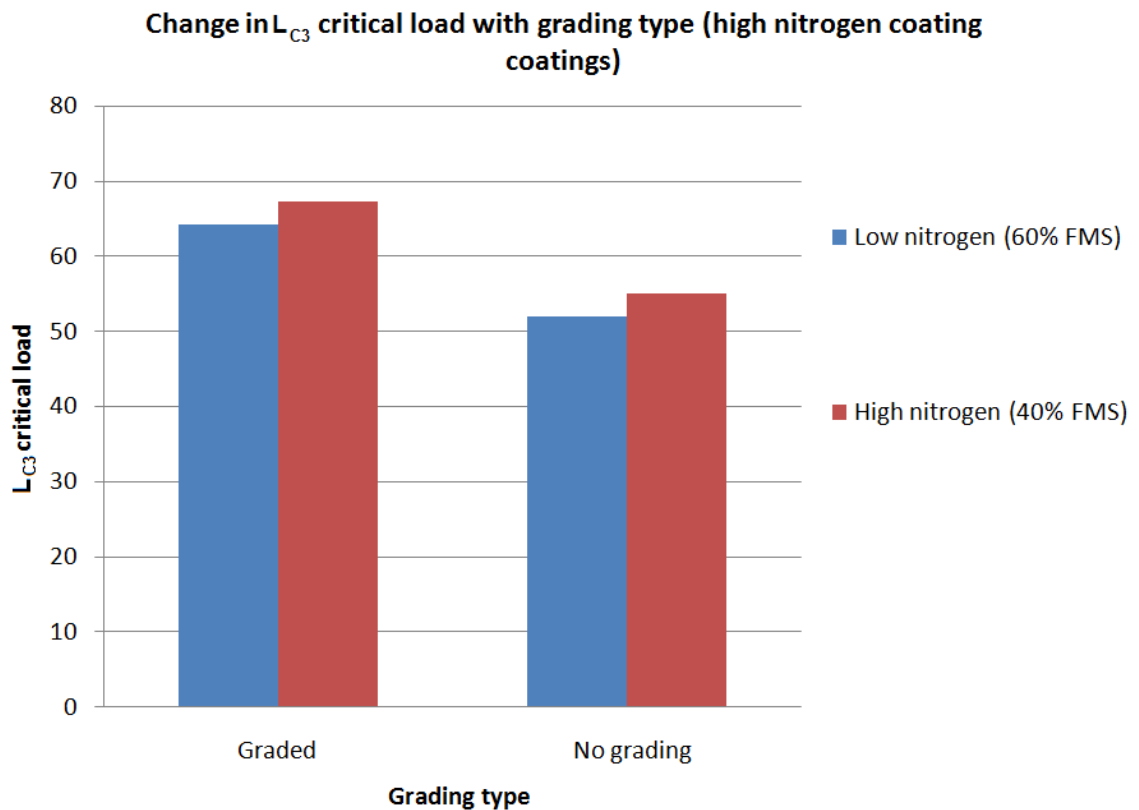


Figure 9.15: Variation in coating adhesion between coatings with a graded interlayer-coating boundary and those with an ungraded boundary.

9.5 Discussion:

Critical load for total coating failure appears to be heavily influenced by coating architectures. In particular the depth of the Cr interlayer and the type of boundary between interlayer and bulk coating are important (Figures 9.12 to 9.15); a deep interlayer with a graded boundary seems likely to provide improved adhesion. Comparison of optical micrographs taken at the L_{c3} points of the coatings with the shallowest and deepest interlayers (figure 9.13 a & b) show the failure modes to be similar. This is surprising as the interlayer material is relatively soft and would not be expected to provide additional load support. Comparison of the changes of friction with load during the scratch test reveals a clear failure point for the shallower interlayer, but a less obvious one for the deeper interlayer (figure 9.14). However optical examination of the track reveals the

coating has failed. Total internal compressive stress also appears to influence coating adhesion (figures 9.4 and 9.5). Surface hardness appears to be an important factor in the overall wear performance of array 1 coatings (figures 9.2 and 9.3). Surface hardness correlates better with overall wear performance than critical load or internal stress and may be the dominating factor controlling wear rate.

The shift from d.c. deposition and 40% FMS to pulsed deposited and 60% FMS shows a marked impact on coating structure (figure 9.7); d.c. deposited layers show signs of a columnar structure, whereas pulsed d.c. layers are smoother in nature. This is consistent with the differences observed in pulsed and d.c. deposited coatings, of identical stoichiometries, in earlier chapters (Chapter 8 figure 8.21). As pulsed deposition begins these columnar structures continue for a short distance into the pulsed layer before petering out, suggesting that the structure of the pulsed deposited layer is being influenced by the underlying d.c. layer. Extremely high magnification TEM images (figure 9.8) reveal that both d.c. and pulsed deposited layers in coating 3a have granular structures on the smallest scales available, with discreet, highly ordered (as determined by fringe counting), grains sitting in a more disordered matrix. This is likely related to the rise in internal stress with the application of pulsed biasing. Although Thornton et al [100] have previously shown that high compressive stresses *can* occur in sputtered chromium based coatings with no significant changes in microstructure, Thornton and other authors have also shown that some components of coating stress are intrinsically present in the crystal structure, (as opposed to thermal stress) [101], and are particularly correlated with grain size and porosity [102], and the accumulation of defects during coating growth [103]. Sergei V Fortuna, amongst others, has related deposition method and grain size to enhanced stress levels, particularly in magnetron sputter deposition [104][105]. Likely stress enhancing mechanisms at work in hard coatings such as those in this study are:

1. Greater initial concentration of lattice defects due to a greater flux of high energy ions during pulsed deposition – especially substitution and interstitial defects.
2. Impedance of the diffusion and movement of crystallographic defects by boundaries between differently oriented and different stoichiometry grains.

XRD analysis of array 2 shows that controlling the relative depths of coating layers may provide a mechanism to control internal compressive stress, or even reverse its nature (figure 9.9). A comparison between spectra obtained in glancing angle and Bragg-Brentano

modes reveals the presence of a surface layer of oxide, but none present in the bulk coating (figure 9.11). All the coatings show a strong {200} plane dominance (figure 9.10), with only small amounts of other planes present, if any. A shallower layer 1 appears to promote greater compressive stress. A deeper layer 1 appears to promote a tensile stress component. However as there is no clear dependence on crystallographic structure we cannot confirm the origin of either stress. There is a clear difference in crystallographic structure between coatings deposited by a combination of d.c. and pulsed bias deposition and those deposited by only one or the other technique. This result suggests that, by controlling coating architectures, overall internal stress can be controlled. Further; the extremely high surface hardness of a high compressive stress coating can be made available with the good adhesion of a relaxed coating, if the correct architecture can be identified.

9.6 Conclusions:

Arrays of Cr_xN coatings have been deposited with layered variations of stoichiometry, pulse regime, interlayer depth, and interlayer boundary grading. The results suggest possible approaches to control internal compressive stress, improve coating adhesion and reduce wear rate. In the next chapter these findings will be used to demonstrate methods of improving coating performance, in wear tests and in real-world applications.

Chapter 10: The effects of internal stress on coating tribology, and drill tests of promising coatings.

10.1: Introduction:

In the previous chapters tribological experiments and microstructure analysis have suggested a number of possible ways to improve the wear properties of Cr_xN coatings. In this chapter it will be shown how these approaches, singularly and in combination, perform in tests approaching a real wear environment. The effects of controlling coating stress by layering are related to tribological and wear performance. Chapter 9 focused mainly on the microstructural and tribological effects of singular features of coating architecture. In this chapter the information gathered on microstructure is tied to effects on tribology by depositing promising coating structures on tool steel coupons and tool steel drill bits, allowing tribological tests and drill tests to be carried out.

The new coatings were modified following the results reported in Chapter 9 to provide the best possible adhesion and wear resistance. These coatings were subject to standard tribological tests, including extensive wear testing. An array of the best performing variations from throughout the course of this project was selected and the coatings deposited onto a series of tool steel drill bits, on which cutting tests into steel ingots were performed.

10.2: Experimental:

Following the results from Chapter 9 all subsequent arrays included the following features:

- Interlayer depth 250 to 350 nm.
- The substrate bias pulsing was not applied until both the ion etching and interlayer deposition were completed.
- Boundaries between interlayer and coating were graded over the course of five minutes.

In Chapter 9 it was demonstrated that internal coating stresses can be modified by controlling the relative depths of pulsed and d.c. deposited layers. To show the effects of changing coating stress on tribology selected coating architectures from Chapter 9 were

deposited onto tool steel coupons for tribological testing in array 1. Array 1 coatings were tested by thrust washer wear testing, nanoindentation and scratch adhesion testing, using identical conditions to Chapter 9.

Although the thrust washer wear test is an excellent indication of wear resistance it is still not identical to a real world application. In order to study how various coating architectures and deposition methods respond to a real world wear challenge, average wear rates from coating architectures (see figure 10.1 below) studied in previous chapters were compared and the five best performing architectures were selected to be coated onto 6mm diameter HSS twist drill bits in array 2. The tool bits were provided by Teer Coatings Ltd., who also provided HSS twist drill bits coated with their standard CrN and CrTiAlN films for comparison. The coatings were deposited to a 2 micron depth. Four drill bits were coated for each coating type. These drill bits were then used to cut 8mm deep holes perpendicularly into an EN9 medium carbon steel (Vickers hardness $190 \text{ Hv} \pm 5 \text{ Hv}$) at 3759 rpm, with a feed rate of 661 mm / minute. The rate of drill failure was found by the number of holes drilled before the power needed to keep a constant rate of bit rotation increased by 25%. This is Teers standard test for coating performance, and was performed in their Droitwich facility. Following the drill tests the drill bit with the failure rate closest to the average for each batch was examined under SEM.

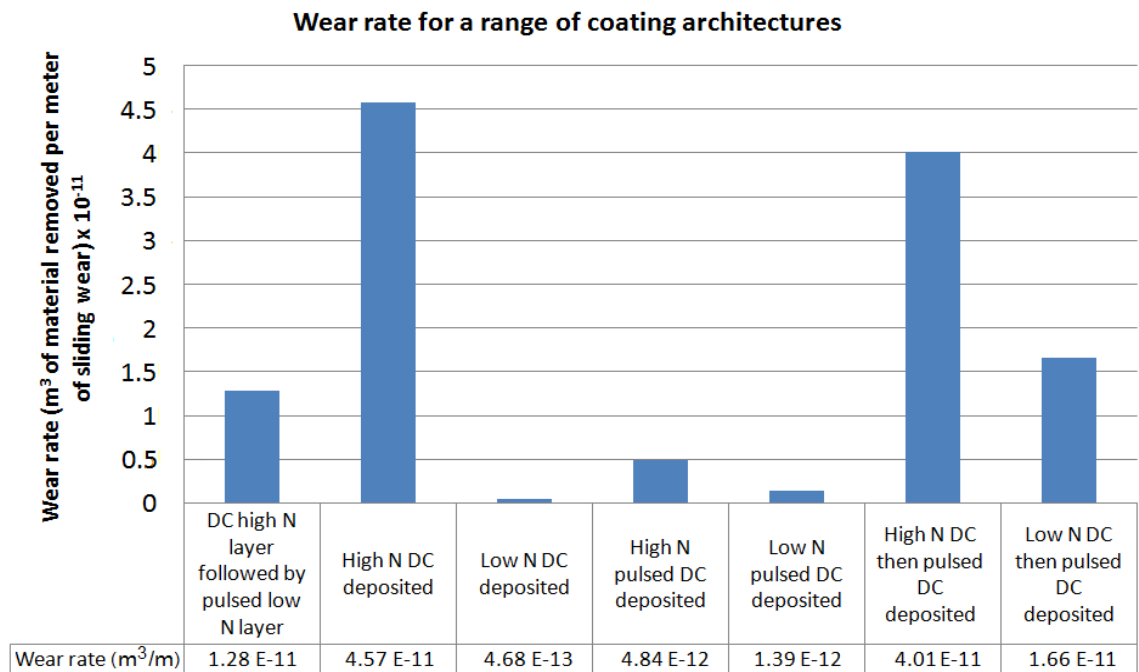


Figure 10.1 : Wear rates for a range of coating architectures deposited during the course of this study.

Table 10.1: Array 1, designed to investigate the effects of relative layer depths on an otherwise fixed coating architecture.

Sample number	Layer 1 depth (nanometers)	Layer 2 depth (nanometers)	Ratio layer 1 thickness to layer 2 thickness
1a	350	950	0.368
2a	600	600	1
3a	1000	200	5.5

Table 10.2: Array 2, coatings deposited onto high speed steel drill bits.

Sample number	Layer 1 description	Layer 2 description	General coating description
1B	d.c. substrate bias deposited, high nitrogen content	Pulsed substrate bias deposited, low nitrogen content	Dual pulse regime, dual layer coating
2B	N/A	N/A	Pulsed substrate bias deposited High nitrogen coating
3B	d.c. substrate bias deposited	Pulsed substrate bias deposited	Dual pulse regime, low nitrogen coating
4B	N/A	N/A	Pulsed substrate bias deposited, low nitrogen content
5B	N/A	N/A	d.c. substrate bias deposited, low nitrogen content

10.3: Results:

Array 1:

The microstructure and intrinsic stresses of the array 1 coatings were investigated, using XRD. The tribological responses of the array 1 coatings were investigated using our standard tribological tests.

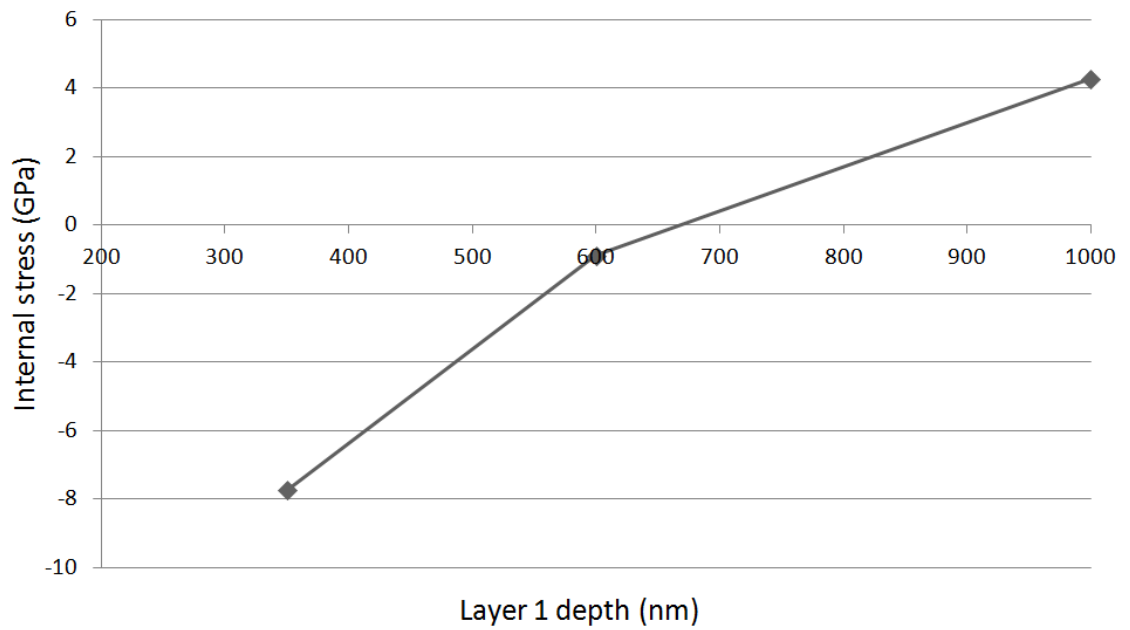


Figure 10.2: Coating stress against sample number, as measured by peak shift of the {200} peak on XRD spectra.

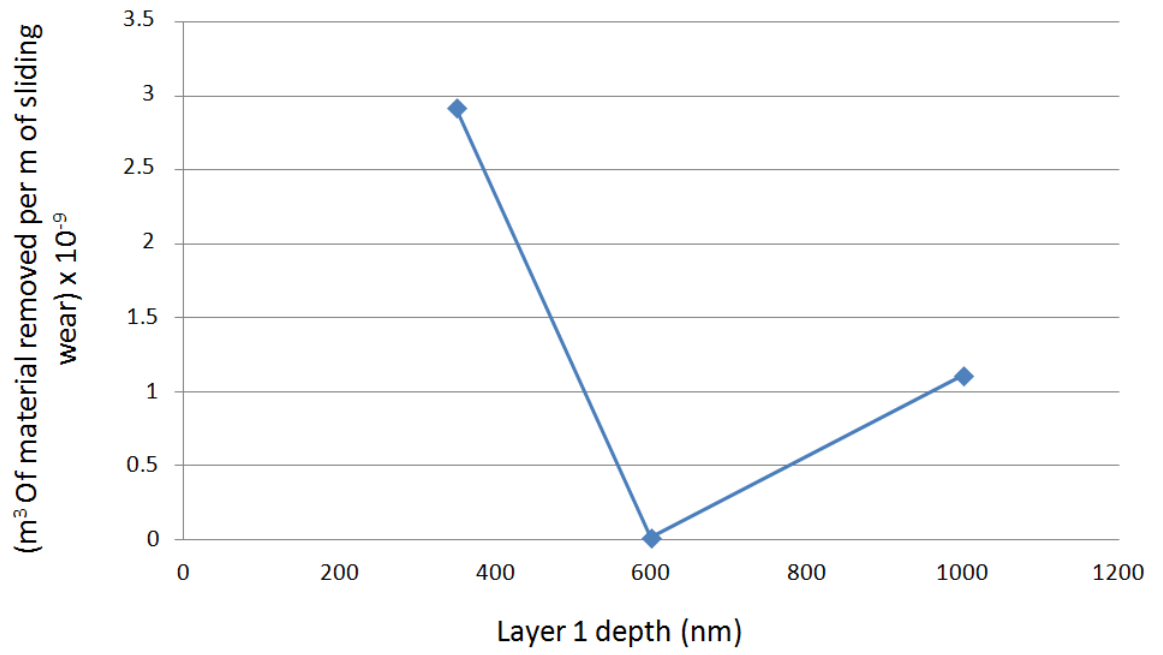


Figure 10.3: Wear rate against layer 1 depth.

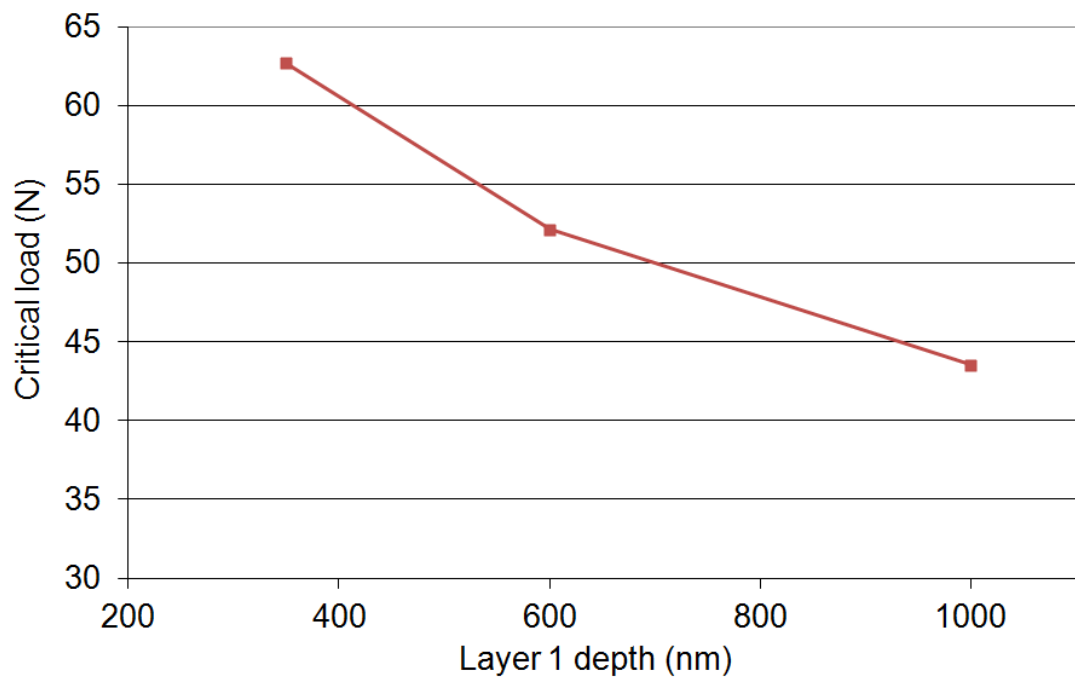


Figure 10.4: Coating adhesion, as found by single pass scratch testing, against layer 1 depth.

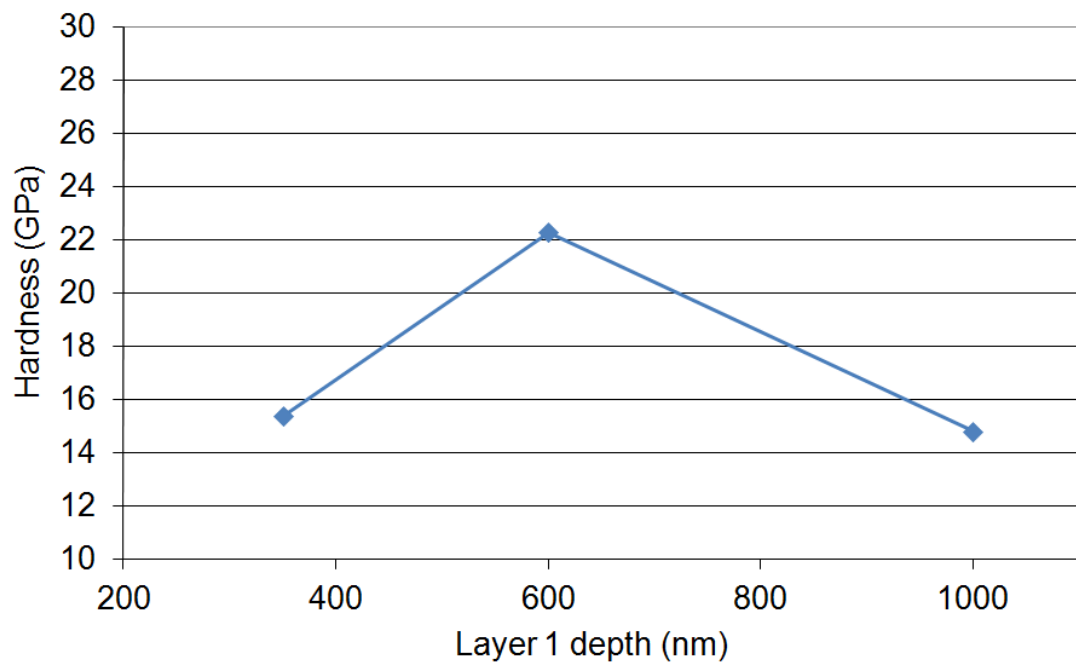


Figure 10.5: Hardness, as measured by the average of 25 nanoindentations, against layer 1 depth. Error bars shown are 1 s.d.

Array 2:

The array 2 coatings, emplaced on high speed steel drill bits, were subjected to Teer Coatings Ltd standard drill testing. The worn cutting edges of the bits were then examined using SEM.

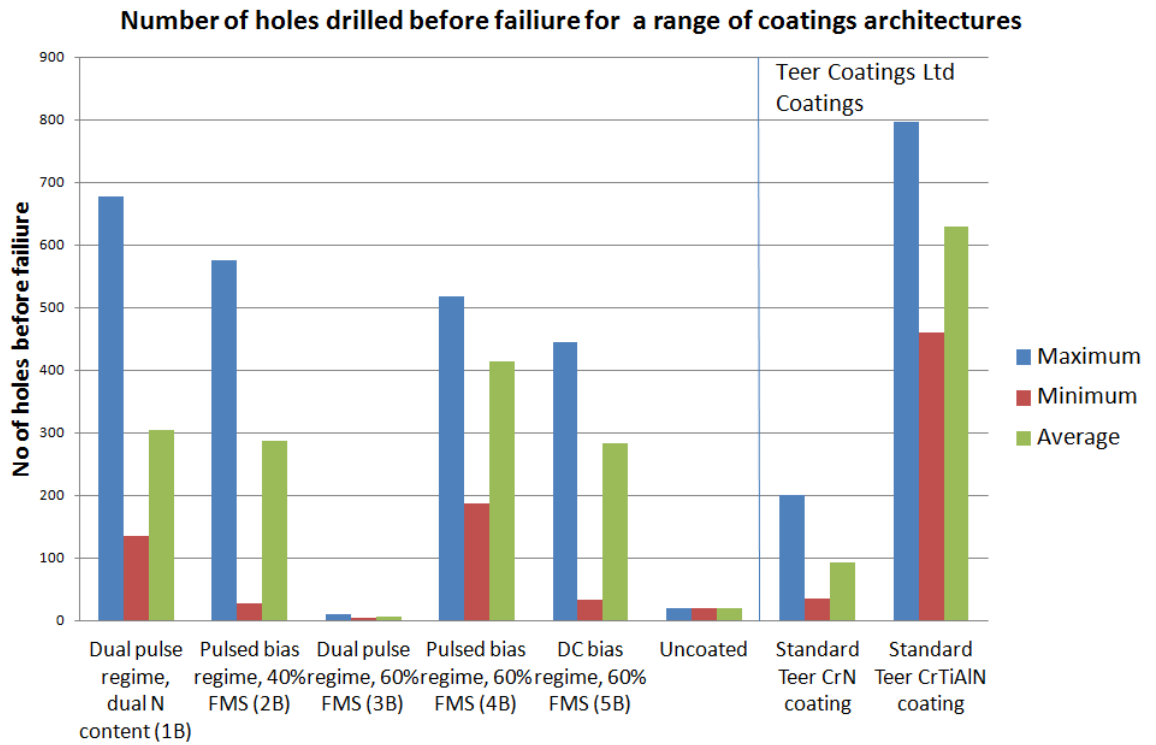


Figure 10.6: The response of the array 2 coatings and three standards (Uncoated drill bits, standard CrN coating, CTiAlN coating) to drill testing. From each set of drill bits tested the minimum, maximum, and average responses are given. Standard coatings were supplied by Teers Coatings Ltd.

Table 10.3: Average drill test values and standard deviation for array 2 coatings and Teer Coatings Ltd standards, and an uncoated control batch:

Coating	Average number of holes drilled before failure	Standard deviation (to 3 s.f)
1B	304	256
2B	286	244
3B	7	3.86
4B	414	153
5B	283	219
Uncoated	20	1.00
Standard Teer CrN coating	92	76.4
Standard Teer CrTiAlN coating	629	238

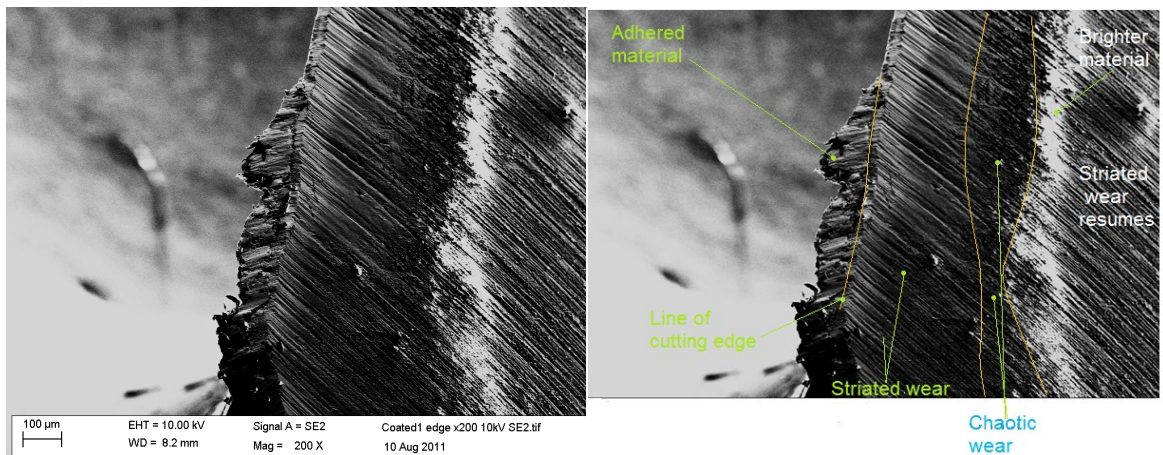


Figure 10.7: SEM micrograph of the cutting edge of drill bit with coating 1b, post failure. Left, raw image, Right annotated.

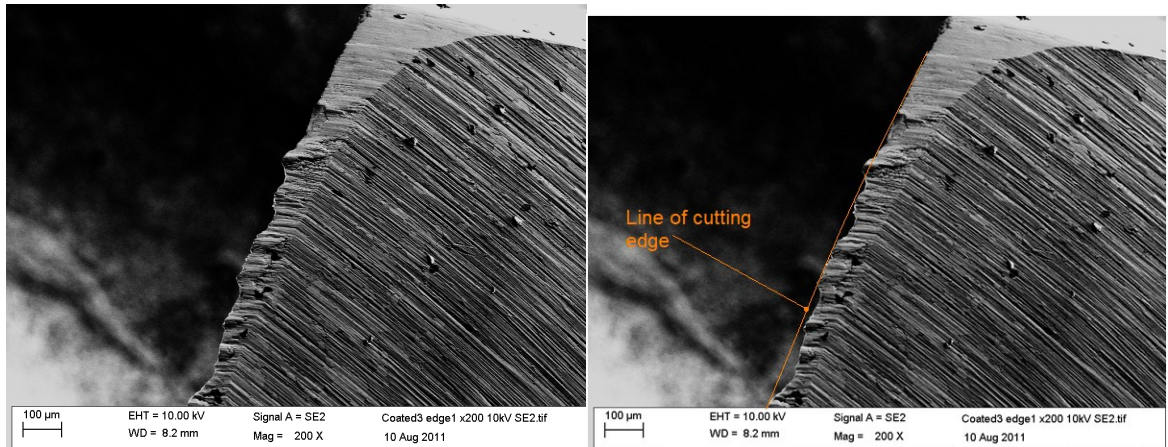


Figure 10.8: SEM micrograph of the cutting edge of drill bit with coating 3b, post failure. Left, raw image, right annotated.

10.4 Discussion :

It has been noted by previous authors that Cr_xN multilayer coatings incorporating a Cr_2N layer provide a better hardness than monolithic or CrN/Cr coatings [151]. Warcholinsky et al suggest that the Cr_2N phase is more prone to developing Cr oxides at wear faces, which has a significant effect upon wear rate [109]. This appears to be partly confirmed by figure 10.1 which demonstrates that Cr_2N stoichiometry coatings universally outperform their CrN stoichiometry counterparts.

However surface chemistry does not account for the range of results obtained here. Array 1 shows good correlations between rate of wear, magnitude of internal stress, and coating hardness (figures 10.2, 10.3, and 10.5). The correlation with surface hardness is the opposite from that suggested by the idea that compressive stress contributes to coating hardness. Instead both higher stress coatings are somewhat less hard than the more relaxed one, and also have poorer wear rates. From figure 9.12 we know that there is relatively little variation in coating crystal orientation with changing stress and layer depth – all coatings being massively or totally dominated by the $\{200\}$ plane. Coating adhesion appears to drop with increasing layer 1 depth (figure 10.4) and shows no strong correlation with stress or crystal orientation (figure 9.12).

Array 2 shows some interesting and surprising results: There is considerable variation within the tested batches, including the standard products to which the project coatings were compared. The two highest average wear resistances (coatings 1b and 4b) also show

the highest minimum wear resistances. These are: 4b the low nitrogen pulsed substrate bias regime, and (1b) the multi Stoichiometry multi pulse regime coating. The minimum cutting performance of these coatings approaches the best performance of the standard CrN coating.

The SEM images of the cutting edges of batch 1B drill bits appear to show them relatively intact with extra material, presumably from the work piece, attached. The line of the cutting edge is visible continuing beneath the adhered material, which extends away from the edge at a sharp angle. To the right of figure 10.7 the drill bit appears to darken, then the texture of the wear changes from parallel striations to a much more broken and chaotic appearance. This region also appears to contain more small particles sitting on the surface. There is then a much lighter toned area where the striated pattern resumes. The changes in apparent brightness may well be reflections of changes in the conductive properties of the material. The changes in the material may also be reflections of changing density, however this seems less likely as the density of steel typically lies between 7,750 and 8,050 kg/m³ which is considerably denser than either CrN or Cr₂N (at 5900 kg/m³ [150] and 6539 kg/m³ [149] respectively) and so should appear brighter than either if density were dominant factor in determining appearance in the SEM. That the changes in brightness appear to coincide with changes in wear pattern supports the hypothesis that we are observing materials with different mechanical and electrical properties – ie the edge of a section of intact coating, although the lighter toned area could also be fine iron particles stuck to the drill surface. It is apparent that the coating has worn away from the edge at a very shallow angle. The chaotic wearing of the darker layer is consistent with the softer d.c. deposited CrN lower layer of the coating being less ordered.

Coating 3b, dual pulsing regime low nitrogen content, performed less well than even the uncoated drill bits. Comparison of SEM micrographs of coating 1b to coating 3b shows an original cutting edge that appears broken into, as material has been removed in scalloped bites from the edge. The tone and texture of the material near the edge is consistent, showing no signs of any remaining coating. This suggests that coating material has been removed from 3b more rapidly and in greater quantity, allowing the underlying substrate to reach a more eroded state more quickly.

The lack of coating suggests an explanation for the poor wear performance of this architecture. Despite the coating's good performance in previous tests the drill tests differ significantly, particularly in the temperature at which the wear is taking place. It has been shown that the Cr_2N phase oxidises at around $500\text{ }^\circ\text{C}$ [110] and that as oxidation proceeds it results in increased surface roughness and grain size [111]. This, combined with the relatively high internal stress of this coating architecture, may have rendered the coating more vulnerable to removal under the high temperature conditions of the moving drill bit cutting edge. This would enhance wear by introducing abrasive scales of Cr_2O_3 to the cutting edge.

10.5 Conclusions:

Tool steel drill bits were coated with five of the best performing wear resistant architectures from the course of the project. They were then tested by repeatedly drilling into tool steel ingots at fixed cutting conditions. All of the coatings except 3b compare favourably with the standard CrN d.c. deposited coating. Coating 1b shows a maximum wear resistance that compares well with the maximum wear resistance of TiAlN coatings. Coating 4b shows an average and minimum wear resistance that compares well to those of TiAlN coatings. Coating 3b was outperformed by the uncoated drill bits, suggesting that this coating enhances wear rate under drill test conditions. These results demonstrate that the wear performance of Cr_xN coatings can be greatly improved by the application of substrate bias pulsed deposition, and most improved by the application of that pulse regime in specific layers as part of a more complex overall nano-architecture.

Chapter 11: Overview and discussion.

11.1: Introduction:

The objectives of this project were:

- To study the relationship between the power supply input parameters, the plasma chemistry within the chamber, and the properties of the deposited coatings.
- To test and validate the application of pulsed magnetron sputtering and pulsed substrate biasing to produce hard wearing Cr_xN coatings.
- To define optimum conditions for the production of Cr_xN .
- To measure the performance of PMS deposited Cr_xN coatings against those deposited by similar sputter deposition methods.

It is fair to say that the development of Cr_xN coatings is an ongoing story, which has progressed much since the turn of the millennium [112] [113], and Cr_xN has been known as a promising material for surface protection for some time before that [114]. Cr_xN coatings have become something of an industrial standard [115] but means of enhancing the deposition process and coating properties are, of course, still being sought even as newer coatings (eg CrTiAlN) [116] begin to make an impact. This is due in part to the maturity and proliferation of reactive sputter technology, and in part to the excellent wear properties of Cr_xN .

The chief interest in Cr_xN began as a search for a coating with tribological properties reaching or exceeding those of TiN but with better thermal stability [117], for high speed dry machining. Following a number of experimental and industrial successes [118] it became a popular alternative/companion coating to TiN .

Pulsed magnetron sputtering was initially developed as a means to reduce arcing [119] but quickly showed promise as a means to control coating properties by enhancing ion current and ion energy at the substrate [120] [121]. Here an overview of the key project findings is presented and discussed.

11.2: Hysteresis and ion chemistry:

Main results:

- The Cr-N sputter system shows little sign of conventional hysteresis, either in d.c. or in any pulse regime (figures 7.11 to 7.13).
- Changes in target bias with reactive gas content can be correlated with changes in coating microstructure (figures 7.9 to 7.13). At lower N₂ flow rates mixed phase Cr₂N/CrN is deposited. Within the target poisoning region CrN is deposited.
- Target poisoning starts between 5 SCCM to 7 SCCM (50% to 70% of FMS) of N₂ inflow (figures 7.8 to 7.11).
- Substrate bias pulsing frequency has an effect on the stoichiometry of coatings (figure 7.10).
- Pulsed substrate bias operation enhances substrate current (figures 8.2, 8.3, 8.4, 8.5).
- Plasma analysis is consistent with the enhanced current being related to highly energetic ions bombarding the substrate (figures 8.9 and 8.12).

The Cr-N sputter system shows little sign of conventional hysteresis, either in d.c. or in any pulse regime:

As discussed in Chapter 7, and noted by other investigators, the hysteresis of the Cr-N sputter system is negligible in any pulse regime [122]. Study of the change in target bias with N₂ inflow reveals a unique ‘double maxima’ pattern (figure 7.11). No other bias pulse regimes (e.g. dual cathode pulsing) show this pattern, although none show evidence of hysteresis either. Instead, for all pulse regimes employing pulsing at the target, after a maximum around 4 SCCM to 6 SCCM the target bias drops relatively sharply into the poisoning region (figure 7.11).

The overall lack of hysteresis behaviour suggests that Cr / N reactive deposition may be easier to control than many oxide systems. However the changes in nitrogen partial pressure and other readings over time (figures 7.4, 7.5 and 7.6) show active control is still needed.

Changes in target bias with reactive gas content can be correlated with changes in coating microstructure. At lower N₂ flow rates mixed phase Cr₂N/CrN is deposited. Within the target poisoning region CrN is deposited.

Using EDS and XRD to examine microstructure, this study and others [123] [124] have linked the nitrogen inflow rate, and hence the hysteresis, to the Stoichiometry and crystal structure present in the coating [125] (figure 7.9 and 7.10). The first maxima (which occurs around 5 SCCM to 7 SCCM of N₂ inflow or 60% of FMS) in target bias correlates with the deposition of mixed Cr₂N and CrN structures. The second maxima (at 9 SCCM to 12 SCCM or 40% FMS) is correlated with the deposition of mainly CrN structures, and beyond this point CrN crystallography dominates. Knowledge of this allows the phase of Cr_xN being deposited to be controlled precisely, and linked to sputter plasma conditions. This could allow the phase of chromium nitride being deposited to be inferred from the target bias, although this would not be trivial as target voltage changes as the target becomes more eroded.

Target poisoning starts between 5 SCCM and 7 SCCM (70 % to 50% FMS respectively) of N₂ inflow:

The change in N₂ partial pressure, with N₂ flow rate and with time across a range of flow rates, (figure 7.8) suggests that target poisoning only begins in earnest above 5 to 7 SCCM of N₂ inflow (equivalent to an OEM signal of 60% to 70 % FMS). It is only after this point that adding more reactive gas to the system leads to a sharp rise in pressure, suggesting that the gettering action of the chamber surfaces is no longer able to remove it. This is supported by the changes in coatings deposited around this point: As discussed above 5 to 7 SCCM is also the last point at which coating stoichiometry is roughly Cr₂N (figures 7.9 and 7.10).

Substrate bias pulsing frequency has an effect on the Stoichiometry of coatings:

It is apparent that, at low N₂ contents at least, the rate of substrate bias pulsing has some influence over stoichiometry (figure 7.10). A higher pulse rate appears to reduce the nitrogen content of coatings deposited at low N₂ flow rate. At higher inflow rates (above 4 SCCM or 80% FMS) any differences in stoichiometry between coatings deposited at different bias pulse rates are small.

It is possible that the introduction of highly energetic ions during pulsed substrate bias deposition (see Chapter 8, figure 8.9 and discussion below) preferentially re-sputters N₂ out of the growing coating at a greater rate than it can be replaced at low N₂ inflow rates. This is consistent with the dependence of coating stoichiometry on bias pulsing frequency; the observed increase in the total current and power received at the substrate at higher bias pulse rates (figures 8.2 and 8.3) would lead to greater levels of re-sputtering.

Pulsed substrate bias operation enhances substrate current:

Our preliminary investigations showed that the increase in current at the substrate during pulsed substrate bias operation is chiefly dependent upon three factors: substrate bias, bias pulse rate, and pulse duration (figures 8.2, 8.3, 8.4, 8.5). There is also a small influence by reactive gas content of the sputtering atmosphere (figure 8.1). The maximum current is available when no reactive gas is present, when pulse rate and bias are maximum, and duty cycle is at 50%.

The Langmuir probe and spectrometry revealed suprathreshold electrons and thermal electrons at the beginning of the pulse (figure 8.9 and 8.12), which are most likely linked to higher energy ions striking the substrate. Consistent with this, XRD, SEM cross sections, and EDS show changes to pulsed deposited coatings beyond what would be expected of simple heating due to a higher electron current; smoother texture, more ordered crystallography in a different orientation (figure 8.18, 8.19 and 8.21), changes in stoichiometry at lower nitrogen levels and higher internal stresses (figure 8.20). Changes occur in both high and low N stoichiometry coatings, across the range of substrate bias values examined.

Plasma analysis is consistent with the enhanced current being related to highly energetic ions bombarding the substrate:

Study of the plasma processes using spectrometry and Langmuir probes, at a distance of 1cm from the substrate along the line joining substrate and target centre points, suggests that a group of high energy ions is present near the substrate immediately after pulse initiation: During the first microsecond after the pulse initiation (figure 8.9) electron energy is suprathreshold. These then cool conventionally. This is consistent with a secondary electron emission at the substrate due to high energy ions, and fits well with the initially high substrate currents due to positive ions and secondary electrons. Ion density (figures 8.10 and 8.15) is around 4 times that of electron density, begins low and steadily grows, likely indicating ionisation occurring near the substrate by injection of energetic electrons.

Our plasma findings are also consistent with substrate bias pulsing promoting greater density of ion species over neutrals.

11.3: Deposition and testing of simple coatings:

Main results (figures found in appendices A and B are prefixed with those letters):

- Pulsing promotes a more ordered crystal structure and microstructure in both chromium nitride phases, and changes crystal orientation in Cr₂N (figures A.1, A.3, A.5, A.7, A.9, 8.21).
- Substrate bias pulsing causes greater compressive stress in both phases of chromium nitride (figure 8.2 and section 8.3).
- The cubic CrN phase is more prone to compressive stress (figures A.1, A.3, A.5, A.7, A.9, 8.20).
- Substrate bias pulsing improves the wear resistance and hardness of Cr₂N coatings, it only improves the wear resistance and hardness of CrN coatings at lower substrate bias values (figures 8.23, 8.24, 8.25, 8.26, 8.28, and 8.29).
- Coating failure during wear tests is by delamination (figure 8.30).

Pulsing promotes a more ordered crystal structure in both chromium nitride phases, and changes crystal orientation in Cr₂N:

SEM cross sections of d.c. deposited coatings show columnar structures across a wide range of nitrogen contents (figures A.1, A.3, A.5, A.7, A.9). SEM cross sections of pulsed substrate bias deposited coatings (figure 8.21) show a smooth, glass like texture, devoid of voids or indications of columnar or granular texture. XRD analysis (Bragg-Brentano and glancing angle to screen for peaks due to surface oxides) shows that the crystallographic texture of CrN and Cr₂N respond differently to pulsed substrate bias deposition: CrN structures become more ordered under pulsed substrate bias deposition but with the same dominant crystal orientation as d.c. deposition (the {111} and {200} planes, figure 8.19), whereas Cr₂N becomes both more ordered and takes on a different orientation (the {200} plane as opposed to the {101} plane, figure 8.19). However there is also evidence for an amorphous Cr_xN phase in Cr₂N coatings, which becomes more pronounced under the influence of bias pulsing (Chapter 8, section 8.3). These observations indicate that pulsed substrate bias deposition influences growing coatings differently according to the Cr_xN phase being grown. Preferential re-sputtering of certain crystal planes in Cr₂N coatings may be enhanced during pulsed substrate deposition due to the greater flux of high energy ions, as suggested by Lee et al [126].

Substrate bias pulsing causes greater compressive stress in both phases of chromium nitride:

Some degree of stress in any coating can be attributed to the mismatch of thermal expansion coefficients between coating and substrates. However work on thermal stresses in Cr_xN coatings agrees with the theory that the magnitude of such stresses in coatings 1 μm to 5 μm thick is on the order of 100MPa; much less than the stresses reported here, and so likely not a major component [127]. Cr₂N coatings avoid the higher levels of compressive stress (figure 8.20). This may be explained by the crystallographic orientation deposited under pulsed substrate bias regime being one less prone to internal stress. This is consistent with the observed changes in orientation, pronounced amorphous phase, and lower stress levels than the CrN equivalents, of Cr₂N coatings deposited by pulsed substrate bias deposition [128] (Chapter 8 section 8.3). Compressive stress can be

attributed to atomic or ionic peening, in which neutral atoms / ions bombard the growing surface causing point defects such as trapped gas atoms and stacking faults [129] [130]. This has been shown to accompany reductions in crystallite size and a corresponding increase in hardness of CrN films [131]. Tensile stress was not observed by XRD peak shift measurements for any monolithic Cr₂N coating, but has been observed by other authors. [132] [133].

The cubic CrN phase is more prone to compressive stress.

Figure 8.20 shows the differences in compressive stress for d.c. and pulsed deposited coatings of both Cr-N phases, as measured by XRD measurements of the {200} peak shift and peak broadening. Compressive stress is higher for CrN in both d.c. and pulsed cases. Optical microscopy of d.c. deposited coating surfaces (figures A.1, A.3, A.5, A.7, A.9) shows evidence for high levels of compressive stress in high nitrogen content (CrN stoichiometry) coatings in the form of fractures in the coating. At moderate N₂ flow rate (5 SCCM) we observe *possible* evidence of mild compressive stress, as features that resemble upwards buckles of the surface. At slightly higher N₂ content (7 to 9 SCCM) we observe no surface evidence of stress, and at high N contents (9 SCCM and above) we observe evidence for significant compressive stresses, as full blown ‘telephone chord’ fractures.

Substrate bias pulsing improves the wear resistance and hardness of Cr₂N coatings; it only improves the wear resistance and hardness of CrN coatings at lower substrate bias values:

The changes in microstructure discussed above appear to relate to changes in tribological behaviour. In coatings with low N content the application of pulsing results in higher hardness, lower adhesion, and higher overall wear rate (figures 8.24, 8.26, 8.29). This is consistent with work by other investigators [134]. In coatings with a more CrN-type stoichiometry the effects of applying pulsed substrate bias deposition depend greatly on the substrate bias used. At a bias of -70V applying pulsed substrate biasing increases both adhesion and coating hardness, and decreases wear rate, relative to d.c. deposited comparisons (figures 8.28, 8.25, 8.23). At -100V substrate bias pulsing decreases both adhesion and hardness. A comparison of CrN wears (figure 8.22) shows

that coatings deposited with a higher substrate bias have a higher wear rate over a 20 minute period. This correlates well with frictional coefficients over the same period (figure 8.27).

Coating failure during wear tests is by delamination:

Optical microscopy of coating wear tracks suggests that coatings fail through delamination (figure 8.30). We observe sharp edged wear tracks and surrounding pits in the coating, with no sign of slopes as would be expected if failure was through abrasion of the coating. Internal stress combined with substrate surface topography is a likely cause; it has been shown that nanometre scale irregularities in substrate topography can act as seeding points for delamination even on an apparently flat substrate. [135]. This suggests that, for simple monolithic coatings such as in array 8.3, the coating-substrate interface is the most vulnerable region. This may be due to the sharp change in microstructure and chemical make up acting as a barrier to migrating faults, causing them to accumulate here.

11.4: Development and testing of layered coatings:

Main results:

- Increasing d.c. deposited interlayer depth, and grading the interlayer-coating boundary, improves coating adhesion for both pulsed substrate bias deposited Cr_xN phases (figures 9.13 and 9.14).
- Layering coatings by pulse regimes shows potential to improve coating performance (figure 8.20, 8.24, 8.26, and 9.3, 9.4, 9.5).
- The relative depth of the layers has an effect on stress but not upon crystallography (figure 9.11 and 9.12).
- Varying the relative layer depths has an effect on wear rate and hardness. As crystallography does not change this is more likely related to coating stress (figures 10.2, 10.3, 10.5, 8.19).
- Stoichiometry has a large effect upon nano-meter scale structures (figures 9.10, 8.25, 8.26)

- Drill testing indicates several architectures that can offer comparable levels of performance to the standard CrTiAlN coatings supplied by Teer coatings (figures 10.6, 8.29):
- One coating that performed well in wear tests was performed very poorly in the drill test (figures 9.2, 9.5, 10.1).
- SEM imaging of the drill cutting edges shows significant differences in the type of wear occurring between the best and worst performing coatings (figures 10.8, 10.7).

Increasing d.c. deposited interlayer depth, and grading the interlayer-coating boundary, improves coating adhesion for both pulsed substrate bias deposited Cr_xN phases:

The introduction of compositional gradients and interlayers is a proven method for improving coating adhesion, although less well studied for Cr based coatings [136] [137] [138]. Grading has been shown to promote better layer-to-layer intimacy [139], and lowering of compositional and stress gradients. Deeper interlayers have been shown to lower the stress gradients between the coating and the substrate [140]. In this study adhesion was found to increase with a Cr interlayer deeper than 250 nm by grading the interlayer-coating boundary (Figures 9.13 and 9.14).

Layering coatings by pulse regime shows potential to improve coating performance:

Array 1 of Chapter 9 investigated the effects of material layered by pulse regime in CrN and Cr₂N stoichiometries, and in a layered stoichiometry. In CrN coatings, layers of d.c. then pulsed deposited material (Chapter 9, sample 1a) produced similar levels of internal stress (figures 8.20 and 9.5) and hardness to D.C. deposited CrN coatings, and a higher critical load than either d.c. or pulsed only deposition (figures 8.23 and 9.4). Cr₂N coatings layered in the same fashion (Chapter 9, sample 2a) show a higher internal stress (figures 9.5 and 8.20), and both higher critical load (figures 9.4 and 8.24) and comparable hardness to pulsed substrate bias deposited coatings (figures 9.3 and 8.26). The most promising results were from the coating consisting of a d.c. deposited CrN layer overcoated by a pulsed substrate bias deposited Cr₂N layer. This coating (Chapter 9, sample 3a) displayed

the lowest internal stress (figure 9.5) and outperformed both the other coatings in wear tests (figure 9.3). Internal compressive stress correlates well with L_{c3} (Figure 9.4).

The relative depth of the layers has an effect on stress but not upon crystallography:

While simply mitigating internal stress is a useful ability, achieving precise control over it, and combining the properties of more flexible and harder materials, is more desirable. Following in the footsteps of ancient smiths, who achieved superior metal performance by forging sandwiches of chemically similar but mechanically dissimilar materials into tools combining the best properties of both, we investigated the potential of layering to control coating properties, in particular stress. Array 2 of Chapter 9 demonstrated a possible method of controlling internal coating stress – by varying the relative depths of the pulsed and d.c. deposited layers. The XRD analysis showed that all the coatings were dominated by the {200} peak, with no variation that matched the observed changes in coating stress (figure 9.12). Hence we are unable to say definitively what the origin of the stress is. The results suggest that the tensile component of coating stress increases with layer 1 (d.c. deposited CrN) depth, and the lowest total stress occurs when the ratio of layer 1 depth to layer 2 depth is in the region of 1:1 (figure 9.11). As CrN has not been shown to develop any form of tensile stress under conditions such as those applied the origin of this tensile component is unclear. However it likely originates from the upper Cr₂N layer, as Cr₂N coatings *have* been shown to develop tensile stresses when sub-stoichiometric [141]. This is supported by the appearance of ‘mud flat’ cracking patterns in coatings deposited at N₂ flow rates of 3 SCCM, a possible indicator of internal tensile stress (figure A.3).

Varying the relative layer depths has an effect on wear rate and hardness. As crystallography does not change this is more likely related to coating stress.

Investigation into coatings where internal stress has been controlled using the mechanism described in Chapter 9 show correlations between wear rate (figure 10.2) and both surface hardness (Figure 10.5) and magnitude of internal stress (figure 10.3). The sign of the internal stress does not appear to be an issue: both tensile and compressively stressed coatings showed higher wear rates. Interestingly the hardest and best wearing coatings show the lowest internal stress, suggesting that the enhanced hardness is due to a change in

coating microstructure, not simply compressive stress. The XRD data shows changes in crystallographic orientation and greater ordering in pulsed substrate bias deposited Cr₂N and CrN coatings (figure 8.18). The tribological results are different to those observed from simple monolithic coatings, which showed increases in hardness following internal stress levels. However given the very different coating structures at work on the 0.1 micron to micron scale, assuming the same stress mechanisms at work and making a direct comparison of tribology would be unwise.

Stoichiometry has a large effect upon nanometre scale structures:

CrN and Cr₂N appear very different at the nanometer scale, which is most likely related to their differing responses to pulsed substrate bias deposition. Microstructural cross sectional analysis using TEM imaging showed distinct differences between low nitrogen content and high nitrogen content layers. High nitrogen content layers demonstrated a disordered matrix with roughly spherical grains of CrN measuring on the order of 30nm across embedded within the matrix. Low nitrogen content layers showed much smaller and more frequent grains with diameters on the order of 5 nm to 10 nm (figure 9.10). The large grains present in the CrN sample bear great similarity to features identified as deformed nano-crystalline clusters in CrN coatings deposited by arc ion plating [142]. The presence of smaller grains in the Cr₂N Stoichiometry coatings may be related to their generally higher hardness and lower wear rates (figures 8.25 and 8.26), as frequent grain boundaries will limit the mobility of crystal faults and hence limit plastic deformation and the growth of stress fractures.

Drill testing indicates several architectures that can offer comparable levels of performance to standard CrTiAlN coatings:

The CrTiAlN coated drill bits provided by Teer Coatings Ltd. are an informative comparison. CrTiAlN is highly regarded as a hard wearing coating, and generally outperforms standard Cr_xN coatings by a wide margin (as shown by figure 10.6). The majority of the layered Cr_xN coatings gave comparable drill test results to CrTiAlN, although none outperformed it. The two best performing Cr_xN coatings (by average

values), 1b and 4b, both featured pulsed substrate bias deposited Cr₂N Stoichiometry layers. As well as high average wear resistances, these coatings showed a better consistency of results than other Cr_xN coatings. This suggests that the Cr₂N phase works well with pulsed substrate bias deposition, especially with a deep interlayer. The d.c. deposited Cr₂N coating performed less well, consistent with wear tests (figure 8.29). The CrN Stoichiometry coating (2b) offered high maximum wear resistances but poor consistency.

One coating that performed well in wear tests was performed very poorly in the drill test:

A promising architecture at the wear testing stage (figure 9.2), the multi-pulse-regime all Cr₂N Stoichiometry architecture (coating 3b), was actually out performed by the uncoated control sample drill bits during drill tests (figure 10.6)! One explanation relates to the Cr₂N Stoichiometry and to coating stress, which the coating architecture in question has shown high levels of (figure 9.5) – higher than a pulsed substrate bias deposited monolithic coating in fact. This factor, combined with a greater vulnerability of Cr₂N to high temperature oxidative wear [143] and the formation of Cr₂O₃ scales makes the coating more vulnerable under the extreme conditions of the cutting edge of the drill bit. Delamination due to high internal stress and oxidative wear [144] [145] would also provide a mechanism for making the performance of the drill bit coated with this architecture *worse* than that of an uncoated drill bit: The hard oxide fragments could cause 3-body abrasion as they are trapped between the tool and the workpiece. Delamination provides a plethora of small hard fragments to enhance the abrasion at the cutting edge; a process which, once begun, may be self reinforcing as abrasive particles remove more coating. This result highlights the important role that stress plays in coating performance, as other coatings featuring pulsed substrate bias deposited Cr₂N performed well.

SEM imaging of the drill cutting edges shows significant differences in the type of wear occurring between the best and worst performing coatings:

SEM examination of the coating 3b drill bit cutting edge (figure 10.8) shows no sign of the coating anywhere near the cutting edge suggesting complete delamination. The cutting edge has been worn away, though sections of its original edge are still visible.

By comparison, coating 1b (figure 10.7), the dual stoichiometry dual pulse regime architecture, shows signs of material adhered to the cutting edge with little sign of wear breaking into it. There are also changes in wear surface texture suggesting the coating may only have been eroded a short distance back from the cutting edge. Clear banding near the coating edge reinforces this notion, as this may relate to changes in surface conductivity and / or density. [146].

Chapter 12: Conclusions:

12.1: Introduction:

We have investigated the effects of substrate bias pulsing (and other pulsed power regimes) on the plasma processes of a closed field unbalanced magnetron sputtering system employing a Cr target and N₂ as a reactive gas, the coatings generated therein, and how substrate bias pulsing may be used in a targeted fashion to improve them.

The project objectives were accomplished by the following broad courses of action:

- The relationship between N₂ inflow rate, target bias, and the intensity of the 325nm Cr emission line, was investigated. This provided an overview of how the system responds, and hysteresis data.
- The effects of substrate bias pulsing on the plasma behaviour were investigated. This was done using Langmuir probe measurements, spectrometry and imaging of the sputter plasma, SEM and TEM imaging of the coatings, X-ray diffraction, and standard tribological tests.
- The crystal structure and tribology of PSB deposited coatings were investigated, and contrasted with d.c. deposited equivalents. This was done using SEM and TEM imaging of the coatings, X-ray diffraction, and standard tribological tests.
- The effects of other pulsing regimes on the deposition, micro structure, and tribological properties of Cr_xN coatings were also investigated.
- The effects of changes in the plasma were related to changes in stress, crystallography, and microstructure, which in turn were related to coating tribology.
- Targeted applications of substrate bias pulsing to control coating microstructure, crystallography, internal stresses, and wear resistance were investigated.
- The effects of combining changes in stoichiometry with changes in pulse regime were investigated with a view to gaining control over internal coating stress.
- The ability to control stress was related to changes in coating tribology.
- The project was concluded by depositing an array of promising coating architectures on to high speed steel drill bits and testing them under conditions closely approximating industrial environment and usage.

12.2: Findings:

- Langmuir probe measurements and optical spectrometry have shown that pulsed substrate biasing does indeed influence the behaviour of the plasma during deposition. Its application generates a higher density of ions, a higher ion flux at the substrate, which increases with pulse frequency and bias voltage, and creates a population of suprathreshold ions which strike the substrate.
- The Cr-N system shows little hysteresis in any pulse regime or d.c.. The variation of target bias with nitrogen content of the chamber appears to be related to the phase of Cr_xN being deposited. The poisoning region begins at around 5 SCCM to 7 SCCM of N_2 flow, equivalent to 70% - 50% of FMS, respectively.
- PSB sputtering can both alter crystal orientation and create a more ordered structure. This effect is partly dependent upon coating stoichiometry. PSB sputtering also increases the compressive stress of coatings. CrN stoichiometry coatings are more prone to this. The degree of the effect of PSB is dependent upon substrate bias level.
- Some of the less useful effects of PSB sputtering as a technique (such as excessive internal stress) may be addressable by careful design of coating structure, which selective use of PSB itself enables. A d.c. deposited Cr interlayer deeper than 250nm and grading the internal boundaries of a coating increases critical load. Layering a coating can improve other aspects such as internal stress and hardness. Where layering is done by both stoichiometry and pulse regime the relative depths of the layers influence stress, hardness, and wear rate but not crystallography.
- As the final phase of the project five coating architectures were selected, both multilayered and monolithic that showed promise as hard wearing coatings, and applied to high speed drill bits. Several of these architectures showed improved wear performance over standard CrN coatings, and compared well to the fundamentally harder [147] CrTiAlN coatings supplied by Teer Coatings Ltd.
- SEM study of the cutting edges of the drill bits post-wear showed significant differences in the wear pattern between the best and worst performing coatings. These suggest that the worst performing coatings suffered large area delamination during the drill test, whereas the best performing suffered abrasive wear near to the cutting edge only.

- The responses of coatings to drill wear test conditions cannot be precisely predicted by standard tribological tests; one coating that showed promise under thrust washer testing was outperformed by uncoated drill bits in the drill testing stage.

12.3: Suggestions for further investigations:

Further investigation into the microstructural origins of the coating stresses observed in this work. The results of this project suggest a strong link to increased ion flux and energy, but the exact mechanisms at work in the coatings are unclear.

Further investigations into the effects of alternate pulsing regimes may shed further light upon the possibility of using dual cathode pulsing as a means of smoothing coating surfaces in the final phases of deposition.

As compounds consisting of Cr, N and at least one other material (often another transition metal such as Ti) are becoming popular in coatings applications a detailed investigation into the effects of various pulsing regimes upon deposition of these materials might also be timely. The investigation detailed above may lead naturally into studies of depositing Cr_xN by HIPIMS (High Power Impulse Magnetron Sputtering) technique. This is a recent and promising development in the field of sputtering, which allows high ion to atom ratios (as in PMS) but importantly, much of the sputtered coating flux becomes ionised, meaning dense coatings can be deposited with low substrate bias voltages and correspondingly low stresses. HIPIMS deposited coatings, like PMS deposited coatings, may produce structures with no voids. A comparison of the detailed microstructure and tribology of Cr_xN coatings deposited by these two techniques, PMS and HIPIMS, could be an informative research path. A comparison between layered d.c./PMS architectures and monolithic HIPIMS deposited coatings could also be of interest.

15: References:

- [1]: M .Berger and P. Stolkley, 'PVD protective coatings for wear parts', Surface Engineering, Volume 2 1st Edition, 1992, page 22.
- [2]: www.webelements.com/compounds/chromium/chromium_nitride.html
- [3]: M.G.Hocking, 'Production of Corrosion and Wear Resistant Coatings', Surface Engineering, Volume 2, 1st Edition, 1992, page 5.
- [4]: K. Yamamoto and D.C Pack , 'Transient free molecular flow through a tube; Rarefied gas dynamics', Proceedings of the Eleventh International Symposium, Cannes, France, Volume 1, (1978) page 207.
- [5]: D Wolfe, 'Titanium carbide coatings deposited by reactive ion beam-assisted, electron beam–physical vapor deposition', Surface and Coatings Technology, Volume 124, Issues 2-3, (2000) 142-153
- [6]: R. O. Dendy , 'Plasma Dynamics', Oxford University Press, 1990
- [7]: I. Safi, 'Recent aspects concerning D.C. reactive magnetron sputtering of thin films: a review', Surface and Coatings Technology, Volume 127, Issues 2-3 (2000) Pages 203-218
- [8]: R. Hippler, 'Low temperature plasmas: fundamentals, technologies, and techniques', Volume 2, Wiley-VCH, 2008, Page 158,
- [9]: Annemie Bogaerts and Renaat Gijbels, 'Fundamental aspects and applications of glow discharge spectrometric techniques', Spectrochimica Acta Part B: Atomic Spectroscopy Volume 53, Issue 1 (1998) 1-42
- [10]: Francis F. Chan and Jane P. Chang, 'Notes on the principles of plasma processing', Kluwer Academic publishing / Plenum publishers, 2003, page 32,
- [11]: I. Langmuir, 'Positive Ion Currents from the Positive Column of Mercury Arcs', Science, Volume 58, Issue 1502 (1923) 290-291
- [12]: Christopher G. Herbert, Robert Alexander Walker Johnstone, 'Mass spectrometry basics', CRC Press 1st edition, 2003, Page 32

- [13]: A. A. Ovsyannikov, 'Plasma Diagnostics', Cambridge International Science Publishing 1st edition, 2003, Page 158
- [14]: Zhehui Wanga and Samuel A. Cohen, 'Geometrical aspects of a hollow-cathode planar magnetron', Physics of Plasmas Volume 6, Issue 5 (1999) page 1655
- [15]: Milton Ohring 'The materials science of thin films: deposition and structure', Academic press, 1992.
- [17]: P.Kelly, 'Characterization Studies of a Closed Field Unbalanced Magnetron Sputtering System', PhD Thesis, 1997, page 83
- [18]: Christopher G. Herbert, Robert Alexander Walker Johnstone, 'Mass spectrometry basics', CRC Press, 2003, Page 31
- [19]: Alexander A. Fridman, Lawrence A. Kennedy, 'Plasma Physics and Engineering', Taylor & Francis, 2004, Chapter 7
- [20]: Michael A. Lieberman and Allan J. Lichtenberg, 'Principles of plasma discharges and materials processing', Wiley-Interscience, 2005, page 175
- [21]: D. M. Mattox, 'Handbook of Physical Vapour Deposition (PVD) Processing: Film Formation', Elsevier, 2010, page 392
- [22]: Stephen M. Rossnagel, J. J. Cuomo, William Dickson Westwood, 'Handbook of plasma processing technology: Fundamentals, etching, deposition', Noyes Publications, 1st Edition, 1990, page 70
- [23]: Stephen M. Rossnagel, J. J. Cuomo, William Dickson Westwood, 'Handbook of plasma processing technology: fundamentals, etching, deposition', Noyes Publications, 1st Edition, 1990, page 73
- [24]: K. S. SreeHarsha, 'Principles of physical vapour deposition of thin films', Elsevier, 1st Edition, 2006, page 566
- [25]: Edward V. Barnat and Toh-Ming Lu, 'Pulsed and pulsed bias sputtering: principles and applications', Springer, 1st Edition, 2003, page 7, section 2
- [26]: Edward V. Barnat and Toh-Ming Lu, 'Pulsed and pulsed bias sputtering: principles and applications', Springer, 2003, page 79, section 3.

- [27]: D. M. Mattox, 'Handbook of Physical Vapour Deposition (PVD) Processing: Film Formation', Elsevier, 2010, page 250, section 4.4.2,
- [28]: D. M. Mattox, 'Handbook of Physical Vapour Deposition (PVD) Processing: Film Formation', Elsevier, 2010, page 686, section 26.5
- [29]: Kenneth Holmberg, Allan Matthews 'Coatings tribology: properties, mechanisms, techniques and applications in surface engineering' Volume 10, Elsevier, 2nd Edition, page 20, section 2.2.3.3,
- [30]: Stephen M. Rossnagel, J. J. Cuomo, William Dickson Westwood, 'Handbook of plasma processing technology: fundamentals, etching, deposition', Noyes Publications, 1st Edition, page 233, section 9.2,
- [31]: L.Lou, G. Macdonough, H. Wald, 'Closed loop control of reactive dual magnetron sputtering', Advanced Energy Industries Inc, 1625 Sharp Point Drive, Fort Collins Colorado, white paper, 1999
- [32]: S Kadlec, J Musil and J Vyskoč, 'Influence of the pumping speed on the hysteresis effect in the reactive sputtering of thin films', Vacuum, Issue 10 (1987), pages 729-738
- [33]: J. Danroc, A. Aubert and R. Gillet, 'Reactive magnetron sputtering of TiN: Analysis of the deposition process' Surface and Coatings Technology, Issue 33 (1987) pages 83-90
- [34]: D. M. Mattox, 'Handbook of Physical Vapour Deposition (PVD) Processing: Film Formation', Elsevier 1st Edition, 2010, chapter 9
- [35]: Kiyotaka Wasa, Makoto Kitabatake, Hideaki Adachi, 'Thin film materials technology: sputtering of compound materials', William Andrew Inc 1st Edition, 2004, Page 2
- [36]: Robert J. Stokes, D. Fennell Evans, 'Fundamentals of interfacial engineering', Wiley-VCH 1st Edition, 1997 page 571
- [37]: Robert J. Stokes, D. Fennell Evans, 'Fundamentals of interfacial engineering', Wiley-VCH 1st Edition, 1997, page 572
- [38]: Ivan V. Markov, 'Crystal growth for beginners: fundamentals of nucleation, crystal growth and epitaxy', World Scientific 2nd Edition, 2004, page 433

- [39]: Robert J. Stokes, D. Fennell Evans, 'Fundamentals of interfacial engineering', Wiley-VCH 1st Edition, 1997, page 584
- [40]: L. B. Freund, Subra Suresh, 'Thin film materials: stress, defect formation, and surface evolution' Cambridge University Press 1st Edition, 2003, page 20
- [41]: Robert J. Stokes, D. Fennell Evans, 'Fundamentals of interfacial engineering', Wiley-VCH 1st Edition, 1997, page 586
- [42]: Robert J. Stokes, D. Fennell Evans, 'Fundamentals of interfacial engineering', Wiley-VCH 1st Edition, 1997, page 590
- [43]: R P Howson, 'The reactive sputtering of oxides and nitrides', Pure & Applied Chemistry Volume 66, Issue 6 (1994) pages 1311-1318
- [44]: D. M. Mattox, 'Handbook of Physical Vapour Deposition (PVD) Processing: Film Formation', Elsevier 1st Edition, 2010, page 482
- [45]: E. Lugscheider, C. Barimania, C. Wolffa, S. Guerreiroa and G. Doeppera, 'Comparison of the structure of PVD-thin films deposited with different deposition energies' Surface and Coatings Technology Volumes 86-87, Issue 1 (1996) pages 177-183
- [46]: A. Misra, M. Nastasi, 'Fundamental aspects of residual stress evolution in thin metal films during energetic particle deposition', Adhesion aspects of thin films, Volume 1, (2001) pages 17 -29
- [47]: L. M. Gratton, A. Miotello and C. Tosello, 'Effective temperature in the impact surface region during 100 keV Xe⁺ implantation of copper bars', Applied Physics A: Materials Science & Processing Volume 36, Issue 3 (1985) pages 139-141,
- [48]: 'I. Petrov, L. Hultman, U. Helmersson, J.-E. Sundgren and J.E. Greene Microstructure modification of TiN by ion bombardment during reactive sputter deposition', Thin Solid Films, Volume 169, Issue 2 (1989) pages 299-314

- [49]: L. Hultman, U. Helmersson, S. Barnett, J. Sundgren, 'Low-energy ion irradiation during film growth for reducing defect densities in epitaxial TiN(100) films deposited by reactive-magnetron sputtering', *Journal of Applied Physics*, Volume: 61, Issue 2 (1987) pages 552 – 555
- [50]: V. Damodara Das and N. Jayaprakash, 'Effect of substrate temperature during growth on defect density in bismuth thin films' *Journal of Vacuum Science and Technology*, Volume 20, Issue 1 (1982) page 58
- [51]: S. Ted Oyama, 'The chemistry of transition metal carbides and nitrides', Blackie Academic and Professional 1st Edition, 1996, Page 1
- [52]: S. Ted Oyama, 'The chemistry of transition metal carbides and nitrides', Blackie Academic and Professional 1st Edition, 1996, Page 2
- [53]: Zenghu Han, Jiawan Tian, Qianxi Lai, Xiaojiang Yu and Geyang Li, 'Effect of N₂ partial pressure on the microstructure and mechanical properties of magnetron sputtered CrN_x films', *Surface and Coatings Technology* Volume 162, Issues 2-3 (2003), pages 189-193
- [54]: D. Gall, C.-S. Shin, and T. Spila, 'Growth of single-crystal CrN on MgO.001.: Effects of low-energy ion irradiation on surface morphological evolution and physical properties' *Journal of Applied Physics*, Volume 91, Issue 6, (2002) 3589
- [55]: Costel Constantin, Muhammad B. Haider, David Ingram, and Arthur R. Smith, 'Metal/semiconductor phase transition in chromium nitride (001) grown by rf-plasma-assisted molecular-beam epitaxy', *Applied Physics Letters*, Volume 85, Issue 26, (2004) page 6371
- [56] P. Hones, R. Sanjines, F. Levy 'Characterization of sputter-deposited chromium nitride thin films for hard coatings' *Surface and Coatings Technology*, Volumes 94-95, (October 1997) pages 398-402
- [57]: S Yang 'CrN-based wear resistant hard coatings for machining and forming tools' 2009 *Journal Physics D: Applied Physics*, Volume 42, Issue 10, (2009) page 104001

- [58]: F.D. Lai, and J.K. Wu, 'Structure, hardness and adhesion properties of CrN films deposited on nitrided and nitrocarburized SKD 61 tool steels', Surface and Coatings Technology, Volume 88, Issue 1-3 (1997) pages 183-189
- [59]: P. J. Kelly and R. D. Arnell, 'Control of the structure and properties of aluminum oxide coatings deposited by pulsed magnetron sputtering', Journal of Vacuum Science and Technology A, Issue 17 (1999) page 945
- [60]: PJ Kelly, T Vom Braucke, Z Liu, RD Arnell and ED Doyle, 'Pulsed D.C. titanium nitride coatings for improved tribological performance and tool life,' Surface and Coatings Technology, Volume 202, Issue 4-7, (2007) pages 774-780
- [61]: PJ Kelly, AA Onifade, Y Zhou, GCB Clarke, M Audronis and JW Bradley, 'The influence of pulse frequency and duty on deposition rate during pulsed magnetron sputtering.' Plasma Processes and Polymers, Volume 4, Issue 3, (2007) pages 246-252
- [62]: I Iordanova, PJ Kelly, R Mirchev, V Antonov, 'Crystallography of magnetron sputtered TiN coatings on steel substrates', Vacuum, Volume 81, Issue 7, (2007) pages 830-842
- [63]: K. L. Mittal, 'Adhesion measurement of films and coatings', VSP-BV 1st Edition, 1995
- [64]: R.Gibson, I.T. Brinkley, and E.M. Waddell, 'Closed field magnetron sputter deposition of carbides and nitrides for optical applications', 51st Annual Technical Conference Proceedings of the Society of Vacuum Coaters, (2008) pages 856-7188
- [65]: J.W. Coburn, 'Plasma etching and reactive ion etching', American Institute of Physics 1st Edition, 1982
- [66] I. Safi, 'Recent aspects concerning D.C. reactive magnetron sputtering of thin films: a review', Surface and Coatings Technology, volume 127, Issues 2-3, (2000) page 219
- [67] I. Safi, 'Recent aspects concerning D.C. reactive magnetron sputtering of thin films: a review', Surface and Coatings Technology, volume 127, Issues 2-3, (2000) page 219

- [68] P. Baroch, J. Musil, J. Vlcek, K.H. Nam and J.G. Han, 'Reactive magnetron sputtering of TiO_x films', Surface and Coatings Technology Volume 193, Issues 1-3, (2005) pages 107-111
- [69] Zenghu Han, Jiawan Tian, Qianxi Lai, Xiaojiang Yu and Geyang Li, 'Effect of N₂ partial pressure on the microstructure and mechanical properties of magnetron sputtered CrN_x films', Surface and Coatings Technology Volume 162, Issues 2-3, (2003), pages 189-193
- [70] H. Shah, V. Chawla, R. Jayaganthan and D. Kaur, 'Microstructural characterizations and hardness evaluation of reactive magnetron sputtered CrN thin films on stainless steel substrate' Bulletin of Materials Science Volume 33, Issue 2 (2010) pages 103–110
- [71] Yan Ping Wu, Yong Xiang Leng, Sun Hong, Sheng Fa Zhu, Nan Huang, Bin Bai, Peng Cheng Zhang, 'The Microstructure and Properties of CrN_x Films Synthesized by Unbalanced Magnetron Sputtering', Key Engineering Materials Volumes 373 – 374, (2008) pages 176-179
- [72] Zenghu Han, Jiawan Tian, Qianxi Lai, Xiaojiang Yu and Geyang Li, 'Effect of N₂ partial pressure on the microstructure and mechanical properties of magnetron sputtered CrN_x films', Surface and Coatings Technology Volume 162, Issues 2-3, (2003), pages 189-193
- [73] I. Shozo, O. Futami, K. Keiji, 'Effect of Target Materials on Deposition of Nitride Films by rf Reactive Magnetron Sputtering', Journal of the Japan Society for Precision Engineering Volume 69, Issue 7 (2003), pages 976
- [74] G.G. Fuentes, R.J. Rodríguez, M. García, L. Galán, I. Montero and J.L. de Segovia 'Spectroscopic investigations of Cr, CrN and TiCr anti-multipactor coatings grown by cathodic-arc reactive evaporation', Applied Surface Science Volume 253, Issue 18, (2007) pages 7627-7631
- [75] D. Depla, S. Mahieu, R. De Gryse, 'Magnetron sputter deposition: Linking discharge voltage with target properties', Thin Solid Films, Volume 517, Issue 9 (2009) pages 2825-2839

[76] Alex A. Volinsky, Neville R. Moody, Dirk C. Meyer, 'Stress induced period fracture patterns in thin films', 11th International Conference on Fracture, 2005.

[77] Henry Windischmann, 'Intrinsic stress in sputter-deposited thin films', *Critical Reviews in Solid State and Materials Sciences* Volume 17, Issue 6 (1992) pages 547-596

[78] Grygoriy A. Kravchenko, 'Crack patterns in thin films and X-ray optics thermal deformations', University of South Florida, PhD thesis, 2008

[79] M.W. Moon, H.M. Jensen, J.W. Hutchinson, H. Oh, A.G. Evans, 'The characterization of telephone cord buckling of compressed thin films on substrates', *Journal of the Mechanics and Physics of Solids*, Volume 50, Issue 11, (2002) pages 2355 – 2377

[80] Z.B. Zhao, Z.U. Rek, S.M. Yalisove, J.C. Bilello, 'Nanostructured chromium nitride films with a valley of residual stress' *Thin Solid Films* Volume 472, Issues 1-2, (2005) pages 96-104

[81] Peter J. Kelly, Ayokola A. Onifade, Yanwen Zhou, Gregory C. B. Clarke, Martynas Audronis, 'The Influence of Pulse Frequency and Duty on the Deposition Rate in Pulsed Magnetron Sputtering', *Plasma Processes and Polymers* Volume 4, Issue 3 (2007) pages 246–252

[82] Iordanova, I; Kelly, P J; Antonov, V; Li, H 'Influence of concentration of Ag on electron and crystallographic structure of reactively co-sputtered CFUBMS TiN/Ag nanocomposite coatings', *Materials Technology: Advanced Performance Materials*, Volume 26, Issue 1 (2011) pages 40-45

[83] PJ Kelly, R Hall, J O'Brien, JW Bradley, P Henderson, G Roche and RD Arnell, 'Studies of mid-frequency pulsed d.c. biasing.' *Journal of Vacuum Science and Technology A*, Volume 19, Issue 6 (2001) pages 2856-2865

[84] P. J. Kelly and R. D. Arnell, 'Magnetron sputtering: a review of recent developments and applications', *Vacuum* Volume 56, Issue 3 (2000) pages 159-172

- [85] Stanislav Mráz, 'Structure evolution of magnetron sputtered TiO₂ thin films', J. Applied Physics, Volume 109, Issue 2 (2011) pages 023512-023512
- [86] Stanislav Mráz, 'Structure evolution of magnetron sputtered TiO₂ thin films', J. Applied Physics, 109 (2011) pages 023512-023512
- [87] P. J. Kelly and R. D. Arnell, 'Magnetron sputtering: a review of recent developments and applications', Vacuum Volume 56, Issue 3, (2000) pages 159-172
- [88] S. Gangopadhyay, R. Acharya, S. Paul, A.K Chattopadhyay, 'Effects of substrate bias voltage on structural and mechanical properties of pulsed d.c. magnetron sputtered TiN-MoS_x composite coatings', Vacuum, Volume 84, Issue 6, (2006) pages 843-850
- [89] W.D. Sproul^a, P.J. Rudnik^a and M.E. Graham, 'The effect of N₂ partial pressure, deposition rate and substrate bias potential on the hardness and texture of reactively sputtered TiN coatings', Surface and Coatings Technology Volumes 39-40, Issue 1, (1989) pages 355-363
- [90] F. Höhl, H.-R. Stock, P. Mayr, 'Examination of residual stress, morphology and mechanical properties of sputtered TiN films', Surface and Coatings Technology, Volumes 54-55, Issue 1, (1992) pages 160-166
- [91] Peter C.T. Ha, D.R. McKenzie, M.M.M. Bilek, E.D. Doyle, D.G. McCulloch and P.K. Chu, 'Protective Coatings and Thin Films Control of stress and delamination in single and multi-layer carbon thin films prepared by cathodic arc and RF plasma deposition and implantation', Surface and Coatings Technology Volume 200, Issues 22-23, (2006) pages 6405-6408
- [92] A. Leyland and A. Matthews, 'On the significance of the H/E ratio in wear control: a nanocomposite coating approach to optimised tribological behaviour', Wear, Volume 246, Issues 1-2, (2000) pages 1-11
- [93] Sheng Han^b, Hong-Ying Chen^c, Zue-Chin Chang^c, Jian-Hong Lin^a, Ching-Jung Yang^c, Fu-Hsing Lu^c, Fuh-Sheng Shieu^c and Han C. Shih, 'Effect of metal vapor vacuum

arc Cr-implanted interlayers on the microstructure of CrN film on silicon' *Thin Solid Films* Volume 436, Issue 2, (2003) pages 238-243

[94] T. Hurkmans, T. Trinh, D.B. Lewis, J.S. Brooks and W.-D. Münz 'Multilayered titanium tungsten nitride coatings with a superlattice structure grown by unbalanced magnetron sputtering' *Surface and Coatings Technology* Volumes 76-77, Issue 1, (1995) pages 159-166

[95] G.A. Fontalvo, R. Daniel and C. Mitterer, 'Interlayer thickness influence on the tribological response of bi-layer coatings', *Tribology International* Volume 43, (2010) pages 108-112

[96] Gaoren Li, Pranav Deshpande, J.H. Li and R.Y. Lin, 'Nano Cr Interlayered CrN Coatings on Steels', *Science & Technology* Volume 10, Issue 1-2 (2005) pages 690-698

[97] Young Su Hong, Se Hun Kwon, Tiegang Wang, Doo-In Kim, 'Effects of Cr interlayer on mechanical and tribological properties of Cr-Al-Si-N nanocomposite coating', *Transactions of the non ferrous metals society of China*, Volume 21, Supplement 1, (2011) pages 62-67

[98] A.A. Voevodin, J.S. Zabinski and C. Muratore, 'Recent Advances in Hard, Tough, and Low Friction Nanocomposite Coatings', *Tsinghua Science & Technology* Volume 10, Issue 6, (2005) pages 665-679

[99] Zhong, D.; Mishra, B.; Moore, J.J.; Madan, A, 'Effect of Pulsed Plasma Processing on Controlling Nanostructure And Properties of Thin Film/Coatings', *Surface Engineering*, Volume 20, Issue 3, (2004) pages 196-204

[100] D.W. Hoffman^a and John A. Thornton, 'Internal stresses in sputtered chromium' *Thin Solid Films* Volume 40, (1977) pages 355-363

- [101] D.S. Rickerby, A.M. Jones and B.A. Bellamy, 'X-ray diffraction studies of physically vapour-deposited coatings', *Surface and Coatings Technology* Volume 37, Issue 1, (1989) pages 111-137
- [102] D. S. Rickerby, A. M. Jones and B. A. Bellamy, 'Internal stress in titanium nitride coatings: Modelling of complex stress systems', *Surface and Coatings Technology* Volume 36, Issues 3-4, (1988) pages 661-674
- [103] John A. Thornton^a and D.W. Hoffman, 'Stress-related effects in thin films', *Thin Solid Films* Volume 171, Issue 1, (1989) pages 5-31
- [104] Sergei V. Fortuna^a, Yurii P. Sharkeev^b, Anthony J. Perry^c, Jesse N. Matossian^d and Ivan A. Shulepov 'Microstructural features of wear-resistant titanium nitride coatings deposited by different methods', *Thin Solid Films* Volumes 377-378, Issue 1, (2000) pages 512-517
- [105] X.L. Wu and E. Ma, 'Accommodation of large plastic strains and defect accumulation in nanocrystalline Ni grains', *Journal of Materials Research*, Volume 22 (2007) pages 2241-2253
- [106] Hamzah, Esah and Ali, Mubarak L. and Ali, Nouman, 'Adhesion strength of tin coatings at various ion etching deposited on tool steels using cathodic arc PVD technique', *Surface Review and Letters*, Volume 16, Issue 1, (2009) pages 29-35
- [107] Cahoreau, M.¹; Lee, G.H.²; Caisso, J.¹; Cailler, M.³, 'Adhesion enhancement of magnetron-sputtered copper films by ion bombardment etching treatment of nickel and Inconel substrates: investigations by Auger electron spectroscopy and secondary ion mass spectroscopy of the ion beam effects', *Journal of Adhesion Science and Technology*, Volume 5, Issue 11 (1991) 987-999
- [108] Henri Janseny, Han Gardeniers, Meint de Boer, Miko Elwenspoek and Jan Fluitman 'A survey on the reactive ion etching of silicon in microtechnology' *Journal of Micromechanics and Microengineering*, Volume 6 (1996) pages 14–28.

- [109] B. Warcholinski, A. Gilewicz, 'Tribological properties of CrN coatings' Journal of achievements in materials and manufacturing engineering Volume 37, Issue 2 (2009), pages 498-504
- [110] Thorsten Kacsich, Klaus-Peter Lieb, 'Oxidation of thin CrN and Cr₂N films analyzed via nuclear reaction analysis and Rutherford backscattering spectrometry' Thin Solid Films Volume 245, Issue 1-2 (1994) Pages 4-6
- [111] T Kacsich, 'Oxidation of thin chromium nitride films: kinetics and morphology' J. Physics.: Condensed Matter, Volume 8, Issue 49 (1996) page 10703-10719
- [112] E Broszeit, C Friedrich, G Berg, 'Deposition, properties and applications of PVD Cr_xN coatings', Surface and Coatings Technology Volume 115, Issue 1 (1999) pages 9-16
- [113] T. Hoornaert, Z. K. Hua and J. H. Zhang, 'Hard Wear-Resistant Coatings: A Review' Engineering Advanced Tribology Part 3, Volume IV (2010) pages 774-779.
- [114] C Friedrich, G Berg, E Broszeit, F Rick, J Holland, 'PVD Cr_xN coatings for tribological application on piston rings' Surface and Coatings Technology Volume 97, Issues 1-3 (1997) pages 661-668
- [115] T. Hoornaert, Z. K. Hua and J. H. Zhang, 'Hard Wear-Resistant Coatings: A Review' Engineering Advanced Tribology Part 3, Volume IV (2010) 774-779,
- [116] Li, HQ and Li, X and Sun, HL and Teer, D and Dong, H, 'Synthesis and characterization of CrXN nano-multilayer coatings', Volumes 373-374 (2008) pages 126-129
- [117] Harish C. Barshilia and K.S. Rajam, 'Raman spectroscopy studies on the thermal stability of TiN, CrN, TiAlN coatings and nanolayered TiN/CrN, TiAlN/CrN multilayer coatings', Journal of Materials Research Volume 19 (2004) pages 3196-3205
- [118] B Navinšek, P Panjan, I Milošev, 'Industrial applications of CrN (PVD) coatings, deposited at high and low temperatures', Surface and Coatings Technology Volume 97, Issues 1-3, (1997) pages 182-191

- [119] W. Olbrich, G. Kampschulte, 'Superimposed pulse bias voltage used in arc and sputter technology' *Surface and Coatings Technology* Volume 59, Issues 1-3, (1993) pages 274-280
- [120] P.J Kelly, R.D Arnell, 'Magnetron sputtering: a review of recent developments and applications' *Vacuum* Volume 56, Issue 3 (2000) pages 159-172
- [121] PJ Kelly and JW Bradley, 'Pulsed magnetron sputtering – Process overview and applications', *Journal Optoelectronics and Advanced Materials*, Volume 11, Issue 8, (2009) pages 1101-1107
- [122] Yan Ping Wu, Yong Xiang Leng, Sun Hong, Sheng Fa Zhu, Nan Huang, Bin Bai, Peng Cheng Zhang, 'The Microstructure and Properties of CrN_x Films Synthesized by Unbalanced Magnetron Sputtering' *Key Engineering Materials*, Volumes 373 – 374, (2008) pages 176-179
- [123] Yan Ping Wu, Yong Xiang Leng, Sun Hong, Sheng Fa Zhu, Nan Huang, Bin Bai, Peng Cheng Zhang, 'The Microstructure and Properties of CrN_x Films Synthesized by Unbalanced Magnetron Sputtering' *Key Engineering Materials*, Volumes 373 – 374, (2008) pages 176-179
- [124] Qinghua Kong^{a, b}, Li Ji^a, Hongxuan Li^a, Xiaohong Liu^a, Yongjun Wang^{a, b}, Jianmin Chen^a, Huidi Zhou, 'Composition, microstructure, and properties of CrN_x films deposited using medium frequency magnetron sputtering', *Applied Surface Science* Volume 257, Issue 6, (2011) pages 2269-2274
- [125] J.A. Freeman, P.J. Kelly, G.T. West, J.W. Bradley, I. Jordanova, 'The effects of composition and pulsed biasing on chromium nitride films', *Surface & Coatings Technology*, Volume 204, Issues 6-7, (2009) pages 907–910
- [126] Jyh-Wei Lee, Shih-Kang Tien and Yu-Chu Kuo, 'The effects of substrate bias, substrate temperature, and pulse frequency on the microstructures of chromium nitride coatings deposited by pulsed direct current reactive magnetron sputtering', *Journal of Electronic Materials* Volume 34, Issue 12, (2005) pages 1484-1492

- [127] G.C.A.M. Janssen, J.-D. Kammingal, W.G.M. Sloof, 'Stress and Hardness of CrN Films', Materials Research Society, Volume 703 (2002) pages 153
- [128] Wu Tang , Kewei Xu , Ping Wang^b, Xian Li , 'Residual stress and crystal orientation in magnetron sputtering Au films', Materials Letters Volume 57, Issue 20 (2003) pages 3101-3106
- [129] Thornell G, Ericson F, Hedlund C, Ohrmair J, Schweitz JA, Portnoff G. 'Residual stress in sputtered gold films on quartz measured by the cantilever beam deflection technique', IEEE Transactions on Ultrasonics Ferroelectrics and Frequency Control, Volume 46, Issue 4, (1999) pages 981-92
- [130] Victor Bellido-Gonzalez, Sarah Powell and D. Monaghan, 'A sputtered nickel under bump metallurgy structure for lead-free solder for use in flip chip packaging', Flip-chip technology workshop and exhibition, Iknow microelectronics, 2003
- [131] Qi-min Wang , Se-Hun Kwon, Kwang-Ho Kim, 'Formation of nanocrystalline microstructure in arc ion plated CrN films', Transactions of the non ferrous metals society of China, Volume 21, Supplement 1, (2011) pages s73-s77)
- [132] Fabis, P. M.; Cooke, R. A.; McDonough, S , 'The influence of microstructure on stress state of sputter deposited chromium nitride films', Journal of Vacuum Science & Technology A: Vacuum Surfaces and Films, Volume 8, Issue 5 (1990) pages 3819 – 3826
- [133] Z.B. Zhao ^a, Z.U. Rek^b, S.M. Yalisove^c, J.C. Bilello, 'Nanostructured chromium nitride films with a valley of residual stress', Thin Solid Films Volume 472, Issue 1-2, (2005) pages 96-104
- [134] P.H. Mayrhofer , G. Tischler, C. Mitterer, 'Microstructure and mechanical/thermal properties of Cr–N coatings deposited by reactive unbalanced magnetron sputtering' Surface and Coatings Technology Volumes 142-144, Issues 1-4, (2001) pages 78-84
- [135] Urban Wicklund, Sture Hogmark, 'Delamination of thin hard coatings induced by combined residual stress and topography', Adhesion aspects of thin films, Volume 1, (2001) pages 51 – 65

[136] G.A. Fontalvo^{a, b}, R. Daniel^b, C. Mitterer , ‘Interlayer thickness influence on the tribological response of bi-layer coatings’, Tribology International Volume 43, Issues 1-2 (2010) pages 108-112

[137] G’ Aldrich-Smith, N.M. Jennett & J Housden, ‘A round robin to measure the adhesion of thin films and coatings’ National Physical Laboratory UK Report 2002

[138] Young Su Hong, Se Hun Kwon, Tiegang Wang, Doo-In Kim, Jihwan Choi, Kwang Ho Kim Effects of Cr interlayer on mechanical and tribological properties of Cr-Al-Si-N nanocomposite coating’, Transactions of the nonferrous metals society of China, Volume 21, Supplement 1, (2011) pages s62-s67

[139] Xianting Zeng, Sam Zhang, Joe Hsieh ‘Development of graded Cr–Ti–N coatings’ Surface and Coatings Technology Volume 102, Issue 1-2, (1998) pages 108-112

[140] J. Gerth, U. Wiklund, ‘The influence of metallic interlayers on the adhesion of PVD TiN coatings on high-speed steel’, Wear, Volume 264, Issues 9-10, (2008) pages 885-892

[141] Z.B. Zhao ^a, Z.U. Rek^b, S.M. Yalisove^c, J.C. Bilello, ‘Nanostructured chromium nitride films with a valley of residual stress’, Thin Solid Films Volume 472, Issues 1-2, (2005) pages 96-104

[142] Qi-min Wang, Se-Hun Kwon, Kwang-Ho Kim, ‘Formation of nanocrystalline microstructure in arc ion plated CrN films’, Transactions of the non ferrous metals society of China, Volume 21, Supplement 1, (2011) pages 73-77.

[143] Jui-Neng Tu^a, Jenq-Gong Duh^a, Shu-Yueh Tsai ‘Morphology, mechanical properties, and oxidation behavior of reactively sputtered Cr–N films’, Surface and Coatings Technology, Volumes 133-134, Issue 1, (2000) pages 181-185

[144] T Kacsich ‘Oxidation of thin chromium nitride films: kinetics and morphology’ Journal of Physics.: Condensed Matter, Volume 8, (1996) page 10703

[145] Thorsten Kacsich, Klaus-Peter Lieb, ‘Oxidation of thin CrN and Cr₂N films analyzed via nuclear reaction analysis and Rutherford backscattering spectrometry’ Thin Solid Films Volume 245, Issues 1-2, (1994) pages 4-6

- [146] Li, HQ and Li, X and Sun, HL and Teer, D and Dong, H, 'Synthesis and characterization of Cr_xN nano-multilayer coatings' Surface Engineering, Volumes 373-374 (2007) pages 126-129
- [147] X. Z. Ding and X. T. Zeng, 'CrAlN coatings deposited by reactive unbalanced magnetron sputtering', Surface and Coatings Technology, Volume 200, Issues 5-6, (2005) pages 1372-1376
- [148] Principe, E L; Gnauck, P; Hoffrogge, P, 'A Three Beam Approach to TEM Preparation Using In-situ Low Voltage Argon Ion Final Milling in an FIB-SEM Instrument', Microscopy and Microanalysis, Volume 11 (2005) pages 830-831.
- [149] Yaogang Li, Lian Gao, Jing Sun, 'Preparation, structure, and properties of Cr₂N reinforced Al₂O₃ composites', Composites Part B: Engineering Volume 37, Issue 6 (2006) pages 395-398
- [150] A. E. Reiter, V. H. Derflinger, B. Hanselmann, T. Bachmann, and B. Sartory, 'Investigation of the properties of Al_{1-x}Cr_xN coatings prepared by cathodic arc evaporation', Surface and Coatings Technology, Volume 200, Issues 5-6, (2005) page 2114
- [151] S.M. Aouadi, D.M. Schultze, S.L. Rohde, K.-C. Wong, K.A.R. Mitchell, 'Growth and characterization of Cr₂N/CrN multilayer coatings', Surface and Coatings Technology Volume 140, Issue 3, (2001) pages 269-277
- [152] J.A. Thornton 'Influence of apparatus geometry and deposition conditions on the structure and topography of thick sputtered coatings', Journal of Vacuum Science and Technology, Volume 11, Issue 4, (1974) pages 666-670
- [153] Michael John Neale, M. G. Gee 'A guide to wear problems and testing for industry' Williams-Andrews Publishing 2nd Edition, 2001, Page 112
- [154] F.H Stott, D.R.G Mitchell, 'The influences of Coatings on Wear at Elevated Temperatures', Surface Engineering Volume 1, The Royal Society of Chemistry, 1st Edition, 1993, Page 141

[155] Ramesh Divakar, P. J. Blau 'Wear testing of advanced materials' American Society for Testing and Materials 1st edition, 1992, Page 48

Appendix A: Optical microscopy of coating surfaces:

A.1: Introduction:

Although not always definitive evidence of microstructure or internal stress, study of the macroscopic topography of coatings can be very informative, and provide supporting evidence for conclusions reached through other methods. Selected coatings were then followed up on using SEM imaging.

A.2: Experimental:

Silicon wafer fragments with a [111] surface texture were used as substrates, and were prepared using our standard 3 stage ultrasound cleaning. Once in the deposition chamber substrates were subjected to 5 minutes of ion etching with a substrate bias of -650 V and a target current of 0.3 amps. Coatings were deposited to depth of approximately one micron at a range on N₂ inflow rates, using a substrate bias of -100 V. No interlayer applied prior to the main coatings. Deposition was performed in the d.c. bias regime, under standard conditions. The coatings were examined by using an optical microscope. The images were recorded using a digital camera attached to the eyepiece. The field of view in all the optical images is 0.5 mm across. The coatings were fractured and their cross sections were imaged using SEM. Selected coatings were subjected to profilometry in order to confirm whether the elevation of the observed defects was positive or negative.

Table A.1: Array 1, conditions for the deposition of five chromium based coatings.

Sample number	N ₂ inflow (SCCM)	Substrate bias pulse rate (kHz)
1a	0	d.c.
2a	3	d.c.
3a	5	d.c.
4a	7	d.c.
5a	9	d.c.

A.3: Results:

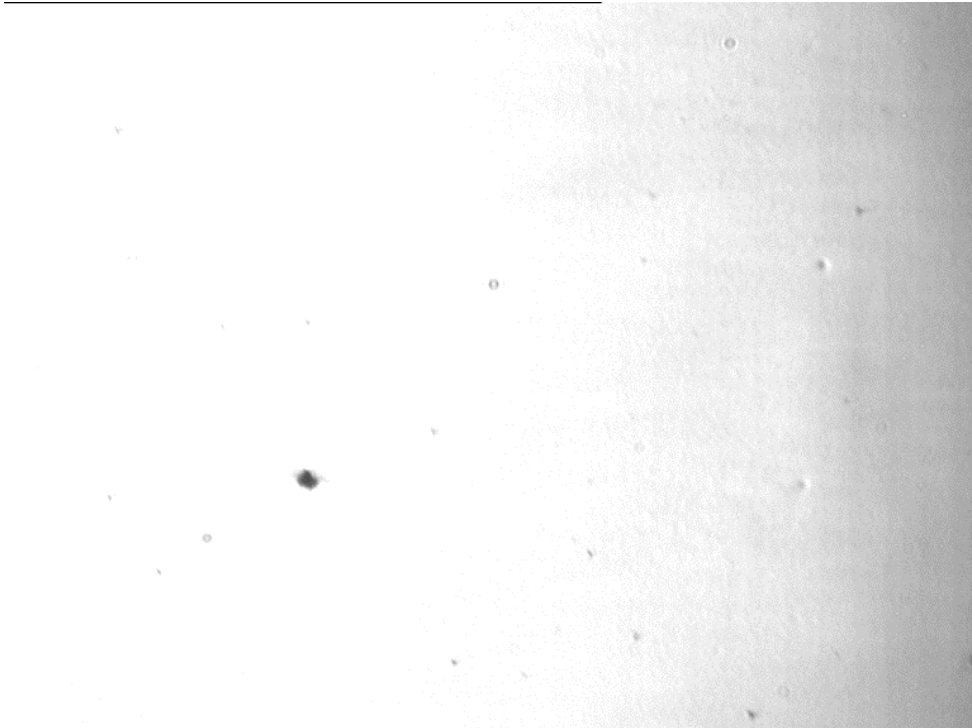


Figure A.1: Optical image of the surface of coating 1a. The image is somewhat overexposed due to the very smooth reflective metallic nature of the surface. The image measures 500 microns along its bottom edge.

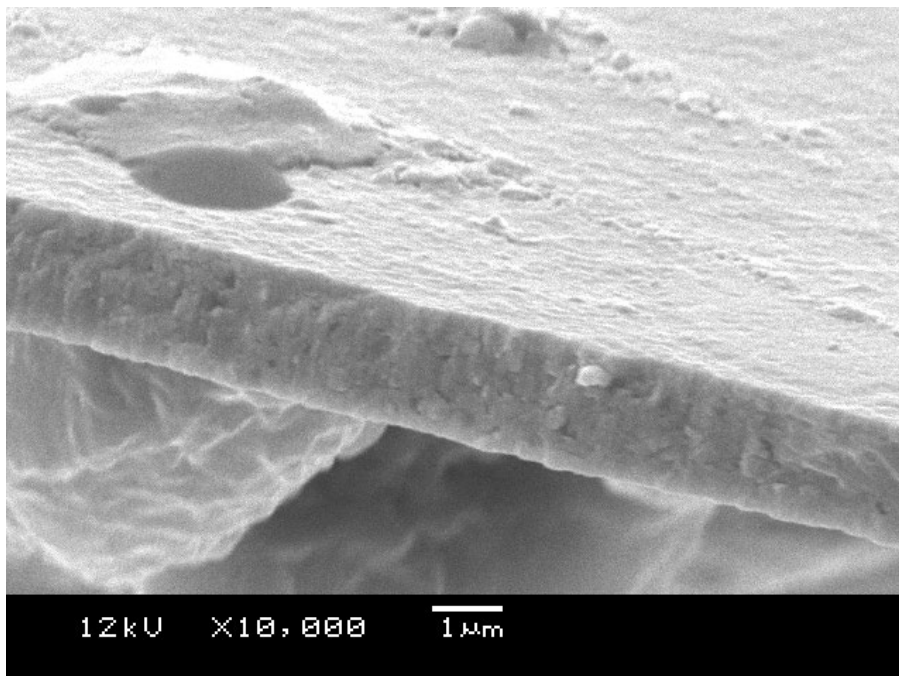


Figure A.2: Fracture cross section of coating 1a. The coating partly delaminated near the fracture, apparently lifting away sections of substrate material, visible in the bottom left hand corner.

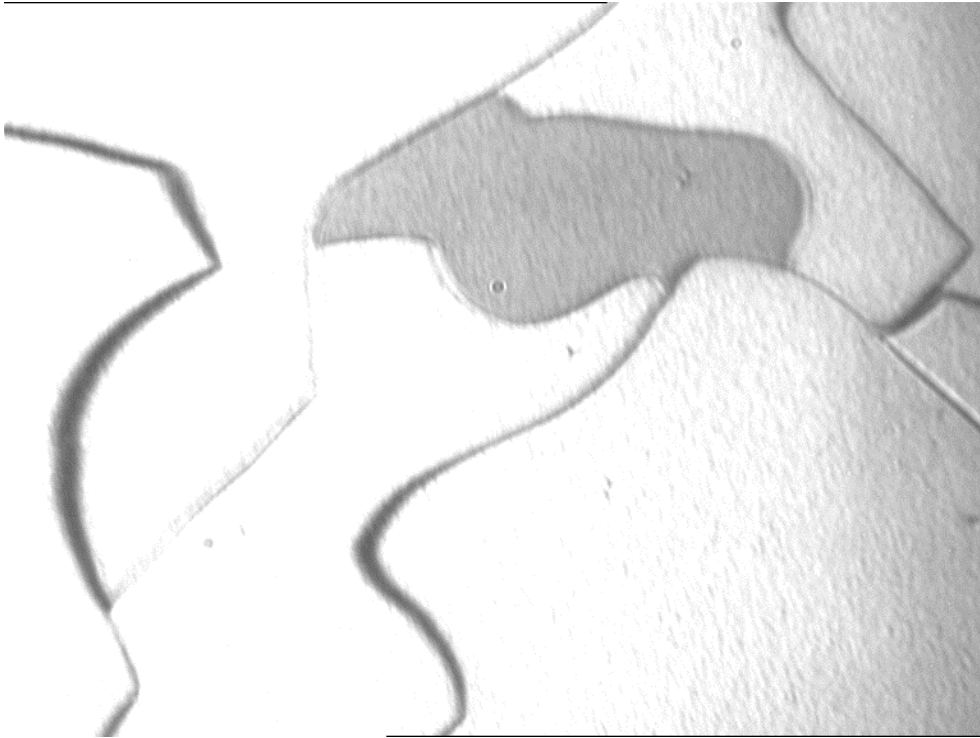


Figure A .3: Optical micrograph of coating 2a. The bright material is the coating, the darker material is the substrate. The image measures approximately 500 microns along its bottom edge.

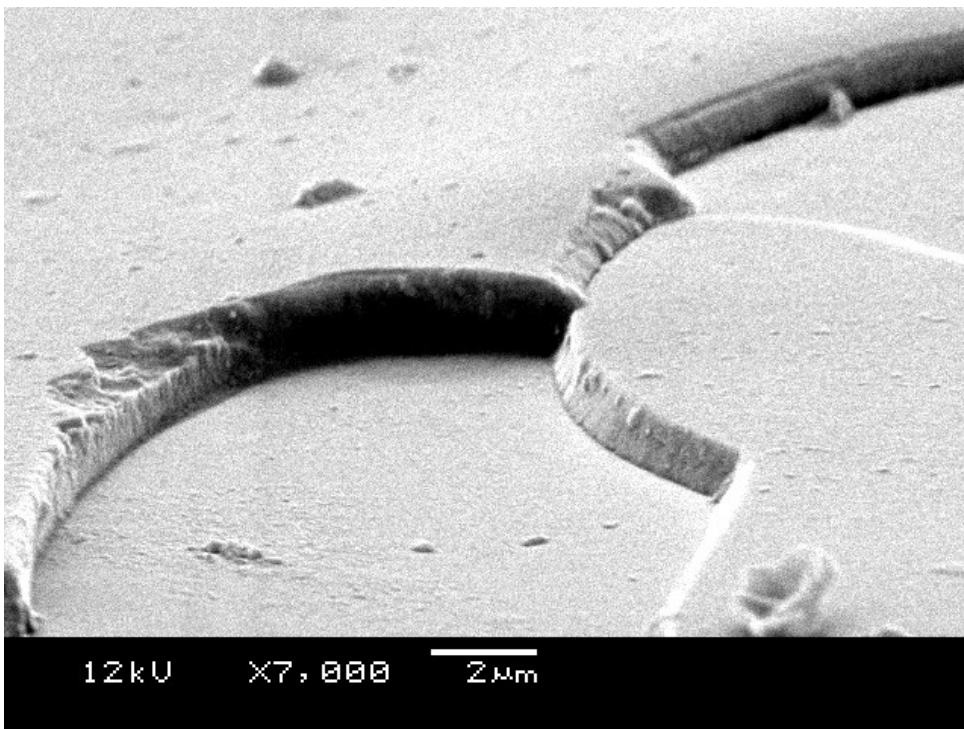


Figure A.4: SEM micrograph of the surface fractures on coating 2a

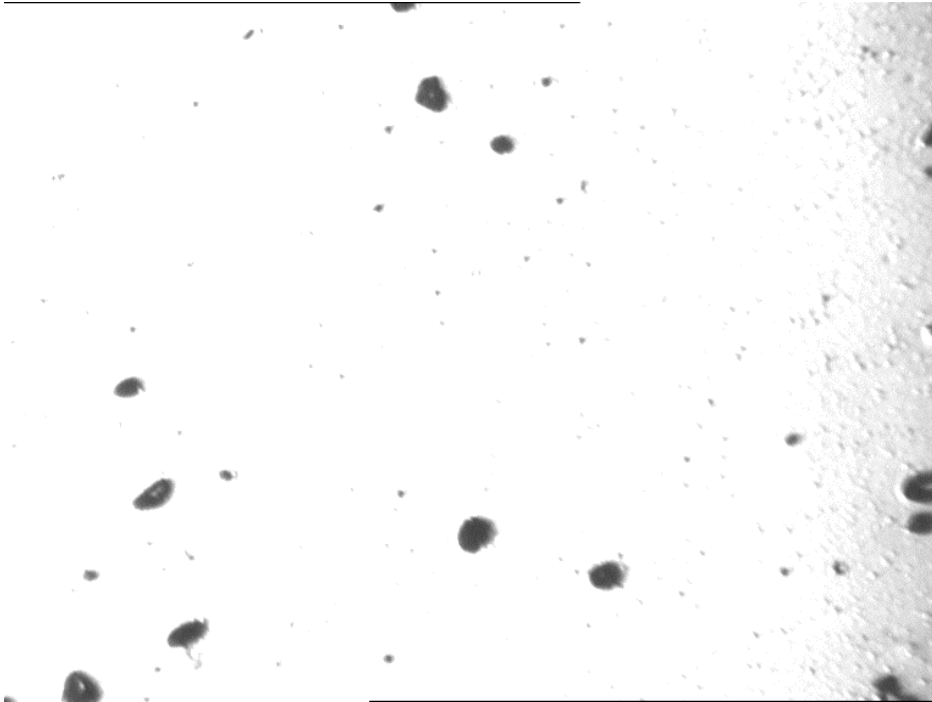


Figure A.5: Optical microscope image of the surface of coating 3a. The light toned material is the coating, the darker toned areas with light centres may be short compression fractures. The image measures approximately 500 microns along its bottom edge.

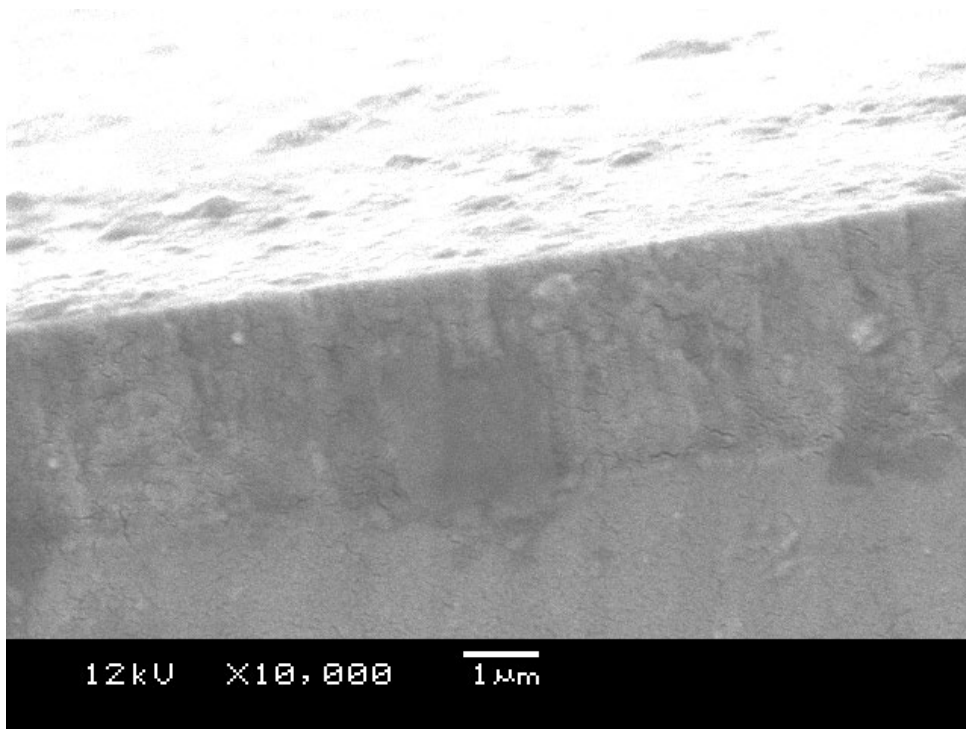


Figure A.6: SEM image of the fracture cross section of coating 3a.

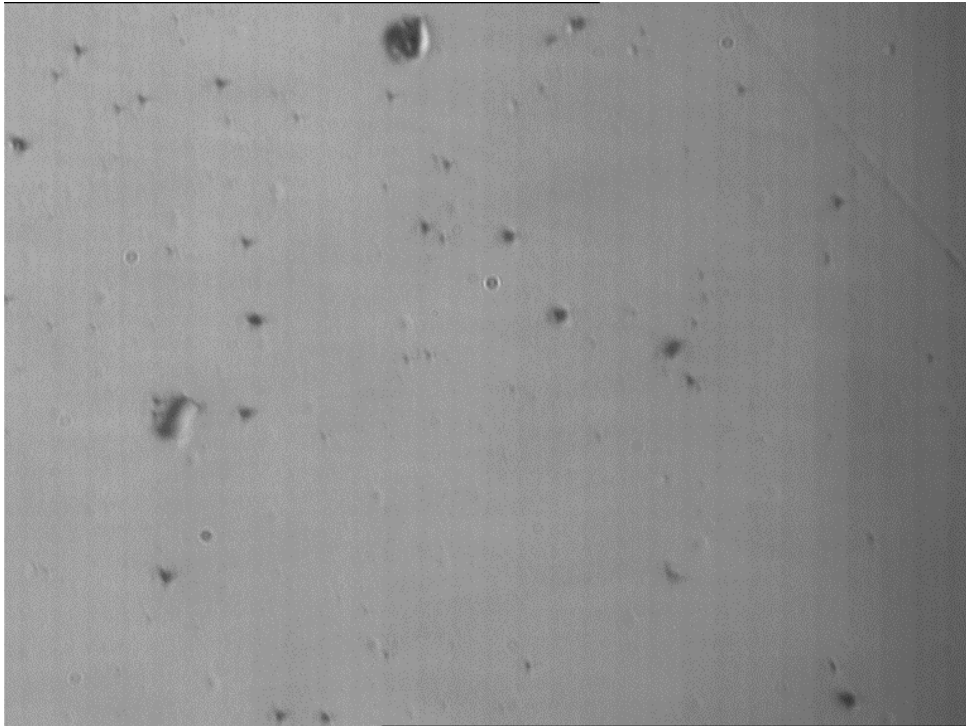


Figure A.7: Optical image of the surface of coating 4a. The image measures approximately 500 microns along its bottom edge.

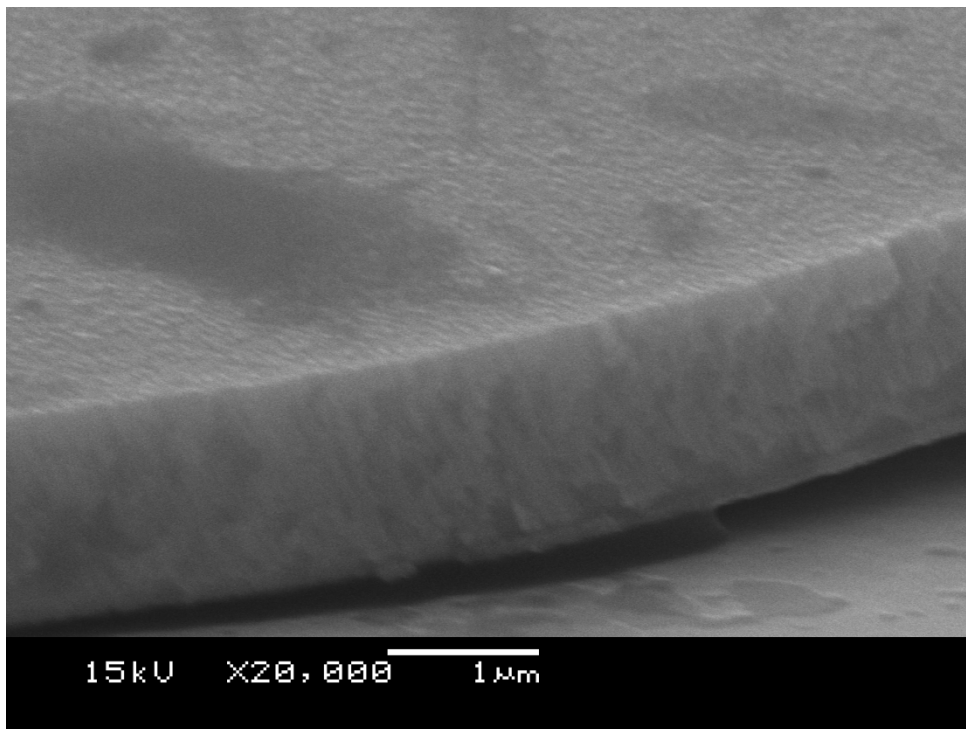


Figure A.8: SEM image of the fracture cross section of coating 4a.

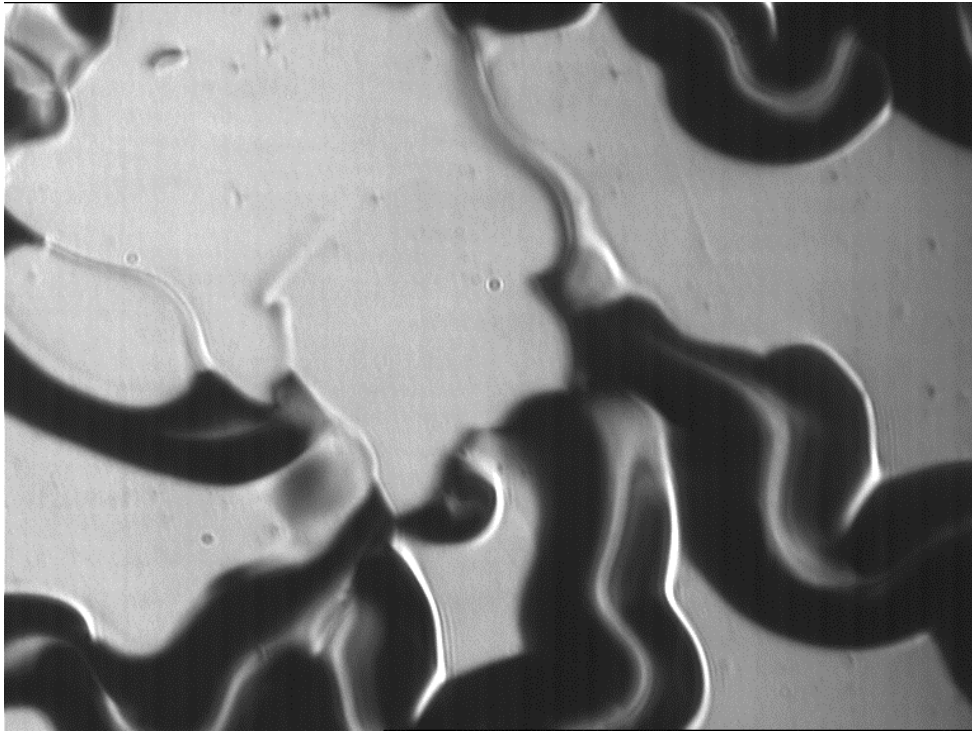


Figure A.9: Optical microscope image of coating 5a. No substrate is visible in this image, the light and dark areas are caused by upwards buckling (telephone chord defects) of the coating. The image measures approximately 500 microns along its bottom edge.

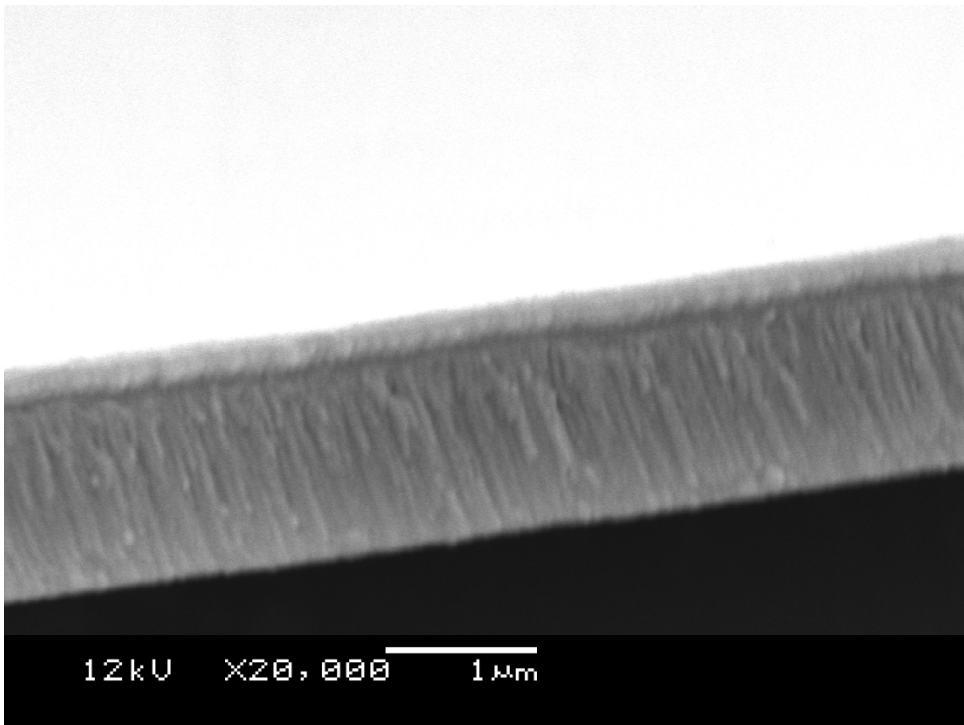


Figure A.10: SEM image of the fracture cross section of coating 5a. Only the coating is visible here as the coating had delaminated away from the fracture for several millimetres in every direction.

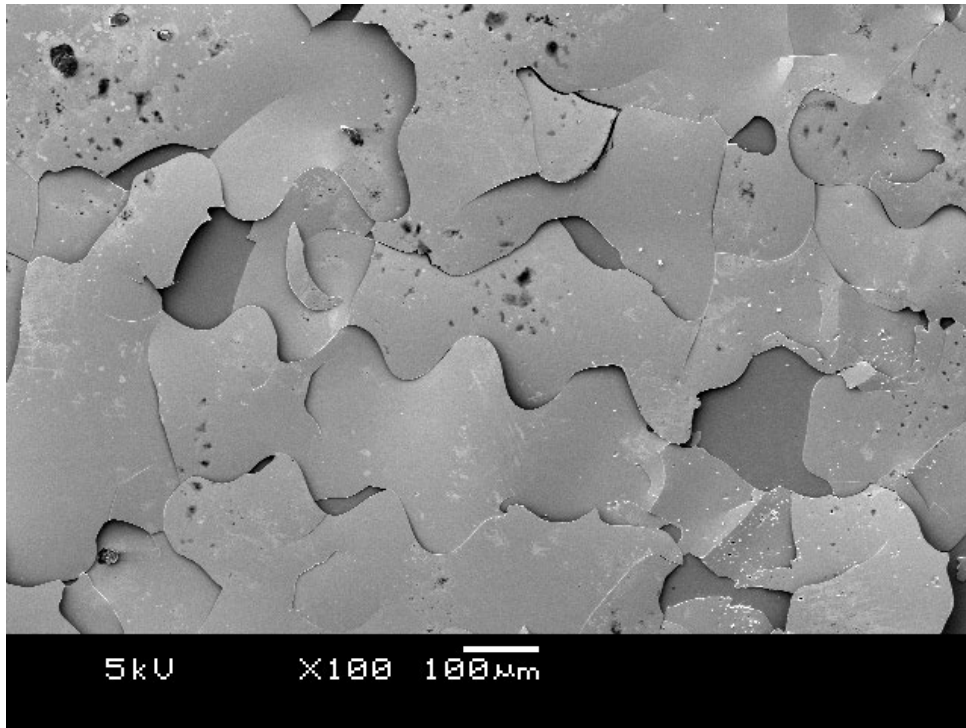


Figure A.11: SEM image of a heavily delaminated section of coating 5a.

A.4: Discussion:

The high substrate bias, application of substrate bias pulsing, and lack of interlayer makes these coating especially vulnerable to delamination and distortion due to internal stresses. In this case we may use this vulnerability as an analytical tool. The optical microscope images reveal detailed changes in topography as nitrogen content increases. Coating 1a deposited with no nitrogen inflow shows a smooth, metallic, surface texture (consistent with Cr) with a small number of defects: two pinhole breaches in the coating are visible on the right hand side, and a ‘pit’ of delaminated material is visible on the left. The SEM shows a fine grained ‘cake mix’ cross section with little sign of true columnar patterning but some evidence of vertical striations. That the coating became delaminated from the substrate during fracturing is a good indication that some internal stress is present.

Coating 2a was deposited with a small level (3 SCCM) of N_2 inflow. The effect upon coating topography has been dramatic: the coating has cracked in a classic ‘mud cracking’ pattern [76] [77][78], with plates of the coating material seemingly separating and shrinking away from each other. This is a strong sign of tensile internal stress. SEM cross

sections show evidence of columnar growth, and some signs of a surface layer of oxide. Coating colour is a light silver colour, often associated with Cr_2N . The XRD analysis of coatings deposited with approximately this level of nitrogen (figure 7.11) shows that it is associated with a mixed phase coating, with abundant Cr_2N structures.

Coating 3a, deposited at 5 SCCM of N_2 inflow (equivalent to 65% of FMS) shows small upward bulging surface defects (as confirmed by dektak profilometry) with bright centres. These are possible indicators of internal compressive stress. The coating appears to be slightly rough in texture, with a light toned, highly reflective, silver coloured surface. SEM imaging of the fracture cross section shows a fine grained texture with no obvious columns or column heads on the surface.

Coating 4a, deposited at 7 SCCM of N_2 inflow, once again shows a smooth texture, though with more defects than coating 1a. The colour of the material has changed significantly, from light silver to a darker grey, and is less reflective. This change is often associated with CrN as opposed to Cr_2N . The SEM cross section shows a dense packed columnar structure. The general texture of the coating is still smooth and metallic, with a dark grey colour. This change in colour is often associated with the transition to CrN . The SEM cross section shows evidence of columnar growth, with easily visible column heads on the surface. There is no obvious oxide layer on the coating surface.

Coating 5a, deposited with 9 SCCM of nitrogen inflow, shows dramatic evidence of classic ‘telephone chord’ cracking [79]. This is a strong indicator of intense compressive stress. Electron micrographs of the fractures show that the coating has delaminated in many places. Coating colour is a dark grey, associated with CrN . XRD of coatings deposited with approximately this N_2 inflow rate show that Cr_2N structures are less abundant, and CrN has come to dominate. SEM cross section shows a densely packed columnar structure, which has been easily delaminated by the fracture formation, another sign of strong internal stress.

Although morphology alone cannot be taken as definitive these images strongly suggest that there is a change taking place in coating microstructure and the kind of internal stresses being developed with increasing N_2 flow rate. It seems that a Cr coating deposited in this fashion will suffer minimal or no stress, a coating with a low N_2 content, in the

region dominated by Cr₂N structures, may develop tensile stresses. A coating with a slightly higher N content however shows possible signs of a low degree of compressive stress. It is most interesting to suppose that such a slight difference in stoichiometry could cause very similar materials to behave in opposite ways! This is consistent with work by Zhao et al [80]. A coating with a moderate N₂ content, probably a more even mix of CrN/Cr₂N structures does not show any immediately obvious signs of stress. A very N₂ rich coating, in the region associated with a more CrN structure and stoichiometry (figures 7.9 and 7.10), appears to develop symptoms of a strong compressive internal stress. These findings are at best qualitative, and do not apply directly to other coatings due to the vulnerable nature of these coatings to symptoms of stress and lack of magnitude measurements for any stresses present. However it may be taken as an indicator of the kinds of stresses likely to occur in coatings of a given stoichiometry.

A.5 Conclusions:

d.c. Substrate biased Cr coatings were deposited with different nitrogen contents at 1 μm thickness on Si wafers and examined by optical microscopy as they emerged from the deposition chamber. We then fractured the substrates and examined the coatings in cross section by SEM. Although such results cannot be quantitative they suggest that a low nitrogen content coating, dominated by Cr₂N structures, may develop a tensile stress capable of changing surface topography, and a high nitrogen content coating may develop a compressive stress capable of changing surface topography. This will inform further studies of Cr_xN coatings.

Appendix B: Alternate pulsing regimes, effects of pulsing during ion etching:

B.1 Introduction:

Although the main thrust of the project was the effects of pulsed d.c. substrate bias, the pinnacle plus power supply is capable of pulsing in other modes, as described in Chapters 5 and 7 (also given in table 1). These are: synchronous, asynchronous, target pulsed and dual cathode. The effects of depositing simple monolithic Cr_xN coatings in each of these regimes were investigated, with a view to adding to our knowledge of pulsing effects and the responses of thin Cr_xN coatings to them. The influence of pulsed substrate bias ion etching on the substrate and subsequent coating growth was also investigated.

Table B.1: Table of pulsing conditions tested and parameters under which the tests were done.

Name	Target pulse duty	Target pulse frequency (kHz)	Target power (kW)	Substrate pulse frequency (kHz)	Substrate pulse duty	Substrate bias, V	Target/substrate phase relationship
Dual cathode	50%	300	1	300	50%	-75	180 deg out of phase
Synch	50%	300	1	300	50%	-75	In phase
Target pulse	50%	300	1	0	0	-75	N/A
Substrate pulse	0	0	1	300	50%	-75	N/A

B.2 Experimental:

The effects of the alternate bias pulsing regimes were also investigated by the deposition of simple monolithic coatings under standard conditions and 45% full metal signal using synchronous, dual cathode, and target pulsed regimes (array 1). The FMS% was set slightly higher than in other nitrogen rich coatings (which used a 40% FMS % for nitrogen rich coatings) as the OEM system experienced more instability and low FMS % under the dual cathode and synchronous pulse regimes. The coatings were deposited for forty minutes onto {111} surface texture Si wafers and tool steel coupons. Substrates were polished to a 1.5 micron finish. Si wafers were fractured to allow SEM cross sections of the coatings to be taken. EDS analysis was applied to measure coating composition.

Deposition rate was found by masking sections of the Si wafers and measuring the depth of deposited coating using a DekTak profilometer.

Table B.2: Experimental array 1, four coatings deposited in each alternate pulse regime at 100 kHz pulse rate

Sample number	Pulse rate (kHz)	Pulse regime
1a	100	Dual cathode
2a	100	Synchronous
3a	100	Target pulsed
4a	100	Substrate pulsed

Two arrays were also performed to measure the effects of substrate bias pulsing (array 2) and conventional biasing (array 3) during ion etching on coating adhesion. Aside from the stated variables standard conditions were employed throughout.

The energy of the ions used for the ion etching process prior to deposition may have an influence over coating adhesion [106] [107]. An ion bombarding the substrate with a higher energy will disrupt the surface more and create more possible nucleation sites. However high energy ions will also cause greater re-sputtering, and may eliminate some nucleation sites, such as steps, peaks and troughs in the coating microstructure. Insufficient ion energy will fail to remove possible contaminants on the substrate surface, also compromising adhesion [108].

Table B.3: Experimental array 2, designed to test the effects of pulse rate during ion etching on coating adhesion.

Sample number	Etching pulse rate (kHz)	Etching bias (V)
1e	0	-400
2e	175	-400
3e	350	-400

Table B.4: Experimental array 3, designed to test the effects of etching bias on coating adhesion.

Sample number	Etching pulse rate (kHz)	Etching bias (V)
1f	0	-400
2f	0	-500
3f	0	-650

B.3 Results:

Experimental array 1: Microstructure:

The microstructure of the array 1 coatings was examined by SEM fracture cross section. Deposition rate was found using masking and profilometry, and surface roughness was evaluated by AFM.

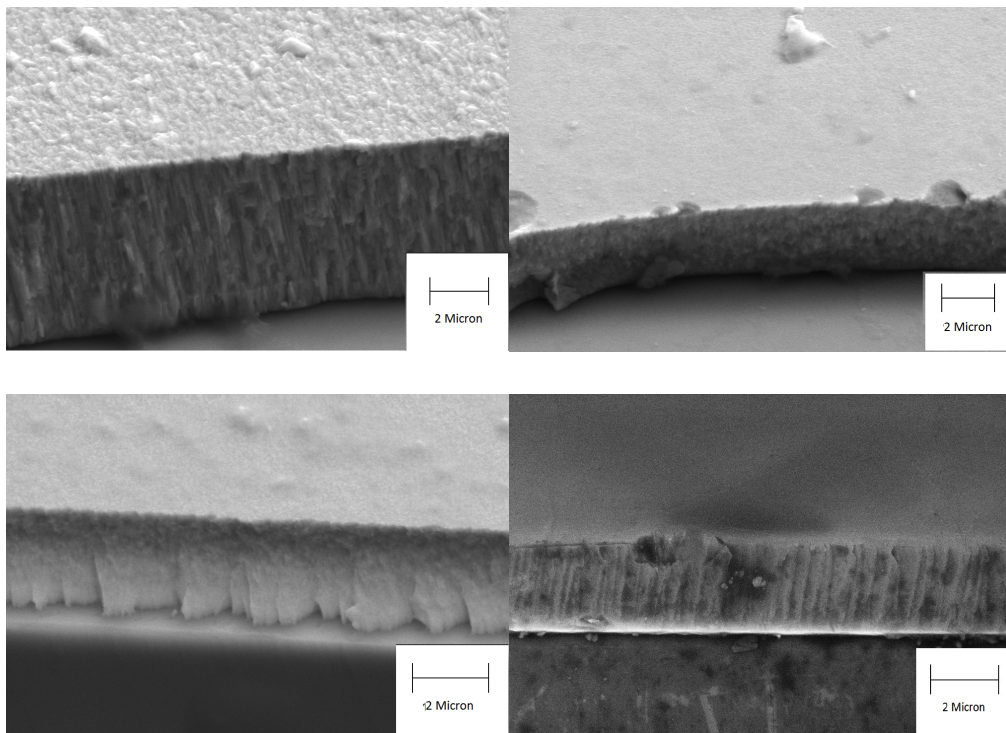


Figure B.1 : Top left: d.c. Comparison. Top right: Dual cathode pulsing. Bottom left: Target pulsing. Bottom right: Substrate pulsing. Images of the synchronously pulsed sample are unavailable as the sample suffered massive spontaneous delamination shortly after being deposited.

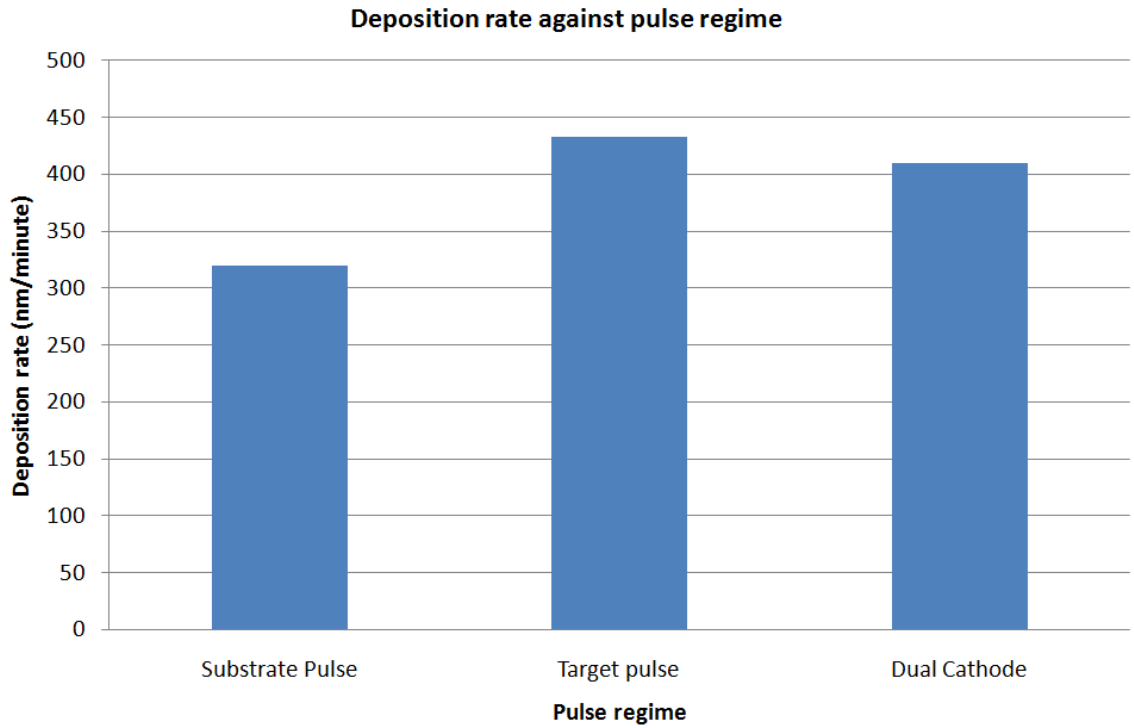


Figure B.2: Deposition rates against pulse regime.

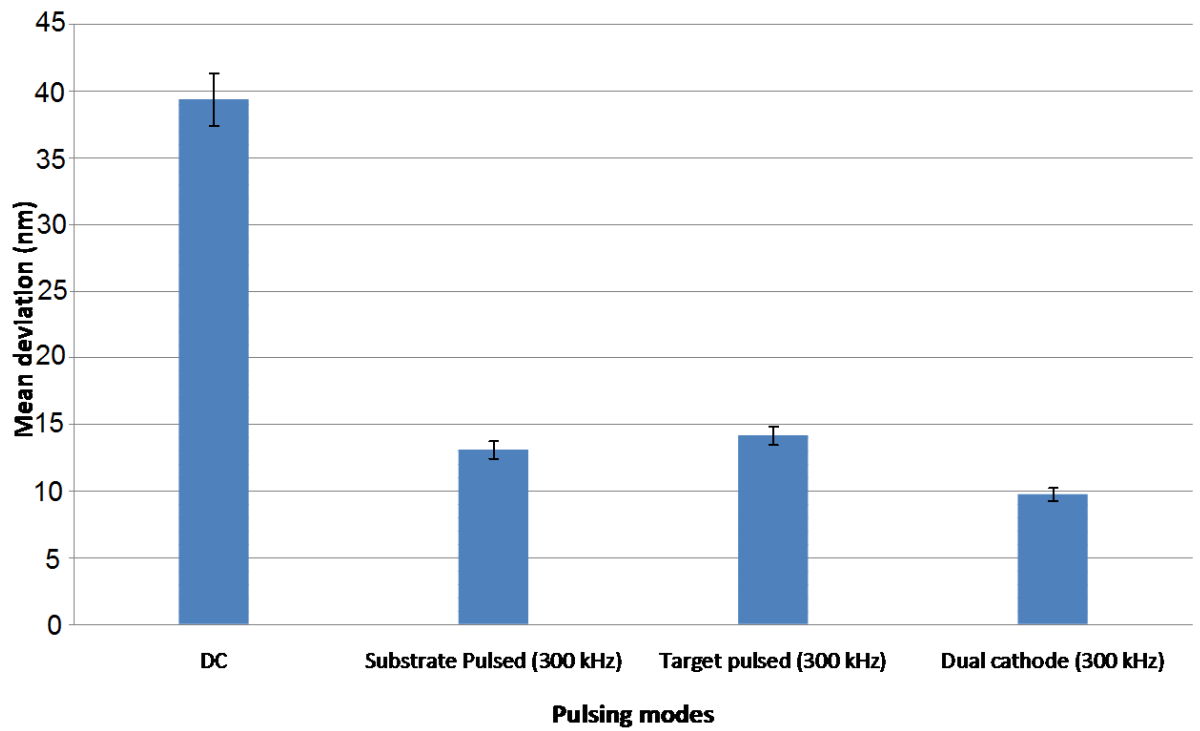


Figure B.3: Mean surface deviation from average level for four films deposited under each of the four pulsing regimes.

Experimental array 1: Tribology:

The array 1 coatings were evaluated scratch adhesion testing and nanoindentation.

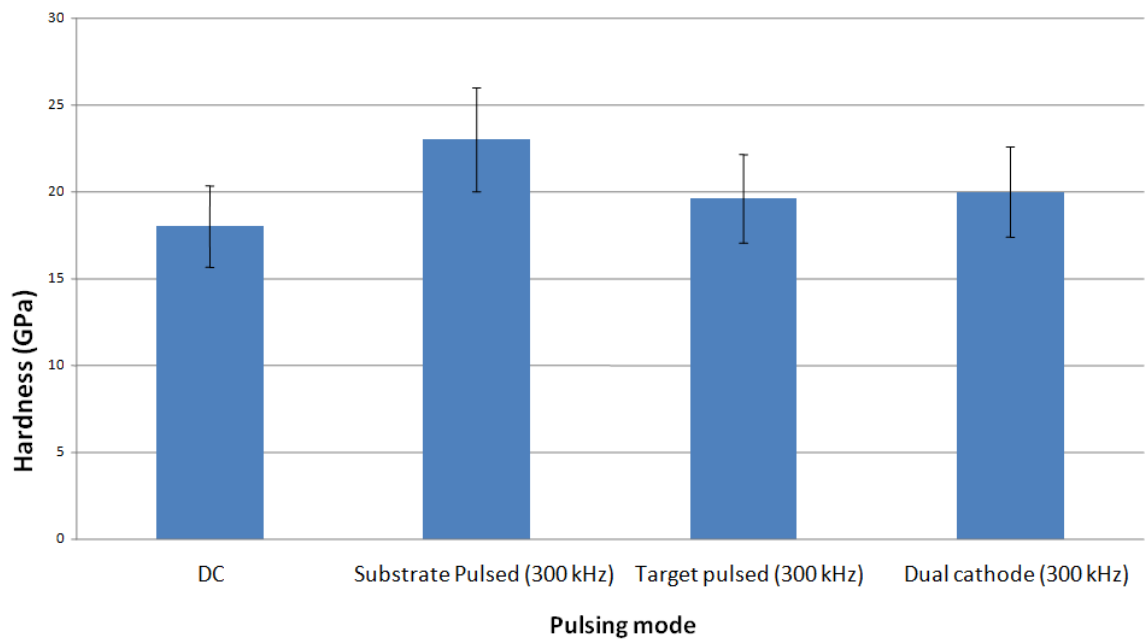


Figure B.4: Hardness values for films deposited under four pulsing regimes.

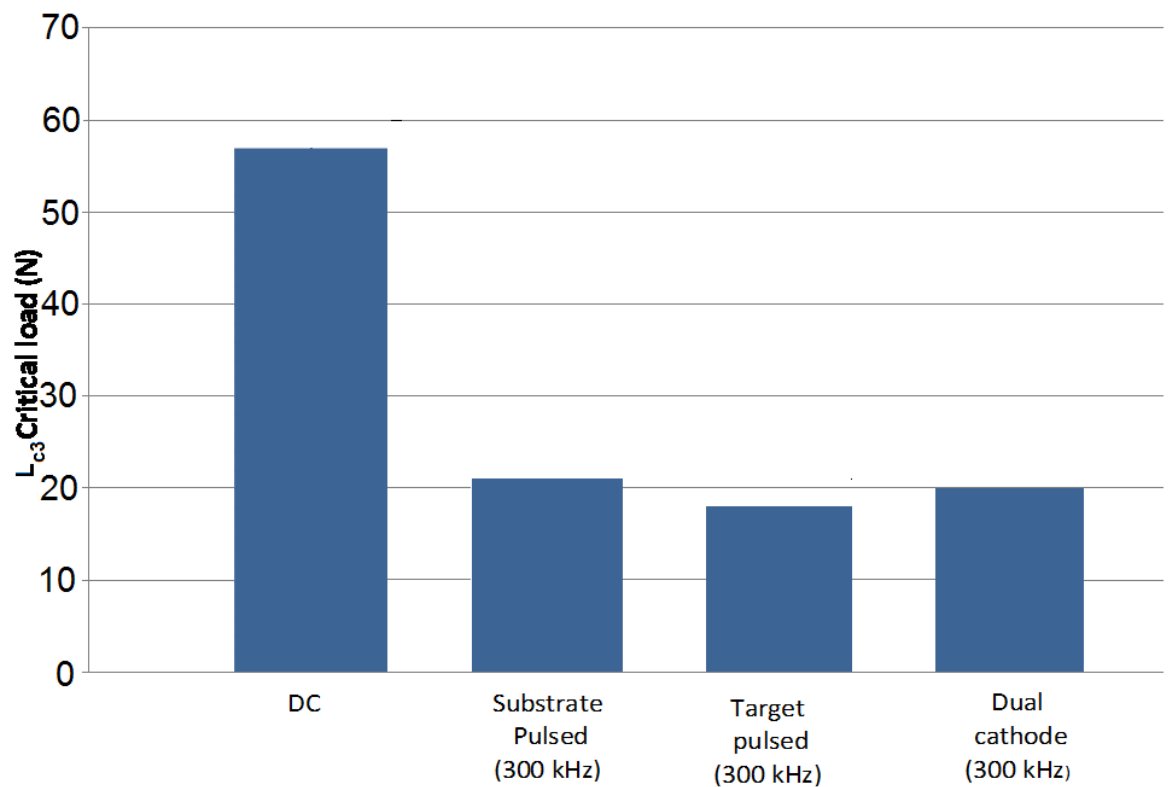


Figure B.5: L_{c3} Critical loads for films deposited under four pulsing regimes.

Experimental arrays 2 and 3:

The adhesion of the coatings in arrays 2 and 3 were evaluated by scratch adhesion testing.

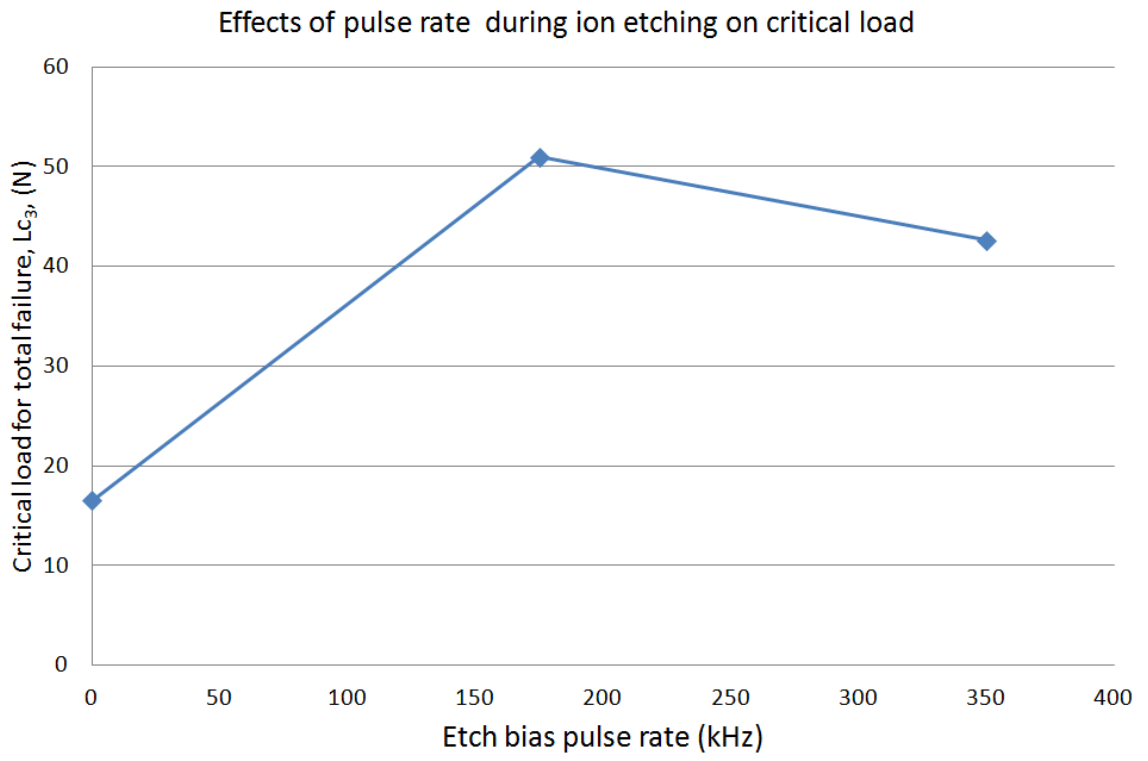


Figure B.6: Variation in L_{c_3} with substrate bias pulse rate during ion cleaning.

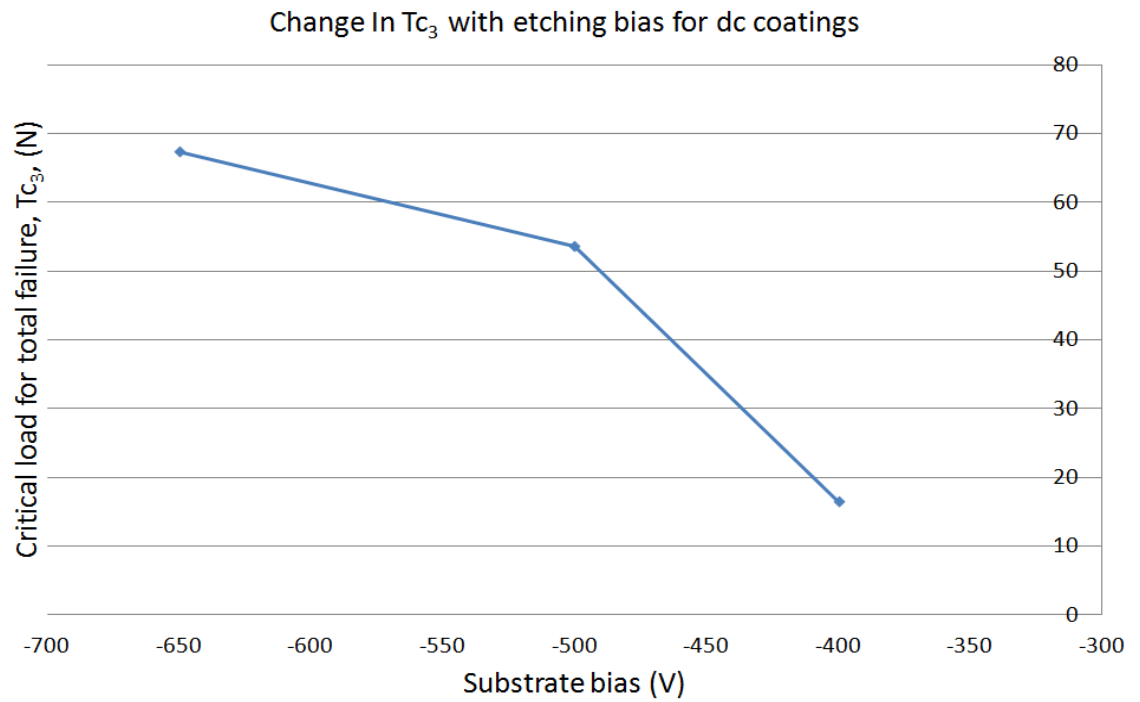


Figure B.7: The change in coating adhesion with substrate bias during ion etching.

B.4 Discussion:

Synchronously pulsed samples suffered massive delamination within minutes of being exposed to atmosphere, and so were unavailable for analysis. Both dual cathode and target pulsing show distinctly higher deposition rates than substrate bias pulsing at the same frequency (figure B.2). AFM results show that all the pulsed regimes produce a significantly smoother coating surface than d.c. deposition, with the lowest mean deviation being the dual cathode pulsed sample (figures B.3 and B.4). All the pulsed coatings show a higher surface hardness, and lower critical load than d.c., as well as a much lower adhesion (figures B.5 and B.6). Dual cathode pulsing and target pulsing both show a ‘fine grained’ texture; distinctly different from the d.c. and substrate pulsed examples (figure B.1). When combined with the observation from Chapter Seven that alternate pulsing regimes develop distinctly different hysteresis curves in a separate, well defined, group it appears likely that all the alternate pulse regimes are being dominated by a common set of processes. While there is no great advantage over substrate pulsed deposition in terms of adhesion or hardness in any of these regimes, a brief burst of target pulsed or dual cathode pulsed deposition may serve to give a coating a smoother surface and reduce friction. The low adhesion of all the alternate pulse regime deposited samples may suggest greater internal stress, although this cannot be confirmed.

Study of the effects of substrate bias pulse rate during etching suggest that mid-range pulsing produces an improvement in coating adhesion over high range pulsing or d.c. (figure B.7). This may reflect a good balance between additional energetic ions removing more contaminant and introducing stress into the subsequent film growth through excessive seeding of defects. Bias value during ion etching seems to be a case of more is better (figure B.8): again the simplest explanation is that lower bias values do not produce sufficient ion energy to remove all contaminants.

B.5 Conclusions:

We have deposited nitrogen rich Cr_xN coatings using three alternate pulsing regimes, and across a range of ion etching conditions. The optimum range of conditions for ion etching, with respect to coating adhesion, appears to be high substrate bias and a mid-range (around 175kHz) substrate bias pulse rate. There alternate bias regimes do not appear to offer

significant advantages of pulsed substrate bias deposition, but the dual cathode pulsing regime may serve to enhance the smoothness of the coating surface if briefly applied at the end of a deposition sequence.